

ISSN 2074-272X

**науково-практичний
журнал**

2022/5



EIE **Електротехніка і** **Електромеханіка**

Electrical Engineering

& Electromechanics

Електротехнічні комплекси та системи

Промислова електроніка

Електроізоляційна та кабельна техніка

Електричні станції, мережі і системи

Журнал включено до найвищої категорії «А»

Переліку фахових видань України

З 2021 р. журнал індексується у Scopus

**З 2015 р. журнал індексується
у Web of Science Core Collection:
Emerging Sources Citation Index**



Electrical Engineering & Electromechanics

Scientific Journal was founded in 2002

Founder – National Technical University «Kharkiv Polytechnic Institute» (Kharkiv, Ukraine)

EDITORIAL BOARD

Sokol Ye.I.	Editor-in-Chief , Professor, Corresponding member of NAS of Ukraine, Rector of National Technical University «Kharkiv Polytechnic Institute» (NTU «KhPI»), Ukraine
Korytchenko K.V.	Deputy Editor , Professor, NTU «KhPI», Ukraine
Rozov V.Yu.	Deputy Editor , Professor, Corresponding member of NAS of Ukraine, A. Pidhorneyi Institute of Mechanical Engineering Problems of NAS of Ukraine, Kharkiv, Ukraine
Bolyukh V.F.	Deputy Editor , Professor, NTU «KhPI», Ukraine
Abu-Siada A.	Professor, Curtin University, Perth, Australia
Aman M.M.	Professor, NED University of Engineering & Technology, Karachi, Pakistan
Baltag O.	Professor, Grigore T. Popa University Medicine and Pharmacy, Romania
Baranov M.I.	Professor, Research and Design Institute «Molniya» of NTU «KhPI», Ukraine
Batygin Yu.V.	Professor, Kharkiv National Automobile and Highway University, Ukraine
Bíró O.	Professor, Institute for Fundamentals and Theory in Electrical Engineering, Graz, Austria
Bouktir T.	Professor, Ferhat Abbas University, Setif 1, Algeria
Buriakovskiy S.G.	Professor, NTU «KhPI», Ukraine
Butkevych O.F.	Professor, Institute of Electrodynamics of NAS of Ukraine (IED of NASU), Kyiv, Ukraine
Colak I.	Professor, Nisantasi University, Istanbul, Turkey
Cruz S.	Professor, University of Coimbra, Portugal
Doležel I.	Professor, University of West Bohemia, Pilsen, Czech Republic
Féliachi M.	Professor, Technological Institute of Saint-Nazaire, University of Nantes, France
Grinchenko V.S.	PhD, A. Pidhorneyi Institute of Mechanical Engineering Problems of NAS of Ukraine, Kharkiv, Ukraine
Gurrero J.M.	Professor, Aalborg University, Denmark
Gurevich V.I.	PhD, Honorable Professor, Central Electrical Laboratory of Israel Electric Corporation, Haifa, Israel
Hajjar A.A.	Professor, Tishreen University, Latakia, Syrian Arab Republic
Ida N.	Professor, The University of Akron, Ohio, USA
Izykowski J.	Professor, Wroclaw University of Science and Technology, Poland
Kildishev A.V.	Associate Research Professor, Purdue University, USA
Klepikov V.B.	Professor, NTU «KhPI», Ukraine
Korzeniewska E.	Professor, Lodz University of Technology, Poland
Ktena A.	Professor, National and Kapodistrian University of Athens, Greece
Kuznetsov B.I.	Professor, A. Pidhorneyi Institute of Mechanical Engineering Problems of NAS of Ukraine, Kharkiv, Ukraine
Kyrylenko O.V.	Professor, Academician of NAS of Ukraine, IED of NASU, Kyiv, Ukraine
Levin B.M.	Professor, Holon Institute of Technology, Tel Aviv-Yafo, Israel
Malik O.P.	Professor, University Of Calgary, Canada
Maslov V.I.	Professor, National Science Center «Kharkiv Institute of Physics and Technology», Ukraine
Mi Zou	PhD, Chongqing University of Posts and Telecommunications, China
Mikhaylov V.M.	Professor, NTU «KhPI», Ukraine
Miljavec D.	Professor, University of Ljubljana, Slovenia
Milykh V.I.	Professor, NTU «KhPI», Ukraine
Nacke B.	Professor, Gottfried Wilhelm Leibniz Universität, Institute of Electrotechnology, Hannover, Germany
Petrushin V.S.	Professor, Odessa National Polytechnic University, Ukraine
Podoltsev A.D.	Professor, IED of NASU, Kyiv, Ukraine
Reutskiy S.Yu.	PhD, A. Pidhorneyi Institute of Mechanical Engineering Problems of NAS of Ukraine, Kharkiv, Ukraine
Rezinkin O.L.	Professor, NTU «KhPI», Ukraine
Rezinkina M.M.	Professor, NTU «KhPI», Ukraine
Shcherbak Ya.V.	Professor, NTU «KhPI», Ukraine
Sikorski W.	Professor, Poznan University of Technology, Poland
Suemitsu W.	Professor, Universidade Federal Do Rio de Janeiro, Brazil
Trichet D.	Professor, Institut de Recherche en Energie Electrique de Nantes Atlantique, France
Vaskovskiy Yu.M.	Professor, National Technical University of Ukraine «Igor Sikorsky Kyiv Polytechnic Institute», Kyiv, Ukraine
Vazquez N.	Professor, Tecnológico Nacional de México en Celaya, Mexico
Vinnikov D.	Professor, Tallinn University of Technology, Estonia
Yagup V.G.	Professor, O.M. Beketov National University of Urban Economy in Kharkiv, Ukraine
Yatchev I.	Professor, Technical University of Sofia, Bulgaria
Zagirnyak M.V.	Professor, Member of NAES of Ukraine, Kremenchuk M.Ostrohradskiy National University, Ukraine
Zgraja J.	Professor, Lodz University of Technology, Poland
Grechko O.M.	Executive Managing Editor , PhD, NTU «KhPI», Ukraine

From no. 1 2021 Journal «Electrical Engineering & Electromechanics» is indexing in **Scopus** and from no. 1 2015 Journal is indexing in **Web of Science Core Collection: Emerging Sources Citation Index (ESCI)**.

Also included in DOAJ (Directory of Open Access Journals), in EBSCO's database, in ProQuest's databases – Advanced Technologies & Aerospace Database and Materials Science & Engineering Database, in Gale/Cengage Learning databases.

Editorial office address:

National Technical University «Kharkiv Polytechnic Institute», Kyrpychova Str., 2, Kharkiv, 61002, Ukraine

phones: +380 57 7076281, +380 67 3594696, e-mail: a.m.grechko@gmail.com (**Grechko O.M.**)

ISSN (print) 2074-272X

ISSN (online) 2309-3404

© National Technical University «Kharkiv Polytechnic Institute», 2022

Printed 07 September 2022. Format 60 × 90 1/8. Paper – offset. Laser printing. Edition 200 copies.

Printed by Printing house «Madrid Ltd» (18, Gudanova Str., Kharkiv, 61024, Ukraine)



Table of Contents

Electrotechnical Complexes and Systems

Buriakovskiy S.G., Asmolova L.V., Maslii An.S., Maslii Ar.S., Obruch I.V. Development and study of a microprocessor automatic control system for a mono-switch tie type with a linear inductive electric motor and a discrete speed controller..... 3

Guezi A., Bendaikha A., Dendouga A. Direct torque control based on second order sliding mode controller for three-level inverter-fed permanent magnet synchronous motor: comparative study 10

Hassainia S., Ladaci S., Kechida S., Khelil K. Impact of fractional filter in PI control loop applied to induction motor speed drive 14

Kuznetsov B.I., Nikitina T.B., Bovdui I.V., Voloshko O.V., Kolomiets V.V., Kobylanskyi B.B. The method of multi objective synthesis of stochastic robust control by multimass electromechanical systems under non-gaussian random external disturbances 21

Industrial Electronics

Chandramouli B., Vijayaprabhu A., Arun Prasad D., Kathiravan K., Udhayaraj N., Vijayasanthi M. Design of single switch-boosted voltage current suppressor converter for uninterrupted power supply using green resources integration 31

Janardhan G., Surendra Babu N.N.V., Srinivas G.N. Single phase transformerless inverter for grid connected photovoltaic system with reduced leakage current 36

Latreche S., Khenfer A., Khemliche M. Sensors placement for the faults detection and isolation based on bridge linked configuration of photovoltaic array 41

Electrical Insulation and Cable Engineering

Poliakov M.O., Vasylevskiy V.V. Method for assessing unevenness of cellulose insulation layers aging of power transformers winding 47

Power Stations, Grids and Systems

Abid M., Laribi S., Larbi M., Allaoui T. Diagnosis and localization of fault for a neutral point clamped inverter in wind energy conversion system using artificial neural network technique..... 55

Muthubalaji S., Devadasu G., Srinivasan S., Soundiraraj N. Development and validation of enhanced fuzzy logic controller and boost converter topologies for a single phase grid system 60

Rachedi M.Y., Bechki D., Marif Y., Bouguetaia H. Solar flat plate collector enhanced by two reflectors: optimum tilts of reflectors 67

Rozov V.Yu., Reutskiy S.Yu., Pelevin D.Ye., Kundius K.D. Approximate method for calculating the magnetic field of 330-750 kV high-voltage power line in maintenance area under voltage 71

S.G. Buriakovskiy, L.V. Asmolova, An.S. Maslii, Ar.S. Maslii, I.V. Obruch

Development and study of a microprocessor automatic control system for a mono-switch tie type with a linear inductive electric motor and a discrete speed controller

Introduction. The article is devoted to the development of the microprocessor automatic control system for a gearless controlled electric drive of a mono-switch tie based on a linear inductor electric motor. This solution provides control the position of the switch point, to carry out the transfer process with a smooth drive of shanks to the frame rail, to protect electric motor elements from overloads. **Goal.** Development and study of the behavior of microprocessor automatic control system for mono-switch tie type with linear inductive electric motor and discrete PID speed controller which coefficients are adjusted according to Chien-Hrones-Reswick method to meet modern traffic safety requirements and improve operational reliability factors. **Methodology.** On the basis of electric drive theory, a kinematic line of a mono-switch tie type with nonlinear friction characteristic is presented. Using differential equation theory and Laplace transformation, a mathematic description of a linear inductor electric motor has been made. Using the z-transform method, a difference equation for describing a discrete PID speed controller is obtained, the coefficients of which are derived using the Chien-Hrones-Reswick method. A simulation mathematical model of the electric drive mono-switch tie type as the microprocessor automatic control system with linear inductive electric motor and discrete PID speed controller and nonlinear friction characteristic was built in MATLAB. **Results.** Simulation modelling of a mathematical model of the microprocessor automatic control system of the electric drive mono-switch tie type with the linear inductive electric motor and discrete PID speed controller and nonlinear friction characteristic have been developed and performed. Studies of dynamics of switch point movement have shown that, a drive time of less than 0.7 s at a constant speed motor armature of 0.2 and 0.3 m/s provides to meet modern requirements for railway switch points. The application of discrete PID speed controller has shown improved dynamics of switch point. **Originality.** First for the electric drive of the mono-switch tie type with linear inductive electric motor a mathematical model of the discrete PID speed controller and nonlinear friction characteristic as an object of speed control of switch point movement, has been developed. **Practical value.** Mathematical model of a railway track switch of the mono-switch tie type with linear inductive electric motor and discrete PID speed controller has been developed to carry out the control of the position of the switch point, process with a smooth drive them to the frame rail, to protect electric motor elements from overloads. References 25, tables 2, figures 12.

Key words: electric drive with linear inductive electric motor, electromechanical system, control system, discrete PID speed controller.

Робота присвячена розробці мікропроцесорної системи автоматичного керування безредукторним регульованим електроприводом стрілочного переводу моношпального типу на базі лінійного індукторного двигуна. Таке рішення дозволяє контролювати положення гостряків, здійснювати процес переводу з плавним доводом гостряків до рамної рейки, захистити елементи електродвигуна від перевантажень. Запропоновано структурну схему дискретного ПІД-регулятора швидкості, синтезованого в z-зображенні та отримано діаграми розподілу його коефіцієнтів за методом Чіна-Хронса-Ресвіка. Наведені результати комп'ютерного моделювання показали, що час переводу гостряків менший ніж 0,7 с при сталому рівні задання швидкості якоря 0,2 і 0,3 м/с, що дозволяє реалізувати сучасні вимоги до стрілочних переводів залізничного транспорту. Бібл. 25, табл. 2, рис. 12.

Ключові слова: електропривод з лінійним індукторним двигуном, електромеханічна система, система керування, дискретний ПІД-регулятор швидкості.

Introduction. The transport system is an important component of the economic growth of the national economies of the world economy. The development of railway international transport networks contributes to the integration of trade between the European Union (EU) and Ukraine. Therefore, the renewal of the transport infrastructure of Ukraine is one of the main directions of the implementation of the National Transport Strategy of Ukraine for the period until 2030 [1], which lays the foundation for changes in the transport sector for the next 8 years, namely the development of new high-speed interregional connections, connections with EU countries and the renewal urban transport infrastructure [2].

Turnouts are an integral part of the railway infrastructure. The development of their automation systems and the improvement of service technologies contribute to a large extent to the increase of traffic safety and the improvement of economic indicators of railway activity [3–5].

Global companies are working on the creation of new types of turnouts [6, 7], namely, their mono-switch

tie implementation. Their general concept, both for normal and high-speed traffic, comes down to ensuring maximum reliability and safety, with minimal ongoing maintenance costs. Modern turnouts are equipped with new electric motors [7–10] and control systems [4, 11].

In Ukraine, the lack of adjustable electric drives for turnouts requires the creation of specialized electric drives. To increase their efficiency, there is a need to create new types of electric drives [12–14]. In [15], the questions of the development of the functionality of the railway turnout by introducing an electric drive with a valve-inductor motor were considered, which is justified by the simplification of the mechanical part of the turnout by replacing the gearbox with a ball-screw pair and placing the entire kinematic line of the turnout on one sleeper.

The replacement of rotary electric motors with linear ones provides even more simplification of the design, which ensures an increase in efficiency, a decrease in maintenance costs, and an increase in the reliability of the

operation of turnouts. A distinctive feature of such motors is their ability to convert electrical energy into mechanical translational movements of the executive mechanisms of the turnouts – points and movable cores of the crossbars, directly, without intermediate mechanical converters. The electric drive taking into account linear electric motors of the electromagnetic type (LMEEMT) was considered in [16]. The rationality of such a technical solution consists in the reserve of excess energy, which takes place at the end of the cycle of the electric drive of the turnout, in order to use it later at the beginning of the movement of the turnout. This article is devoted to the improvement of the microprocessor system of automatic control of the gearless adjustable electric drive of the mono-switch tie type based on the linear motor of the inductor type to obtain a given law of control of the movement of the sharps and reduce the time of the switch transfer.

The peculiarity of turnouts of this type is that, thanks to the unique properties of the structures and the capabilities of the control systems, they ensure high accuracy of the positioning of the spikes and the necessary controllability of the traction force, taking into account the increase in speed and cargo flow of transportation.

Thus, the way proposed in the article to create a new control system for the electric drive of the turnout is relevant from the point of view of the need to transition to a new modern element base of automation systems and new design solutions.

The purpose of the article is the development of a microprocessor-based system for automatic control of a mono-switch tie type turnout with a linear inductive electric motor (LIEM) and a discrete proportional-integral-differential (PID) speed controller with adjusted coefficients according to the Chien-Hrones-Reswick method to ensure modern traffic safety requirements.

To achieve the intended goal, the following tasks are set:

- development of a system of automatic control of a mono-switch tie type turnout with LIEM, which allows the transfer process to be carried out with a smooth approach of the spikes to the frame rail, protection of the motor from overloads and control of the position of the spikes for high-speed and ultra-high-speed electric transport railways;
- synthesis of a discrete PID speed controller for an electric drive with an inductive motor, as an element of improvement of the microprocessor system of automatic control of the turnout transfer to improve its operation both in regular and non-stationary modes.

Research material. The functional diagram of the electric drive of the turnout is shown in Fig. 1, which includes three units: a LIEM, a speed regulator with a power converter as part of the control unit, and a sensor for the position of the spikes, which monitors the movement of the spikes and their close fit to the frame rail.

Figure 2,*a* shows the cross-section of the LIEM, which is placed in the sleeper as shown in Fig. 2,*b*.

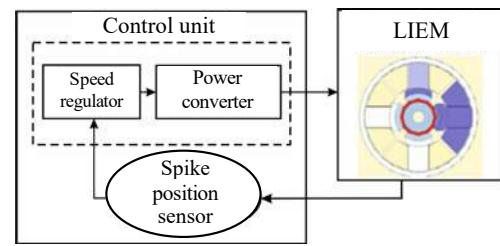


Fig. 1. Functional diagram of the electric drive of the turnout with LIEM

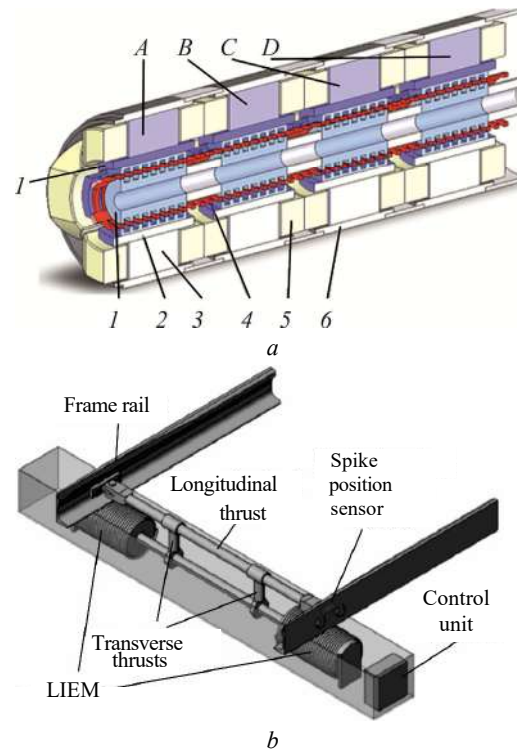


Fig. 2. Design of LIEM (*a*)

and placing it in one sleeper (*b*):

- 1 – stator; 2 – pole tips of the external stator;
3 – poles; 4 – armature; 5 – phase coils; 6 – housing

The linear electric motor has four phases *A, B, C, D* and consists of two stators 1 (internal and external), which makes it possible to obtain a minimum air gap in the inter-tooth area with small dimensions of the machine, concentrating the magnetic flux in the tooth area. Alternating switching on of the phases of the electric motor (*A, B, C, D*) ensures a uniform distribution of the electromagnetic force during the movement of the armature 4. When increasing the number of coils (phases), it is possible, if necessary, to significantly reduce the fluctuation of the force acting on the armature during its movement. Additional armature advantage of this design of the induction motor is the relatively long length of the armature compared to the electromagnet, which will allow to easily implement the movement of the spikes without changing other overall dimensions of the motor.

Depending on the signal from the sensor of the position of the spikes, which are installed on the outside of the frame rail and provide control over the tight fit of the spike to it, the power converter, located in the control unit and made on the basis of field-effect or IGB transistors, connects the stator coil to the power source.

And the electric motor converts electrical energy into mechanical energy, setting the armature in motion.

Such an electric motor requires a different automatic control system than LMEMT and, as a result, another solution, but provides reverse operation without the use of additional springs [16].

The mathematical description and simulation model of LIEM based on the solution of the Lagrange equation is given in [17] and in the normal Cauchy form has the form:

$$\left\{ \begin{aligned} \frac{di_A}{dt} &= \frac{1}{\frac{\partial \Psi_A(i_A, x)}{\partial i_A}} \left(U_A - r_A i_A - \frac{\partial \Psi_A(i_A, x)}{\partial x} v \right); \\ \frac{di_B}{dt} &= \frac{1}{\frac{\partial \Psi_B(i_B, x)}{\partial i_B}} \left(U_B - r_B i_B - \frac{\partial \Psi_B(i_B, x)}{\partial x} v \right); \\ \frac{di_C}{dt} &= \frac{1}{\frac{\partial \Psi_C(i_C, x)}{\partial i_C}} \left(U_C - r_C i_C - \frac{\partial \Psi_C(i_C, x)}{\partial x} v \right); \\ \frac{di_D}{dt} &= \frac{1}{\frac{\partial \Psi_D(i_D, x)}{\partial i_D}} \left(U_D - r_D i_D - \frac{\partial \Psi_D(i_D, x)}{\partial x} v \right); \\ \frac{dv}{dt} &= \frac{F_{el} - F_{on} - \alpha v}{m}; \\ \frac{dx}{dt} &= v, \end{aligned} \right. \quad (1)$$

where U_A, U_B, U_C, U_D is the voltage of power sources; $r_A, r_B, r_C, r_D, i_A, i_B, i_C, i_D$ are the active resistances and currents in the corresponding phases of the stator; $\Psi_A, \Psi_B, \Psi_C, \Psi_D$ are the flux linkages of the respective phases; x is the displacement of the armature; F_{on} is the resistance force; α is the coefficient of friction between the guide and the armature; v is the armature movement speed; m is the mass of the armature; F_{el} is the driving force of the electric motor.

An electronic switch is required to connect the motor phases to the power source and adjust the voltage on it. Since the operation of the LIEM does not depend on the direction of the current in the phase, a half-bridge circuit is usually used to switch the current in it [18]. A fragment of the circuit of the electronic switch (for phase A) is shown in Fig. 3.

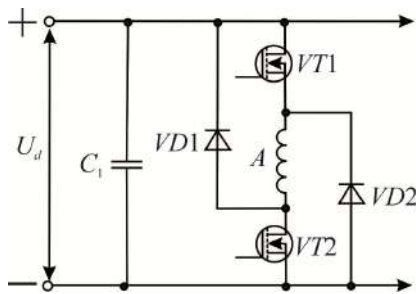


Fig. 3. Schematic of phase A of the electronic switch for a 4-phase LIEM

Phases (A, B, C, D) are included between semiconductor switches (phase A – VT1 – VT2; phase B –

VT3 – VT4; phase C – VT5 – VT6; phase D – VT7 – VT8) operating in PWM mode depending from the position of the spikes and the direction of their movement. Protective diodes (for phase A – VD1 – VD2; for phase B – VD3 – VD4; for phase C – VD5 – VD6; for phase D – VD7 – VD8) ensure the flow of current after closing the upper or lower switches in the phases.

To control the LIEM, a digital PID speed controller was synthesized, which is described by the transfer function:

$$W_p(z) = K_p + K_i \frac{T_0 z}{z-1} + K_d \frac{z-1}{T_0 z}, \quad (2)$$

where K_p is the transfer coefficient of the proportional component; K_i is the transfer coefficient of the integral component; K_d is the transfer coefficient of the differential component; T_0 is the period of discretion, s.

Based on the transfer function (2), a difference equation was obtained that describes the algorithm of the discrete PID controller:

$$\begin{aligned} u[n] &= K_p e[n] + K_i (u[n-1] + T_0 e[n]) + \\ &+ \frac{K_d}{T_0} (e[n] - e[n-1]) = \\ &= K_p e[n] + K_i T_0 e[n] + \frac{K_d}{T_0} (e[n] - e[n-1]) + K_i u[n-1]. \end{aligned} \quad (3)$$

According to (3), the structural diagram shown in Fig. 4 is built.

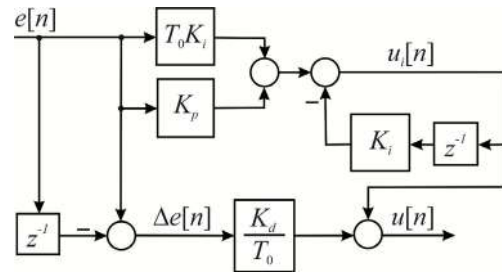


Fig. 4. The structure of the discrete PID controller

Since the LIEM is described by a nonlinear function [17], the standard methods used for adjustment of linear objects are not suitable for adjustment of the coefficients of the PID controller [6, 19]. Therefore, their calculation was performed according to the Chien-Hrones-Reswick method [20], which allows obtaining a larger stability margin than the traditional Ziegler-Nichols method [21, 22].

According to the Chien-Hrones-Reswick method for calculating the coefficients of the PID controller the response of the control object to the step input signal is observed. The elements of the control object, which have an aperiodic characteristic (Fig. 5), are approximated by the serial connection of the aperiodic link and the delay link.

From Fig. 5 it can be seen that two parameters a and L are used to calculate the coefficients of the PID regulator using the Chien-Hrones-Reswick method. Their calculation was performed under the conditions of the absence of overregulation (CHR0%) and its presence in 20% (CHR20%). The formulas by which the coefficients K_p, K_i and K_d are calculated are given in Table 1.

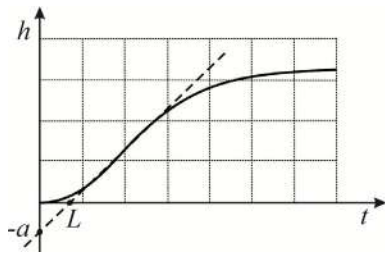


Fig. 5. An example of the acceleration curve of the control object

Table 1
Calculation of the coefficients of the PID regulator according to the Chien-Hrones-Resvik method in the absence of overregulation and its presence

Method	K_p	K_i	K_d
CHR0%	$\frac{0,6}{a}$	$\frac{L}{K_p}$	$\frac{0,5L}{K_p}$
CHR20%	$\frac{0,95}{a}$	$\frac{1,4L}{K_p}$	$\frac{0,47L}{K_p}$

The calculated parameters of the PID controller were adjusted manually to improve the quality of the control, since the analytical expressions are based on simplified models of the object and give an error. Adjusting the parameters of the regulators is performed according to the following rules: an increase in the proportional coefficient K_p increases the speed of operation and reduces the margin of stability; with a decrease in the integral component K_i , the adjustment error decreases faster over time; reduction of integration constant T_i reduces the margin of stability; increasing the differential component K_d increases the speed.

After adjusting the coefficients of the PID speed controllers, they take the form shown in Fig. 6.

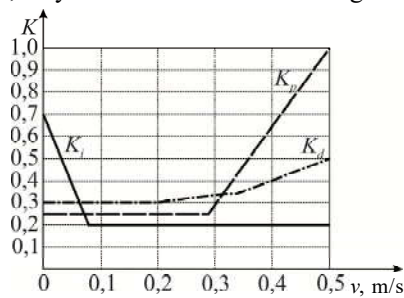


Fig. 6. Coefficients of the PID regulator

From Fig. 6 it can be seen that all coefficients depend on the speed of movement of the spikes, namely: the coefficient of the proportional link K_p increases sharply from 0.25 to 1 at speed above 0.3 m/s; the coefficient of the integral link K_i has a sharply decreasing linear characteristic at low speeds of movement up to 0.08 m/s and changes in the range from 0.7 to 0.2; the coefficient of the differential link K_d has a gentler characteristic and varies from 0.3 to 0.5 at the speed of movement of the spikes above 0.2 m/s.

Taking into account this Fig. 4 will look as shown in Fig. 7.

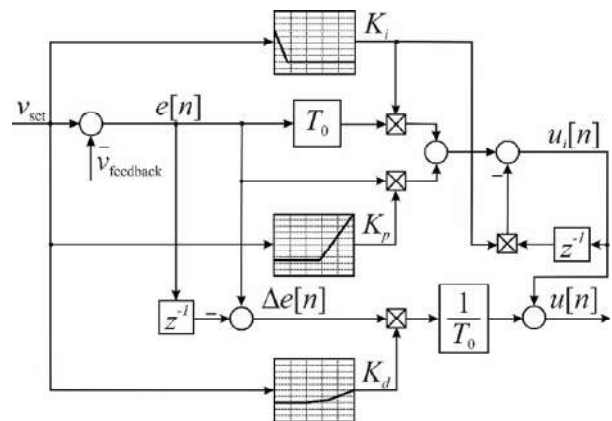


Fig. 7. The structure of the discrete PID speed controller with adjusted coefficients according to the Chien-Hrones-Resvik method

The detailed functional scheme of the turnout transfer is shown in Fig. 8, where LIEM with a sensor of the position of the spikes, an electronic switch (Fig. 3), a distributor with a pulse converter and a speed regulator (Fig. 7), which are parts of the control unit, is separated by dashed line.

The control system of the mono-switch lie type turnout is considered as a two-loop system of subordinate coordinate regulation with a PID speed controller, which, together with the LIEM, is reduced to a general simulation model in MATLAB [23, 24], taking into account all elements, parameters and relationships between them in Fig. 9, and Fig. 10 shows the diagram of the mechanical part.

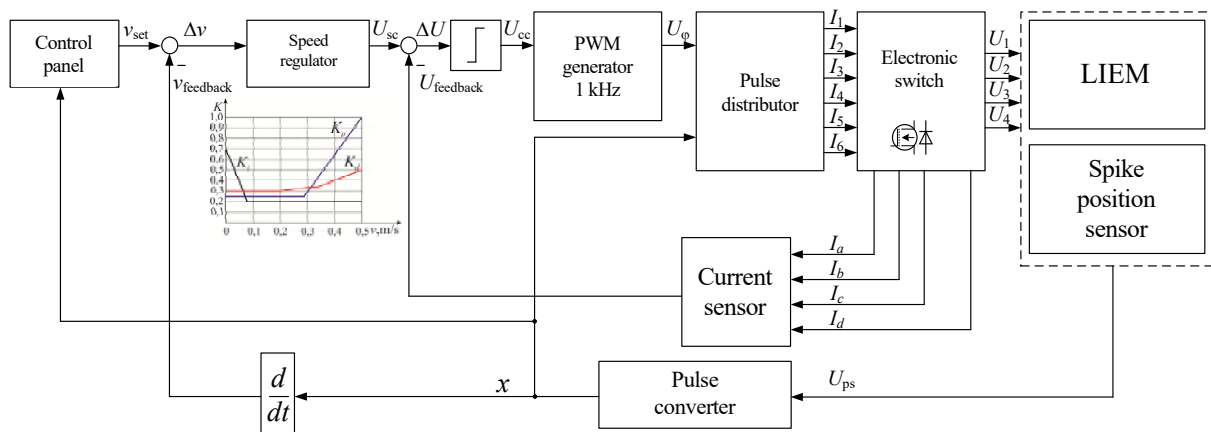


Fig. 8. Expanded functional scheme of the electric drive of the turnout with LIEM

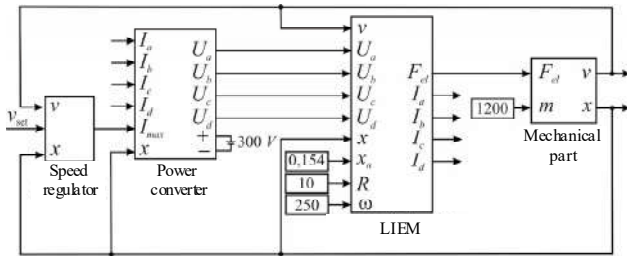


Fig. 9. Generalized simulation model of turnout with LIEM in the MATLAB environment

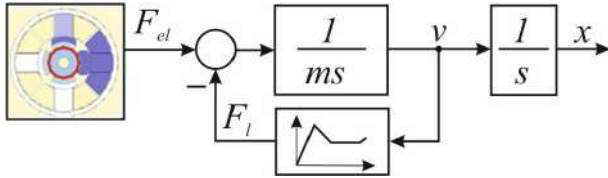


Fig. 10. Structural diagram of the mechanical part of the turnout with LIEM

In the feedback of the system, there is a load block $v = f(F_c)$, which reflects the friction characteristic [25], since the turnouts operate in different weather conditions under the influence of random factors (fallen leaves, rain, snow, substances that spill from the cars, etc.). The average values of the coefficient of friction on the rail-cushion surface (steel-steel) are given in the Table 2.

Table 2

Friction materials	Coefficient of friction			
	at rest		in a sliding state	
	without lubrication	with lubrication	without lubrication	with lubrication
rail – cushion	0.8	0.5-0.4	0.15-0.3	0.05-0.18

Figures 11, 12 show the transients of the electric drive of the turnout, namely the movement of the spikes and the speed of the turnout with a PID speed controller, taking into account the nonlinear characteristic of friction at different settings of the speed of movement of the spikes.

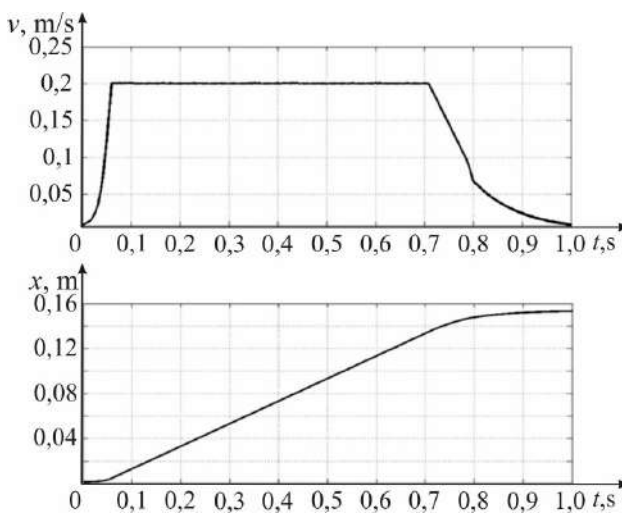


Fig. 11. Transients in mono-switch tie type with PID speed controller when setting the speed $v_3 = 0.2$ m/s

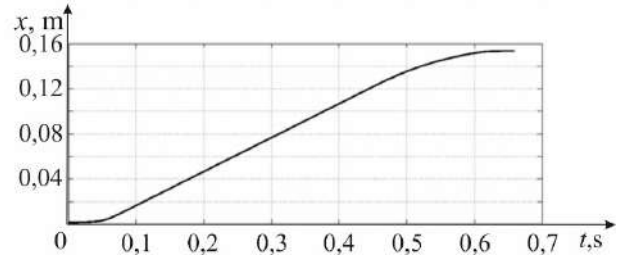
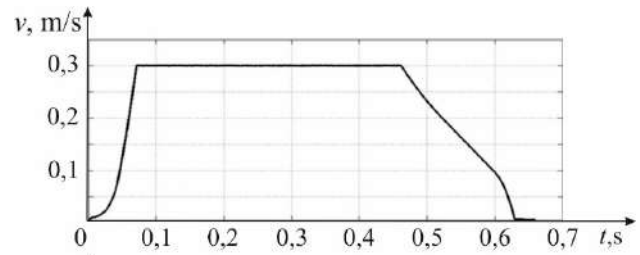


Fig. 12. Transients in mono-switch tie type with PID speed controller when setting the speed $v_3 = 0.3$ m/s

From the obtained graphs of transients, it was established that the PID controller supports the set speed of movement of the spikes of 0.2 m/s (Fig. 11) and 0.3 m/s (Fig. 12), which allows control of the position of the spikes. It also provides a transfer process with a smooth transition of the spikes to the frame rail, which protects the elements of the electric motor from mechanical overloads.

The graphs of the transients of the movement of the spikes show their impact-free tweaking to the frame rail, which is confirmed by the speed curves at the end of the transfer process at $t > 0.6$ s.

Conclusions.

1. A microprocessor-based system for automatic control of a mono-switch tie type with LIEM and a discrete PID speed controller was proposed and researched, which made it possible to improve the quality of the dynamics of its operation.

2. On the basis of the analytical methods of z-transformation, a discrete PID speed controller was synthesized and its simulation model was developed taking into account the nonlinear characteristic of friction, which confirmed the improvement of the dynamics of the operation of the turnout drive with LIEM.

3. Using the Chien-Hrones-Resvik method, distribution diagrams of the PID regulator coefficients were obtained depending on the speed of the armature movement: the coefficient of the proportional link increases sharply from 0.25 to 1 at speeds above 0.3 m/s; the coefficient of the integral link has a sharply decreasing linear characteristic at low speeds of movement up to 0.08 m/s and varies from 0.7 to 0.2; the coefficient of the differential link has the smoothest characteristic and varies from 0.3 to 0.5 at a speed of movement of spikes above 0.2 m/s.

4. On the basis of the study of the transients of the movement of the spikes, the possibility of shock-free bringing them to the frame rail is shown, which is confirmed by the speed curves at the end of the turnout transfer process, which go to 0 as well as the possibility of obtaining the transfer time of the spikes in less than 0.7 s

at a constant setting level of speed of 0.2 and 0.3 m/s of armature movement for LIEM.

Conflict of interest. The authors of the article declare no conflict of interest.

REFERENCES

1. *Pro skhvalennia Natsionalnoi transportnoi strategii Ukrainy na period do 2030 roku: rozporiadzhennia Kabinetu Ministriv Ukrainy vid 30 travnia 2018 r. № 430-r* [On approval of the National Transport Strategy of Ukraine for the period up to 2030. Order of the Cabinet of Ministers of Ukraine of May 30, 2018 № 430-r]. Available at: <https://zakon.rada.gov.ua/go/430-2018-%D1%80> (Accessed 14 February 2022). (Ukr).
2. *Ministerstvo infrastruktury Ukrainy. Informatsiia pro ukrainski zaliznytsi* [Ministry of Infrastructure of Ukraine. General information about railway transport]. Available at: <https://mtu.gov.ua/en/content/informaciya-pro-ukrainski-zaliznici.html> (Accessed 14 February 2022). (Ukr).
3. Buryakovskiy S., Masliy Ar., Masliy An. Prospects modernization of electric drive of pointer translations. *Electromechanical and energy saving systems*, 2013, no. 2 (22), part 2, pp. 124-127. Available at: [http://saue.kdu.edu.ua/files/EES_2-2013\(22\)_Part_2.pdf](http://saue.kdu.edu.ua/files/EES_2-2013(22)_Part_2.pdf) (Accessed 14 February 2022). (Rus).
4. Kande M., Isaksson A., Thottappillil R., Taylor N. Rotating Electrical Machine Condition Monitoring Automation – A Review. *Machines*, Oct. 2017, vol. 5, no. 4, p. 24. doi: <https://doi.org/10.3390/machines5040024>.
5. Bemment S.D., Goodall R.M., Dixon R., Ward C.P. Improving the reliability and availability of railway track switching by analysing historical failure data and introducing functionally redundant subsystems. *Proceedings of the Institution of Mechanical Engineers, Part F: Journal of Rail and Rapid Transit*, Sep. 2017, vol. 232, no. 5, pp. 1407-1424. doi: <https://doi.org/10.1177/0954409717727879>.
6. Rasmussen P.O. *Design and Advanced Control of Switched Reluctance Motors*. Institut for Energiteknik, Aalborg Universitet, 2002. 274 p.
7. *Design of High-Speed Railway Turnouts*. Southwest Jiao Tong University Press. Published by Elsevier Inc. 2015. Available at: <https://www.xnjdcbs.com/upfile/file/201705/14937827805937.pdf> (Accessed 14 February 2022).
8. Arslan B., Tiryaki H. Prediction of railway switch point failures by artificial intelligence methods. *Turkish Journal of Electrical Engineering & Computer Sciences*, Mar. 2020, vol. 28, no. 2, pp. 1044-1058. doi: <https://doi.org/10.3906/elk-1906-66>.
9. Sezen S., Karakas E., Yilmaz K., Ayaz M. Finite element modeling and control of a high-power SRM for hybrid electric vehicle. *Simulation Modelling Practice and Theory*, Mar. 2016, vol. 62, pp. 49-67. doi: <https://doi.org/10.1016/j.simpat.2016.01.006>.
10. Dorohin B.P., Serdyuk T.M. Implementation of new types of points motors. *Electromagnetic compatibility and safety on railway transport*, 2013, no. 6, pp. 71-84. Available at: <http://ecsrt.diiit.edu.ua/article/view/51291> (Accessed 14 February 2022). (Rus).
11. Fathy Abouzeid A., Guerrero J.M., Endemaño A., Muniategui I., Ortega D., Larrazabal I., Briz F. Control strategies for induction motors in railway traction applications. *Energies*, Feb. 2020, vol. 13, no. 3, art. no. 700. doi: <https://doi.org/10.3390/en13030700>.
12. Lagos R.F., San Emeterio A., Vinolas J., Alonso A., Aizpun M. The influence of track elasticity when travelling on a railway turnout. *Proceedings of the Second International Conference on Railway Technology: Research, Development and Maintenance*, 2014, p. 11. doi: <https://doi.org/10.4203/ccp.104.208>.
13. Kuznetsov B.I., Nikitina T.B., Kolomiets V.V., Bovdvi I.V. Improving of electromechanical servo systems accuracy. *Electrical Engineering & Electromechanics*, 2018, no. 6, pp. 33-37. doi: <https://doi.org/10.20998/2074-272X.2018.6.04>.
14. Moiseenko V.I., Poddubnyak V.I. *Avtomatika i komp'uternye sistemy na stantsiiakh* [Automation and computer systems in stations]. Kiev, Transport of Ukraine Publ., 1999. 142 p. (Rus).
15. Buriakovskiy S.G., Masliy A.S., Asmolova L.V., Goncharuk N.T. Mathematical modelling of transients in the electric drive of the turnout of the mono-sleeper type with switched-inductor motor. *Electrical Engineering & Electromechanics*, 2021, no. 2, pp. 16-22. doi: <https://doi.org/10.20998/2074-272X.2021.2.03>.
16. Forster N., Gerlach A., Leidhold R., Buryakovskiy S., Masliy A., Lyubarskiy B.G. Design of a Linear Actuator for Railway Turnouts. *IECON 2018 - 44th Annual Conference of the IEEE Industrial Electronics Society*, 2018, pp. 463-470. doi: <https://doi.org/10.1109/IECON.2018.8591471>.
17. Byrakovskiy S., Ljubarskiy B., Masliy A., Masliy A. Mathematical modeling of the electric drive turnouts based on a linear motor. *Electrotechnic and Computer Systems*, 2019, no. 19 (95), pp. 75-78. Available at: <https://eltecs.op.edu.ua/index.php/journal/article/view/1838> (Accessed 14 February 2022).
18. Buryakovskiy S.G., Karpenko N.P., Lyubarskiy B.G., Masliy Ar.S., Masliy An.S. Mathematical description of linear motor for inductor-type turnouts. *Collection of materials of the International scientific and technical conference «Problems of energy and resource saving in electrical systems. Science, education and practice»*, 2016, no. 1 (4), pp. 258-260. (Rus).
19. Kuznetsov B.I., Nikitina T.B., Bovdvi I.V. Multiobjective synthesis of two degree of freedom nonlinear robust control by discrete continuous plant. *Technical Electrodynamics*, 2020, no. 5, pp. 10-14. <https://doi.org/10.15407/techned2020.05.010>.
20. *Chien-Hrones-Reswick Autotuning Method*. Available at: <https://www.ni.com/docs/ru-UA/bundle/labview-2021/page/lvpidmain/chienforms.html> (Accessed 14 February 2022).
21. *Ziegler-Nichols Tuning Rules for PID*. Available at: <https://www.mstarlabs.com/control/znrule.html> (Accessed 14 February 2022).
22. Huba M., Chamraz S., Bistak P., Vrancic D. Making the PI and PID Controller Tuning Inspired by Ziegler and Nichols Precise and Reliable. *Sensors*, 2021, vol. 21, no. 18, art. no. 6157. doi: <https://doi.org/10.3390/s21186157>.
23. Chernykh I. V. *Modelirovanie elektrotekhnicheskikh ustrojstv v MATLAB. SimPowerSystems i Simulink* [Modeling of Electrical Devices in MATLAB. SimPowerSystems and Simulink]. Moscow, DMK Press Publ., 2007. 288 p. (Rus).
24. Balamurugan S., Umarani A. Study of Discrete PID Controller for DC Motor Speed Control Using MATLAB. *2020 International Conference on Computing and Information Technology (ICCIT-1441)*, 2020, pp. 1-6. doi: <https://doi.org/10.1109/ICCIT-144147971.2020.9213780>.
25. Yuan Z., Wu M., Tian C., Zhou J., Chen C. A Review on the Application of Friction Models in Wheel-Rail Adhesion Calculation. *Urban Rail Transit*, 2021, vol. 7, no. 1, pp. 1-11. doi: <https://doi.org/10.1007/s40864-021-00141-y>.

Received 17.03.2022

Accepted 23.06.2022

Published 07.09.2022

S.G. Buriakovskiy¹, Doctor of Technical Science, Professor,
L.V. Asmolova², PhD, Assistant Professor,
An.S. Maslii³,
Ar.S. Maslii⁴, PhD, Assistant Professor,
I.V. Obruch², PhD,
¹ Research and Design Institute «Molniya»
of National Technical University «Kharkiv Polytechnic
Institute»,
47, Shevchenko Str., Kharkiv, 61013, Ukraine,
e-mail: sergbyr@i.ua

² National Technical University «Kharkiv Polytechnic Institute»,
2, Kyrpychova Str., Kharkiv, 61002, Ukraine,
e-mail: Larysa.Asmolova@khpi.edu.ua (Corresponding Author),
Ihor.Obruch@khpi.edu.ua
³ LTD «SCB-GROUP»,
42, Odeska Str., Kharkiv, 61009, Ukraine,
e-mail: asa.anc.corp@gmail.com
⁴ Ukrainian State University of Railway Transport,
7, Feiebakh Square, Kharkiv, 61050, Ukraine,
e-mail: a.masliy@ukr.net

How to cite this article:

Buriakovskiy S.G., Asmolova L.V., Maslii An.S., Maslii Ar.S., Obruch I.V. Development and study of a microprocessor automatic control system for a mono-switch tie type with a linear inductive electric motor and a discrete speed controller. *Electrical Engineering & Electromechanics*, 2022, no. 5, pp. 3-9. doi: <https://doi.org/10.20998/2074-272X.2022.5.01>

A. Guezi, A. Bendaikha, A. Dendouga

Direct torque control based on second order sliding mode controller for three-level inverter-fed permanent magnet synchronous motor: comparative study

Introduction. The permanent magnet synchronous motor (PMSM) has occupied a large area in the industry because of various benefits such as its simple structure, reduced moment of inertia, and quick dynamic response. Several control techniques have been introduced for the control of the PMSM. The direct torque control strategy associated to three-level clamped neutral point inverter has been proven its effectiveness to solve problems of ripples in both electromagnetic torque and stator flux with regard to its significant advantages in terms of fast torque response. **Purpose.** The use of a proportional integral speed controller in the direct torque control model results in a loss of decoupling with regard to parameter fluctuations (such as a change in stator resistance value induced by an increase in motor temperature), which is a significant drawback for this method at high running speeds. **Methods.** That is way a second order sliding mode controller based on the super twisting algorithm (STA) was implemented instead of PI controller to achieve a decoupled control with higher performance and to insure stability while dealing with parameter changes and external disturbances. **Results.** The simulation results carried out using MATLAB/Simulink software show that the model of direct torque control based on a three-level inverter-fed permanent magnet synchronous motor drive has better performance with second order sliding mode speed controller than the proportional integral controller. Through the response characteristics we see greater performance in terms of response time and reference tracking without overshoots. Decoupling, stability, and convergence toward equilibrium are all guaranteed. References 9, table 2, figures 9.

Key words: permanent magnet synchronous motor, direct torque control, second order sliding mode controller.

Вступ. Синхронний двигун з постійними магнітами (СДПМ) зайняв велике місце в промисловості завдяки різним перевагам, таким як його проста конструкція, зменшений момент інерції та швидкий динамічний відгук. Для керування СДПМ було введено декілька методів керування. Стратегія прямого управління крутним моментом, пов'язана з трирівневим інвертором з фіксованою нейтральною точкою, довела свою ефективність для вирішення проблем пульсацій як електромагнітного крутного моменту, так і магнітного потоку статора, враховуючи його значні переваги з точки зору швидкої реакції крутного моменту. **Мета.** Використання пропорційно-інтегрального регулятора швидкості моделі прямого управління крутним моментом призводить до втрати розв'язки по відношенню до коливань параметрів (такі як зміна значення опору статора, викликане підвищенням температури двигуна), що є істотним недоліком для цієї моделі на високих робочих швидкостях. **Методи.** Таким чином, замість ПІ-регулятора був реалізований ковзний регулятор другого порядку, заснований на алгоритмі суперскручування (STA), для досягнення розв'язаного управління з більш високою продуктивністю та забезпечення стабільності при роботі зі змінами параметрів та зовнішніми збуреннями. **Результати** моделювання, виконаного з використанням програмного забезпечення MATLAB/Simulink, показують, що модель прямого керування крутним моментом, заснована на трирівневому приводі синхронного двигуна з постійними магнітами з інверторним живленням, має кращу ефективність з регулятором швидкості з ковзним режимом другого порядку, ніж пропорційний інтегральний контролер. Завдяки характеристикам відгуку бачимо більш високу ефективність з точки зору часу відгуку та відстеження посилань без перерегулювання. Розв'язка, стабільність та збіжність до рівноваги гарантовані. Бібл. 9, табл. 2, рис. 9.

Ключові слова: синхронний двигун з постійними магнітами, пряме керування крутним моментом, контролер режиму ковзання другого порядку.

Introduction. In recent years, thanks to the rapid development of power electronics technology, permanent magnet synchronous motor (PMSM) has taken a wide space in the industry due to many advantages such as higher energy efficiency and higher torque to weight ratio. In the term of its control, several techniques have been presented in the literature; such as voltage/frequency control, which is limited to low-performance uses, and field oriented control, which has a complex process and is highly sensitive to parameter changes. nevertheless, the direct torque control (DTC) has been the most attractive control due to its notable advantages regarding its simplicity and its rapid torque response [1], This command need an external loop to control the speed either by the classic PID controller [8] or through other methods of control such as: fuzzy logic control [9], sliding mode [2], as well as the second order sliding mode controller (SOSMC) [2] which is designed to achieve high performance for systems with parametric variation and to ensure closed loop stability.

The purpose of this work is to compare between the PI and the second order sliding mode speed controllers in a direct torque control for three-level neutral point multilevel inverter-fed permanent magnet synchronous motor drive system.

In this paper, the mathematical model of PMSM has been introduced. In order to obtain a better performance for the PMSM, the technique of DTC associated to three-level neutral point clamped (NPC) multilevel inverters with a PI controller has been used. However, this solution has a major drawback represented by the speed's sensitivity to load variation. In order to remedy this problem, the DTC with the sliding mode controller (SMC) was generally used to improve its robustness and its insensitivity to parameter variations and external disturbances. However, the presence of the chattering is a major drawback for conventional SMC controllers. In order to minimize the phenomena, a SOSMC was used. For the purpose of evaluating and testing the different control techniques proposed for the PMSM fed by three-level NPC inverters drive system, a simulation study was carried out. The comparison study based on the obtained simulation results confirms the efficiency of the second order sliding mode controller over the PI controller under different operating conditions. [2].

Model and equations of the PMSM. The two-phase model of the PMSM is carried out by a transformation of the real three-phase reference into a fictitious two-phase reference, which is in fact only a change of base on the physical quantities (tensions, fluxes and currents), it leads

© A. Guezi, A. Bendaikha, A. Dendouga

to a reduction of the machine equations. The transformation best known by electrical technicians is that of Park, the representation is shown in Fig. 1.

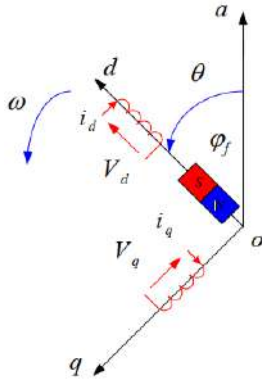


Fig. 1. Two-phase representation of PMSM

The stator voltage equations are given by the following equations in the matrix form [3]:

$$[V_{dq}] = [R_s] \cdot [i_{dq}] + \frac{d}{dt} [\varphi_{dq}] + p \cdot \Omega [\varphi_{dq}^*], \quad (1)$$

where

$$[V_{dq}] = \begin{bmatrix} V_d \\ V_q \end{bmatrix}, \quad (2)$$

$$[R_s] = \begin{bmatrix} R_s & 0 \\ 0 & R_s \end{bmatrix}, \quad (3)$$

$$[i_{dq}] = \begin{bmatrix} i_d \\ i_q \end{bmatrix}, \quad (4)$$

$$[\varphi_{dq}] = \begin{bmatrix} \varphi_d \\ \varphi_q \end{bmatrix}, \quad \varphi_{dq}^* = \begin{bmatrix} -\varphi_q \\ \varphi_d \end{bmatrix}. \quad (5)$$

We note also that:

$$\begin{bmatrix} \varphi_d \\ \varphi_q \end{bmatrix} = \begin{bmatrix} L_d & 0 \\ 0 & L_q \end{bmatrix} \cdot \begin{bmatrix} i_d \\ i_q \end{bmatrix} + \begin{bmatrix} \varphi_f \\ 0 \end{bmatrix}. \quad (6)$$

where $V_d, V_q, i_d, i_q, L_d, L_q, \varphi_d$ and φ_q are the dq components of the stator voltage, current, inductance and flux linkage, respectively; R_s is the stator resistance; φ_f is the rotor flux linkage generated by the permanent magnets; p is the pairs of poles.

The electromagnetic torque expression is given by:

$$T_e = (3/2) \cdot p \cdot [(L_d - L_q) \cdot i_d \cdot i_q + \varphi_f \cdot i_q]. \quad (7)$$

In the case where the machine has non-salient poles ($L_d = L_q$), this equation (7) is simplified to:

$$T_e = (3/2) \cdot p \cdot \varphi_f \cdot i_q. \quad (8)$$

DTC with three-level inverter. The principle of the DTC is to maintain the stator flux within a specific range [3, 4]. This technique is based on the direct determination of the commands sequences applied to the switches of a three level inverter. This strategy is generally based in the use of hysteresis comparators whose role is to control the amplitudes of the stator flux and the electromagnetic torque. The synoptic of DTC control is shown in Fig. 2.

The stator flux equation is expressed as:

$$\overline{\hat{\phi}_s} = \hat{\phi}_{s\alpha} + j\hat{\phi}_{s\beta}, \quad (9)$$

where

$$\begin{cases} \hat{\phi}_{s\alpha} = \int_0^t (V_{s\alpha} - R_s I_{s\alpha}) dt; \\ 0 \\ \hat{\phi}_{s\beta} = \int_0^t (V_{s\beta} - R_s I_{s\beta}) dt; \\ 0 \end{cases} \quad (10)$$

where $V_{s\alpha}, V_{s\beta}, i_{s\alpha}, i_{s\beta}$, are the $\alpha\beta$ components of the stator voltage and current, respectively.

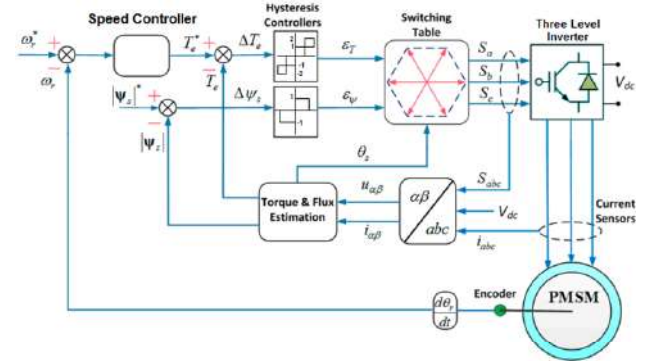


Fig. 2. The synoptic of DTC control

Once the 2 flux components are obtained, the electromagnetic torque can be estimated by the formula below:

$$\hat{C}_e = \frac{3}{2} p [\hat{\phi}_{s\alpha} I_{s\beta} - \hat{\phi}_{s\beta} I_{s\alpha}]. \quad (11)$$

Moreover, in order to obtain the sector, the rotor flux angle is determined by:

$$\theta = \arctg \frac{\hat{\phi}_{s\beta}}{\hat{\phi}_{s\alpha}}. \quad (12)$$

This model is updated with 3 level hysteresis controller for the flux and 5 level for the torque in order to build the optimized switching table as illustrated in Table 2 that led to determine a vector between 27 state vectors to apply to a three level NPC inverter (Fig. 3) noting that those vectors are distributed on 12 sectors of the stator flux plane Fig. 4.

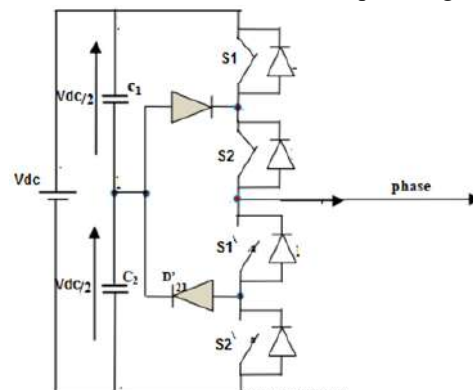


Fig. 3. One leg of 3 level inverter layout

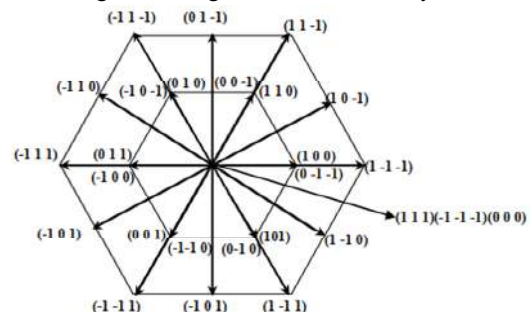


Fig. 4. 12 sectors with switching vectors

In 3-level NPC inverter there are 3 switching state for each leg (S1, S2); (S1, S1'); (S1', S2') which result in 3 voltages levels respectively V_{dc} , $V_{dc}/2$, 0. Consequence of these switching possibilities, 27 state vectors will be obtained as shown in Table 1 [5, 6].

Table 1
Distribution of the 3-level inverter voltage vectors into 4 groups

Zero state vectors	$V_1 V_8 V_{15}$ (0, 0, 0) (1, 1, 1) (-1, -1, -1)
Short Vectors	$V_2 V_3 V_4 V_5 V_6 V_7$ (1, 0, 0) (1, 1, 0) (0, 1, 0) (0, 1, 1) (0, 0, 1) (1, 0, 1) $V_8 V_9 V_{10} V_{11} V_{12} V_{13}$ (0, -1, -1) (0, 0, -1) (-1, 0, -1) (-1, 0, 0) (-1, -1, 0) (0, -1, 0)
Long vectors	$V_{16} V_{17} V_{18} V_{19} V_{20} V_{21}$ (1, -1, -1) (1, 1, -1) (-1, 1, -1) (-1, 1, 1) (-1, -1, 1) (1, -1, 1)
Medium vectors	$V_{22} V_{23} V_{24} V_{25} V_{26} V_{27}$ (1, 0, -1) (0, 1, -1) (-1, 1, 0) (-1, 0, 1) (0, -1, 1) (1, -1, 0)

Table 2

Φ		DTC modified switching table											
		Stator flux sectors											
T_e		1	2	3	4	5	6	7	8	9	10	11	12
+1	+2	22	17	23	18	24	19	25	20	26	21	27	16
	+1	22	3	23	4	24	5	25	6	26	7	27	2
	0	1	8	15	1	8	15	1	8	15	1	8	15
	-1	27	2	22	3	23	4	24	5	25	6	26	7
	-2	27	16	22	17	23	18	24	19	25	20	26	21
0	+2	23	18	24	19	25	20	26	21	27	16	22	17
	+1	23	4	24	5	25	6	26	7	27	2	22	3
	0	1	8	15	1	8	15	1	8	15	1	8	15
	-1	26	7	27	2	22	3	23	4	24	5	25	6
	-2	26	21	27	16	22	17	23	18	24	19	25	20
-1	+2	18	24	19	25	20	26	21	27	16	22	17	23
	+1	4	24	5	25	6	26	7	27	2	22	3	23
	0	1	8	15	1	8	15	1	8	15	1	8	15
	-1	6	26	7	27	2	22	3	23	4	24	5	25
	-2	20	26	21	27	16	22	17	23	18	24	19	25

PI speed controller. The PI controller determines the reference torque in order to maintain the corresponding speed [2]. The speed dynamics is given by the following mechanical equation:

$$\Omega = \frac{T_e - T_L}{JP + f_r}, \quad (13)$$

where T_e , T_L , J , f_r , P are the motor torque, load torque, moment of inertia, viscous friction factor and Laplace operator, respectively.

The functional diagram of speed controller is shown in Fig. 5.

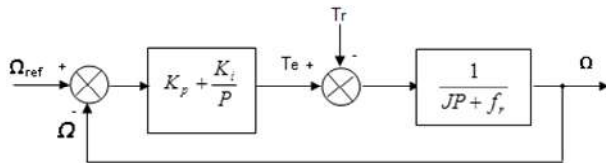


Fig. 5. Speed control loop

Adopting the pole placement method considering that the closed loop speed transfer function is given by:

$$F_C = \frac{\Omega}{\Omega_{ref}} = \frac{K_p \cdot \left(P + \frac{K_i}{K_p} \right)}{J \cdot P^2 + (f_r + K_p) \cdot P + K_i}. \quad (14)$$

The controller parameters K_p , K_i become as:

$$\begin{cases} K_i = 2 \cdot \rho^2 \cdot J; \\ K_p = 2 \cdot \rho \cdot J - f_r, \end{cases} \quad (15)$$

where ρ represents the module of the real part and imaginary part of the 2 poles.

Conventional sliding mode controller. The sliding mode controller has been built to control the speed to ensure good tracking, accurate response and insensitivity to changes in drive system [2, 7]. The sliding surface has been selected as:

$$S_\Omega = \Omega_{ref} - \Omega. \quad (16)$$

In addition, the electromechanical equation of the motor is expressed by:

$$J \cdot \frac{d\Omega}{dt} + f_r \cdot \Omega = T_e - T_L. \quad (17)$$

By considering (17), the derivative of (16) becomes:

$$\dot{S}_\Omega = \dot{\Omega}_{ref} - \frac{1}{J} \cdot (T_e - T_L - f_r \cdot \Omega). \quad (18)$$

The reference control variable is written such as:

$$T_{ref} = T_{eq} - T_n, \quad (19)$$

where T_{eq} and T_n are the equivalent and switching components of the control variable, respectively.

In the sliding mode ($\dot{S} = 0$), the equivalent component is determined by:

$$T_{eq} = J \cdot \dot{\Omega}_{ref} + T_L + f_r \cdot \Omega. \quad (20)$$

Moreover, the switching component is written by

$$T_n = K_\Omega \cdot \text{sign}(S_\Omega), \quad (21)$$

where K_Ω is the positive coefficient.

Second order sliding mode controllers (SOSMC).

The conventional sliding mode controller is known by the chattering phenomena, to address this issue, we proposed to extend the basic SMC model to a second derivative of the sliding surface (SOSMC), with the objective of minimizing the chattering band [2]. The equivalent component remains the same, the switching component become:

$$T_n = K_{\Omega 1} \sqrt{|S_\Omega|} \text{sign}(S_\Omega) + K_{\Omega 2} \int \text{sign}(S_\Omega) dt, \quad (23)$$

where $K_{\Omega 1}$ and $K_{\Omega 2}$ are the positive constants.

Simulation results. Digital simulation using MATLAB/Simulink has been used to test the techniques described in this paper. In this simulation, the frequency is 50 Hz, stator resistance is 2.3 Ω , inductance $L_d = L_q = 7.6$ mH, moment of inertia is 0.032 kg·m², permanent flux is 0.4 T and number of poles is 4. The PMSM starts with a constant reference speed equal to 100 rad/s. At $t = 0.2$ s the rotor speed decreases to 80 rad/s. At $t = 0.5$ s a reverse of rotation to -100 rad/s was performed finally at $t = 0.7$ s, a nominal load torque $T_L = 5$ N·m was applied, then removed at $t = 0.9$ s.

In the instant $t = 0.7$ s when applying the load, a speed drop from -100 rad/s to -101 rad/s was noticed with the PI controller unlike the SOSMC model where the speed remains in an excellent range maintaining its reference (Fig. 6, 7). Also an overshoot of the speed is observed when decreasing the speed to 80 rad/s ($t = 0.2$ s), contrary to the SOSMC results where the speed keep tracking the reference without overshooting (Fig. 6, 7).

As can be seen, compared with model of PI-DTC, the model of SOSMC-DTC has a better dynamic response for both speed and torque indicating that SOSMC controller was less sensitive to the load disturbance.

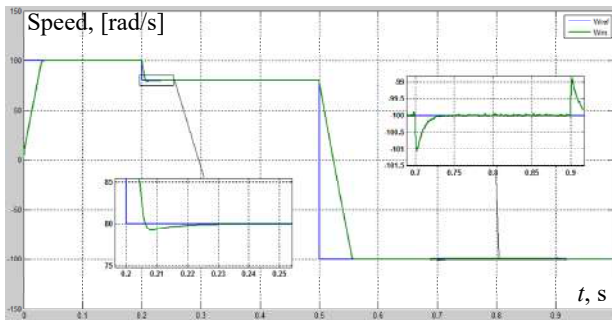


Fig. 6. Rotor speed response with PI controller

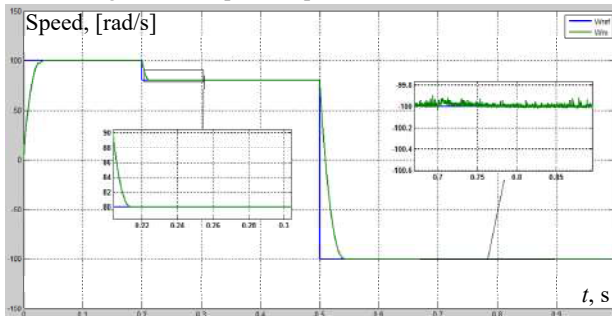


Fig. 7. Rotor speed response with SOSMC

When the rotation speed was reversed, the motor torque required longer time to reach equilibrium (0.06 s), this time was clearly reduced in SOSMC model (Fig. 8, 9).

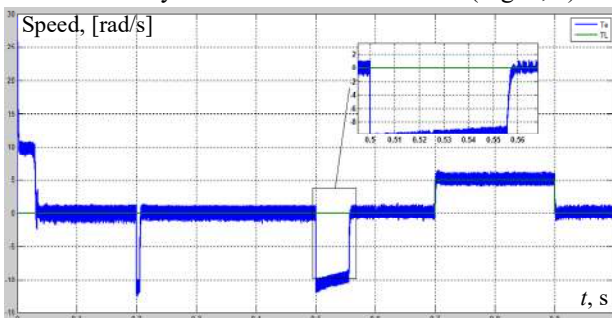


Fig. 8. Motor torque response with PI controller

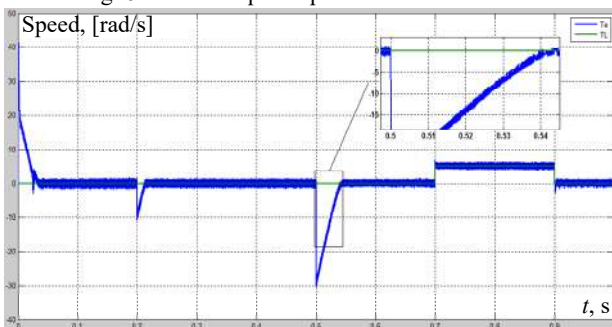


Fig. 9. Motor torque response with SOSMC

Conclusions. In this paper a comparative study of proportional integral and second order sliding mode controller in a direct torque control system based on a 3-level neutral point clamped inverter-fed permanent magnet synchronous motor drive has been presented.

Simulation results prove that second order sliding mode controller provide better tracking performances than the proportional integral in terms of rise time and overshoot as well as less sensitivity of motor speed to load disturbance.

How to cite this article:

Guezi A., Bendaikha A., Dendouga A. Direct torque control based on second order sliding mode controller for three-level inverter-fed permanent magnet synchronous motor: comparative study. *Electrical Engineering & Electromechanics*, 2022, no. 5, pp. 10-13. doi: <https://doi.org/10.20998/2074-272X.2022.5.02>

The return to the equilibrium point was 0.02 s less than the proportional integral controller. In the other hand, the dynamic performance and steady-state accuracy of the PI controller were not very satisfactory since the motor speed sensitivity to load disturbance and motor variations was very high (1 rad/s) then it was improved and reduced to 0.1 rad/s with the sliding mode controller.

Conflict of interest. The authors declare that they have no conflicts of interest.

REFERENCES

1. Meng L., Yang X. Comparative analysis of direct torque control and DTC based on sliding mode control for PMSM drive. *2017 29th Chinese Control And Decision Conference (CCDC)*, 2017, pp. 736-741. doi: <https://doi.org/10.1109/CCDC.2017.7978529>.
2. Dendouga A. Conventional and Second Order Sliding Mode Control of Permanent Magnet Synchronous Motor Fed by Direct Matrix Converter: Comparative Study. *Energies*, 2020, vol. 13, no. 19, art. no. 5093. doi: <https://doi.org/10.3390/en13195093>.
3. Chen Ming, Gao Hanying, Song Hongming. Simulation study on a DTC system of PMSM. *Proceedings of 2011 6th International Forum on Strategic Technology*, 2011, pp. 564-569. doi: <https://doi.org/10.1109/IFOST.2011.6021087>.
4. Sekhar O.C., Sekhar K.C. Simulation and Comparison of 2-L and 3-L Inverter Fed Induction Motor DTC Drives. *International Journal of Computer and Electrical Engineering*, 2011, vol. 3, no. 5, pp. 676-681. doi: <https://doi.org/10.7763/IJCEE.2011.V3.402>.
5. Sadeghi Larijani A., Shahparasti M., Fatemi A., Amiri A., Mohammadian M. DTC drive of induction motor using three-Level inverter with optimized switching table and minimizing the deviation of neutral point voltage. *2010 1st Power Electronic & Drive Systems & Technologies Conference (PEDSTC)*, 2010, pp. 255-260. doi: <https://doi.org/10.1109/PEDSTC.2010.5471819>.
6. Farajpour Y., Alzayed M., Chaoui H., Kelouwani S. A Novel Switching Table for a Modified Three-Level Inverter-Fed DTC Drive with Torque and Flux Ripple Minimization. *Energies*, 2020, vol. 13, no. 18, art. no. 4646. doi: <https://doi.org/10.3390/en13184646>.
7. Krim S., Gdaim S., Mtibaa A., Mimouni M.F. Real time implementation of DTC based on sliding mode speed controller of an induction motor. *2015 16th International Conference on Sciences and Techniques of Automatic Control and Computer Engineering (STA)*, 2015, pp. 94-100. doi: <https://doi.org/10.1109/STA.2015.7505139>.
8. Maji P., KPanda P.G., KSaha P.P. Field Oriented Control of Permanent Magnet Synchronous Motor Using PID Controller. *International Journal of Advanced Research in Electrical, Electronics and Instrumentation Engineering*, 2015, vol. 4, no. 2, pp. 632-639. doi: <https://doi.org/10.15662/ijareeie.2015.0402019>.
9. Mishra A., Mahajan V., Agarwal P., Srivastava S.P. Fuzzy logic based speed and current control of vector controlled PMSM drive. *2012 2nd International Conference on Power, Control and Embedded Systems*, 2012, pp. 1-6. doi: <https://doi.org/10.1109/ICPCES.2012.6508131>.

Received 25.03.2022

Accepted 28.06.2022

Published 07.09.2022

Abderrahmane Guezi¹, PhD Student,
 Abdelmalik Bendaikha¹, PhD, Doctor of Electrical Engineering,
 Associate Professor,
 Abdelhakim Dendouga², Doctor of Electrical Engineering, Full
 Professor,
¹ University Mohamed Boudiaf of M'sila, Algeria,
 e-mail: abderrahmane.guezi@univ-msila.dz (Corresponding Author),
 abdlmalik.bendaikha@univ-msila.dz
² University of Mohamed Khider Biskra, Algeria,
 e-mail: a.dendouga@univ-biskra.dz

Impact of fractional filter in PI control loop applied to induction motor speed drive

Introduction. One of the main problems of electrical machine control systems is to obtain a satisfactory performance in the rejection of load disturbances, as well as in the set-point tracking tasks. Generally, the development of control algorithms does not take into account the presence of noise. Appropriate filtering is, therefore, essential to reduce the impact of noise on the output of the controller, in addition to the machine output. Recently, there has been a great tendency toward using fractional calculus to solve engineering problems. The filtering is one of the fields in which fractional calculus has received great attention. The importance of filters in signal processing and other engineering areas is unquestionable **Novelty.** The proposed work is intended to be a contribution in the recent works conducted on the influence of the fractional filtering on the control robustness of induction machines control. **Purpose.** The main contribution of this research is the application of fractional filtering to the standard PI control loop for an induction motor speed drive. **Methods.** In order to assess its impact and benefit, different structures for introducing the filters are investigated, A first order filter is considered in different positions, whether before or after the controller or even in both positions at the same time, with a noise source. A review of the index performance evolution (the Integral Square Error, Integral Absolute Error and Integral Time Absolute Error) has allowed a configuration design of the filter. **Results.** Intensive simulations were performed with a control setup using integer and fractional order filters, which permitted to conclude that the fractional filters give better performance indices compared to the integer one and thus improve the dynamic characteristics of the system. References 27, tables 4, figures 12.

Key words: fractional filter, first order filter, index performance, induction machine, PI controller.

Вступ. Однією з основних проблем систем керування електричними машинами є отримання задовільних характеристик при придушенні збурень навантаження, а також завдання відстеження уставок. Зазвичай, при розробці алгоритмів керування наявність шуму не враховується. Тому потрібна відповідна фільтрація для зниження впливу шуму на вихідний сигнал контролера на додаток до вихідного сигналу машини. Останнім часом спостерігається чітка тенденція до використання дробового обчислення для вирішення інженерних завдань. Фільтрація – це одна з областей, в якій дрібному обчисленню приділяється велика увага. Важливість фільтрів у обробці сигналів та інших галузях техніки незаперечна. **Новизна.** Запропонована робота покликана стати внеском у недавні роботи, присвячені впливу дробової фільтрації на надійність керування асинхронними машинами. **Мета.** Основним внеском цього дослідження є застосування дробової фільтрації до стандартного контуру ПІ-регулювання для приводу швидкості асинхронного двигуна. **Методи.** Щоб оцінити його вплив та користь, досліджуються різні конструкції для введення фільтрів. Фільтр першого порядку розглядається в різних положеннях до або після контролера або навіть в обох положеннях одночасно з джерелом шуму. Огляд розвитку показників ефективності (інтегральна квадратична помилка, інтегральна абсолютна помилка та інтегральна абсолютна помилка за часом) дозволив розробити конфігурацію фільтра. **Результати.** Значний обсяг моделювання був проведений з налаштуванням керування з використанням фільтрів цілочисельного та дробового порядку, що дозволило зробити висновок, що дробові фільтри дають кращі показники ефективності порівняно з цілочисельним і таким чином покращують динамічні характеристики системи. Бібл. 27, табл. 4, рис. 12.

Ключові слова: дробовий фільтр, фільтр першого порядку, показник ефективності, асинхронна машина, ПІ-регулятор.

Introduction. In recent decades several scientific research efforts have focused on the use of fractional order systems in identification, modeling, and control engineering. Applications cover a wide number of physical science fields, including mechanics, electricity, chemistry, biology, economics, modeling, and notably control theory, mechatronics and robotics [1, 2]. Fractional order control is nowadays one of the emerging research topics gathering a growing number of works [3, 4]. The main reason is that fractional order systems allow more powerful control performances and robustness compared to classical integer order ones [5, 6].

Actually, one of the main issues in machine control systems is often to achieve a satisfactory performance in the load disturbance rejection and in the set-point following tasks, simultaneously. The PID algorithm is the core function in low-level controllers. The majority of design strategies ignore measurement noises [7, 8]. Filtering the control loop signals is one possible solution to this problem. In [9], authors investigate how filtering the observed signal affects unwanted control actions caused by measurement noises, the load disturbance response and process uncertainty. The analyses are reduced to a set of design rules.

In another work, Hägglund has proposed a signal filtering in PID control loop [10]. Set-point, process output,

and measurable load disturbances are the three basic analog input signals for the controller. Before entering the PID controller, these signals should be filtered. The process output filter is used to remove unwanted components from the signal such as measurement noise and to compensate for undesirable process dynamics.

With the successful implementation of non-integer order fractance devices, interest in using fractional order filters has grown. Seminal works on fractional order filters presented in [11, 12], were concerned with applying filter design theory to the fractional-order domain. Since then, several studies on the design of fractional order filters have been conducted, including [13, 14]. In [15] discussed the design and optimization of fractional filters, as well as their use in adaptive control of industrial processes [16].

Recently, the concept to «fractionalization» was proposed in [17]. It consists in replacing the classical integrator in a control loop by a combination of two fractional order integrators, which adds in fact fractional order filters in the feedback control loop, hence, improving the robustness against noises. Consequently, fractional order filters better approximate the ideal response than the classical ones; this fact makes their generalization for industrial control systems very advantageous.

This present work aims for the improvement of the induction machine speed control robustness applying fractional order filters in a simple PI feedback control scheme. Different structures of introducing the filters are investigated, whether before or after the controller or even in both positions at the same time (see Fig.1).

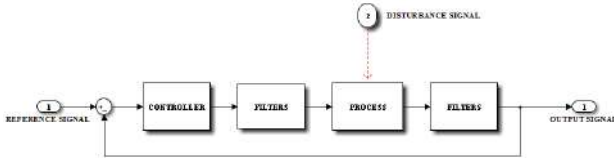


Fig. 1. The basic feedback loop with process, controller and the filters

Fundamentals of fractional calculus. Definitions.

The concept of fractional calculus has been there since the inception of regular (integer-order) calculus, with the first reference most likely attributed to Leibniz and l'Hopital in 1695 [18], where the half-order derivative was discussed. The generalization of integration and differentiation is fractional calculus.

Fractional-order fundamental operator ${}_a D_t^\alpha$ is defined as in (1), where a and t are the limits and α is the order of the operation [19]

$${}_a D_t^\alpha = \begin{cases} \frac{d^\alpha}{dt^\alpha} & \text{if } \alpha > 0; \\ 1 & \text{if } \alpha = 0; \\ \int_a^t (d\tau)^\alpha & \text{if } \alpha < 0. \end{cases} \quad (1)$$

The most commonly used definitions for fractional-order integral and derivative are Grunwald-Letnikov (G-L) and Riemann-Liouville (R-L) definition.

Definition of Riemann-Liouville (R-L). The fractional-order integral, in the sense of Riemann-Liouville, is defined as

$$I_t^\alpha f(t) = \frac{1}{\Gamma(\alpha)} \int_{t_0}^t (t-\tau)^{\alpha-1} f(\tau) d\tau, \quad (2)$$

and the fractional order derivative is expressed as

$$D_t^\alpha f(t) = \frac{1}{\Gamma(1-\alpha)} \frac{d}{dt} \int_{t_0}^t (t-\tau)^{-\alpha} f(\tau) d\tau, \quad (3)$$

with the Gamma function given by

$$\Gamma(x) = \int_{t_0}^t y^{x-1} e^{-y} dy, \quad (4)$$

where $\Gamma(x)$ is the Euler's Gamma function; t_0 and t are the operation bounds; α is the number identifying the fractional order; τ is the time constant

In this paper, α is taken as a real number that satisfies the restriction $0 < \alpha < 1$ [2, 19]. Besides, it is assumed that $a = 0$ and the convention ${}_a D_t^\alpha = D_t^\alpha$ is used.

Definition of Grunwald-Leitnikov (G-L). The fractional-order integral, in the sense of Grunwald-Leitnikov, is defined as [19, 20]:

$${}_a I_t^\alpha f(t) = \lim_{h \rightarrow 0} h^\alpha \sum_{j=0}^{j=(t-a)/h} \frac{\Gamma(-\alpha+1)}{j! \Gamma(\alpha)} f(t-jh), \quad (5)$$

and the fractional order derivative is expressed as

$${}_a D_t^\alpha f(t) = \lim_{h \rightarrow 0} h^{-\alpha} \sum_{j=0}^{j=(t-a)/h} (-1)^j \frac{\Gamma(\alpha)}{j! \Gamma(\alpha-j+1)} f(t-jh), \quad (6)$$

where h is the sampling period.

For many engineering applications, the control laws are implemented in the frequency domain, using the Laplace transform method. The Laplace transform of the G-L and R-L fractional derivative/integral, under zero initial conditions for order α is given by [21]:

$$L(D_t^{\pm\alpha} f(t)) = s^{\pm\alpha} F(s). \quad (7)$$

Approximation methods. One of the most difficult aspects of dealing with fractional order operators and systems is figuring out how to implement them using rational functions. Many researchers have concentrated on this problem and many approximation strategies, such as Oustaloup's recursive algorithm and Charef's singularity Function approximation method, have been presented [18, 22].

The Oustaloup approximation algorithm is based on the approximate transfer function of a continuous filter for s^α with rational functions as follows [23] by a rational function:

$$s^\alpha = C \prod_{k=1}^N \frac{s + \omega'_k}{s + \omega_k}, \quad (8)$$

where the poles, zeros, and gain are computed from [18]:

$$\omega'_k = \omega_l \omega_u^{(2k-1+\alpha)/N}; \quad (9)$$

$$\omega_k = \omega_l \omega_u^{(2k-1+\alpha)/N}; \quad (10)$$

$$C = \omega_h^\alpha, \quad (11)$$

where $\omega_u = \sqrt{\omega_h/\omega_l}$ is the unity frequencies' gain and the central frequency of a band of frequencies distributed geometrically; ω_h and ω_l are respectively the upper and lower frequencies, α is the order of derivative, and N is the filter order.

Charef and al presented the singularity function approximation method [22], which is very similar to Oustaloup's method basing on the function approximation of the type s^α by a quotient of polynomials in s in a factorized form as follows [24]

$$s^\alpha = K_d \frac{\prod_{i=0}^N (1 + s/z_i)}{\prod_{i=0}^N (1 + s/p_i)}, \quad (12)$$

computed on the frequency interval $\omega \in [\omega_l, \omega_h]$, such that

$$K_d = \omega_c^\alpha, \quad (13)$$

where ω_c is the cutting frequency computed as

$$\omega_c = \omega_l \sqrt[10]{10^{(\frac{\varepsilon}{10\alpha}-1)}}, \quad (14)$$

and the coefficients are calculated to obtain a maximum deviation of ε (dB) from the original magnitude response in the frequency domain defining

$$a = 10^{\varepsilon/(10(1-\alpha))}, \quad b = 10^{\varepsilon/10\alpha}, \quad (15)$$

The poles and zeros of the approximated rational function are obtained applying

$$z_0 = \omega_c \cdot \sqrt{b}. \quad (16)$$

$$z_i = z_0 \cdot (a \cdot b)^i, \quad p_i = a \cdot z_0 \cdot (a \cdot b)^i. \quad (17)$$

The number of poles and zeros is related to the desired band-width and the error criteria formulated by the expression:

$$N = \frac{\log(\omega_h / p_0)}{\log(a.b)} + 1, \quad (18)$$

where ε is the acceptable error chosen by the designer following the desired precision such that $\varepsilon \leq 3$ dB.

Fractional order filters. Fractional-order low-pass filter. The generalized transfer function of a fractional order low pass filter was proposed in [11] as:

$$F(s) = \frac{K}{1 + \tau.s^\alpha} = \frac{d}{s^\alpha + a}, \quad (19)$$

where $d = K/\tau$ and $a = 1/\tau$.

To determine the characteristics of this filter, a frequencies analysis is deemed necessary. For this purpose, the operator s is set as $s = j\omega$ to obtain

$$F(j.\omega) = \frac{d}{\omega^\alpha . \cos(\alpha.\pi/2) + a + j.\omega^\alpha . \sin(\alpha.\pi/2)}. \quad (20)$$

The magnitude response and phase of the filter is expressed as

$$|F(j.\omega)| = \frac{d}{\sqrt{\omega^{2.\alpha} . + 2.a.\omega^\alpha . \cos(\alpha.\pi/2) + a^2}}; \quad (21)$$

$$\text{Arg}(F(j.\omega)) = -\arctg \frac{\omega^\alpha . \sin(\alpha.\pi/2)}{\omega^\alpha . \cos(\alpha.\pi/2) + a}. \quad (22)$$

Figure 2 shows the Bode representation of different approximations of the fractional filter and the original one with

$$F(s) = \frac{K}{1 + \tau.s^\alpha} \quad (K=1, \tau=0.006, \alpha=0.6).$$

From the frequency representation (Fig. 2), it can be seen that singularity function approximation method provided a better fit, hence this latter is the one to be opted for in this paper.

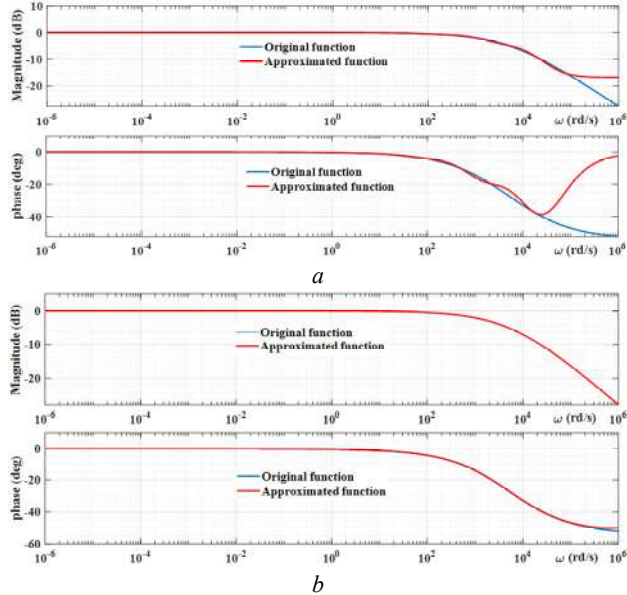


Fig. 2. Bode representation of the filter transfer function:
a – oustaloop recursive algorithm;
b – singularity function approximation

Induction machine model and control strategy.

The dynamic model of the induction machine described in the arbitrary Park referential considering state variables stator current and the rotor flux $[i_{ds} \ i_{qs} \ \Phi_{dr} \ \Phi_{qr}]^T$ is given as follows [25]:

- voltage equations:

$$\begin{aligned} V_{ds} &= R_s.i_{ds} + \sigma.L_s \frac{di_{ds}}{dt} + e_{ds}, \\ V_{qs} &= R_s.i_{qs} + \sigma.L_s \frac{di_{qs}}{dt} + e_{qs}, \\ V_{dr} &= 0 = R_r.i_{dr} + \frac{d\Phi_{dr}}{dt} + e_{dr}, \\ V_{qr} &= 0 = R_r.i_{qr} + \frac{d\Phi_{qr}}{dt} + e_{qr}. \end{aligned} \quad (23)$$

- mechanical equations:

$$J \frac{d\Omega}{dt} + f\Omega = T_{em} - C_r, \quad (24)$$

$$T_{em} = p. \frac{M}{L_r} (\Phi_{dr}.i_{qs} - \Phi_{qr}.i_{ds}), \quad (25)$$

- auto drive equation:

$$\omega_s = \omega_r + p.\Omega. \quad (26)$$

The e_d and e_q terms are the consequence of electromechanical and electromagnetic coupling between the windings, which is analogous to the electromotive forces produced by a direct current machine, expressed as follows:

$$\begin{aligned} e_{ds} &= -\frac{M.R_r}{L_r^2} . \Phi_{dr} - \sigma.L_s.\omega_s.i_{qs} - \frac{M}{L_r} . p.\Omega.\Phi_{qr} \\ e_{qs} &= \frac{M}{L_r} . p.\Omega.\Phi_{dr} + \sigma.L_s.\omega_s.i_{ds} - \frac{M.R_r^2}{L_r^2} . \Phi_{qr} \\ e_{dr} &= -(\omega_s - p.\Omega).\Phi_{qr} + \frac{M.R_r}{L_r} . i_{ds} \\ e_{qr} &= (\omega_s - p.\Omega).\Phi_{dr} - \frac{M.R_r}{L_r} . i_{qs} \end{aligned} \quad (27)$$

Thus the induction machine model is illustrated by the causal informational graph (Fig. 3) [26]. All symbols from figures are described in Appendix.

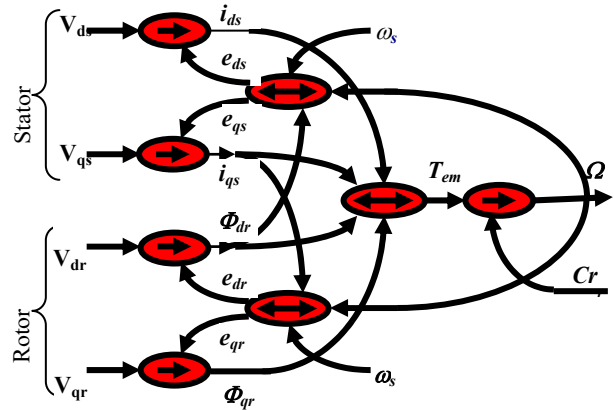


Fig. 3. Causal informational graph representation of the induction motor

Strategy of control. The flux and the current creating the torque must be decoupled in order to control the induction machine. To do this we use a control known as vector control or field oriented drive, which directs the flux along the Park referential's axis.

The rated flux is aligned along the d -axis for rotor field orientation, thus $\Phi_{dr} = \Phi_{ref}$ and $\Phi_{qr} = 0$. Using the voltage equations of the rotor, we will come to

$$M \cdot i_{ds} = \Phi_{dr} + \frac{L_r}{R_r} \frac{d\Phi_{dr}}{dt} \quad (28)$$

$$\omega_r \cdot \Phi_{dr} = \frac{M \cdot R_r}{L_r} i_{qs}$$

The q -axis current is used to adjust the torque as follows:

$$T_{em} = p \cdot \frac{M}{L_r} \cdot (\Phi_{dr} \cdot i_{qs}) \quad (29)$$

Two magnitudes, the flux and its position, are to be controlled using (28), (29). The current i_{ds} govern the flux, so V_{ds} , while the torque is controlled by the current i_{qs} , so V_{qs} . For an indirect control, we impose: $\Phi_{dr} = \Phi_{ref} = \text{const}$.

The scheme control is depicted in Fig. 4 with speed and currents controllers [26] using the principles of inversion of the causal informational graph. Thus the induction machine model with oriented control field

proposed and the filters are illustrated by Simulink scheme block in Fig. 5. The parameters of the induction machine are shown in Table 1.

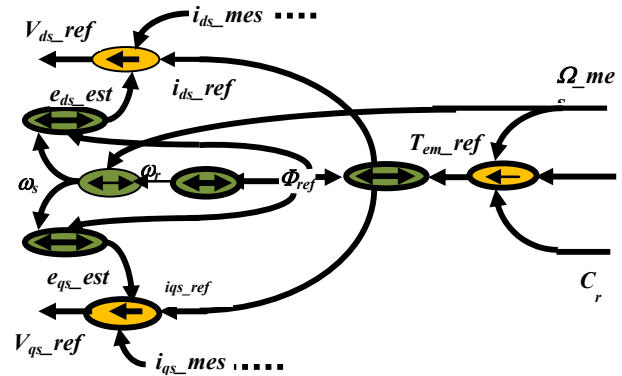


Fig. 4. Control scheme of the induction machine

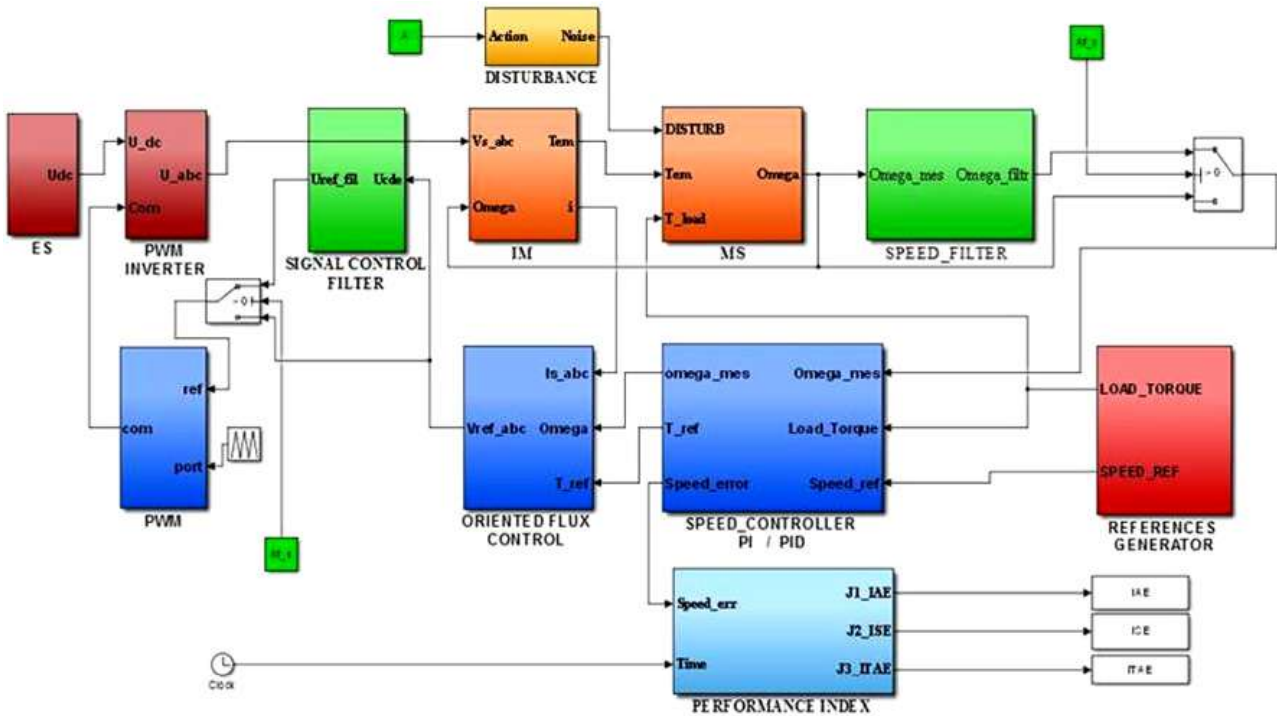


Fig. 5. Simulink model of the induction machine with field control and filters

Design of controllers. One important feature of the proposed method is the use of standard and simple PI controllers, which are very easy to tune.

For the speed control, we have considered the MATLAB tuner for PI controller; whereas, for the current control we have considered the pole assignment approach for the PI parameters' adjustment. The resulting controllers gains are given in Table 2.

Table 1
Parameters of the induction machine

Stator resistance	$R_s = 1.02 \Omega$
Rotor resistance	$R_r = 0.495 \Omega$
Stator inductance	$L_s = 0.035 \text{ H}$
Rotor inductance	$L_r = 0.032 \text{ H}$
Mutual inductance	$M = 0.032 \text{ H}$
Friction coefficient	$f = 0.0000620 \text{ N}\cdot\text{s}/\text{rad}$
Moment of inertia	$J = 0.000494 \text{ kg}\cdot\text{m}^2$
Reference flux	0.2 Wb
Reference speed	1200 rpm

Table 2
Parameters of the controllers

	K_p	K_i
Current controller	3.3068	80.9024
Speed controller	135.6340	445.692

Design of filters. There are several performance indexes that can be used for this purpose. The most frequently used are the integral absolute error (IAE) index, the integral square error (ISE) index or the integral time absolute error (ITAE) index [27] respectively defined as follow.

The integral absolute error (IAE):

$$J_{IAE} = \int |e(t)| dt = \int |r(t) - y(t)| dt \quad (30)$$

The integral square error (ISE):

$$J_{ISE} = \int e^2(t) dt = \int (r(t) - y(t))^2 dt \quad (31)$$

The integral time absolute error (ITAE):

$$J_{ITAE} = \int t.|e(t)|.dt = \int t.|(r(t)-y(t))|.dt, \quad (32)$$

where $r(t)$ and $y(t)$ are respectively the desired value and the output value of closed control loop.

For the PI control, the filter time constant is a fraction of the system time constant. Thus, the considered integer filter is

$$F(s) = \frac{K}{1 + \tau.s}, \quad (33)$$

with $K = 1.01$ for $\tau = 6$ ms.

To configure the filters to be introduced in the control loop, the model is simulated with different positions of integer filters, then the three performance indexes are evaluated. It is, therefore, noticed that for a standard PI controller, the minimum value of J_{IAE} performance index is obtained when the additional filter is placed after the controller, as shown in Fig. 1.

Simulation results are carried out using the MATLAB/Simulink environment. To evaluate the added filters, the test of the process in a noisy environment is proposed with PI controllers tuned as in Table 2. For this, the process is simulated in the feedback control closed loop injecting random noise with mean value magnitude of 5 % added to the system output. Considering a fractional 1st order-like low pass filter of transfer function:

$$F(s) = \frac{K}{1 + \tau.s^\alpha}, \quad (34)$$

with $K = 1.01$ and $\tau = 6$ ms and the order α varies from 0.05 to 1 with a step of 0.05 as shown in Fig. 6.

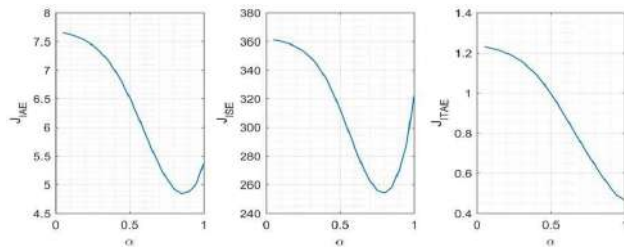


Fig. 6. Performance Index representation vs the fractional order α

From the simulation results represented in Fig. 6, minimum values of J_{IAE} , J_{ISE} and J_{ITAE} performance indexes are obtained for the order α values 0.85, 0.8 and 1 respectively.

Simulation results for the machine speed control without additional filters are represented in Fig. 7, 8 for the safe and noisy cases, respectively, while Fig. 9 illustrates the system response with an integer order filter.

Table 3 shows that the optimal index performance values for J_{IAE} or J_{ISE} are obtained with a fractional filter order $\alpha = 0.85$ (filter 1), $\alpha = 0.8$ (filter 2), respectively, and the third criterion J_{ITAE} is minimized in case of integer value $\alpha = 1$.

According to these values, the response of the machine is depicted in Fig. 10, 11. The dynamic characteristics are shown in Table 4.

A comparative output response for these different cases is given in Fig. 12. It indicates an improvement of the dynamic characteristics (overshoot and oscillations) when using the second fractional order filter minimizing the J_{ISE} criterion.

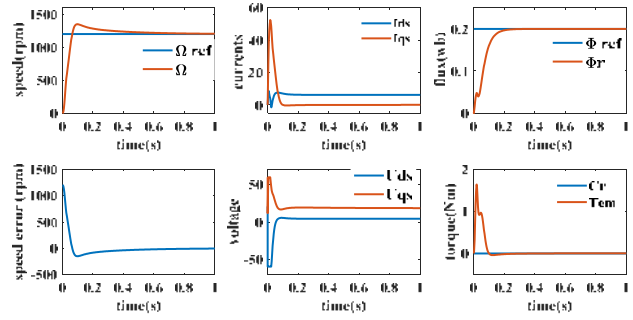


Fig. 7. Response of the machine safe case

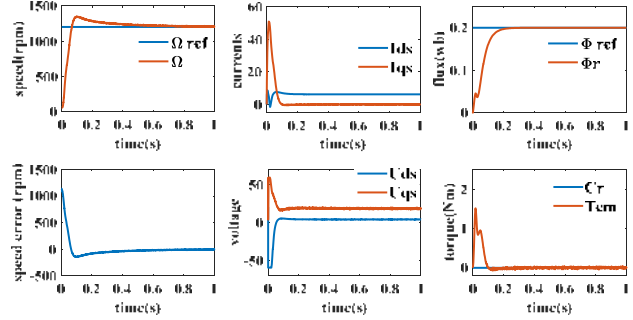


Fig. 8. Response of the machine: noisy case without filter

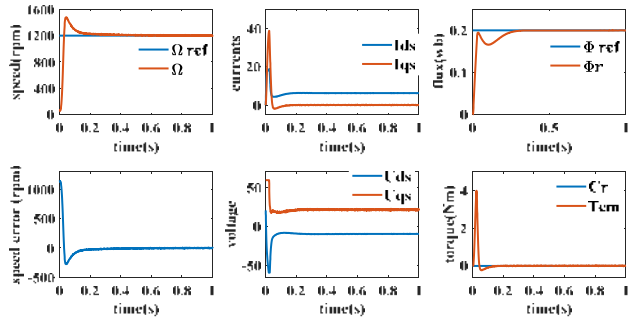


Fig. 9. Response of the machine noisy case with integer filter

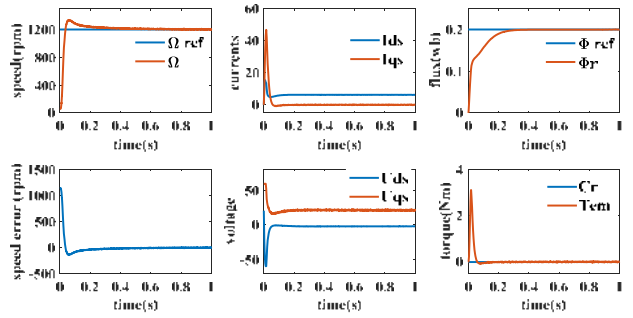


Fig. 10. Response of the machine: noisy case with fractional filter 1

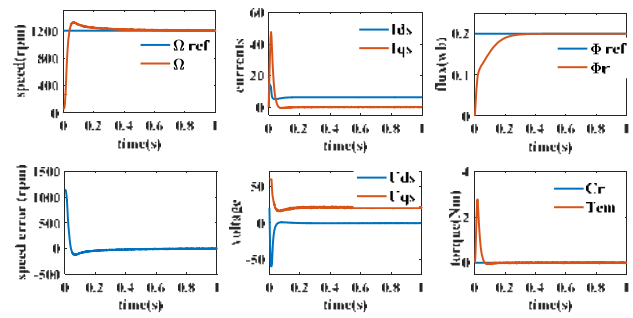


Fig. 11. Response of the machine noisy case with fractional filter 2

Table 3

Performance indexes evaluation

	J_{IAE}	J_{ISE}	J_{ITAE}
Safe case	7.8722	388.6414	1.2588
Noisy case	7.6084	354.8585	1.2262
Noisy case with integer filter	5.0743	292.8749	0.4876
Noisy case with fractional filter 1	4.7587	245.1812	0.6070
Noisy case with fractional filter 2	4.8903	244.6224	0.6589

Table 4

Dynamic characteristics evaluation

	Rise time, s	Settling time, s	Overshoot, %
Safe case	0.0445	0.4811	12.0944
Noisy case	0.0454	0.5800	11.8373
Noisy case with integer filter	0.0149	0.3111	23.2262
Noisy case with fractional filter 1	0.0194	0.3559	11.4581
Noisy case with fractional filter 2	0.0221	0.3913	10.0467

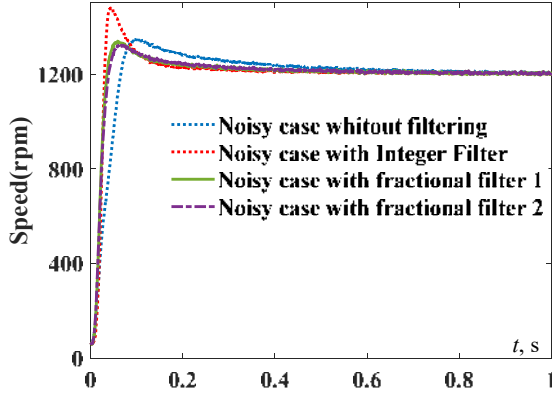


Fig. 12. Machine speed response for different filter fractional orders

Conclusions. The main contribution of this paper is the application of fractional filtering to standard PI control loop for an induction motor speed drive. To evaluate its impact and benefit, intensive simulations have

been realized with a control configuration using an integer and fractional order filters.

As a result of the conducted simulation, it is concluded that the fractional filters give better index performances ($J_{IAE} = 4.7587$ and $J_{ISE} = 245.1812$ for the fractional filter 1 and $J_{IAE} = 4.8903$ and $J_{ISE} = 244.6224$ for the fractional filter 2), as compared to integer one ($J_{IAE} = 5.0743$ and $J_{ISE} = 292.8749$), which improves the system robustness against noises and disturbance.

As regards the dynamic characteristics and though a slight degradation of the rise and the settling times, a significant amelioration of the overshoot is obtained, namely a lesser overshoot of 10.04 %, compared to a result of 23.22 % and 11.83 % with integer filter and without filtering, respectively.

This study may provide an opportunity for further research on considering other sources of disturbance.

Conflict of interest. The authors declare that they have no conflicts of interest.

APPENDIX

R_s	Stator resistance	X_{dr}	Rotor variable on the d axis
R_r	Rotor resistance	X_{qr}	Rotor variable on the q axis
L_s	Stator inductance	X_{mes}	Measured variable
L_r	Rotor inductance	X_{est}	Estimated variable
M	Mutual inductance	X_{ref}	Reference value
p	Number of pole pairs	Φ	Flux
f	Friction coefficient	Φ_{ref}	Flux reference
J	Moment of inertia	T_{em}	Electromagnetic torque
$\sigma = 1 - \frac{M^2}{L_s \cdot L_r}$	Blondel's dispersion coefficient	C_r	Load torque
V	Voltage	ω_s	Stator pulse
i	Current	ω_r	Rotor pulse
(d, q)	Park axis	Ω	Speed
X_{ds}	Stator variable on the d axis	Ω_{ref}	Speed reference
X_{qs}	Stator variable on the q axis	τ	Time constant

REFERENCES

- Ahmed S., Ahmed A., Mansoor I., Junejo F., Saeed A. Output Feedback Adaptive Fractional-Order Super-Twisting Sliding Mode Control of Robotic Manipulator. *Iranian Journal of Science and Technology, Transactions of Electrical Engineering*, 2021, vol. 45, no. 1, pp. 335-347. doi: <https://doi.org/10.1007/s40998-020-00364-y>.
- Djebbri S., Ladaci S., Metatla A., Balaska H. Fractional-order model reference adaptive control of a multi-source renewable energy system with coupled DC/DC converters power compensation. *Energy Systems*, 2020, vol. 11, no. 2, pp. 315-355. doi: <https://doi.org/10.1007/s12667-018-0317-5>.
- Ladaci S., Charef A. On Fractional Adaptive Control. *Nonlinear Dynamics*, 2006, vol. 43, no. 4, pp. 365-378. doi: <https://doi.org/10.1007/s11071-006-0159-x>.
- Azimi M., Toossian Shandiz H. Simultaneous Fault Detection and Control Design for Linear Fractional-Order Systems. *Iranian Journal of Science and Technology, Transactions of Electrical Engineering*, 2020, vol. 44, no. 1, pp. 485-494. doi: <https://doi.org/10.1007/s40998-019-00250-2>.
- Khosravi S., Hamidi Beheshti M.T., Rastegar H. Robust Control of Islanded Microgrid Frequency Using Fractional-Order PID. *Iranian Journal of Science and Technology, Transactions of Electrical Engineering*, 2020, vol. 44, no. 3, pp. 1207-1220. doi: <https://doi.org/10.1007/s40998-019-00303-6>.
- Rafei S.A., Sheikhzadeh H., Sabbaqi M. A New Reduced-Interference Source Separation Method Based on a Complementary Combination of Masking Algorithm and Mixing Matrix Estimation. *Iranian Journal of Science and Technology, Transactions of Electrical Engineering*, 2020, vol. 44, no. 4, pp. 1529-1547. doi: <https://doi.org/10.1007/s40998-020-00326-4>.
- Boudana M., Ladaci S., Loiseau J.-J. Fractional Order PI λ D μ Control Design for a Class of Cyber-Physical Systems with Fractional Order Time-Delay models. *International Journal of Cyber-Physical Systems*, 2019, vol. 1, no. 2, pp. 1-18. doi: <https://doi.org/10.4018/IJCP.S.2019070101>.
- Astrom K.J., Hagglund T. *Advanced PID control*. ISA Publ., 2006. 461 p.
- Segovia V.R., Hagglund T., Astrom K.J. Noise filtering in PI and PID Control. *2013 American Control Conference*, 2013, pp. 1763-1770. doi: <https://doi.org/10.1109/ACC.2013.6580091>.

10. Hägglund T. A unified discussion on signal filtering in PID control. *Control Engineering Practice*, 2013, vol. 21, no. 8, pp. 994-1006. doi: <https://doi.org/10.1016/j.conengprac.2013.03.012>.
11. Radwan A.G., Soliman A.M., Elwakil A.S. First-order filters generalized to the fractional domain. *Journal of Circuits, Systems and Computers*, 2008, vol. 17, no. 01, pp. 55-66. doi: <https://doi.org/10.1142/S0218126608004162>.
12. Radwan A.G., Elwakil A.S., Soliman A.M. On the generalization of second-order filters to the fractional-order domain. *Journal of Circuits, Systems and Computers*, 2009, vol. 18, no. 02, pp. 361-386. doi: <https://doi.org/10.1142/S0218126609005125>.
13. Kubanek D., Freeborn T.J., Dvorak J.K., Dvorak J. Transfer Functions of Fractional-Order Band-Pass Filter with Arbitrary Magnitude Slope in Stopband. *2019 42nd International Conference on Telecommunications and Signal Processing (TSP)*, 2019, pp. 655-659. doi: <https://doi.org/10.1109/TSP.2019.8769089>.
14. Pakhira A., Das S., Acharya A., Pan I., Saha S. Optimized quality factor of fractional order analog filters with band-pass and band-stop characteristics. *2012 Third International Conference on Computing, Communication and Networking Technologies (ICCCNT'12)*, 2012, pp. 1-6. doi: <https://doi.org/10.1109/ICCCNT.2012.6396000>.
15. Matos C., Ortigueira M.D. Fractional Filters: An Optimization Approach. In: Camarinha-Matos L.M., Pereira P., Ribeiro L. (eds) *Emerging Trends in Technological Innovation. DoCEIS 2010. IFIP Advances in Information and Communication Technology*, 2010, vol 314. Springer, Berlin, Heidelberg. doi: https://doi.org/10.1007/978-3-642-11628-5_39.
16. Ladaci S., Loiseau J.-J., Charef A. Using Fractional order Filter in Adaptive Control of Noisy plants. *Third International Conference on Advances in Mechanical Engineering And Mechanics, ICAMEM 2006*, vol. 3.
17. Ladaci S., Bensafia Y. Fractionalization: A New Tool for Robust Adaptive Control of Noisy Plants. *IFAC Proceedings Volumes*, 2013, vol. 46, no. 1, pp. 379-384. doi: <https://doi.org/10.3182/20130204-3-FR-4032.00148>.
18. Monje C.A., Chen Y., Vinagre B.M., Xue D., Feliu V. *Fractional-order Systems and Controls*. Springer London, 2010. 415 p. doi: <https://doi.org/10.1007/978-1-84996-335-0>.
19. Podlubny I. Fractional Differential Equations. *Mathematics in Science and Engineering*, 1999, vol. 198, 340 p.
20. Rabah K., Ladaci S., Lashab M. A novel fractional sliding mode control configuration for synchronizing disturbed fractional-order chaotic systems. *Pramana*, 2017, vol. 89, no. 3, p. 46. doi: <https://doi.org/10.1007/s12043-017-1443-7>.
21. Oldham K., Spanier J. *The fractional calculus*. New York-London, Academic Press, 1974.
22. Charef A., Sun H.H., Tsao Y.Y., Onaral B. Fractal system as represented by singularity function. *IEEE Transactions on Automatic Control*, 1992, vol. 37, no. 9, pp. 1465-1470. doi: <https://doi.org/10.1109/9.159595>.
23. Bensafia Y., Ladaci S., Khettab K., Chemori A. Fractional order model reference adaptive control for SCARA robot trajectory tracking. *International Journal of Industrial and Systems Engineering*, 2018, vol. 30, no. 2, p. 138. doi: <https://doi.org/10.1504/IJISE.2018.094839>.
24. Neçaibia A., Ladaci S., Charef A., Loiseau J.J. Fractional order extremum seeking approach for maximum power point tracking of photovoltaic panels. *Frontiers in Energy*, 2015, vol. 9, no. 1, pp. 43-53. doi: <https://doi.org/10.1007/s11708-014-0343-5>.
25. De Fornel B., Louis J.-P. *Electrical Actuators: Applications and Performance*. John Wiley & Sons, 2013. 528 p.
26. Hassainia S., Toufouti R., Meziane S., Kechida S. Modeling and Control of Induction Motor using Causal Informational Graph. *International Journal of Computer Applications*, 2014, vol. 104, no. 1, pp. 34-38. doi: <https://doi.org/10.5120/18170-9051>.
27. Saleem A., Soliman H., Al-Ratrouf S., Mesbah M. Design of a fractional order PID controller with application to an induction motor drive. *Turkish Journal of Electrical Engineering & Computer Sciences*, 2018, vol. 26, no. 5, pp. 2768-2778. doi: <https://doi.org/10.3906/elk-1712-183>.

Received 08.03.2022
Accepted 20.06.2022
Published 07.09.2022

Saida Hassainia¹, Senior Lecturer,
Samir Ladaci², Professor,
Sihem Kechida³, Professor,
Khaled Khelil¹, Professor,
¹Laboratory of Electrotechnics and Renewable Energies,
Mohamed Cherif Messaadia University,
Souk Ahras, Algeria,
e-mail: saida.hassainia@univ-soukahras.dz (Corresponding Author),
khaled.khelil@univ-soukahras.dz
²Laboratory of Signal Processing,
National Polytechnic School of Algiers, Algeria,
e-mail: samir.ladaci@gmail.com
³Laboratory of Automatics and Informatics,
8 Mai 1945 University, Guelma, Algeria,
e-mail: kechida.sihem@univ-guelma.dz

How to cite this article:

Hassainia S., Ladaci S., Kechida S., Khelil K. Impact of fractional filter in PI control loop applied to induction motor speed drive. *Electrical Engineering & Electromechanics*, 2022, no. 5, pp. 14-20. doi: <https://doi.org/10.20998/2074-272X.2022.5.03>

B.I. Kuznetsov, T.B. Nikitina, I.V. Bovdvi, O.V. Voloshko, V.V. Kolomiets, B.B. Kobylanskyi

The method of multi objective synthesis of stochastic robust control by multimass electromechanical systems under non-gaussian random external disturbances

Aim. Development of the method of multi objective synthesis of stochastic robust control by multimass electromechanical systems to satisfy various requirements for the operation of such systems in various modes under non-gaussian random external disturbances. **Methodology.** The problem of multi objective synthesis of stochastic robust control by multimass electromechanical systems to satisfy various requirements for the operation of such systems in various modes under non-gaussian random external disturbances solved based on the choosing of weight matrices in the robust control goal vector. The calculation of the target vector is performed based on the solution of the zero-sum vector antagonistic game. The components of the game payoff vector are variable quality indicators that are applied to the system operation in various modes. The calculation of the components of payoff vector game are performed based on the simulation of the initial system closed by the synthesized stochastic controllers in various operating modes and under various external influences and variations in the parameters of the uncertainty of the initial plant. **Results.** The results of multi objective synthesis of stochastic robust two-mass electromechanical servo systems modes under non-gaussian random external disturbances in which differences requirements for the operation of such systems in various modes were satisfied are given. Based on the results of modeling and experimental studies it is established, that with the help of synthesized robust nonlinear controllers, it is possible to improve of quality indicators of two-mass electromechanical servo system in comparison with the system with standard regulators. **Originality.** For the first time the method of multi objective synthesis of stochastic robust control by multimass electromechanical systems to satisfy various requirements for the operation of multimass systems in various modes is developed. **Practical value.** From the point of view of the practical implementation the possibility of solving the problem of multi objective synthesis of stochastic robust control systems to satisfy various requirements for the operation of multimass electromechanical systems in various modes is shown. References 38, figures 3.

Key words: multimass electromechanical systems, stochastic robust control, multi objective synthesis, zero-sum vector game solution, computer simulation, experimental research.

Ціль. Розробка методу багатокритеріального синтезу стохастичного робастного керування багатомасовими електро механічними системами для задоволення різноманітних вимог до роботи багатомасових систем в різних режимах при негаусових випадкових зовнішніх збуреннях. **Методологія.** Задача багатокритеріального синтезу стохастичного робастного керування багатомасовими електро механічними системами для задоволення різноманітних вимог до роботи систем в різних режимах при негаусових випадкових зовнішніх збуреннях вирішена на основі вибору вагових матриць у векторі цілі робастного керування. Обчислення вектору цілі виконується на основі рішення векторної антагоністичної гри з нульовою сумою. Компонентами вектора цілі гри є показники якості, які пред'являються до роботи системи в різних режимах. Обчислення компонентів вектора цілі гри виконано на основі моделювання вихідної системи, замкненої синтезованими стохастичними регуляторами в різних режимах роботи та при різних зовнішніх впливах та варіаціях параметрів невизначеності вихідної системи. **Результати.** Наведено результати багатокритеріального синтезу стохастичних робастних двомасових електро механічних сервосистем при негаусових випадкових зовнішніх збуреннях, в яких задовольняються вимоги до роботи таких систем у різних режимах. На основі результатів моделювання та експериментальних досліджень встановлено, що за допомогою синтезованих стохастичних робастних регуляторів можна підвищити якісні показники двомасової електро механічної сервосистеми в порівнянні з системою зі стандартними регуляторами. **Оригінальність.** Вперше розроблено метод багатокритеріального синтезу стохастичного робастного керування багатомасовими електро механічними системами для задоволення різноманітних вимог до роботи таких систем у різних режимах. **Практична цінність.** З точки зору практичної реалізації, показано можливість вирішення задачі багатокритеріального синтезу стохастичних робастних систем керування для задоволення різноманітних вимог до роботи багатомасових електро механічних систем в різних режимах. Бібл. 38, рис. 3.

Ключові слова: багатомасові електро механічні системи, стохастичне робастне керування, багатокритеріальний синтез, рішення векторної антагоністичної гри з нульовою сумою, комп'ютерне моделювання, експериментальні дослідження.

Introduction. The central problem of the modern theory of robust control is the creation of systems that can function effectively under conditions of uncertainty in the values of parameters, and possibly also in the structure of models of the plant, disturbances and measurement noise.

To date, impressive results have been obtained in the synthesis of robust controllers, which make it possible to obtain guaranteed results in control and identification problems and are designed for the most unfavorable case. However, the payoff for obtaining a guaranteed result in the most unfavorable case is the excessive «caution» of such regulators.

Recently, the theory of stochastic robust control has been intensively developed [1–4]. Stochastic robust control systems have a number of advantages. First, they are robustly stable, i.e. maintain stability when changing the parameters of the control object within certain limits.

Secondly, they have a significantly lower sensitivity to changes in the parameters of the control object compared to optimal systems, despite the fact that the dynamic characteristics of stochastic robust systems may differ slightly from the corresponding characteristics of optimal systems. Therefore, the issues of designing control systems operating under random setting and disturbing influences are relevant.

The problem of designing an anisotropic controller minimizing the anisotropic norm of a closed system was posed and solved in [1–4]. This refers to the synthesis of controllers for systems whose model parameters are fully known. However, there is no complete information about the object model, which entails the need to develop methods that are robust not only to external disturbances, but also robust to the model parameters.

When creating methods for the synthesis of robust control, a new area of application of the theory of

dynamic games has appeared, when one of the players is the control, with the help of which the norm of the goal vector is minimized, and the other player is an external influence, which is considered independent during the synthesis of the system is determined from the condition maximum «evilness» (worst-case disturbance) – the maximum deviation of the norm of the same goal vector.

When synthesizing an anisotropic controller that minimizes the anisotropic norm of a closed system, it is assumed that the goal vector of robust control is given. In as a result of the synthesis, a control is found, with the help of which the anisotropic norm of the target vector, i.e. a scalar value, is minimized. However, for multimass electromechanical control systems, in addition to the requirements for the accuracy of processing or compensation of random input signals, certain requirements are often imposed on the quality requirements of its work in various modes of operation.

Until now, in the theory of synthesis of anisotropic controllers, the problem of multicriteria synthesis of anisotropic controllers, robust to inaccuracies in setting the parameters of the object model of multimass electromechanical systems has not been solved [5, 6]. Therefore, the development of a method for the multicriteria synthesis of anisotropic controllers those are insensitive to the parameters of the object model of multimass electromechanical systems and allows taking into account all the requirements for the operation of such systems in various operating modes is an urgent problem.

The purpose of the work is to develop the method of multi objective synthesis of stochastic robust control by multimass electromechanical systems to satisfy various requirements for the operation of multimass systems in various modes under non-gaussian random external disturbances.

Statement of the problem. The current state of the theory of robust systems is characterized by a wide variety of problem statements and formulations of criteria for the synthesis of robust controllers. It is customary to distinguish between classes of parametric (structured) and non-parametric (unstructured) uncertainties. In practice, there are cases of joint uncertainty (both parametric and non-parametric) [7–10].

Non-parametric uncertainty is understood as such uncertainty in the control object, which affects the structure of the object, changing its order [11–14]. Parametric uncertainty is understood as changes in the coefficients of an object in a certain area [15–19].

The main approach to the synthesis of robust control in the time domain is based on solving the optimal control problem [20–23]. However, unlike the classical approach to the synthesis of optimal control systems, with robust control, in addition to the control vector, the equation of state of the original control object also includes the vector of external influences [24, 25]. Moreover, the vector of external influences characterizes the change in the state of the system due to parametric and structural changes in the model of the control object.

For a discrete robust plant of a multimass system with state vector x_k , control vector u_k , the vector y_k of measurable variables and the vector z_k of the robust control target the difference equation of state is represented in the standard form adopted in robust control theory:

$$\begin{cases} x_{k+1} = Ax_k + B_0\omega_k + B_2u_k, \\ z_k = C_1x_k + D_{12}u_k, \\ y_k = C_2x_k + D_{21}\omega_k. \end{cases} \quad -\infty < k < \infty \quad (1)$$

The anisotropic regulator is adopted in the form of a discrete dynamical system, which is given by the difference equation:

$$\begin{aligned} \xi_{k+1} &= \hat{A}\xi_k + \hat{B}y_k \dots, \\ \dots u_k &= \hat{C}\xi_k. \end{aligned} \quad (2)$$

The input of this dynamic system (2) is the vector y_k of measuring variables, and its output is the control vector u_k of the control object (1).

An advanced system that includes a control object (1) closed by a controller (2) has a state vector that includes the state vector x_k of the control object and the state vector ξ_k of the controller. The input vectors of this extended system are the vectors ω_k of external signal and parametric perturbations, and the output vector of the system is the target vector z_k of robust control. We introduce the matrix of this extended system in the state space is taken as

$$\begin{aligned} &\left[\begin{array}{cc|cc} A & B_2\hat{C} & B_0 & B_1 \\ \hat{B}C_2 & \hat{A} & \hat{B}D_{21} & 0 \\ \hline C_1 & D_{12}\hat{C} & 0 & 0 \end{array} \right] \equiv \dots \\ &\dots \equiv \left[\begin{array}{c|cc} A_t & B_t & F_t \\ \hline C_t & 0 & 0 \end{array} \right]. \end{aligned} \quad (3)$$

When synthesizing an anisotropic controller that minimizes the anisotropic norm of a closed system, the vector z_k of the robust control goal is specified as a vector of some variables that are functions of time and represent a linear transformation of the variables of the state vector x_k and control vector u_k , of the original system (1). In as a result of the synthesis, a control u_k is found, with the help of which the anisotropic norm of the target vector z_k , i.e. a scalar value, is minimized.

Notice, that when synthesizing a robust deterministic controller, the target vector is also specified as a vector function of time, however, during the synthesis, a scalar variable is minimized in the form of the H_∞ norm of this target vector. We also note that under the classical optimal control, a scalar variable is minimized in the form of a H_2 norm of a linear transformation of the variables of the state vector and control of the original system.

However, for multimass electromechanical control systems, in addition to the requirements for the accuracy of processing or compensation of random input signals, certain requirements are often imposed on the quality of transient processes – the time of the first coordination, the time of regulation, re-regulation, etc. Thus, in addition to the requirements for the operation of the system with random input signals, there are certain requirements for working out by the system of deterministic influences – stepwise signals. Moreover, these requirements can differ significantly for transient processes when the system works out «small» and «large» impacts.

In addition, certain requirements are often imposed on multimass electromechanical systems for processing harmonic signals of fixed frequencies, or a given frequency range, which are also deterministic signals.

These requirements can be satisfied with a deterministic approach to the synthesis of the designed system.

Naturally, the designed system must simultaneously satisfy all the requirements for the operation of the system in various modes and with various input signals.

When designing a system, it is necessary to set the goal vector of robust control in such a way that the designed system must simultaneously satisfy all the requirements for the operation of the system in various modes and with various input signals.

Solution method. Consider the method for calculating the target vector of anisotropic robust control that the designed systems satisfy all the requirements for the operation of the system in various modes and with various input signals.

Let us introduce the vector of the desired parameters θ , the components of which are the elements of the C_1 and D_{12} matrices in (1), with the help of which the goal vector z_k of the stochastic robust control is formed in the form of a linear combination of the variables of state vector x_k of the original system and of the component of control vector u_k .

Let us introduce the vector J of quality indicators that apply to the operation of the system in various operating modes. The components of this vector, in particular, can be: the transient times are usually specified when certain input signals are applied: the accuracy of working off the specified minimum speed value the uneven movement of the working body at the minimum speed: minimum value of the stabilization dispersion of a given random change in the reference action is usually required under the action of random disturbing influences caused, for example, by a random change in the road profile.

Let us also introduce the vector B of binary preference relations for pairwise comparison of performance indicators of the system in different modes, with different input signals and with different uncertainty parameters of the original multimass system.

In addition, we introduce a vector G of limitations, the components of which can be the limiting values of voltages, currents, rates of change of currents, moments, elastic moments, rates of change of moments (jerks), speeds of various elements of a multimass electromechanical system, their positions, etc.

We also introduce the vector δ of uncertainties in the parameters of the initial system and external influences. The components of this vector, in particular, can be changes in the moments of inertia of the working body.

The dynamic characteristics of the synthesized stochastic robust system are determined by the model of the initial system, external master and disturbing influences, and, of course, the parameters of the synthesized stochastic robust controllers. The control system designer can only change the stochastic robust control target vector.

For a given value of the vector θ of the desired parameters, with the help of which the goal vector of the stochastic robust control is formed, a stochastic robust controller can be calculated. For this synthesized stochastic controller, the values of the components of the vector J of quality indicators, the vector G of restrictions and the vector of B of binary preference relations can be calculated in the course of simulating the operation of a closed system in various operating modes,

for various input signals and for various values of the vector parameters of uncertainties of the initial system.

Then, using the given value of the vector θ of these desired parameters, the vector J of the values of quality indicators that are imposed on the system operation, and the vector G of the restrictions when the system is operating in various operating modes and for various setting and disturbing and for various values of the vector δ of the uncertainty of the initial system parameters and external influences the problem of multi objective synthesis of non-linear robust control can be formulated as the zero-sum vector antagonistic game [25, 26].

$$J(\theta, \delta) = [J_1(\theta, \delta), J_2(\theta, \delta), \dots, \dots, J_m(\theta, \delta)]^T. \quad (4)$$

In this game, the first player is the vector of the desired parameters θ , the components of which are the elements of the C_1 and D_{12} matrices (1), with the help of which the goal vector z_k of the stochastic robust control is computed, and its strategy is to minimize the game pay vector J . The second player is the vector δ of uncertainties in the parameters of the initial system and external influences, and its strategy is to maximize the same game pay vector J . This approach is the standard approach in the robust control synthesis for the «worst» case.

Naturally, in this case, it is necessary to take into account restrictions on the strategy vectors of the first and second players in the form of a vector inequality

$$G(\theta, \delta) \leq G_{\max} \quad (5)$$

the components of which are the limiting values of voltages, currents, rates of change of currents, moments, elastic moments, rates of change of moments, speeds of various elements of a multimass electromechanical system.

To correctly calculate the solution of this vector antagonistic game from the set of Pareto-optimal solutions, binary preference relations of local performance criteria B are used.

In conclusion, we note that the computation of the payoff game vector J , the constraint vector G , and the vector B of binary preference relations is algorithmic in nature and requires large computational resources. First, to calculate the stochastic robust control. Then, in order to calculate the values of payoff game vector J , the constraint vector G , and the vector B of binary preference relations it is necessary to simulate the initial non-linear system closed by synthesized stochastic robust controllers for given system operation modes and for given driving and perturbing influences at given values of the stochastic vector certainty of the parameters of the original system.

The algorithm for calculating the solution of a multicriteria game. Let us consider the algorithm for calculating the solution of a multicriteria game (4) with constraints (5) from the set of Pareto-optimal solutions, taking into account binary preference relations [26–30], based on the particle multiswarm optimization (PSO) algorithm [31–34]. To date, a large number of particle swarm optimization algorithms have been developed – PSO algorithms based on the idea of collective particle swarm intelligence, such as gbest PSO and lbest PSO algorithms. The use of stochastic multi-agent optimization methods to solve vector antagonistic game today causes some difficulties and this area continues to develop

intensively. To solve the initial vector antagonistic game with constraints, we construct an algorithm for stochastic multiagent optimization based on a set of swarms of particles, the number of which is equal to the number of components of the pay vector game.

In the standard optimization algorithm by a swarm of particles, the change in particle velocities is usually carried out according to linear laws [35–38]. To increase the speed of finding a global solution, a nonlinear optimization algorithm by a multiswarm of particles, proposed in [36], is used, in which the motion of i particle – of j swarm is described by the following expressions

$$\begin{aligned} v_{ij}(t+1) = & w_{1j}v_{ij}(t) + c_{1j}r_{1j}(t) * \dots \\ & \dots * H(p_{1ij}(t) - \varepsilon_{1ij}(t)) [y_{ij}(t) - \dots \\ & \dots - x_{ij}(t)] + c_{2j}r_{2j}(t) H(p_{2ij}(t) - \dots \\ & \dots - \varepsilon_{2ij}(t)) [y_j^*(t) - x_{ij}(t)] \end{aligned} \quad (6)$$

$$\begin{aligned} u_{ij}(t+1) = & w_{2j}u_{ij}(t) + c_{3j}r_{3j}(t) H * \dots \\ & \dots * (p_{3ij}(t) - \varepsilon_{3ij}(t)) [z_{ij}(t) - \delta_{ij}(t)] + \dots \\ & \dots + c_{4j}r_{4j}(t) H(p_{4ij}(t) - \varepsilon_{4ij}(t)) * \dots \\ & \dots * [z_j^*(t) - \delta_{ij}(t)] \end{aligned} \quad (7)$$

$$\theta_{ij}(t+1) = \theta_{ij}(t) + v_{ij}(t+1), \quad (8)$$

$$\delta_{ij}(t+1) = \delta_{ij}(t) + u_{ij}(t+1), \quad (9)$$

where $\theta_{ij}(t)$, $\delta_{ij}(t)$ position and $v_{ij}(t)$, $u_{ij}(t)$, velocities of i particle of j swarm.

Note that due to the fact that the solution of the multicriteria game (4) are two vectors of strategies of the first θ and second δ players, each i particle of j swarm has two position components $\theta_{ij}(t)$, $\delta_{ij}(t)$, and two velocity components $v_{ij}(t)$, $u_{ij}(t)$, to find two vectors strategies of the first and second players.

In (6) – (7), $y_{ij}(t)$, $z_{ij}(t)$ and y_j^* , z_j^* are the best local and global positions of i particle found, respectively, by only one i particle and all i particles by j swarm. Moreover, the best components of the local $y_{ij}(t)$ and global $y_j^*(t)$ position i particle of the j swarm are understood in the sense of the strategy of the first player $\theta_{ij}(t)$ to minimize the components of the vector payoff (4). However, in this case, the best components of the local $z_{ij}(t)$ and global z_j^* position of the same i particle of the same j swarm are understood in the sense of the strategy of the second player $\delta_{ij}(t)$ to maximize the same components of the vector payoff (4). This approach corresponds to the motion of particles along the gradient and antigradient when using deterministic algorithms for solving games [24].

Four independent random numbers $r_{1j}(t)$, $r_{2j}(t)$, $r_{3j}(t)$, $r_{4j}(t)$ are in the range [0, 1.0] and determine the stochastic components of the particle velocity components.

Positive constants c_{1j} , c_{2j} and c_{3j} , c_{4j} determine the cognitive and social weights of the particle velocity components.

Note that the peculiarity of the solution of this game is that the components of the strategy vector $\theta_{ij}(t)$ of the first player are the components of which are the elements of the C_1 and D_{12} matrices in (1), with the help of which the goal vector z_k of the stochastic robust control is formed in the form of a linear combination of the

variables of state vector x_k of the original system and of the component of control vector u_k .

Therefore, the values of these constants c_{1j} , c_{2j} and c_{3j} , c_{4j} are chosen taking into account the range of possible changes in the strategies $\theta_{ij}(t)$, $\delta_{ij}(t)$, of the players.

A feature of the solution of this multicriteria game (4) with restrictions (5) is the presence of «ravines» and «ridges» in the vector payoff (4). This is due, firstly, to the fact that the values of the components of the strategies $\theta_{ij}(t)$, $\delta_{ij}(t)$, of the players and differ by more than an order of magnitude. Secondly, a change in some components of the players' strategies leads to insignificant changes in the vector payoff of the game (4).

Therefore, to improve the speed of finding a global solution with small increments of the vector payoff (4) to determine the strategies $\theta_{ij}(t)$, $\delta_{ij}(t)$, of players, in (6) – (7) a non-linear search algorithm (Cuckoo Search) [34] is used for stochastic optimization by a multiswarm of particles. The Heaviside function H [35] is used as a non-linear function for switching the particle motion to the local $y_{ij}(t)$, $z_{ij}(t)$ and global $y_j^*(t)$, z_j^* optima, respectively.

The switching parameters p_{1ij} , p_{3ij} cognitive and social p_{2ij} , p_{4ij} components of the particle velocity components to the local $y_{ij}(t)$, $z_{ij}(t)$ and to the global $y_j^*(t)$, z_j^* optima were taken as increments of changes in the components of the vector payoff (4) for the strategies of the players $\theta_{ij}(t)$, $\delta_{ij}(t)$, when moving, respectively, to the local and global optima.

Random numbers $\varepsilon_{1ij}(t)$, $\varepsilon_{2ij}(t)$, $\varepsilon_{3ij}(t)$ and $\varepsilon_{4ij}(t)$ determine the parameters for switching the motion of particles, respectively, to the local and global optimums. If $p_{1ij} < \varepsilon_{1ij}(t)$ and $p_{2ij} < \varepsilon_{2ij}(t)$, then the component $v_{ij}(t)$ of the velocity of movement of i particle of j swarm does not change at the t step, and this particle moves in the same direction as at the previous optimization step. Similarly, if $p_{3ij} < \varepsilon_{3ij}(t)$ and $p_{4ij} < \varepsilon_{4ij}(t)$, then the component $u_{ij}(t)$ of the velocity of movement of i particle of j swarm does not change at the step t either.

To improve the quality of the process of finding a solution, inertia coefficients w_{1j} , w_{2j} are used, in the range (0.5 – 0.9).

Note that the solutions of the original vector game (4) are the Pareto set of optimal solutions. The narrowing of this set occurs at the stage of search by taking into account constraints (5) on the state variables and control of the original system. As limitations G (5) in this game, first of all, the limiting values of voltages, currents, rates of change of currents, moments, elastic moments, rates of change of moments (jerks), speeds of various elements of a multimass electromechanical system, their positions, etc are taken into account.

In the considered problem of synthesis of the servo system, in particular, the limitations on the armature current of the drive motor and the speed of rotation of this motor is hindered to decrease the time of the first coordination in the mode of working out large angular mismatches by this servo system.

The maximum particle velocities $v_{ij}(t)$, $u_{ij}(t)$ were also limited, based on the desired accuracy of obtaining solutions to the corresponding components of the strategy vectors $\theta_{ij}(t)$ and $\delta_{ij}(t)$, as well as to improve the convergence of the solution to the game (4).

To find the global optimum solution of the multicriteria game (4) in the course of searching for local optimal solutions to this game, individual particles and swarms exchange information with each other. At the same time, to calculate the speed of a particle of one swarm, information about the global optimum obtained by particles of another swarm is used, which makes it possible to identify all possible Pareto-optimal solutions. To do this, at each step t of the movement of i particle of j swarm, the functions of binary preference relations of local solutions obtained by all swarms are used.

The solution $\theta_j^*(t)$ obtained in the course of solving the game $J(\theta_j^*(t), \delta(t))$ with the help of j swarm is more preferable than the solution $\theta_k^*(t)$ of the game $J(\theta_k^*(t), \delta(t))$ obtained with the help of k swarm, if the condition

$$B(J(\theta_j^*(t), \delta(t))) < B(J(\theta_k^*(t), \delta(t))) \quad (10)$$

In this case, as the global optimal solution $\theta_k^*(t)$ obtained by the k swarm, the global solution $\theta_j^*(t)$ obtained by the j swarm is used, which is more preferable than the global solution $\theta_k^*(t)$ obtained by the k swarm based on the binary preference relation (10).

An example of such a binary preference can be a situation where a decrease in the time of the transient process when working out small mismatches leads to an increase in the dispersion of the tracking error. Due to an increase in the component of the dispersion for measurement noise due to the expansion of the system bandwidth. In this case, it is more preferable to reduce the dispersion of the tracking error. Since it is this quality indicator that determines the potential accuracy of the tracking system and the possibility of capturing and auto-tracking the target.

In fact, this approach implements the main idea of the method of successively narrowing the area of compromise solutions – Pareto-optimal solutions from the initial set of possible solutions based on information about the relative importance of local solutions that cannot be chosen in accordance with the -formation about binary preference relations (10).

Solutions are removed until a globally optimal solution is found. As a result of applying this approach, the potentially optimal solution will not be removed at each stage of the narrowing. Note that the art of applying the multiswarm particle optimization (PSO) algorithm lies in the reasonable choice of its tuning constants.

In conclusion, we note that the original multicriteria game (9) – (10), taking into account the algorithm for solving it (11) – (13), is a multicriteria stochastic dynamic game, since it clearly has time and random search [26].

Calculation of the Anisotropic norm. Stochastic approach to H_∞ -optimization of automatic control systems based on the use of the quality criterion of the stochastic norm of the system. Such a norm quantitatively characterizes the sensitivity of the system output to random input disturbances, the probability distribution of which is not known exactly. The concretization of this approach, obtained by combining the concept of the stochastic norm of the system and the average anisotropy of the signal [1 – 4], leads to a special version of the stochastic norm – the anisotropic norm.

Average anisotropy is a characteristic of the space-time coloring of a stationary Gaussian signal, which is closely related, on the one hand, to the information-theoretic approach to the quantitative description of chaos using the Kolmogorov entropy of probability distributions, and on the other hand, to the principle the isotropy principle of a finite-dimensional Euclidean space. The anisotropic norm of a system characterizes its sensitivity to input Gaussian noises, the average anisotropy of which is limited from above by some non-negative parameter.

This norm is used when a priori information about the input disturbance is that the disturbance is a Gaussian random sequence with zero mean and mean anisotropy bounded from above [4]. The latter is a measure of the correlation of the components of a random vector in a sequence (or, as they say, «coloring») or, which is the same, a measure of the deviation of a sequence of a random variable from Gaussian white noise.

The main concepts of the anisotropic theory of stochastic robust control are the anisotropy of a random vector, the average anisotropy of a random vector, and the anisotropic norm of the system. The anisotropy functional is an entropy measure of the deviation of a probability distribution in Euclidean space from Gaussian distributions with zero mean and scalar covariance matrices.

The average anisotropy of a stationary random sequence characterizes the magnitude of the statistical uncertainty, understood as the discrepancy between the inaccurately known actual noise distribution and the family of nominal perturbation models in the form of a stationary discrete Gaussian white noise.

The anisotropic norm of a discrete linear stationary system quantitatively determines the capabilities of the system to suppress disturbances by the largest ratio of the power norm of the output of the system to the power norm of its input, provided that the average anisotropy of the input signal does not exceed a given non-negative level.

The keypoint is the definition of the anisotropy of a random vector, the mean anisotropy of a Gaussian sequence, and the anisotropy norm of the transfer function of a closed system. Covariance matrix, therefore, to calculate the anisotropic norm, it is necessary to solve the Riccati equation – as a necessary condition for the minimum Kullback-Leibler informational deviation [3].

Consider the original system (1) closed by a stochastic controller (2) in the form of the state equation of discrete system

$$\begin{cases} x_{k+1} = Ax_k + B\omega_k; \\ z_k = Cx_k + D\omega_k. \end{cases} \quad (11)$$

To calculate the anisotropic norm of this system must solve the Riccati equation with respect to the matrix

$$R \in R^{n \times n}; \quad R = ARA^T + BB^T - \Lambda\Theta\Lambda^T, \quad (12)$$

where

$$\begin{aligned} \Lambda &= (ARC^T + BD^T)\Theta^{-1}, \\ \Theta &= CRC^T + DD^T. \end{aligned}$$

Then the average anisotropy is calculated based on the following expression

$$\bar{A}(G) = -\frac{1}{2} \ln \det \left(\frac{m\Theta}{\text{Trace}(CPC^T + DD^T)} \right), \quad (13)$$

where P is the controllability Gramian that satisfies the Lyapunov equation

$$P = APA^T + BB^T.$$

Calculating of the payoff vector of the game. To calculate the values of the vector of quality indicators, the initial nonlinear system is modeled, closed by the synthesized anisotropic controller in various operating modes and under various input influences. The central idea of the synthesis of robust control systems is related to the synthesis of a system that minimizes the quality criterion according to the control norm, but maximizes the same criterion according to the norm of the vector of external influences. At the same time, due to the introduction of the norm of the vector of external influences with a minus sign into the Hamilton function, the synthesized system minimizes the sensitivity of the system to the variable parameters of the control object, and therefore ensures the robustness of the system.

This approach corresponds to the game approach to the optimization problem, when the first player «control» minimizes the goal function, and the second player «undefined parameters of the plant» maximizes the same goal function. Moreover, since the original system is described by a system of differential equations - a matrix equation of state, and both players use the same goal function, then such a game is called a zero-sum differential game.

We synthesize a complete anisotropic controller of multimass electromechanical systems with parametric uncertainty by reducing it to the solution of the optimization problem without parametric uncertainty by introducing an additional input, so that the obtained problem is a mixed / optimization problem.

We use the results of differential games to solve the problem of synthesis of anisotropic regulators. To find the worst input, forming vector of structural perturbations, that maximizes the anisotropic norm of the system, solve the following first Riccati's equation

$$\tilde{Y} = A_t^T \tilde{Y} A_t + L_t^T \Pi L_t + Q, \quad (14)$$

where

$$L_t = \Pi^{-1} F_t^T \tilde{Y} A_t, \quad \Pi = \Gamma - F_t^T \tilde{Y} F_t,$$

To find the worst input, forming vector of parametric perturbations, that maximizes the anisotropic rate of the system, solve the following second Riccati's equation

$$R = A_\omega^T R A_\omega + q C_\omega^T C_\omega + L^T \Sigma^{-1} L, \quad (15)$$

where

$$L = \Sigma \left(B_\omega^T R A_\omega + q D_\omega^T C_\omega \right), \\ \Sigma = \left(I_{m1} - B_\omega^T R B_\omega \right)^{-1}.$$

For the synthesis of anisotropic observers of the state of multimass electromechanical systems with parametric uncertainty, which are necessary for the realization of anisotropic regulators of complete order, we solve the third Riccati equation

$$S = \tilde{A}_{11} S \tilde{A}_{11}^T + \tilde{B}_1 \tilde{B}_1^T - \Lambda \Theta \Lambda^T, \quad (16)$$

where

$$\Theta = \tilde{C}_{21} S \tilde{C}_{21}^T + \tilde{D} \tilde{D}^T, \\ \Lambda = \left(\tilde{A}_{11} S \tilde{C}_{21}^T + \tilde{B}_1 \tilde{D}^T \right) \Theta^{-1}.$$

To synthesize the optimal anisotropic state regulator that minimizes the anisotropic norm of the system, we solve the fourth Riccati equation

$$T = A_u^T T A_u + C_u^T C_u - N^T \Psi N, \quad (17)$$

where

$$\Psi = B_u^T T B_u + D_{12}^T D_{12}, \\ N = -\Psi^{-1} \left(B_u^T T A_u + D_{12}^T C_u \right).$$

The obtained algorithm for the synthesis of anisotropic regulators is reduced to an iterative solution of the problem of stochastic robust optimization. The solution of the problem begins for fixed values of tolerance parameters, the values of which must be large enough for the equations to have solutions. Then we solve a system of four related Riccati equations (14) – (17), Lyapunov equation and special expression (13). This system of equations is numerically solved using the homotopy method, which includes vectorization of matrices and iterations according to Newton's method.

The optimal anisotropic controller of the complete order is the optimal estimator of the optimal control law in the problem with complete information about the system state vector for the case of the worst input. The principle of separation in the mixed problem of robust control does not mean the independence of the Riccati equations. Unlike classical H_2 and H_∞ optimization, the problem of estimator synthesis and the problem of synthesis of the optimal static regulator in the form of feedback cannot be solved independently of each other.

This generalized distribution principle allows us to interpret the results obtained in terms of the theory of differential games. Control of the system in the presence of external perturbations is considered as a differential game between two players – nature and the regulator. The optimal strategy of the first player – the regulator, is to obtain optimal control, and the optimal strategy of the second player – nature, is to obtain the «worst» perturbation in the form of parametric uncertainty of the control object. At the same time, each of the players knows about the optimal strategy of his opponent.

Simulation results. Let us consider multi objective synthesis of stochastic robust control by two-mass electromechanical servo systems to satisfy various requirements for the operation of such systems in various modes under non-gaussian random external disturbances. One of the most stressful modes of operation of such a servo system is the guidance mode with a random velocity celm under the action of random non-Gaussian perturbations on the plant. On Fig. 1 are shown the implementation of random processes of state variables: rotation speed $\omega_M(t)$ of the motor (a), rotation speed $\omega_P(t)$ of the plant (b) and the disturbances $M_D(t)$ acting on the plant (c).

An analysis of these implementations shows that the system accurately processes the low-frequency components of the master random process; however, when processing the high-frequency components, the system error is about 20 %.

In this example anisotropic controllers demonstrated the best quality of suppression of external disturbances and tracking at the lowest control costs, and closed systems with anisotropic controllers have greater noise immunity.

Taking into account apriori information about the input action, which consists in the limitation from above of the functional of the average anisotropy of the input perturbation by a known parameter, makes it possible to

obtain controllers that are more robust with respect to the specified action than H_2 controllers and less conservative than H_∞ regulators, which makes them very attractive for practical use instead of classical LQR regulators

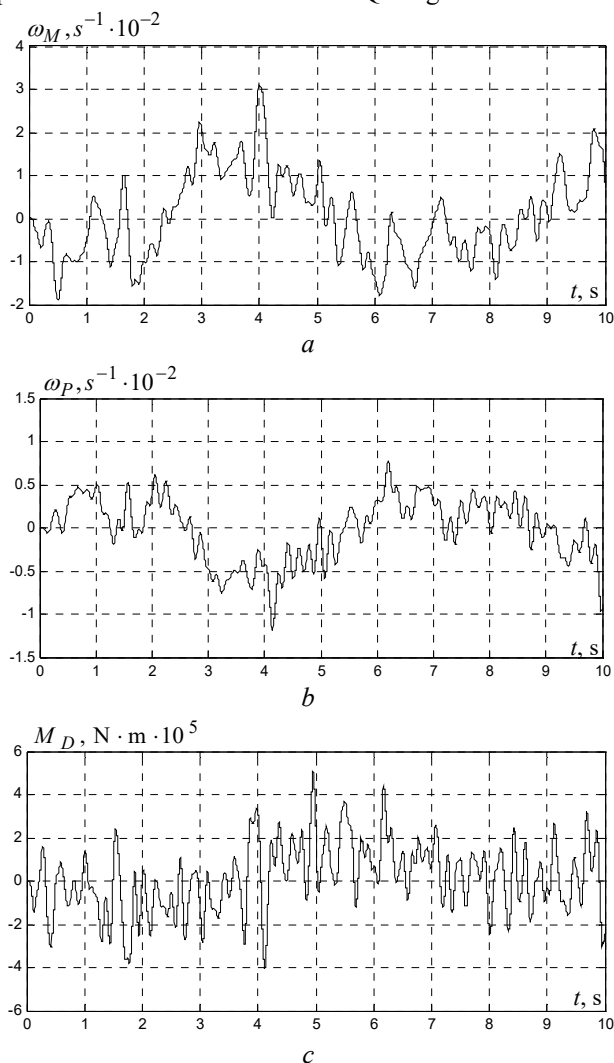


Fig. 1. The implementation of random processes of state variables of two-mass electromechanical servo systems

Note that the solutions of the original vector game (4) are the Pareto set of optimal solutions. The narrowing of this set occurs at the stage of search by taking into account constraints (5) on the state variables and control of the original system. In particular, the decrease in the time of the first coordination in the mode of working out large angular mismatches by the servo system is hindered by limitations on the armature current of the drive motor and the speed of rotation of this motor.

Further narrowing of this set at the search stage occurs on the basis of binary preference relations. In particular, in the mode of working out small mismatch angles, with a decrease in the time of the first matching, the dispersion of the tracking error increased due to the expansion of the system bandwidth at the amplification of the noise of the meters. For the tracking system under consideration, the error variance is a more preferable criterion, since it determines the potential accuracy of the tracking system. Therefore, the solution corresponding to the shorter time of the first matching in the mode of working out small angles was discarded.

Experimental research. For experimental research of the dynamic characteristics of synthesized stochastic systems the research stand of a stochastic two-mass electromechanical system was developed. The scheme of this stand of a stochastic two-mass electromechanical system is shown in Fig. 2.

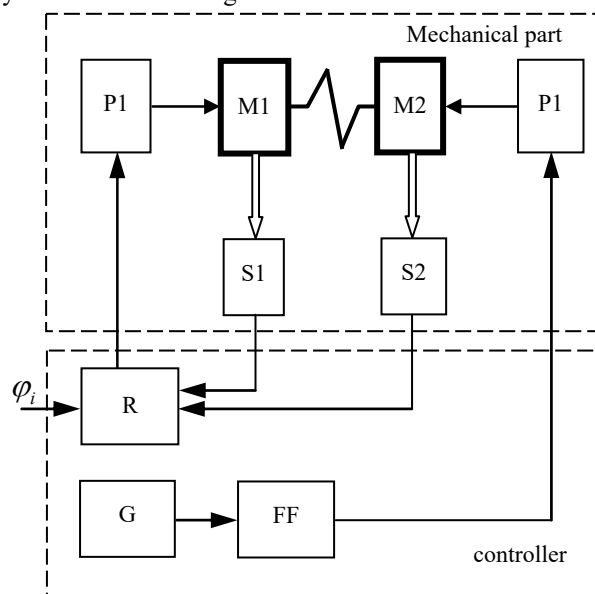


Fig. 2. The scheme of research stand of a stochastic two-mass electromechanical system

The mechanical part of the stand is made on the basis of two identical micromotors of direct current motor – DCM 25-N2.

The converter of electric motor into mechanical is the micromotor M1, and the micromotor M2 forms the amount of load for M1. The shafts of engines M1 and M2 are connected by an elastic transmission. With the help of the second motor M2 the loading moment is created.

The angle of turn of shaft of motors M1 and M2 is measured the optical sensors of angle of turn S1 and S2. The sources of power of P1 and P2 provide the power of current load of motors M1 and M2. Forming of controls influence for the sources of power is executed in the regulator of position (G). To simulate a random effect on the system at the input of the M2 is a random signal from the output of the forming filter (FF) in the form of an oscillating link. A white noise signal from a random signal generator (RSG) is fed to the input of the generating filter. Characteristics of random change of loading moment are defined by parameters of the forming filter and actually the motor M2.

Experimental studies of the dynamic characteristics of a two-mass electromechanical system with typical regulators and with synthesized anisotropic regulators were carried out at the stand.

On Fig. 3 are shown the implementation of random processes of state variables of research stand of a stochastic two-mass electromechanical system. In Fig. 3 are shown the following state variables: rotation speed $\omega_{M1}(t)$ of the motor M1 (a); rotation speed $\omega_{M2}(t)$ of the motor M2 (b), the armature current $I_{M1}(t)$ of the motor M1 (c) and the armature current $I_{M2}(t)$ of the motor M2 (d).

It is shown that the use of stochastic robust control of the stand of a two-mass electromechanical system with

a random change in the load moment allows to reduce the control error of the rotation speed of the second motor by more than 1.5 times and to reduce the error in regulating the angle of rotation of the shaft of the second motor by more than 2 times in comparison with a system with typical regulators.

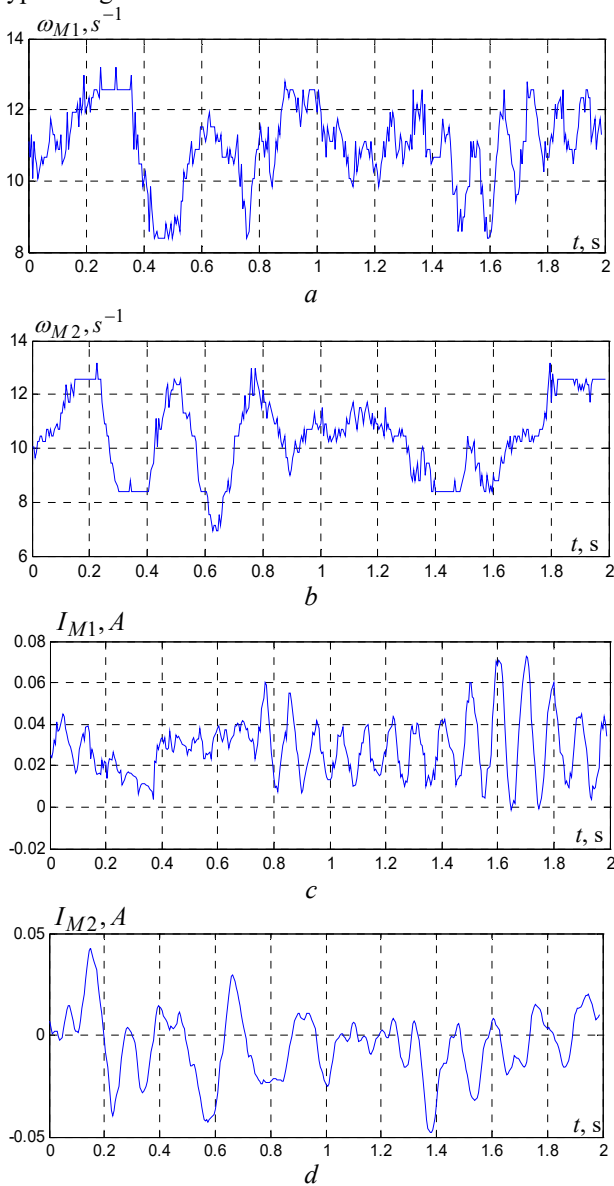


Fig. 3. The implementation of random processes of state variables of research stand of a stochastic two-mass electromechanical system

Discussion. The construction of various robust controllers under the action of external uncontrolled disturbances showed that these controllers, along with a number of undeniable advantages, also have disadvantages. The main feature of H_∞ -regulators is the fact that in the process of functioning of a robust system only a priori information about possible external disturbances is used. This leads to the fact that robust control systems are characterized by some conservatism.

This is explained by the fact that robust systems must remain operational (maintain robust stability and a given level of quality) under the maximum permissible perturbations, without «having information» about when this perturbation will occur, i.e. the regulator is «always ready» for the worst case.

This is a common characteristic feature of all minimax controllers (which include H_∞ -regulators).

When using anisotropic controllers built at an appropriate level of average anisotropy of the input signal, a significantly smaller control achieves almost the same quality of transient processes in terms of controlled variables compared to a H_∞ controller. The calculation of anisotropic robust controllers and anisotropic robust observers is similar to the calculation of deterministic robust controllers and deterministic robust observers in the four Riccati approach. The solution of the Riccati equation used as a necessary condition for the extremum of the corresponding quality criterion in the corresponding variables. When synthesizing an anisotropic robust controller and an anisotropic robust observer, a game approach is used.

The first game related to the synthesis of a robust anisotropic controller. The payoff of the first game is the anisotropic norm of the target vector. In this game, the first player is the anisotropic controller and its strategy is to minimize the anisotropic norm of the control goal vector. To calculate this controller, the fourth Riccati equation (17) is solved. The second player in this game is the vector of external structural disturbances acting on the original system, and its strategy is to maximize the same anisotropic norm of the target vector over the vector of external disturbances in accordance with the worst case. To calculate this vector of external perturbations, the first Riccati equation (14) is solved.

The second game related to the synthesis of a robust anisotropic observer. The payoff of the second game is the anisotropic norm of the error vector of restoring the state vector of the original system with the help of an observer. In this game, the anisotropic observer is the first player, and his strategy is to minimize the anisotropic norm of the error vector of restoring the state vector of the original system with the help of the observer from the gain vector of the synthesized aniso-triple observer. To calculate this observer, the third Riccati equation (16) is solved.

The second player in this game is the vector of external noise measuring the output vector of the original system and acting on the observer, and its strategy is to maximize the same anisotropic norm of the vector of the error vector of restoring the state vector of the original system with the help of the observer from the vector of external parametric disturbances in accordance with the worst case by chance. To calculate this vector of external parametric disturbances, the second Riccati equation (15) is solved. Thus, the solution of the stochastic robust optimization problem is reduced to the calculation of four algebraic Riccati equations, the Lyapunov equation, and an expression of a special form for calculating the level of anisotropy of the input signal.

Thus, with zero average anisotropy of the input signal corresponding to a signal of the white noise type, the anisotropic controller is the optimal stochastic controller that minimizes the H^2 norm. With an infinite average anisotropy of the input signal corresponding to a fully defined deterministic signal, the anisotropic controller is the optimal deterministic robust controller that minimizes the H^∞ norm. With values of the average anisotropy of the input signal in the $0 < a < \infty$ range, the anisotropic controller occupies an intermediate position between the controllers that minimize H^2 and H^∞ norms.

Conclusions.

1. For the first time the method of multi objective synthesis of stochastic robust control by multimass electromechanical systems to satisfy various requirements for the operation of such systems in various modes under non-gaussian random external disturbances is developed.

2. The problem of multi objective synthesis of stochastic robust control by multimass electromechanical systems to satisfy various requirements for the operation of such systems in various modes under non-gaussian random external disturbances is formulated by solving a zero-sum vector antagonistic game.

3. The computation of the game payoff vector, the constraint vector, and the vector of binary preference relations is algorithmic in nature and requires large computational resources. To calculate the stochastic robust control it is need to solve the algebraic Riccati equations, the Lyapunov equation, and an equation of a special form for calculating the level of anisotropy of the input signal. Then as a result of modeling a closed system, the vector of the values of the quality indicators that are imposed on the system operation, and the vector of the restrictions, when the system is operating in various operating modes and for various setting and disturbing and for various values of the vector of the initial uncertainty of the system parameters and external influences are calculated.

4. The results of multi objective synthesis of stochastic robust control by servo two-mass electromechanical systems under non-gaussian random external disturbances in which differences requirements for the operation of such systems in various modes were satisfied are given. The results of modeling and experimental studies of and realizations of state variables of of servo two-mass electromechanical system under random external influences are presented.

5. Based on the results of modeling and experimental studies of a servo two-mass electromechanical system with a random change in the load moment it is established, that with the help of synthesized robust stochastic controllers, it is possible to reduce the error of the rotation speed of the plant by more than 1.5 times and to reduce the error in regulating the angle of rotation of the shaft of the plant by more than 2 times in comparison with a system with typical regulators.

Conflict of interest. The authors declare that they have no conflicts of interest.

REFERENCES

1. Kurdyukov A.P., Maximov E.A., Tchaikovsky M.M. Anisotropy-based bounded real lemma. *Proceedings of the 19th International Symposium on Mathematical Theory of Networks and Systems (MTNS 2010)*, 5-9 July, 2010. Budapest, Hungary pp. 2391-2397. Available at: http://www.conferences.hu/mtns2010/proceedings/Papers/426_1_18.pdf (accessed 16 March 2022).
2. Tchaikovsky M. Static output feedback anisotropic controller design by LMI-based approach: General and special cases. *2012 American Control Conference (ACC)*, 2012, pp. 5208-5213. doi: <https://doi.org/10.1109/ACC.2012.6315306>.
3. Tchaikovsky M.M., Kurdyukov A.P., Timin V.N. Strict Anisotropic Norm Bounded Real Lemma in Terms of Inequalities. *IFAC Proceedings Volumes*, 2011, vol. 44, no. 1, pp. 2332-2337. doi: <https://doi.org/10.3182/20110828-6-IT-1002.01016>.
4. Tchaikovsky M.M., Kurdyukov A.P. Reduced-order stochastic robust controller design for aircraft control in landing approach. *Proceedings 18th IFAC Symposium on Automatic Control in Aerospace*, Nara, Japan, September 6-10, 2010. p. 21.
5. Scherer C.W. An efficient solution to multi-objective control problems with LMI objectives. *Systems & Control Letters*, 2000,

- vol. 40, no. 1, pp. 43-57. doi: [https://doi.org/10.1016/S0167-6911\(99\)00122-X](https://doi.org/10.1016/S0167-6911(99)00122-X).
6. Scherer C., Gahinet P., Chilali M. Multiobjective output-feedback control via LMI optimization. *IEEE Transactions on Automatic Control*, 1997, vol. 42, no. 7, pp. 896-911. doi: <https://doi.org/10.1109/9.599969>.
7. Volosyuk V., Zhyla S., Pavlikov V., Ruzhentsev N., Tserne E., Popov A., Shmatko O., Dergachov K., Havrylenko O., Ostroumov I., Kuzmenko N., Sushchenko O., Averyanova Yu., Zaliskyi M., Solomentsev O., Kuznetsov B., Nikitina T. Optimal Method for Polarization Selection of Stationary Objects Against the Background of the Earth's Surface. *International Journal of Electronics and Telecommunications*, 2022, vol. 68, no. 1, pp. 83-89. doi: <https://doi.org/10.24425/ijet.2022.139852>.
8. Shmatko O., Volosyuk V., Zhyla S., Pavlikov V., Ruzhentsev N., Tserne E., Popov A., Ostroumov I., Kuzmenko N., Dergachov K., Sushchenko O., Averyanova Y., Zaliskyi M., Solomentsev O., Havrylenko O., Kuznetsov B., Nikitina T. Synthesis of the optimal algorithm and structure of contactless optical device for estimating the parameters of statistically uneven surfaces. *Radioelectronic and Computer Systems*, 2021, no. 4, pp. 199-213. doi: <https://doi.org/10.32620/reks.2021.4.16>.
9. Ostroverkhov M., Chumack V., Monakhov E., Ponomarev A. Hybrid Excited Synchronous Generator for Microhydropower Unit. *2019 IEEE 6th International Conference on Energy Smart Systems (ESS)*, Kyiv, Ukraine, 2019, pp. 219-222. doi: <https://doi.org/10.1109/ess.2019.8764202>.
10. Ostroverkhov M., Chumack V., Monakhov E. Output Voltage Stabilization Process Simulation in Generator with Hybrid Excitation at Variable Drive Speed. *2019 IEEE 2nd Ukraine Conference on Electrical and Computer Engineering (UKRCON)*, Lviv, Ukraine, 2019, pp. 310-313. doi: <https://doi.org/10.1109/ukrcon.2019.8879781>.
11. Krot P.V., Korennoy V.V. Nonlinear Effects in Rolling Mills Dynamics. *Proceedings of the 5th International Conference on Nonlinear Dynamics ND-KhPI2016*, September 27-30, 2016, Kharkov, Ukraine. Available at: https://www.researchgate.net/publication/308901445_Nonlinear_Effects_in_Rolling_Mills_Dynamics (accessed 06 October 2021).
12. Kugi A., Schlacher K., Novak R. Nonlinear control in rolling mills: a new perspective. *IEEE Transactions on Industry Applications*, 2001, vol. 37, no. 5, pp. 1394-1402. doi: <https://doi.org/10.1109/28.952515>.
13. Martynenko G. Practical application of the analytical method of electromagnetic circuit analysis for determining magnetic forces in active magnetic bearings. *2020 IEEE Problems of Automated Electrodrive. Theory and Practice (PAEP)*, 2020, pp. 1-4, doi: <https://doi.org/10.1109/paep49887.2020.9240774>.
14. Martynenko G., Martynenko V. Modeling of the dynamics of rotors of an energy gas turbine installation using an analytical method for analyzing active magnetic bearing circuits. *2020 IEEE KhPI Week on Advanced Technology (KhPIWeek)*, 2020, pp. 92-97. doi: <https://doi.org/10.1109/KhPIWeek51551.2020.9250156>.
15. Buriakovskiy S.G., Maslii A.S., Pasko O.V., Smirnov V.V. Mathematical modelling of transients in the electric drive of the switch – the main executive element of railway automation. *Electrical Engineering & Electromechanics*, 2020, no. 4, pp. 17-23. doi: <https://doi.org/10.20998/2074-272X.2020.4.03>.
16. Tytiuk V., Chorny O., Baranovskaya M., Serhienko S., Zachepa I., Tsvirkun L., Kuznetsov V., Tryputen N. Synthesis of a fractional-order PI^mD^n -controller for a closed system of switched reluctance motor control. *Eastern-European Journal of Enterprise Technologies*, 2019, no. 2 (98), pp. 35-42. doi: <https://doi.org/10.15587/1729-4061.2019.160946>.
17. Zagimyak M., Chorny O., Zachepa I. The autonomous sources of energy supply for the liquidation of technogenic accidents. *Przegląd Elektrotechniczny*, 2019, no. 5, pp. 47-50. doi: <https://doi.org/10.15199/48.2019.05.12>.
18. Chorny O., Serhienko S. A virtual complex with the parametric adjustment to electromechanical system parameters. *Technical Electrodynamics*, 2019, pp. 38-41. doi: <https://doi.org/10.15407/techned2019.01.038>.

19. Shchur I., Kasha L., Bukavyn M. Efficiency Evaluation of Single and Modular Cascade Machines Operation in Electric Vehicle. *2020 IEEE 15th International Conference on Advanced Trends in Radioelectronics, Telecommunications and Computer Engineering (TCSET)*, Lviv-Slavske, Ukraine, 2020, pp. 156-161. doi: <https://doi.org/10.1109/tcset49122.2020.235413>.
20. Shchur I., Turkovskiy V. Comparative Study of Brushless DC Motor Drives with Different Configurations of Modular Multilevel Cascaded Converters. *2020 IEEE 15th International Conference on Advanced Trends in Radioelectronics, Telecommunications and Computer Engineering (TCSET)*, Lviv-Slavske, Ukraine, 2020, pp. 447-451. doi: <https://doi.org/10.1109/tcset49122.2020.235473>.
21. Ostroumov I., Kuzmenko N., Sushchenko O., Pavlikov V., Zhyla S., Solomentsev O., Zaliskiy M., Averyanova Y., Tserne E., Popov A., Volosyuk V., Ruzhentsev N., Dergachov K., Havrylenko O., Kuznetsov B., Nikitina T., Shmatko O. Modelling and simulation of DME navigation global service volume. *Advances in Space Research*, 2021, vol. 68, no. 8, pp. 3495-3507. doi: <https://doi.org/10.1016/j.asr.2021.06.027>.
22. Averyanova Y., Sushchenko O., Ostroumov I., Kuzmenko N., Zaliskiy M., Solomentsev O., Kuznetsov B., Nikitina T., Havrylenko O., Popov A., Volosyuk V., Shmatko O., Ruzhentsev N., Zhyla S., Pavlikov V., Dergachov K., Tserne E. UAS cyber security hazards analysis and approach to qualitative assessment. In: Shukla S., Unal A., Varghese Kureethara J., Mishra D.K., Han D.S. (eds) *Data Science and Security. Lecture Notes in Networks and Systems*, 2021, vol. 290, pp. 258-265. Springer, Singapore. doi: https://doi.org/10.1007/978-981-16-4486-3_28.
23. Zaliskiy M., Solomentsev O., Shcherbyna O., Ostroumov I., Sushchenko O., Averyanova Y., Kuzmenko N., Shmatko O., Ruzhentsev N., Popov A., Zhyla S., Volosyuk V., Havrylenko O., Pavlikov V., Dergachov K., Tserne E., Nikitina T., Kuznetsov B. Heteroskedasticity analysis during operational data processing of radio electronic systems. In: Shukla S., Unal A., Varghese Kureethara J., Mishra D.K., Han D.S. (eds) *Data Science and Security. Lecture Notes in Networks and Systems*, 2021, vol. 290, pp. 168-175. Springer, Singapore. doi: https://doi.org/10.1007/978-981-16-4486-3_18.
24. Sushchenko O.A. Robust control of angular motion of platform with payload based on H_∞ -synthesis. *Journal of Automation and Information Sciences*, 2016, vol. 48, no. 12, pp. 13-26. doi: <https://doi.org/10.1615/jautomatinfscien.v48.i12.20>.
25. Zhyla S., Volosyuk V., Pavlikov V., Ruzhentsev N., Tserne E., Popov A., Shmatko O., Havrylenko O., Kuzmenko N., Dergachov K., Averyanova Y., Sushchenko O., Zaliskiy M., Solomentsev O., Ostroumov I., Kuznetsov B., Nikitina T. Statistical synthesis of aerospace radars structure with optimal spatio-temporal signal processing, extended observation area and high spatial resolution. *Radioelectronic and Computer Systems*, 2022, no. 1, pp. 178-194. doi: <https://doi.org/10.32620/reks.2022.1.14>.
26. Gal'chenko V.Y., Vorob'ev M.A. Structural synthesis of attachable eddy-current probes with a given distribution of the probing field in the test zone. *Russian Journal of Nondestructive Testing*, Jan. 2005, vol. 41, no. 1, pp. 29-33. doi: <https://doi.org/10.1007/s11181-005-0124-7>.
27. Halchenko V.Y., Ostapushchenko D.L., Vorobyov M.A. Mathematical simulation of magnetization processes of arbitrarily shaped ferromagnetic test objects in fields of given spatial configurations. *Russian Journal of Nondestructive Testing*, Sep. 2008, vol. 44, no. 9, pp. 589-600. doi: <https://doi.org/10.1134/S1061830908090015>.
28. Ostroumov I., Kuzmenko N., Sushchenko O., Zaliskiy M., Solomentsev O., Averyanova Y., Zhyla S., Pavlikov V., Tserne E., Volosyuk V., Dergachov K., Havrylenko O., Shmatko O., Popov A., Ruzhentsev N., Kuznetsov B., Nikitina T. A probability estimation of aircraft departures and arrivals delays. In: Gervasi O. et al. (eds) *Computational Science and Its Applications – ICCSA 2021. ICCSA 2021. Lecture Notes in Computer Science*, vol. 12950, pp. 363-377. Springer, Cham. doi: https://doi.org/10.1007/978-3-030-86960-1_26.
29. Chystiakov P., Chorny O., Zhautikov B., Sivyakova G. Remote control of electromechanical systems based on computer simulators. *2017 International Conference on Modern Electrical and Energy Systems (MEES)*, Kremenchuk, Ukraine, 2017, pp. 364-367. doi: <https://doi.org/10.1109/mees.2017.8248934>.
30. Zagirnyak M., Bisikalo O., Chorna O., Chorny O. A Model of the Assessment of an Induction Motor Condition and Operation Life, Based on the Measurement of the External Magnetic Field. *2018 IEEE 3rd International Conference on Intelligent Energy and Power Systems (IEPS)*, Kharkiv, 2018, pp. 316-321. doi: <https://doi.org/10.1109/ieps.2018.8559564>.
31. Ummels M. *Stochastic Multiplayer Games Theory and Algorithms*. Amsterdam University Press, 2010. 174 p.
32. Shoham Y., Leyton-Brown K. *Multiagent Systems: Algorithmic, Game-Theoretic, and Logical Foundations*. Cambridge University Press, 2009. 504 p.
33. Xin-She Yang, Zhihua Cui, Renbin Xiao, Amir Hossein Gandomi, Mehmet Karamanoglu. *Swarm Intelligence and Bio-Inspired Computation: Theory and Applications*, Elsevier Inc., 2013. 450 p.
34. Zilzter Eckart. *Evolutionary algorithms for multiobjective optimizations: methods and applications*. PhD Thesis Swiss Federal Institute of Technology, Zurich, 1999. 114 p.
35. Xiaohui Hu, Eberhart R.C., Yuhui Shi. Particle swarm with extended memory for multiobjective optimization. *Proceedings of the 2003 IEEE Swarm Intelligence Symposium. SIS'03 (Cat. No.03EX706)*, Indianapolis, IN, USA, 2003, pp. 193-197. doi: <https://doi.org/10.1109/sis.2003.1202267>.
36. Pulido G.T., Coello C.A.C. A constraint-handling mechanism for particle swarm optimization. *Proceedings of the 2004 Congress on Evolutionary Computation (IEEE Cat. No.04TH8753)*, Portland, OR, USA, 2004, vol. 2, pp. 1396-1403. doi: <https://doi.org/10.1109/cec.2004.1331060>.
37. Michalewicz Z., Schoenauer M. Evolutionary Algorithms for Constrained Parameter Optimization Problems. *Evolutionary Computation*, 1996, vol. 4, no. 1, pp. 1-32. doi: <https://doi.org/10.1162/evco.1996.4.1.1>.
38. Parsopoulos K.E., Vrahatis M.N. Particle swarm optimization method for constrained optimization problems. *Proceedings of the Euro-International Symposium on Computational Intelligence*, 2002, pp. 174-181.

Received 28.04.2022

Accepted 13.06.2022

Published 07.09.2022

B.I. Kuznetsov¹, Doctor of Technical Science, Professor,
 T.B. Nikitina², Doctor of Technical Science, Professor,
 I.V. Bovdii¹, PhD, Senior Research Scientist,
 O.V. Voloshko¹, PhD, Junior Research Scientist,
 V.V. Kolomiets², PhD, Assistant Professor,
 B.B. Kobylanskyi², PhD, Associate Professor,
¹A. Pidhornyi Institute of Mechanical Engineering Problems of the National Academy of Sciences of Ukraine,
 2/10, Pozharskogo Str., Kharkiv, 61046, Ukraine,
 e-mail: kuznetsov.boris.i@gmail.com (Corresponding author)
²Educational scientific professional pedagogical Institute of Ukrainian Engineering Pedagogical Academy,
 9a, Nosakov Str., Bakhmut, Donetsk Region, 84511, Ukraine,
 e-mail: tatjana55555@gmail.com; nnpipiua@ukr.net

How to cite this article:

Kuznetsov B.I., Nikitina T.B., Bovdii I.V., Voloshko O.V., Kolomiets V.V., Kobylanskyi B.B. The method of multi objective synthesis of stochastic robust control by multimass electromechanical systems under non-gaussian random external disturbances. *Electrical Engineering & Electromechanics*, 2022, no. 5, pp. 21-30. doi: <https://doi.org/10.20998/2074-272X.2022.5.04>

B. Chandramouli, A. Vijayaprabhu, D. Arun Prasad, K. Kathiravan, N. Udhayaraj, M. Vijayasanthi

Design of single switch-boosted voltage current suppressor converter for uninterrupted power supply using green resources integration

Introduction. Uninterrupted power supply is the major requirement in the areas since it involves human lives. In the current scenario the demand and price of fossil fuels is increasing rapidly and availability also is not sufficient to the needs, an alternative identification to power generation is solar and wind energies. The **purpose** of designing an aimed, single switch boosted voltage and current suppressor (SS-BVCS) converter topology that interfaces both the wind and solar hybrid model. The **method** involves in the proposed chopper converter is derived by simply merging a switch and a pair of diodes and CLC filter which is used in realization of zero voltage switching for the main switch and a reversing diode to extract high voltage gain. The designed SS-BVCS converter topology can able to have a tight self-control on two power-processing paths. The **novelty** of the SS-BVCS converter module is designed to ensure maximum throughput, feeding to the load with high quality uninterrupted output, by boosting the DC voltage to a required amount and thereby suppressing the current. **Practical value** obtained by the developed model utilizes both the sources for supply to the load individually or combined based on the extraction availability of the feeder. Also, the proposed SS-BVCS module delivers with efficient lesser component count and gaining maximum power from the harvest of green energy. References 30, tables 1, figures 13.

Key words: single switch-boosted voltage current suppressor converter, green energy, switch smoothening, uninterrupted power supply.

Вступ. Джерело безперебійного живлення є основною вимогою в галузях, що пов'язані з людськими життями. У поточній ситуації, коли попит та ціна на викопне паливо швидко зростають, а їх доступність також недостатня для задоволення потреб, альтернативною технологією виробництва електроенергії є сонячна та вітрова енергія. **Метою** є розробка цільової топології перетворювача з підвищеною напругою та пригнічувачем струму з одним перемикачем (SS-BVCS), яка взаємодіє як з вітровою, так і з гібридною моделлю сонячної енергії. **Метод** включає запропонований перетворювач переривника, отриманий шляхом простого злиття перемикача, пари діодів і CLC-фільтра, який використовується для реалізації перемикання при нульовому напрузі для основного ключа і реверсивного діода для вилучення високого коефіцієнта посилення по напрузі. Розроблена топологія перетворювача SS-BVCS може забезпечити жорсткий самоконтроль на двох ланцюгах обробки енергії. **Новизна** модуля перетворювача SS-BVCS призначена для забезпечення максимальної пропускної здатності, живлення навантаження з якісним безперебійним виходом шляхом підвищення напруги постійного струму до необхідної величини і, таким чином, придушення струму. **Практична цінність**, отримана завдяки розробленій моделі, дозволяє використовувати як джерела живлення навантаження окремо, так і комбіновано залежно від можливості відбору фідера. Крім того, запропонований модуль SS-BVCS забезпечує ефективно використання меншої кількості компонентів та отримання максимальної потужності за рахунок збирання зеленої енергії. Бібл. 30, табл. 1, рис. 13.

Ключові слова: перетворювач напруги струму з одним перемикачем, зелена енергія, згладжування перемикачів, джерело безперебійного живлення.

1. Introduction. An attentiveness of green revolution over the years has been greatly increased due to the reducing availability of the ground supplies such as coal and other fossil fuels. To overcome this problem, the role of producing energy from the solar and wind power plays vital. If also the energy is harvested from the natural resources there is a need for the efficient utilization of the generated power there by integrated power converters are designed using the semiconductor switches to attain the solid conversion for the desired application with compact structure at low cost. The nature of the solar and wind plants outputs is inconsistent and it cannot be directly fed to application, hence it requires an efficient conversion topology with a battery backup is normally required.

Nowadays the large wind turbines are increased in numbers and are more efficient. A group of wind turbines collectively forms a grid. The appealing of the system turns to much higher cost. On looking to the smaller applications like road signs, small buildings, there is need for small wind turbines for the closest customers [1, 2].

The flawless working of a small wind turbine (SWT) is a major issue due to its poor throughput and high cost. As discussed in [3], the SWT throughput falls on several factors which include power converters, the integration of low-cost power converters leading to a poor efficiency of SWTs. The another important factor expands in [4], is the

power generator, comparatively to all generators, permanent magnet synchronous generators (PMSGs) have a greater efficiency due to the cu losses in the rotor are small and a larger energy density, PMSGs allows the generator to directly coupled with the wind turbine and can be used at low varying speed applications [5, 6].

The overall design topology for the proposed model is shown in the Fig. 1 where inputs from renewable energy resources are fed to the proposed converter through a filter for the ups application.

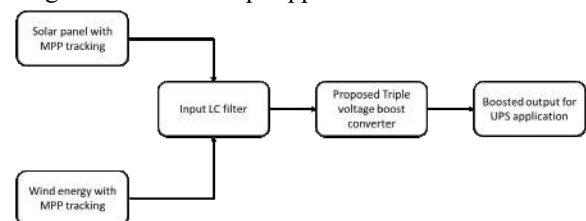


Fig. 1. Block diagram of the proposed model

Viewing solar energy as one of the vital resources in green energy, standalone photovoltaic panels are used for this energy source. To grasp a continuing energy from the source a string of PV arrays is integrated. In order to supply to the load which is generated from the photovoltaic (PV) array, their voltage level must be increased while converted in to another form. Due to the

limited power generation by the PV panels because of maximum radiation at the day time only, and energy production costs higher. Key to note the efficiency of these structures is viewed seriously [7-9].

For low level power applications, simple PV systems development and precise control approach of converter provides higher efficiency. In addition, grid is deployed for storing the excessive power generated at the peak hours by gaining maximum power using tracking approach and AC inverter module is much needed for conversion and energy storing in grid it matches the losses between the PV arrays and efficiency is improved comparatively [10-14].

Regulated voltage can be supplied to the load by integrating the inverter stage and the converter module through a transformer will adjust the galvanic isolation between the converter and inverter stage [15, 16]. To reduce the overall system size and cost factor of the proposed multiple source input DC-DC conversion module, it requires multiple inverter module for DC-AC (two-stage) inverter. To overcome this issue, the chopper topology and inverter module are merged and maximum power point tracking (MPPT) provides the increased voltage level to the single converter [17, 18].

In [19, 20], a system with more than one input module of solar and wind is discussed, the drawback of non-isolation provides increase in leakage current which causes its application limited. In [21, 22] proper choice for high power applications is a multiple input inverter using multi-string have discussed. A single-phase multi-input single output system with a new converter introduced in the [23-26] have a greater number of semiconductor switches since both the converters are magnetically coupled lead to increase in the cost and system structure size. Followed in [27] without reducing the number of semiconductor switches the transformers of N number of inverters are merged. In [28] a multiple input system is evaluated and for each input an individual chopper boost converter is proposed and output is produced by paralleled the converter circuits, which increases the number of semiconductor elements thereby increasing the cost of the system thereby two auxiliary circuits are necessary to provide soft switching.

The objective is to develop a low-cost, reliable, and efficient wind energy conversion system (WECS) and PV array power supply unit and integration of both the unit by using the proposed converter for uninterrupted power supply applications. A new boost converter module with a freewheeling diode produces the blocking of reverse current flow and to obtain the protection of the converter switch and by using high stability IGBT switching device is used in the topology. This configuration results in increased in the output voltage level and produces continuous voltage and minimum current by tracking the renewable system efficiently.

2. Methodology.

2.1. Energy Conservation Process. The WECS is made of a permanent magnet synchronous machine. The PMSG wind turbine produces torque from wind power. Then the generated torque is shifted through the generator shaft to the rotor of the generator. Then the electrical torque is produced by the generator, and the mechanical

torque from the wind turbine differences with the electrical torque from the generator determines the mechanical system gaining speed, lowering speed or no change at constant speed. The maximum power at base wind speed 12 m/s produced is shown in Fig. 2.

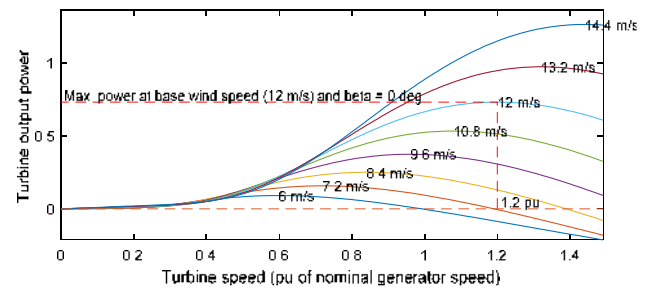


Fig. 2. Turbine power characteristics for different values of wind speed

In [29] a Darrieus vertical axis wind turbine is analyzed. The generator receives the mechanical power output from the turbine is expressed as

$$P_t = C_p(\lambda) \cdot P_w = \frac{1}{2} \cdot C_p(\lambda, \beta) \cdot \rho \cdot A \cdot V_w^3, \quad (1)$$

where P_w is the power supplied by the wind, W ; A is the area of the turbine, m^2 ; V_w is the wind speed, m/s ; ρ is the air density (around 1.2 kg/m^3 in the usual condition of temperature and humidity); C_p is the power coefficient of the turbine; λ is the turbine shaft speed, rad/s ; β is the blade pitch angle, deg .

The power coefficient C_p can be estimated by a fourth-order polynomial is expressed as

$$C_p(\lambda) = \sum_{k=0}^4 C \cdot k \cdot \lambda^k, \quad (2)$$

where k refers to the gain.

2.2. MPPT of the solar panel. The tracking method of solar is modelled as switching frequency (f_s) is modulated with a carrier of sinusoidal variation, input voltage (V_{in}) and reference voltage (V_{ref}) are detected. Then by gain parameter β is used to scale V_{in} and made it compared with V_{ref} . The AC component is obtained from V_{in} by using a peak detector obtained in V_{ref} . The low-pass filter removes the switching frequency component in V_{in} . The required value of duty cycle d is obtained by utilizing the error amplifier which controls the pulse width modulator to adjust of internal resistance R_{in} . This process will have record of the output characteristics of solar panel by not evaluating the V-I relationship [30].

Figure 3 reflects the characteristics output of current to voltage and power to voltage waveforms of the proposed solar panel.

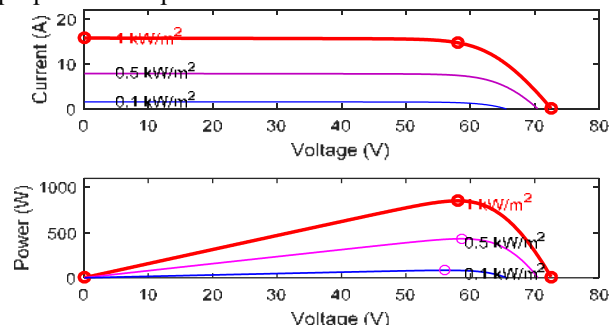


Fig. 3. I-V and P-V characteristics of 1Soltech ISTH 220-P

2.3. Proposed high step up boost converter. The proposed integrated single switch boosted voltage and current suppressor (SS-BVCS) module is made of IGBT switch, C_{in} , L1, input side filtering followed by a conversion IGBT switch along with charging capacitor C1 with reverse blocking diodes D1 and D2, the output filtering uses C2, L2, C3 components followed by a RL load to determine the output voltage. Figure 4 represents the overall block model and Table 1 represents the parameters of the proposed model.

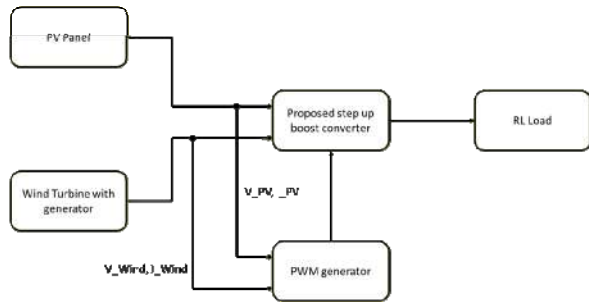


Fig. 4. Proposed model structure

Parameters of the proposed model

Table 1

Input rated voltage, V	71.97	Snubber capacitance C_{ss} , nF	250
Capacitor C_{in} , C1, C2, μ F	100	Resistance R_{on} , m Ω	1
Inductor L1, mH	3	Inductor L2, mH	3
Capacitor C1, μ F	100	RL load resistance, Ω	20
Diode 1, Diode 2 (L_{on} , H)	0	RL inductance, mH	1
Forward voltage V_f , V	0.8	Output boosted voltage, V	114.4
Snubber resistance R_{ss} , Ω	500		

2.4. Operating principles of the proposed boost converter. In the operating mode 1 (Fig. 5), when the voltage is applied it follows through the path (L1–SW1–C1–D2–(C2, L2, C3)–Load) the inductor L1 charges the current and switch on the switch SW1, the capacitor C2 charges and flows through the diode D2 and it charges the capacitor C2 which allows through the LC filter produces the boosted output across the load.

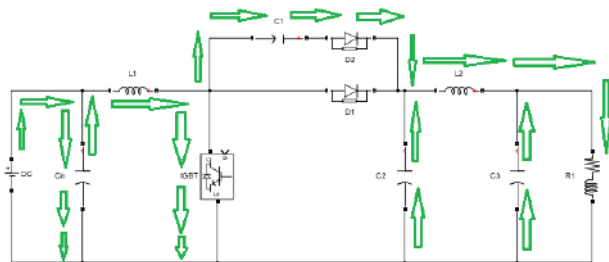


Fig. 5. Operating mode 1

In the operating mode 2 (Fig. 6), when voltage is applied it flows through the inductor (L1–(C2, D2, D1)–C2–L2–C2–Load), though in the reverse voltage it follows the path that is already charge inductor current L1 flows through the mentioned path to produce the uninterrupted power supply to the load.

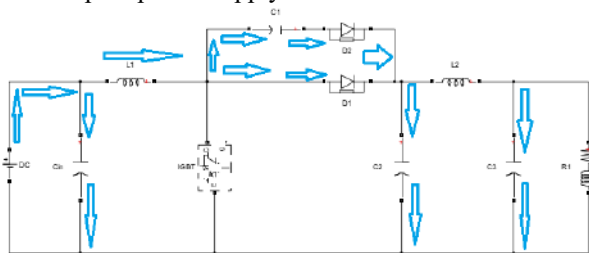


Fig. 6. Operating mode 2

The switching triggering pulse applied to the switch SW1 is tracking back from the proposed SS-BVCS converter output voltage and compared with the voltage required and along with MPPT algorithm is evaluated in order to extract the maximum possible output, since the input varies according to the irradiation of wind and solar the switching sequence to the switch also varies based on the algorithm designed. The switching PWM pulse is shown in the Fig. 7.

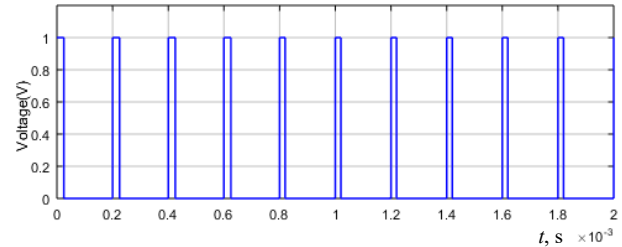


Fig. 7. PWM pulse to the switch

3. Simulation results. The proposed SS-BVCS converter with the integrated renewable sources model has simulated using MATLAB software for evaluation. The proposed simulated model is shown in the Fig. 8. The PV and PMSG are fed as an input source to the proposed SS-BVCS converter, since the output of both the sources is not constant all the time due to climatic and seasonal changes. The MPPT is implemented to track the maximum power from the input renewable resources. According to the input is sampled from both the energy sources, the frequency to the switches is tuned to gain the maximum power output from the proposed model.

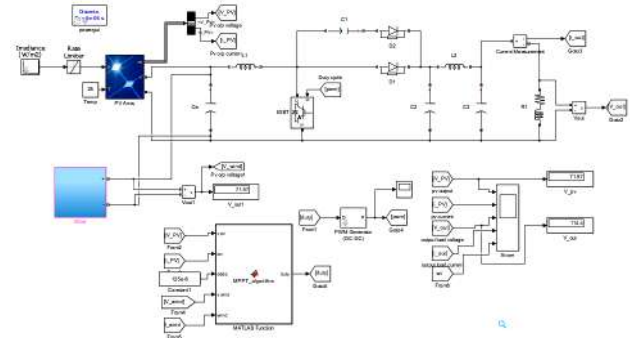


Fig. 8. Overall Simulink model for the proposed design

The proposed SS-BVCS converter has been tested with constant and also with varying wind and solar energy. The duty cycle achieved in the Fig. 8 is for the generated power from the wind speed equal to 12 m/s and PV array power of 850 W.

1Soltech 1STH-215-9 PV module is utilized as a solar energy generation system and its model parameters are next. The proposed solar of 1Soltech 1STH-215-9 module with an irradiance of [1000, 500, 100] (W/m^2), produces the maximum power of 213.15 W, 60 (N_{cell}) cells per module, produces a voltage V_{mp} at maximum power point 29 V and current I_{mp} at maximum power point of 7.35 A. The permanent magnet synchronous machine is used for wind energy generation system. Further, its electrical and mechanical specifications are as follows. The PMSG produces a mechanical output power of $1.5 \cdot 10^6$ VA with the base power of the electrical generator is $1.5 \cdot 10^6$ VA/0.9 pu, produces a base wind

speed of 12 m/s with a maximum power at base wind speed is 0.73 (pu of nominal mechanical power).

Figure 9 shows the simulated wind generator output voltage and current, and Fig. 10 represents the rotor speed of the PMSG generator. Figure 11 shows the rotor angle of the PMSG turbine generator, and Fig. 12 shows the DC output after rectification from wind turbine generator.

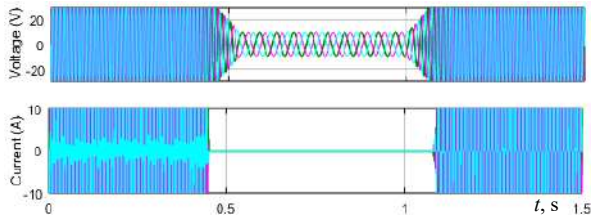


Fig. 9. Wind output voltage and current waveforms

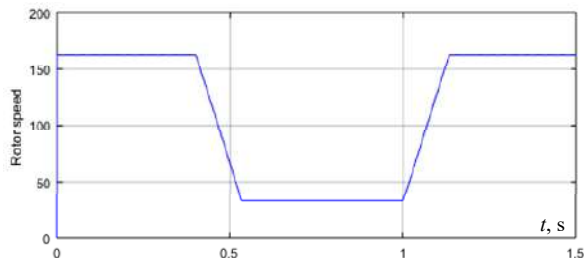


Fig. 10. Rotor speed of the wind waveform

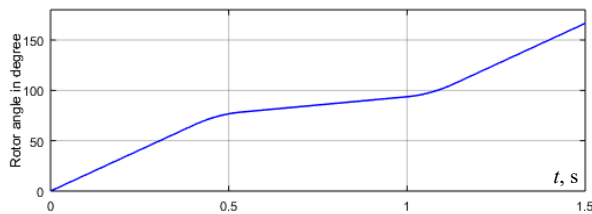


Fig. 11. Rotor angle of the wind

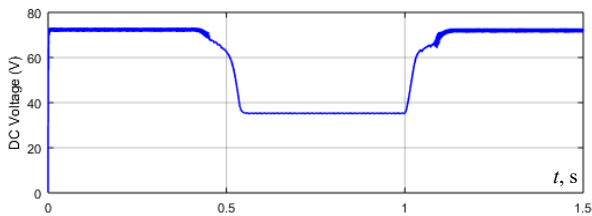


Fig. 12. DC output after rectification from wind output

Figure 13 represents the stimulated waveforms of proposed SS-BVCS converter output voltage of 114.5 V with a output current rating of 5.37 A, produced by the lower input fed by the wind and PV respectively.

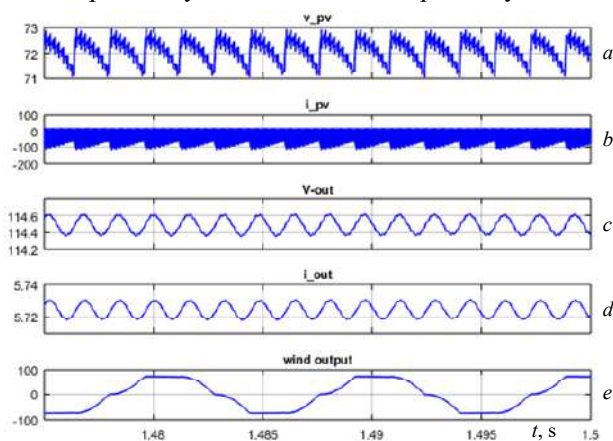


Fig. 13. a – PV input voltage; b – PV input current; c – boosted output; d – output current; e – wind output waveform

4. Conclusions.

In this work an adequate modelling of permanent magnet synchronous generators wind energy and solar power conversion process has been presented. A maximum power point tracking was designed, which permanently controls the duty cycle of the boost converter by retrieving the variable input from the renewable resources to improve the power supply to the load, by viewing the simulation results verifies that it attains zero voltage switching by makes use of the input filter and also produces the high voltage gain by suppressing the current in the output, the overall output show the output rated voltage is step up conveniently for the uninterrupted power supply by using renewable energy resources.

Conflict of interest. The authors declare that they have no conflicts of interest.

REFERENCES

1. Druga M., Nichita C., Barakat G. Performances study of direct coupled PM generator based small wind converters. *The XIX International Conference on Electrical Machines - ICEM 2010*, pp. 1-6. doi: <https://doi.org/10.1109/ICELMACH.2010.5607989>.
2. Mirecki A., Roboam X., Richardeau F. Architecture Complexity and Energy Efficiency of Small Wind Turbines. *IEEE Transactions on Industrial Electronics*, 2007, vol. 54, no. 1, pp. 660-670. doi: <https://doi.org/10.1109/TIE.2006.885456>.
3. Mahdi A.J., Tang W.H., Jiang L., Wu Q.H. A Comparative Study on Variable-Speed Operations of a Wind Generation System using Vector Control. *Renewable Energy and Power Quality Journal*, 2010, vol. 1, no. 08, pp. 605-610. doi: <https://doi.org/10.24084/repqj08.418>.
4. Esmaili R., Xu L. Sensorless Control of Permanent Magnet Generator in Wind Turbine Application. *Conference Record of the 2006 IEEE Industry Applications Conference Forty-First IAS Annual Meeting*, 2006, vol. 4, pp. 2070-2075. doi: <https://doi.org/10.1109/IAS.2006.256820>.
5. Vijayaprabhu A., Kumaresan M. PMSG Wind Turbine Based Current Fed Three Phase Inverter with Model Predictive Control. *International Journal of Electrical and Electronics Research*, 2022, vol. 10, no. 2, pp. 282-289. doi: <https://doi.org/10.37391/ijeer.100238>.
6. Vijayaprabhu A., Bhaskar K.B., Jasmine susila D., Dinesh M. Review and Comparison of Various Types of Generation Using WECS Topologies. *IOP Conference Series: Materials Science and Engineering*, 2021, vol. 1177, no. 1, pp. 012004. doi: <https://doi.org/10.1088/1757-899X/1177/1/012004>.
7. Blaabjerg F., Ma K., Yang Y. Power electronics for renewable energy systems – Status and trends. *CIPS 2014 – 8th International Conference on Integrated Power Electronics Systems, Proceedings*. 2014, pp. 1-11.
8. Meinhardt M., Crame G. Multi-string-converter: the next step in evolution of string-converter technology. *Proceedings of Evolution of the European Power Electronics Conference*, 2001.
9. Kabalci E. Review on novel single-phase grid-connected solar inverters: Circuits and control methods. *Solar Energy*, 2020, vol. 198, pp. 247-274. doi: <https://doi.org/10.1016/j.solener.2020.01.063>.
10. Kjaer S.B., Pedersen J.K., Blaabjerg F. A Review of Single-Phase Grid-Connected Inverters for Photovoltaic Modules. *IEEE Transactions on Industry Applications*, 2005, vol. 41, no. 5, pp. 1292-1306. doi: <https://doi.org/10.1109/TIA.2005.853371>.
11. Sathyan S., Suryawanshi H.M., Ballal M.S., Shitole A.B. Soft-Switching DC–DC Converter for Distributed Energy Sources With High Step-Up Voltage Capability. *IEEE Transactions on Industrial Electronics*, 2015, vol. 62, no. 11, pp. 7039-7050. doi: <https://doi.org/10.1109/TIE.2015.2448515>.
12. Alluhaybi K., Batarseh I., Hu H. Comprehensive Review and Comparison of Single-Phase Grid-Tied Photovoltaic

- Microinverters. *IEEE Journal of Emerging and Selected Topics in Power Electronics*, 2020, vol. 8, no. 2, pp. 1310-1329. doi: <https://doi.org/10.1109/JESTPE.2019.2900413>.
13. Shen Y., Wang H., Shen Z., Yang Y., Blaabjerg F. A 1-MHz Series Resonant DC-DC Converter With a Dual-Mode Rectifier for PV Microinverters. *IEEE Transactions on Power Electronics*, 2019, vol. 34, no. 7, pp. 6544-6564. doi: <https://doi.org/10.1109/TPEL.2018.2876346>.
14. Moradi-Shahrbabak Z., Tabesh A., Yousefi G.R. Economical Design of Utility-Scale Photovoltaic Power Plants With Optimum Availability. *IEEE Transactions on Industrial Electronics*, 2014, vol. 61, no. 7, pp. 3399-3406. doi: <https://doi.org/10.1109/TIE.2013.2278525>.
15. Mohammadi M., Safari N., Milimonfared J., Moghani J.S. Application of a new high step-up double-input converter in a novel module-integrated-inverter photovoltaic system. *The 6th Power Electronics, Drive Systems & Technologies Conference (PEDSTC2015)*, 2015, pp. 53-58. doi: <https://doi.org/10.1109/PEDSTC.2015.7093249>.
16. Yaow-Ming Chen, Yuan-Chuan Liu, Feng-Yu Wu. Multi-input DC/DC converter based on the multiwinding transformer for renewable energy applications. *IEEE Transactions on Industry Applications*, 2002, vol. 38, no. 4, pp. 1096-1104. doi: <https://doi.org/10.1109/TIA.2002.800776>.
17. Okedu K.E., Al Tobi M., Al Araimi S. Comparative Study of the Effects of Machine Parameters on DFIG and PMSG Variable Speed Wind Turbines During Grid Fault. *Frontiers in Energy Research*, 2021, vol. 9, art. no. 681443. doi: <https://doi.org/10.3389/fenrg.2021.681443>.
18. Chen Y.-M., Liu Y.-C., Hung S.-C., Cheng C.-S. Multi-Input Inverter for Grid-Connected Hybrid PV/Wind Power System. *IEEE Transactions on Power Electronics*, 2007, vol. 22, no. 3, pp. 1070-1077. doi: <https://doi.org/10.1109/TPEL.2007.897117>.
19. Jiang W., Fahimi B. Multi-port Power Electric Interface for Renewable Energy Sources. *2009 Twenty-Fourth Annual IEEE Applied Power Electronics Conference and Exposition*, 2009, pp. 347-352. doi: <https://doi.org/10.1109/APEC.2009.4802680>.
20. Alejandro A.T., Cardenas V., Pacas M. Single-phase MISO HF-link isolated grid-connected inverter for renewable energy sources applications. *PCIM Europe 2015: International Exhibition and Conference for Power Electronics, Intelligent Motion, Renewable Energy and Energy Management; Proceedings of.*, art. no. 7149035.
21. Keyhani H., Toliyat H.A. Single-Stage Multistring PV Inverter With an Isolated High-Frequency Link and Soft-Switching Operation. *IEEE Transactions on Power Electronics*, 2014, vol. 29, no. 8, pp. 3919-3929. doi: <https://doi.org/10.1109/TPEL.2013.2288361>.
22. Cheng G.S.X., Mulkey S.L. *Power Inverters With Multiple Input Channels*. Patent No. US 9,257,916 B2. Feb. 9, 2016. Available at: <https://patentimages.storage.googleapis.com/bf/04/df/6c982d9ac71bc/d/US9257916.pdf> (accessed 16 May 2021).
23. Cheng G.S.X., Mulkey S.L. *Scalable and Redundant Mini-Inverters*. Patent No. US 9,093,902 B2. Jul. 28, 2015. Available at: <https://patentimages.storage.googleapis.com/cd/92/93/13d1916ecd7252/US9093902.pdf> (accessed 16 May 2021).
24. Brahmi J., Krichen L., Ouali A. A comparative study between three sensorless control strategies for PMSG in wind energy conversion system. *Applied Energy*, 2009, vol. 86, no. 9, pp. 1565-1573. doi: <https://doi.org/10.1016/j.apenergy.2008.11.010>.
25. Rolan A., Luna A., Vazquez G., Aguilar D., Azevedo G. Modeling of a variable speed wind turbine with a Permanent Magnet Synchronous Generator. *2009 IEEE International Symposium on Industrial Electronics*, 2009, pp. 734-739. doi: <https://doi.org/10.1109/ISIE.2009.5218120>.
26. Meneses D., Garcia O., Alou P., Oliver J.A., Cobos J.A. Grid-Connected Forward Microinverter With Primary-Parallel Secondary-Series Transformer. *IEEE Transactions on Power Electronics*, 2015, vol. 30, no. 9, pp. 4819-4830. doi: <https://doi.org/10.1109/TPEL.2014.2365760>.
27. Lodh T., Pragallapati N., Agarwal V. Novel Control Scheme for an Interleaved Flyback Converter Based Solar PV Microinverter to Achieve High Efficiency. *IEEE Transactions on Industry Applications*, 2018, vol. 54, no. 4, pp. 3473-3482. doi: <https://doi.org/10.1109/TIA.2018.2818655>.
28. De Moraes J.C. dos S., De Moraes J.L. dos S., Gules R. Photovoltaic AC Module Based on a Cuk Converter With a Switched-Inductor Structure. *IEEE Transactions on Industrial Electronics*, 2019, vol. 66, no. 5, pp. 3881-3890. doi: <https://doi.org/10.1109/TIE.2018.2856202>.
29. Zhang F., Xie Y., Hu Y., Chen G., Wang X. A Hybrid Boost-Flyback/Flyback Microinverter for Photovoltaic Applications. *IEEE Transactions on Industrial Electronics*, 2020, vol. 67, no. 1, pp. 308-318. doi: <https://doi.org/10.1109/TIE.2019.2897543>.
30. Zhu B., Zeng Q., Chen Y., Zhao Y., Liu S. A Dual-Input High Step-Up DC/DC Converter With ZVT Auxiliary Circuit. *IEEE Transactions on Energy Conversion*, 2019, vol. 34, no. 1, pp. 161-169. doi: <https://doi.org/10.1109/TEC.2018.2876303>.

Received 23.03.2022

Accepted 30.06.2022

Published 07.09.2022

Chandramouli Bethi¹, Professor,
 Vijayaprabhu Arumugam², Assistant Professor,
 Arun Prasad Deenadayalan³, Assistant Professor,
 Kathiravan Kannan⁴, Assistant Professor,
 Udhayaraj Natarajan⁵, Assistant Professor,
 Vijayasanthi Maineni⁶, Associate Professor,

¹ Department of Electrical and Electronics Engineering,
 Chaitanya (Deemed to be University),
 Hanamkonda, Telangana, 506001, India,
 e-mail: chandu.bethi@gmail.com

² Department of Electronics and Communication Engineering,
 Sri Venkateswara College of Engineering and Technology,
 Thirupachur, 631203, India,
 e-mail: vijayaprabhu85@gmail.com (Corresponding Author)

³ Department of Electrical and Electronics Engineering,
 PSNA College of Engineering and Technology,
 Dindigul, Tamil Nadu, 624622, India,
 e-mail: sdarunprasad@gmail.com

⁴ Department of Electrical and Electronics Engineering,
 Theni Kammavar Sangam College of Technology,
 Veerapandi, Theni, Tamil Nadu, 625534, India,
 e-mail: rndkathiravan@gmail.com

⁵ Department of Electrical and Electronics Engineering,
 Vel Tech Rangarajan Dr. Sagunthala R&D Institute of Science
 and Technology,
 Chennai, Tamil Nadu, 600028, India,
 e-mail: udhaya63@gmail.com

⁶ Department of Electrical and Electronics Engineering,
 CMR College of Engineering & Technology,
 Hyderabad, Telangana, 501401, India,
 e-mail: mvijayasanthi@cmrct.ac.in

How to cite this article:

Chandramouli B., Vijayaprabhu A., Arun Prasad D., Kathiravan K., Udhayaraj N., Vijayasanthi M. Design of single switch-boosted voltage current suppressor converter for uninterrupted power supply using green resources integration. *Electrical Engineering & Electromechanics*, 2022, no. 5, pp. 31-35. doi: <https://doi.org/10.20998/2074-272X.2022.5.05>

G. Janardhan, N.N.V. Surendra Babu, G.N. Srinivas

Single phase transformerless inverter for grid connected photovoltaic system with reduced leakage current

Introduction. Transformerless inverters are of vital importance in the field of grid connected solar photovoltaic systems offering higher efficiency than the conventional one. i.e., using transformer. General grid connected inverters are constituting of transformers requires more area besides the loss in them. **Problem.** Eliminating transformers can cause leakage current due to the variation of common mode voltage which in turn due to parasitic capacitance effect. Research literature in transformerless inverters has addressed the problems of common mode leakage current issues by offering the study of different inverter topologies like H4, H5, H6 and HERIC etc. utilizing variety of modulation strategies like unipolar, bipolar pulse width modulations. **Goal.** The paper significantly presents a new transformerless inverter topology, analyzes common mode voltage and leakage current behavior of the system. The simulation is carried out for comparing the leakage current profiles with other transformerless inverter topologies in literature. **Novelty.** This paper gives an impression of the efficient transformerless inverter for grid connected photovoltaic system. **Results.** The various inverter topologies full bridge with different pulse width modulation techniques are analyzed and to determine the common mode voltages and leakage currents. References 13, tables 2, figures 17.

Key words: transformerless inverter, leakage current, photovoltaic system.

Вступ. Безтрансформаторні інвертори мають життєво важливе значення в області сонячних фотоелектричних систем, підключених до мережі, та забезпечують більш високу ефективність, ніж звичайні, завдяки трансформатору. Підключені до загальної мережі інвертори, які складаються з трансформаторів, потребують більшої площі через втрати у них. **Проблема.** Усунення трансформаторів може спричинити струм витоку через зміну синфазної напруги через вплив паразитної ємності. Дослідницька література з безтрансформаторних інверторів присвячена проблемам синфазних струмів витоку, пропонуючи дослідження різних топологій інверторів, таких як H4, H5, H6, HERIC та ін., з використанням різних стратегій модуляції, таких як уніполярна, біполярна широтно-імпульсна. **Мета.** У статті докладно подано нову топологію безтрансформаторного інвертора, проаналізовано поведінку синфазної напруги та струму витоку в системі. Моделювання проводиться для порівняння профілів струму витоку з іншими топологіями безтрансформаторних інверторів, описаних у літературі. **Новизна.** Ця стаття містить ефективний безтрансформаторний інвертор для фотоелектричної системи, підключеної до мережі. **Результати.** Проаналізовано різні топології інверторів з повним мостом та різними методами широтно-імпульсної модуляції, а також визначено синфазну напругу та струми витоку. Бібл. 13, табл. 2, рис. 17.

Ключові слова: безтрансформаторний інвертор, струм витоку, фотогальванічна система.

Introduction. Fossil fuels are getting depleted over past few years. Renewable energy sources are facing a huge demand despite the rise in energy requirements of the world. Photovoltaic (PV) generation is the highest among all the renewable energy sources due to its simplicity and little or no maintenance. PV systems are of two types of standalone, and grid connected. Grid connected PV system has been widely in commercial use due to its modularity in scaling and ease in its energy conversion process. As per a study by council on energy, environment and water, India set a goal of raising 450 GW to reach by the year 2030 [1]. Conventional grid connected inverters will use a transformer which will provide galvanic isolation. It can be a low or power frequency transformer on ac side of the inverter i.e., grid side, or a high frequency transformer is used on DC side of the inverter. Transformer will increase the size of the inverter and will cause loss in transformer by which efficiency of the inverter would be reduced. By eliminating the transformer galvanic isolation will not be available.

It causes leakage currents from PV panel to ground due to the parasitic capacitance effect between PV panel and ground. The range of parasitic capacitance will be 7 nF/kW to 220 nF/kW. As shown in Table 1 the leakage currents are indicated against the time within which circuit must be isolated. However, protection equipment will be engaged to protect the circuit from leakage currents [2].

It is expected to break the circuit within 0.3 s if the leakage current exceeds 300 mA and a sudden change in the current must be within the range of prescribed limits and it also advisable to monitor grid frequency for the reliable and stable grid. The reduction in leakage currents

Table 1
Leakage currents against the time

Leakage current	Time
$i > 300 \text{ mA}$	300 ms
$\Delta i > 30 \text{ mA}$	300 ms
$\Delta i > 60 \text{ mA}$	150 ms
$\Delta i > 150 \text{ mA}$	40 ms

can be achieved either by incorporating the hardware changes i.e., different inverter topologies or software manipulations i.e., different pulse width modulation (PWM) techniques. Basic half bridge inverter produces a constant common mode voltage resulting zero leakage current. But the output voltage 50 % of the output voltage given by full bridge inverter for the same input voltage [3].

The full bridge inverter with bipolar switching technique will give constant common mode voltage results zero leakage current. Unipolar PWM with full bridge inverter will cause leakage currents though it has higher conversion efficiency. Based on isolating DC side to ac side, different inverter configurations are broadly classified into two types. First that uses switches to isolate on DC side and the second using switches on AC side [4]. The variation in capacitor voltage will cause larger change in leakage currents. Figure 1 indicates an inverter connected to PV on DC side and is connected to grid on ac side. Figure 2 shows some of transformerless inverter topologies.

Common mode voltage Avoiding transformer in grid connected PV systems will result in common mode leakage currents which are caused because of variable common

mode voltage that is given by (1) i.e. average of the voltages of mid points of respective legs of an inverter with respect to negative of DC bus point as shown in Fig. 3:

$$V_{Common\ mode} = (V_{AN} + V_{BN})/2, \quad (1)$$

where V_{AN} is the voltage at midpoint of the first leg of the single-phase inverter with respect to neutral point; V_{BN} is the voltage at midpoint of second leg of the single-phase inverter with respect to neutral point.

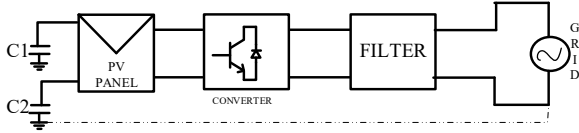


Fig. 1. Schematic of transformerless inverter

Main aim is to reduce the ripples in common mode voltage and achieve constant voltage such that leakage current limited to very small value

$$V_{Common\ mode} = (V_{AN} + V_{BN} + V_{CN})/3, \quad (2)$$

where V_{AN} , V_{BN} and V_{CN} are the inverter leg midpoint voltages with respect to negative of DC bus.

Equation (2) shows common mode voltage of a three phase inverter circuit.

Transformerless inverter topologies The widely used common mode topologies are H4, H5, H6, HERIC (Highly Efficient and Reliable Inverter Concept) as shown in Fig. 2. H5 inverter topology is adding a switch on DC side to a basic full bridge inverter, H6 topology is formed by incorporating two switches on DC side of full bridge [5]. H5 inverter shown in Fig. 2,a configuration is formed by adding one extra switch on DC side of the full bridge inverter with one capacitor on DC side. The use of this type of transformerless inverter circuit is limited due to the variable common mode voltage resulting considerable magnitude of leakage current, besides it gives good performance under resistive loads. Figure 2,b indicates HERIC is framed by explicitly adding extra leg of switches on ac side of the inverter. It will isolate the PV from grid on ac side unlike H5 inverter which disconnects the circuit on PV side [6] H6 inverter circuit is two DC link capacitors.

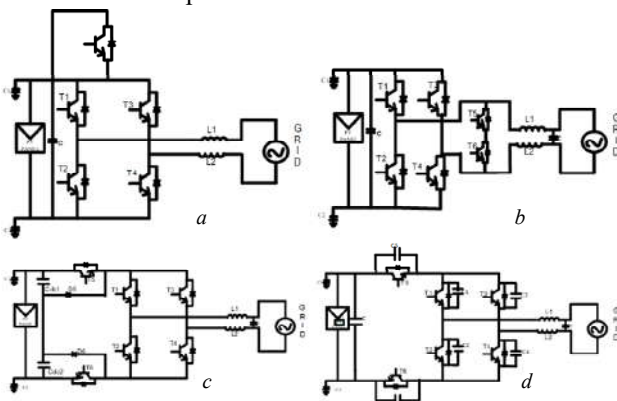


Fig. 2. a – H5 inverter topology; b – HERIC inverter topology; c – H6 inverter topology; d – improved H6 inverter topology

The power dissipation in this type of inverter is smaller compared to H5 circuit [7]. In H6 inverter circuit switching scheme will be unique to the switches position and it is not complementary to the other switches. Because of the usage of diodes reverse operation of the diodes will cause reverse recovery time delay. Common mode can be made invariable with the help of the

capacitances across each device as shown in Fig. 2,d. As the circuit contains capacitors and inductors resonance in the circuit will occur for common mode voltage. Though capacitances at the junction would cause oscillations and the effect of stray capacitances on the board may also have an influence [8-13]. The mentioned circuit topologies in Fig. 2 indicate transformerless inverter topologies for handling common mode voltage, leakage current of the system and isolating DC (i.e. PV) from grid.

Proposed T2D4 inverter topology The proposed T2D4 inverter topology shown in Fig. 3 uses 4 diodes in upper half of the circuit and 2 IGBTs in lower half of the circuit. The respective diodes acts in forward mode and will act as freewheeling diodes during which IGBT switches are in on and off position respectively. The switches are operated at high frequency and their operation is complementary. The operating principle mentioned in terms of phases in the next section of the paper.

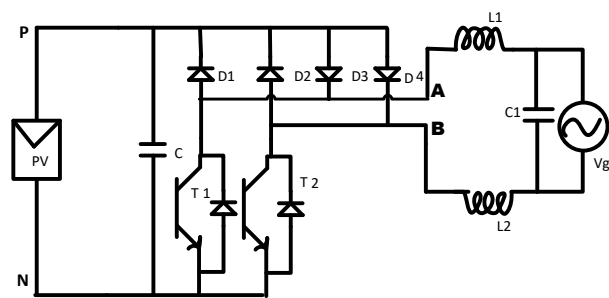


Fig. 3. T2D4 inverter topology

Operating phases of the circuit.

Phase 1. During positive half cycle the switch T2 is turned on and the current flows in the direction P–D3–L1–Grid–L2–T2–N yielding a voltage $V_{AN} = V_{PV}$ and common mode voltage is $0.5V_{PV}$.

Phase 2. T2 is switched off during freewheeling action and the current closes its path via diodes D2, instead of T2 and the current paths will be as follows D2–D3–L1–Grid–L2–D2 so that $V_{AN} = V_{BN} = V_{PV}$, $V_{AB} = 0$ and $V_{CM} = 0.5V_{PV}$.

Phase 3. In this phase of negative half of grid current flows via P–D4–L2–Grid–L1–T1–N. Switch T1 is switched on during this phase, so $V_{AN} = 0$, $V_{BN} = V_{PV}$, $V_{AB} = V_{PV}$ and $V_{CM} = 0.5V_{PV}$.

Phase 4. In this phase D1, D4 will be in forward biased and form freewheeling path so that current through the grid held constant isolating PV from the inverter via the path D1–D4–L2–Grid–L1–D1, so $V_{AN} = V_{BN} = V_{PV}$, $V_{AB} = 0$ and $V_{CM} = 0.5V_{PV}$.

In T2D4 inverter topology the 2 switches T1, T2 are switched alternately at grid frequency and the diodes are conducted during freewheeling period. However, diodes D3 and D4 will be conducted during the turn on period of T1, T2 respectively [9, 10]

Control scheme. Figure 4 shows control flow of grid connected transformerless inverter which is fed with PV at the input side. The gate pulses to the inverter are fed from PWM pulses that are generated from $\alpha\beta$ to dq transformation. The d axis current is controlled by the reference input as shown in Fig. 4.

Perturb and observe MPPT is being used to track the peak power point in PV.

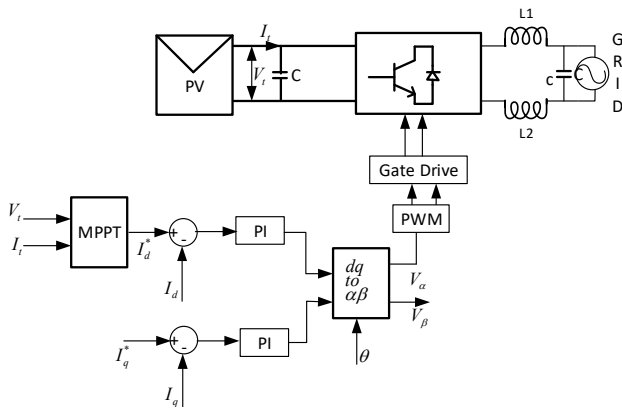


Fig. 4. Control structure for single phase transformerless inverter

Bipolar PWM technique is used to design a controller that controls the output voltage of the inverter following reference value set. A phase locked loop (PLL) gives the phase angle after it receives grid voltage as the input. PLL used to synchronize the output voltage of the inverter with grid voltage (Fig. 5).

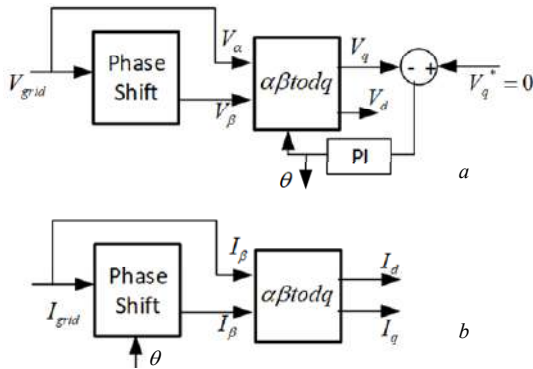


Fig. 5. a – PLL for measuring phase angle; b – generation of I_d and I_q

Simulation results. MATLAB simulation is carried for analysing various inverter configurations and observe common mode voltage and leakage currents. The parameters to perform the simulation are shown in Table 2.

Table 2

Simulation parameters			
Parameter	Values	Parameter	Values
DC bus voltage	400 V	Filter inductor	3.6 mH
Grid voltage	230 V	Rated power	3.6 kW
DC bus capacitor	1000 μ F	Filter capacitor	3.1 μ F

Bipolar PWM is the common method sinusoidal PWM in which a sinusoidal of supply frequency is compared with a high frequency carrier signal so that the resulting modulating signals are fed as gating signals to IGBTs of a H bridge inverter. It gives 2 levels of output voltage of the inverter $+V_{dc}$ and $-V_{dc}$. Bipolar PWM technique results in greater total harmonic distortion when compared to its counterpart i.e. unipolar PWM.

Unipolar PWM technique is pursued by considering two sinusoidal signals which are phase shifted by 180° are compared with a high frequency triangular waveform to obtain the gating signals to IGBTs of the inverter.

Figure 6 indicates bipolar PWM and Fig. 7 – unipolar PWM. Common mode voltage and leakage current using bipolar PWM is shown in Fig. 8, Fig. 9. Common mode voltage is constant when used bipolar PWM whereas it is varying when used unipolar PWM as shown in Fig. 10, Fig. 11.

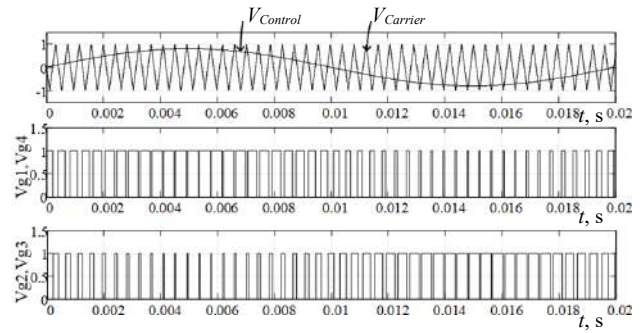


Fig. 6. Bipolar PWM

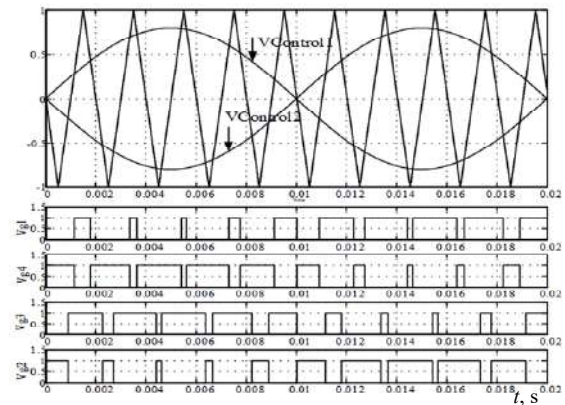


Fig. 7. Unipolar PWM

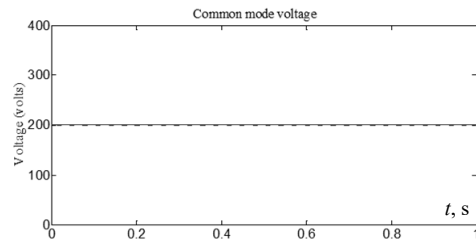


Fig. 8. Common mode voltage using bipolar PWM

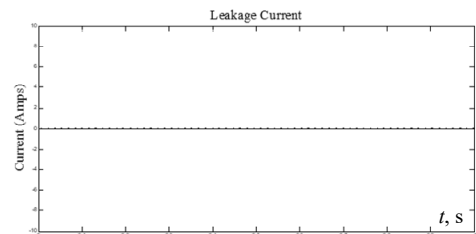


Fig. 9. Leakage current using bipolar PWM

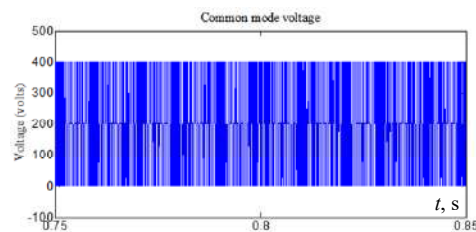


Fig. 10. Common mode voltage using unipolar PWM

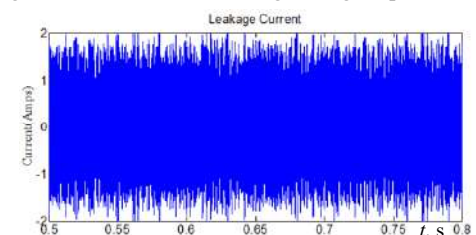


Fig. 11. Leakage current using unipolar of H bridge inverter

Common mode voltage and leakage currents of H5 inverter is shown in Fig. 12 and Fig. 13, indicating the leakage current is getting varied in terms of hundreds of milliamp.

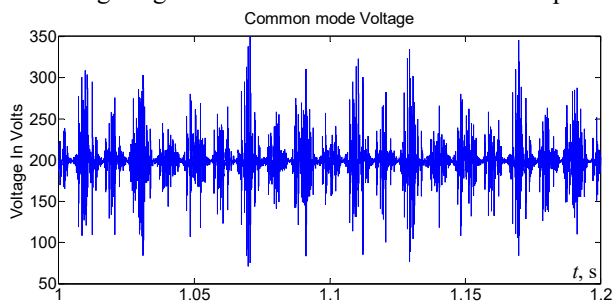


Fig. 12. Common mode voltage of H5 inverter

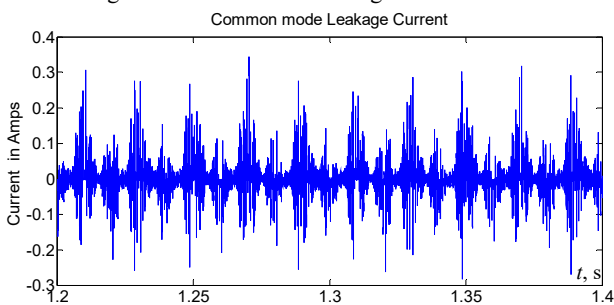


Fig. 13. Common mode leakage current of H5 inverter

The common mode voltage and leakage current of H6 inverter are shown in Fig. 14 and Fig. 15. It is observed that the variation in common mode voltage is small in H6 inverter when compared to H5 and H4 bridge inverter unipolar PWM.

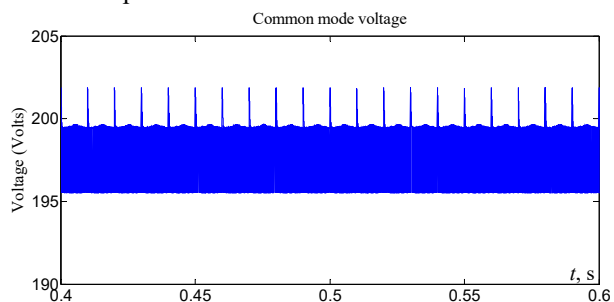


Fig. 14. Common mode voltage of H6 inverter

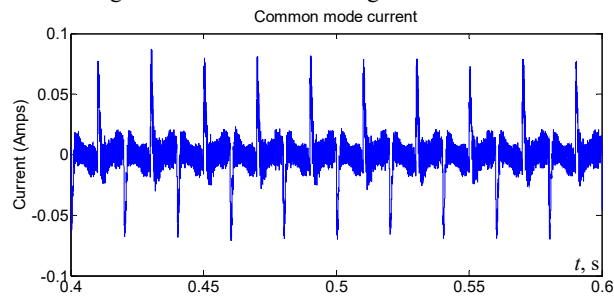


Fig. 15. Leakage current of H6 inverter

The main focus is on T2D4 inverter topology whose inverter common mode voltage and the leakage current profiles are compared with other Transformerless inverters. From Fig. 16 and Fig. 17, it is observed that T2D4 transformerless inverter topology found to give constant common mode voltage in zero or in the order of micro amps of leakage current so that H2D4 inverter found to be one of the efficient transformerless inverter. This indicates that the leakage current profile of T2D4 inverter offers superior leakage current profile.

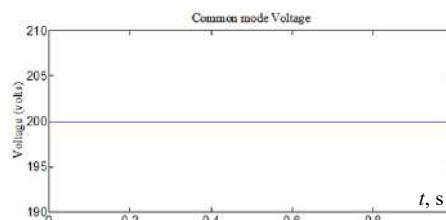


Fig. 16. Common mode voltage for T2D4 inverter

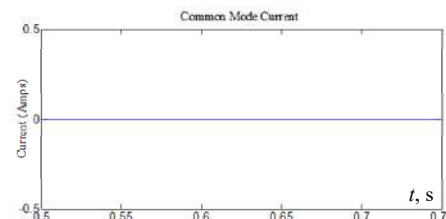


Fig. 17. Leakage current of T2D4 inverter

Conclusions.

The common mode voltage profile is the measure of efficiency of the inverter topology which describes the performance of the system. The various inverter topologies full bridge, H5, H6 and H2D4 with different pulse width modulation techniques are analyzed and to determine the common mode voltages and leakage currents.

The performance of the H2D4 inverter in terms of leakage current is found to be superior with constant common mode voltage of 200 V and leakage current in the order of nano Amps when compared to other inverter configurations. In addition to the inverter topologies discussed in the paper, there are various other configurations are also present in the literature for which evaluation is not pursued in this paper.

Conflict of interest. The authors declare that they have no conflicts of interest.

REFERENCES

1. Salmi T., Bouzguenda M., Gastli A., Masmoudi A. Review of Common-Mode Voltage in Transformerless Inverter Topologies for PV Systems. In: M'Sirdi N., Namaane A., Howlett R.J., Jain L.C. (eds) *Sustainability in Energy and Buildings. Smart Innovation, Systems and Technologies*, 2012, vol 12. Springer, Berlin, Heidelberg. doi: https://doi.org/10.1007/978-3-642-27509-8_49.
2. Albalawi H., Zaid S. An H5 Transformerless Inverter for Grid Connected PV Systems with Improved Utilization Factor and a Simple Maximum Power Point Algorithm. *Energies*, 2018, vol. 11, no. 11, art. no. 2912. doi: <https://doi.org/10.3390/en11112912>.
3. Janardhan G., Srinivas G.N., Surendra Babu N.N.V. Realization of Constant Common Mode Voltage in Transformerless Photo Voltaic Inverter Topologies. *2018 International Conference on Circuits and Systems in Digital Enterprise Technology (ICCSDET)*, 2018, pp. 1-5. doi: <https://doi.org/10.1109/ICCSDET.2018.8821224>.
4. Nagarjuna Reddy J., Jyothi K. Analysis and Modeling of Transformerless Photovoltaic Inverter Systems. *International Journal of Modern Engineering Research*, 2013, vol. 3, no. 5, pp. 2932-2938. Available at: http://www.ijmer.com/papers/Vol3_Issue5/CB3529322938.pdf (accessed 16 May 2021).
5. Figueredo R.S., de Carvalho K.C.M., Ama N.R.N., Matakas L. Leakage current minimization techniques for single-phase transformerless grid-connected PV inverters – An overview. *2013 Brazilian Power Electronics Conference*, 2013, pp. 517-524. doi: <https://doi.org/10.1109/COBEP.2013.6785164>.
6. Hassaine L., Bengourina M.R. Design and digital implementation of power control strategy for grid connected

photovoltaic inverter. *International Journal of Power Electronics and Drive Systems*, 2019, vol. 10, no. 3, pp. 1564-1574. doi: <https://doi.org/10.11591/ijpeds.v10.i3.pp1564-1574>.

7. Wu T.-F., Nien H.-S., Shen C.-L., Chen T.-M. A Single-Phase Inverter System for PV Power Injection and Active Power Filtering With Nonlinear Inductor Consideration. *IEEE Transactions on Industry Applications*, 2005, vol. 41, no. 4, pp. 1075-1083. doi: <https://doi.org/10.1109/TIA.2005.851035>.

8. Binh T.C., Tuan-Dat M., Dung N.M., An P.Q., Truc P.D., Phuc N.H. Active and Reactive Power Controller for Single-Phase Grid-Connected Photovoltaic Systems. *The 1st Regional Workshop in New/Renewable Energy of AUN/SEED-Net*, 2009. Available at: http://www4.hcmut.edu.vn/~tcbinh/Papers/HCMUT_VN_paper_Single-Phase%20Grid-Connected%20PV%20Systems_Feb21_2009_V2.pdf (accessed 16 May 2021).

9. Khan M.N.H., Forouzesh M., Siwakoti Y.P., Li L., Kerekes T., Blaabjerg F. Transformerless Inverter Topologies for Single-Phase Photovoltaic Systems: A Comparative Review. *IEEE Journal of Emerging and Selected Topics in Power Electronics*, 2020, vol. 8, no. 1, pp. 805-835. doi: <https://doi.org/10.1109/JESTPE.2019.2908672>.

10. Panda S.R., Babu B.C. Phase estimation for grid synchronization using CORDIC algorithm with SRF-PLL. *2012 IEEE Students' Conference on Electrical, Electronics and Computer Science*, 2012, pp. 1-4, doi: <https://doi.org/10.1109/SCEECS.2012.6184724>.

11. Syed Sha Mohammed. Transformerless H6 Grid Tied Inverter For Photovoltaic Generation. *International Journal Of Modern Engineering Research*, 2014, vol. 4, no. 12, pp. 16-24. Available at: https://www.ijmer.com/papers/Vol4_Issue12/Version-2/C04012_02-1624.pdf (accessed 16 May 2021).

How to cite this article:

Janardhan G., Surendra Babu N.N.V., Srinivas G.N. Single phase transformerless inverter for grid connected photovoltaic system with reduced leakage current. *Electrical Engineering & Electromechanics*, 2022, no. 5, pp. 36-40. doi: <https://doi.org/10.20998/2074-272X.2022.5.06>

12. Golestan S., Monfared M., Freijedo F.D., Guerrero J.M. Design and Tuning of a Modified Power-Based PLL for Single-Phase Grid-Connected Power Conditioning Systems. *IEEE Transactions on Power Electronics*, 2012, vol. 27, no. 8, pp. 3639-3650. doi: <https://doi.org/10.1109/TPEL.2012.2183894>.

13. Yang B., Li W., Gu Y., Cui W., He X. Improved Transformerless Inverter With Common-Mode Leakage Current Elimination for a Photovoltaic Grid-Connected Power System. *IEEE Transactions on Power Electronics*, 2012, vol. 27, no. 2, pp. 752-762. doi: <https://doi.org/10.1109/TPEL.2011.2160359>.

Received 06.03.2022

Accepted 14.06.2022

Published 07.09.2022

Gurram Janardhan¹, ME, Assistant Professor,

N.N.V. Surendra Babu², PhD, Professor,

G.N. Srinivas³, PhD, Professor,

¹ Department of Electrical and Electronics Engineering,

CVR College of Engineering,

Vasthunagar, Mangalpalli, Hyderabad-500070, India,

e-mail: Janumtech009@gmail.com (Corresponding Author)

² Kombolcha Institute of Technology (KIOT), Wollo University,

p.o. box, 208, Kombolcha, Ethiopia,

e-mail: surendrababu@ieee.org

³ University College of Engineering Hyderabad,

Jawaharlal Nehru Technological University,

Kukatpally, Hyderabad-500 085, Telangana, India,

e-mail: gnsngns.srinivas785@gmail.com

S. Latreche, A. Khenfer, M. Khemliche

Sensors placement for the faults detection and isolation based on bridge linked configuration of photovoltaic array

Introduction. The photovoltaic market has been increased over the last decade at a remarkable pace even during difficult economic times. Photovoltaic energy production becomes widely used because of its advantages as a renewable and clean energy source. It is eco-friendly, inexhaustible, easy to install, and the manufacturing time is relatively short. Photovoltaic modules have a theoretical lifespan of approximately 20 years. In real-life and for several reasons, some photovoltaic modules start to fail after being used for a period of 8 to 10 years. Therefore, to ensure safe and reliable operation of photovoltaic power plants in a timely manner, a monitoring system must be established in order to detect, isolate and resolve faults. The **novelty** of the proposed work consists in the development of a new model of sensors placement for faults detection in a photovoltaic system. The fault can be detected accurately after the analysis of changes in measured quantities. **Purpose.** Analysis of the possibility of the number and the position of the sensors into the strings in function of different faults. **Methods.** This new method is adapted to the bridge linked configuration. It can detect and locate failure points quickly and accurately by comparing the measured values. **Results.** The feasibility of the chosen model is proven by the simulation results under MATLAB/Simulink environment for several types of faults such as short-circuit current, open circuit voltage in the photovoltaic modules, partially and completely shaded cell and module. References 21, tables 6, figures 7.

Key words: sensors placement, fault detection and isolation, healthy and faulty operating, photovoltaic field.

Вступ. Ринок фотоелектричної енергії зріс за останнє десятиліття неймовірними темпами навіть у складні економічні часи. Виробництво фотоелектричної енергії стає широко використовуваним через його переваги як відновлюваного та чистого джерела енергії. Він екологічно чистий, невичерпний, простий в установці, а час виготовлення відносно короткий. Фотоелектричні модулі мають теоретичний термін служби приблизно 20 років. У реальному житті з кількох причин деякі фотоелектричні модулі починають виходити з ладу після використання протягом 8-10 років. Тому для своєчасного забезпечення безпечної та надійної роботи фотоелектричних електростанцій необхідно створити систему моніторингу для виявлення, локалізації та усунення несправностей. **Новизна** запропонованої роботи полягає в розробці нової моделі розміщення датчиків для виявлення несправностей у фотоелектричній системі. Несправність можна точно виявити після аналізу змін вимірюваних величин. **Мета.** Аналіз можливості кількості та розташування датчиків у рядках залежно від різних несправностей. **Методи.** Цей новий метод адаптовано до конфігурації, пов'язаної з мостом. Він може швидко й точно виявляти та локалізувати точки збою, порівнюючи виміряні значення. **Результати.** Здійсненість обраної моделі підтверджується результатами моделювання в середовищі MATLAB/Simulink для кількох типів несправностей, таких як струм короткого замикання, напруга холостого ходу в фотоелектричних модулях, частково та повністю затемнена комірка та модуль. Бібл. 21, табл. 6, рис. 7.

Ключові слова: розміщення датчиків, виявлення та усунення несправностей, справна та несправна робота, фотоелектричне поле.

Introduction. Photovoltaic (PV) market has been increased over the last years at a remarkable rate despite the economic difficulties. Worldwide photovoltaic energy production has surpassed 100 GW during the last decade reaching 138.9 GW in 2013 [1]. PV energy production becomes widely used because of its advantages as a renewable and clean energy source. It is eco-friendly, inexhaustible, easy to install, and the manufacturing time is relatively short. PV modules have a theoretical lifespan of approximately 20 years. In real-life and for several reasons, some PV modules start to fail after being used for a period of 8 to 10 years [2, 3]. Therefore, to ensure safe and reliable operation of PV power plants in a timely manner, a monitoring system must be established in order to detect, isolate and resolve faults.

The goal of the paper is the use of the bridge linked configuration to improve the performance of the photovoltaic field. The current of each string is measured continuously, however the voltage of each two successive modules and the overall voltage are measured only when the current of a string is reduced compared to the other strings. The photovoltaic generator operates at the maximum power point with the maximum power point tracking (MPPT) function regardless of the environmental effects.

Subject of investigations. This paper carries out a comprehensive study of the selection and the analysis of different topologies of sensors placement in the photovoltaic field. The conversion of solar radiation into

DC occurs thanks to PV cell which represents the main component of PV array. One diode PV cell model shown in Fig. 1 is widely used regarding to its simplicity.

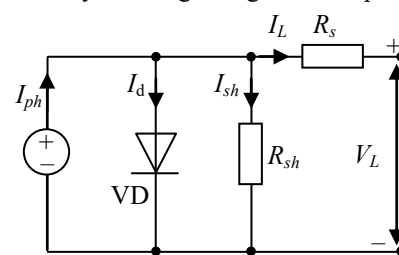


Fig. 1. One diode model of PV cell

Several electric models have been proposed to represent this model. PV cell is characterized by its characteristic current-voltage (I/V) which represent all its electrical configuration [4]. PV cell curve illustrated in Fig. 2 is defined by 3 essential variables: open circuit voltage (V_{oc}), short circuit current (I_{sc}) and maximum power point (MPP). Maximum power is obtained with an optimal voltage (V_{ppm}) and optimal current (I_{ppm}) [5, 6]. Operating the PV generator at its MPP is the role of MPP tracker.

The voltage generated by a PV cell is approximately 0.6 V. They should therefore be associated in series in modules [7, 8] (Fig. 3). The experimental results obtained from the 3 kinds of coupling series-parallel connection (SP), total cross tied connection (TCT), bridge linked

(BL) connection presented in [3], show that the TCT and BL wiring schemes have lower mismatch losses comparing to the SP structure leading to increase the power supplied by the PV field.

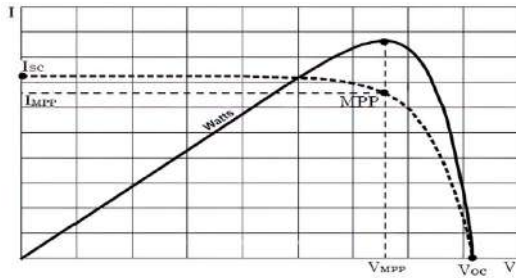


Fig. 2. Current-voltage (I/V) characteristic

In our case we are interested only in the BL configuration shown in Fig. 3f. This topology reduces the number of connections between the modules by about half compared to the TCT topology, which significantly reduces the amount deducted and the length of the wiring of the PV array.

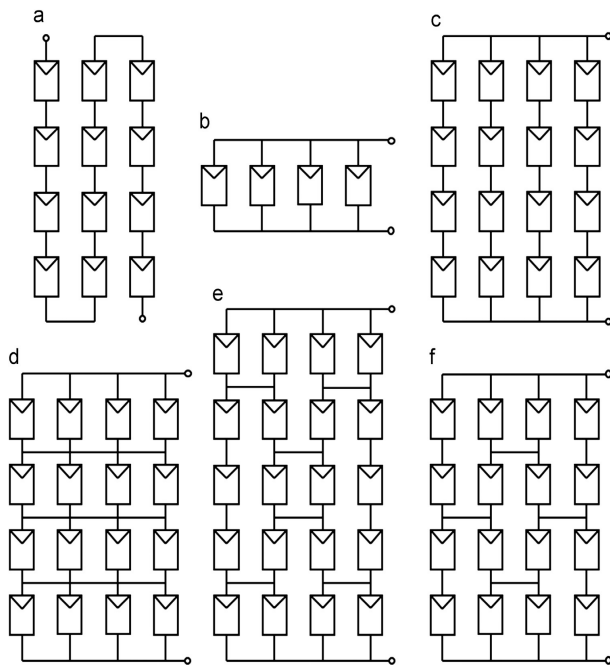


Fig. 3. Main interconnection models of PV modules: (a) serial connection, (b) parallel connection, (c) series-parallel connection (SP), (d) total cross tied connection (TCT), (e) honey-comb connection (HC), (f) bridge linked connection (BL)

Faults detection and isolation. The process of voltage and current sensors placement is illustrated in Fig. 4. One voltage sensor is placed for two successive PV modules linked by node and one current sensor is placed at the end of each string. For each field (M, N), N current sensors and $[(N-1) \cdot (N+1)/2]$ voltage sensors are needed. If $[(N-1) \cdot (N+1)]$ is odd we use the integer number for voltage sensors which use (m, n) label as follows.

This new model allows detection and isolation of the faults by comparing the following measured quantities:

- the current of each string ($I_1 \dots I_M$);
- the overall output voltage U ;
- the voltage of 2 successive modules connected by a node U_{mn} .

By this way, the string fault can be detected by current analysis of all strings and accurately locate the fault according to U_{mn} . In the healthy operating state, the currents of each string in the same PV modules number are identical and the voltages of each two successive modules linked by node are identical.

Different topologies of connecting PV modules. Like it is shown in Fig. 3, several PV module's interconnection topologies are proposed in the literature [9, 10].

Different types of faults. The main type faults and their causes are detailed in Table 1 [2].

Table 1

Categories of faults		
Types of faults	Causes	
Module damage (aging)	Increase of the series resistor R_s .	
	Decrease in shunt resistor R_{sh} . Deterioration of the antireflection layer of the cell.	
Short circuit	Cell	This failure easily occurs in thin film cells because the top and bottom electrodes are much closer together.
	Module	Resulting faults in the manufacturing process.
Open circuit	Cell	Fragmentation of cells
	Module	Loose wires
Hot point	Partial and total shading	

Method for voltage and current measurement.

The collection of measured values using current and voltage sensors at different points of the PV field allows to detect precisely the fault and to isolate it through comparison of these measures with nominal data. A brief summary of literature works in this context is presented in Table 2. According to authors in Table 2, voltage and current measurement methods focus on two axes:

- methods designed for TCT coupling;
- the proposed methods for SP coupling.

The following methods can be cited as follow.

Methods of voltage measurement. This method is described by authors in Table 2.

Table 2

Methods of voltage measurement proposed in the literature

Methods of voltage and current measurement		
Types of coupling	Reference	Analysis
Total cross tied (TCT) connection	[11, 12]	This model is used for coupling. In each string is placed one voltage sensor for measurement with parallel connection. Each string is subdivided into group which use current sensor.
Series-parallel (SP) connection	[13, 14]	This sensor placement model is used for PV field connected series-parallel. Each bloc can present one group of PV modules with current sensor. The faults position can be located by analyzing the current and voltage variation of each branch.

Method of an infrared imaging. The faults in PV array can be precisely located using a thermal camera [15].

Method of operating point analyzing. This method is based on analysis and comparison of the current with the expected MPP [16].

Other methods. In [17], authors used artificial neural networks analysis and in [18] and [19], fuzzy control theory is used for diagnosis.

New voltage and current measurement method.

This new method is adapted to the BL configuration. Fault points can be detected and isolated quickly and accurately by comparing the measured values. Considering that a PV array consists of N strings containing M modules per string, we can determine $[(M-1) \cdot (N-1)/2]$ connections (if $(M-1) \cdot (N-1)$ is an odd integer is used $[(M-1) \cdot (N-1)/2]$). The connection is labeled (m, n) if it is located below and to the right of the (m, n) module [18, 20, 21].

Sensor's placement technique. In this case, a voltage sensor is placed for two successive modules connected by a node, and a current sensor is placed at the end of each string as illustrated in Fig. 4. Then a field for (M, N) needs N current sensors and $[(M-1) \cdot (N+1)/2]$ voltage sensors (if $(M-1) \cdot (N+1)$ is an odd integer is used $[(M-1) \cdot (N+1)/2]$). Each voltage sensor takes the label (m, n) with:

$$\left. \begin{array}{l} N : \text{pair} \\ \text{where:} \end{array} \right\} \begin{array}{l} m = 1 \dots M - 1. \\ n = (2k) - (1 - m \bmod 2). \\ k = 1 \dots N/2 (m : \text{pair}). \\ k = 1 \dots (N/2) + 1 (m : \text{impair}). \end{array} \quad (1)$$

$$\left. \begin{array}{l} N : \text{impair} \\ \text{where:} \end{array} \right\} \begin{array}{l} m = 1 \dots M - 1. \\ n = (2k) - (1 - m \bmod 2). \\ k = 1 \dots (N + 1)/2. \end{array} \quad (2)$$

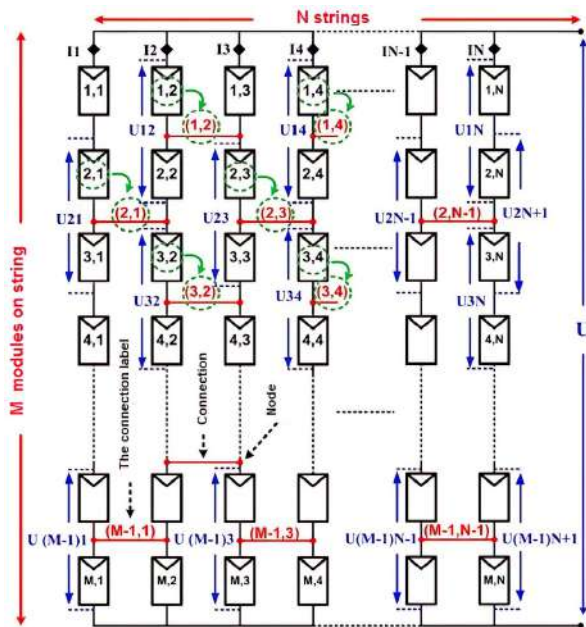


Fig. 4. New sensor placement scheme in PV array

Faults diagnosis principle. This new fault diagnosis model is used to isolate the detected fault point by comparing the following measured quantities:

The current of each string ($I_1 \dots I_M$), the overall output voltage U and the voltage of two successive modules connected by a node U_{mn} . The thong fault can be detected by current analysis of all the strings and precise location of the fault can be localized according U_{mn} .

In healthy operating state, the current of each string to identical number of PV modules is the same. Thus, the fault in a string is confirmed if the current is dropped compared to another healthy string.

A criterion I_S (standard current) is specified to distinguish between real faults and small perturbations.

For example, in a $(3, 3)$ PV array as it is shown in Fig. 5, this criterion is given by:

$$I_S = 90\% I_{\max}, \text{ where } I_{\max} = \max \{I_1, I_2, \dots, I_M\}.$$

If the first string is supposed to be faulty, then $I_1 < I_S$, and the standard current $I_S = 90\% I_{\max}$, where $I_{\max} = \max (I_2, I_3)$.

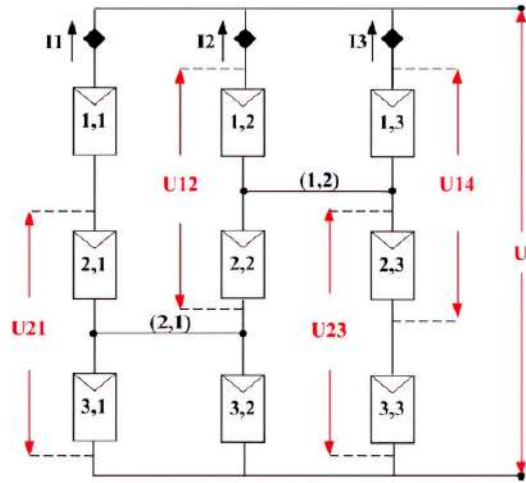


Fig. 5. $(3, 3)$ PV array

- U_{12} and U_{21} are the voltage values of the first faulty string.
- U_{12} and U_{23} are the voltage values of the second faulty string.
- U_{14} and U_{23} are the voltage values of the third faulty string.
- $U_S = 2/3 U$ is the standard voltage.

The result between U_{12} , U_{21} and U_S allows locating the faults in the faulty string.

Three cases are possible:

- if $U_{12} < U_S, U_{21} > U_S$ and $I_1 < I_S$ then module(1,1) is faulty,
- if $U_{12} < U_S, U_{21} < U_S$ and $I_1 < I_S$ then module(2,1) is faulty;
- if $U_{12} > U_S, U_{21} < U_S$ and $I_1 < I_S$ then module(3,1) is faulty.

According to this criterion, a fault in the string is determined if the current is less than the standard current I_S when the faulty state is not confirmed.

The voltage U_{mn} of two successive modules connected by one node is identical to the healthy operating state and vice versa.

After determining the k^{th} faulty string, the fault point location in this string is located in function of its voltage.

The values of i and j are given by the following relationship:

$$\left\{ \begin{array}{l} i = 1 \dots M - 1. \\ j = k + i \bmod 2 (k : \text{impair}) \\ j = k + 1 - i \bmod 2 (k : \text{pair}). \end{array} \right. \quad (4)$$

The criterion for a fault point location is $U_S = 2U/M$, where U is the output voltage of the PV field; M is the number of modules per string. When U_{ij} exceeds U_S , it means that there is no fault in these 2 modules. Finally, the fault point will be located after the comparison between each voltage of U_{ij} and U_S .

Faults detection and isolation algorithm. The algorithm of the faults detection and isolation (FDI) is illustrated in Fig. 6.

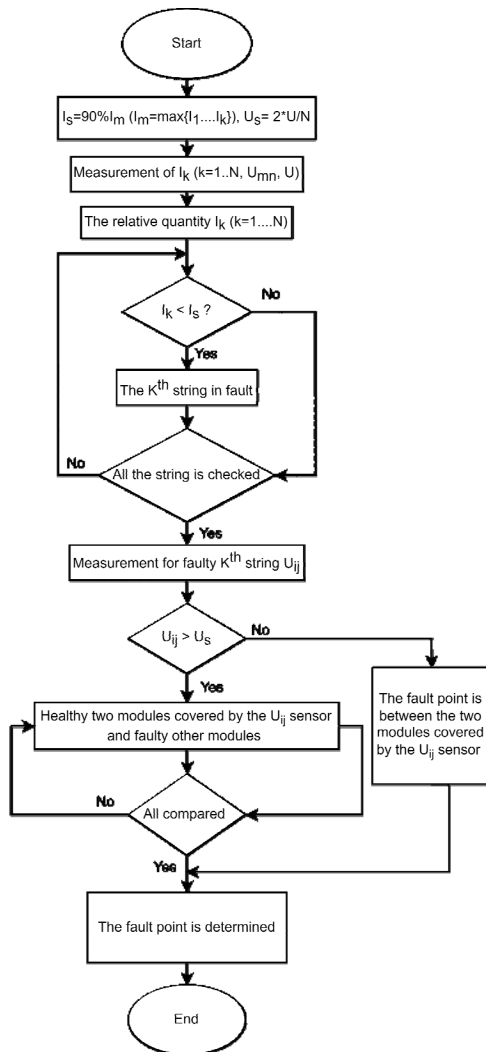


Fig. 6. FDI algorithm

Simulation results. The feasibility of the sensor placement model proposed in this work is proven by simulation results under MATLAB/Simulink environment for several types of defects.

The PV module used in this simulation is «Solarex MSX-60» with 36 cells in series. The electrical characteristics are represented in Table 3.

The criterion of the selection of the standard current is specified in order to distinguish between the real fault and the perturbations.

If the current decreases less than 10 % of the nominal current then no fault was detected because this situation cannot be dysfunction the model.

This criterion explains how the 90 % threshold was chosen to distinguish a defective string from the string with a maximum current.

The simulated model contains 9 (3, 3) modules (Fig. 7). 5 voltage sensors and 3 current sensors have to be placed.

The simulation is carried out under standard conditions (solar irradiance is 1000W/m², atmospheric mass is 1.5 and cell temperature is 25°C.

The BL configuration illustrated by Fig. 7 in the paper with sensors placement is realized under MATLAB/Simulink and after simulation of this model we obtained the results of 3 scenario of Table 4 and 5. This model can be realized in real time with more material tool which is not available at our laboratory.

The simulation parameters of the module are chosen as follows: serial resistor $R_S = 0.23 \Omega$, parallel resistor $R_{SH} = 6720.65 \Omega$, photo-current $I_{ph} = 3.81 \text{ A}$ and ideality factor $n = 1.29$. In the simulation the module faults (disconnected, short-circuited) and shadow faults (hot point phenomenon) are considered.

Three different scenarios can be proposed: the module is disconnected (scenario 1); short-circuited cell, several short-circuited cells, short-circuited module (scenario 2) and different levels of shading (scenario 3).

Table 3

Methods of voltage measurement proposed in literature

Faulty strings	String 1			String 2			String 3		
Standard current I_S	90% max(I_2, I_3)			90% max(I_1, I_3)			90% max(I_1, I_2)		
Faulty string current	$I_1 < I_S$			$I_2 < I_S$			$I_3 < I_S$		
Faulty module	(1, 1)	(2, 1)	(3, 1)	(1, 2)	(2, 2)	(3, 2)	(1, 3)	(2, 3)	(3, 3)
Standard voltage U_S	$(2/3)U$			$(2/3)U$			$(2/3)U$		
Voltage of two successive modules with faulty string	$U_{12} < U_S$	$U_{12} < U_S$	$U_{12} > U_S$	$U_{13} < U_S$	$U_{13} < U_S$	$U_{13} > U_S$	$U_{14} < U_S$	$U_{14} < U_S$	$U_{14} > U_S$
	$U_{21} > U_S$	$U_{21} < U_S$	$U_{21} < U_S$	$U_{23} > U_S$	$U_{23} < U_S$	$U_{23} < U_S$	$U_{24} > U_S$	$U_{24} < U_S$	$U_{24} < U_S$

First scenario. In this scenario, we disconnect a string of modules. All other elements of the field are in normal conditions. From the results of Table 4, the open-circuit fault is confirmed due to the zero value of the first-string current of PV array.

The faulty module number is limited between (1, 1) and (2, 1) as $U_{12} < 2/3U$, but the (2, 1) module is confirmed flawless because U_{21} value is greater than $2/3U$, this analysis can confirm that there is an open-circuit fault at the module level (1, 1).

Second scenario. In this scenario, three faulty states are treated: a shorted cell, a group of short-circuited cells (18 cells) and a short-circuited module (36 cells at a time).

According to the results in Table 4, the output current and voltage decreased due to the short circuit fault. It is found that the faultier cells increase over the current and voltage also decreases.

However, the operating state is almost the same as the healthy state when the fault occurred at a single cell, because of this small decrease cannot confirm whether a default has occurred or not at installation.

The standard current I_S is equal to 90 % I_{max} with $I_{max} = \max \{I_1, I_2, I_3\}$. According to this criterion, the fault is confirmed in the system when a group of 18 cells (82.7 % $I_1 = I_2$) or when a module is completely shorted ($I_1 I_2 = 80 \%$). In both cases the current string in fault I_1 is less than I_S . On to less than $2/3U$, U_{12} and U_{21} voltages are higher than $2/3U$, so the fault is located at the module level (1, 1).

Third scenario. In this scenario, different shading rates are applied on a cell module covering the cell partially and completely. Shading of the PV cell greatly affects the power output of the plant.

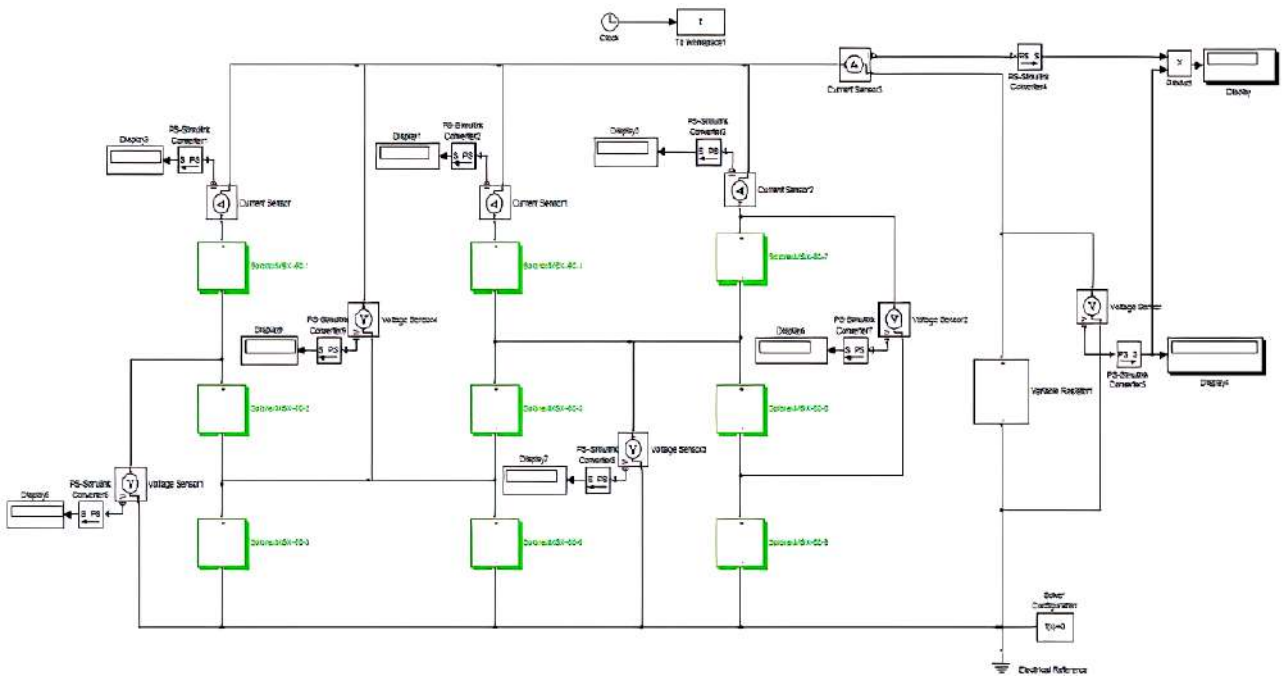


Fig. 7. The simulated model under Matlab/Simulink environment

Scenarios 1 and 2

	Normal state	Scenario 2			
		Open circuit	1 cell	18 cells	36 Cells
I_1	3.54	0	3.52	3.12	3.04
I_2	3.54	3.57	3.56	3.77	3.80
I_3	3.54	3.57	3.56	3.77	3.80
U_{12}	34.03	32.25	33.81	27.41	18.43
U_{21}	34.03	40.91	34.17	35.65	35.95
U_{14}	34.03	34.49	33.88	29.64	23.69
U_{23}	34.03	35.17	33.91	30.30	24.51
$2/3U$	34.03	34	33.88	29.86	23.96

Table 4

Table 5

Scenario 3

	Normal state	Scenario 3			
		1 cell shaded at 10 %	1 cell shaded at 30 %	1 cell shaded at 50%	1 cell shaded at 100 %
I_1	3.54				
I_2	3.54				
I_3	3.54				
U_{12}	34.03	34.59			
U_{21}	34.03	34.38	34.2	34.29	33.83
U_{14}	34.03	34.47	35.06	34.63	36.25
U_{23}	34.03	34.41	34.42	34.6	34.28
$2/3U$	34.03	34.17	34.84	35.28	35.6

According to the results of Table 5, the power is reduced to 29 % of the real value when PV cell is completely shaded.

When the shaded area of the cell is less than or equal to 50 % of the total area, the fault cannot be confirmed because of the value of the current I_1 fault string exceeds I_S ($I_1 > I_2$ 90 %).

In the case when a cell in a PV module is completely shaded, 83 % $I_1 = I_2$, then the fault is confirmed. Because of the value of U_{12} is greater than $2/3U$ and U_{21} is less than $2/3U$, I_S is produced at the module level (3, 1).

The comparison between SP and BL configurations can be summarized in Table 6.

Results of SP and BL configurations

Table 6

	Normal state		Open circuit	
	SP	BL	SP	BL
I_1, A	6.79	3.54	0	0
I_2, A	6.79	3.54	6.87	3.57
I_3, A	6.79	3.54	6.87	3.57
U_{12}, V	54.99	34.03	42.95	32.25
U_{21}, V	54.99	34.03	65.80	40.91

The voltage in the faulty string of BL configuration is less than the voltage in SP configuration.

Conclusions.

In this paper, a new sensor placement combination for the detection and isolation of faults in the photovoltaic field and the simulation results for different types of faults are presented.

The number of sensors required and the costs are reduced significantly in this model compared to other existing models.

The faults detection and isolation method developed in this work is confirmed by three different scenarios by showing how different faults affecting the photovoltaic field such as short-circuit current, open circuit voltage, partial and total shading can be presented.

This study opens many perspectives:

- applying this method to the real photovoltaic field;
- applying one structure for faults identification;
- for the diagnostic multi faults cumulated can be expected.

Acknowledgement. The authors would like to thank Monitoring Team of Automation Laboratory – LAS, University of Setif 1, Setif, Algeria.

Conflict of interest. The authors declare that they have no conflicts of interest

REFERENCES

1. European Photovoltaic Industry Association (EPIA). *Global Market Outlook for Photovoltaics 2014-2018*. Available at: https://helapco.gr/wp-content/uploads/EPIA_Global_Market_Outlook_for_Photovoltaics_2014-2018_Medium_Res.pdf (accessed 16 May 2021).
2. Al-Sheikh H., Moubayed N. Fault detection and diagnosis of renewable energy systems: An overview. *2012 International Conference on Renewable Energies for Developing Countries (REDEC)*, 2012, pp. 1-7. doi: <https://doi.org/10.1109/REDEC.2012.6416687>.
3. Sholapur S., Mohan K.R., Narsimhegowda T.R. Boost Converter Topology for PV System with Perturb And Observe MPPT Algorithm. *IOSR Journal of Electrical and Electronics Engineering*, 2014, vol. 9, no. 4, pp. 50-56. doi: <https://doi.org/10.9790/1676-09425056>.
4. Ghazanfari J., Maghfoori Farsangi M. Maximum Power Point Tracking Using Sliding Mode Control for Photovoltaic Array. *Iranian Journal of Electrical and Electronic Engineering*, 2013, vol. 9, no. 3, pp. 189-196. Available at: <http://ijeece.iust.ac.ir/article-1-523-en.pdf> (accessed 16 May 2021).
5. Latreche S., Badoud A.E., Khemliche M. Implementation of MPPT Algorithm and Supervision of Shading on Photovoltaic Module. *Engineering, Technology & Applied Science Research*, 2018, vol. 8, no. 6, pp. 3541-3544. doi: <https://doi.org/10.48084/etasr.2354>.
6. Nebti K., Lebied R. Fuzzy maximum power point tracking compared to sliding mode technique for photovoltaic systems based on DC-DC boost converter. *Electrical Engineering & Electromechanics*, 2021, no. 1, pp. 67-73. doi: <https://doi.org/10.20998/2074-272X.2021.1.10>.
7. Levron Y., Shmilovitz D. Maximum Power Point Tracking Employing Sliding Mode Control. *IEEE Transactions on Circuits and Systems I: Regular Papers*, 2013, vol. 60, no. 3, pp. 724-732. doi: <https://doi.org/10.1109/TCSI.2012.2215760>.
8. Meng Z., Shao W., Tang J., Zhou H. Sliding-mode control based on index control law for MPPT in photovoltaic systems. *CES Transactions on Electrical Machines and Systems*, 2018, vol. 2, no. 3, pp. 303-311. doi: <https://doi.org/10.30941/CESTEMS.2018.00038>.
9. Picault D. *Reduction of mismatch losses in grid-connected photovoltaic systems using alternative topologies*. Sciences de l'ingénieur [physics]. Institut National Polytechnique de Grenoble, 2010. France. Available at: https://tel.archives-ouvertes.fr/file/index/docid/545432/filename/Thesis_dpicauld.pdf (accessed 16 May 2021).
10. La Manna D., Li Vigni V., Riva Sanseverino E., Di Dio V., Romano P. Reconfigurable electrical interconnection strategies for photovoltaic arrays: A review. *Renewable and Sustainable Energy Reviews*, 2014, vol. 33, pp. 412-426. doi: <https://doi.org/10.1016/j.rser.2014.01.070>.
11. Yanli Liu, Bingfeng Li, Ze Cheng. Research on PV module structure based on fault detection. *2010 Chinese Control and Decision Conference*, 2010, pp. 3891-3895. doi: <https://doi.org/10.1109/CCDC.2010.5498470>.
12. Xu X., Wang H., Xu X., Zuo Y. Method for Diagnosing Photovoltaic Array Fault in Solar Photovoltaic System. *2011 Asia-Pacific Power and Energy Engineering Conference*, 2011, pp. 1-5. doi: <https://doi.org/10.1109/APPEEC.2011.5747701>.
13. Huang Zhiqiang, Guo Li. Research and implementation of microcomputer online fault detection of solar array. *2009 4th International Conference on Computer Science & Education*, 2009, pp. 1052-1055. doi: <https://doi.org/10.1109/ICCSE.2009.5228541>.
14. Jianeng T., Yongqiang Z., Wenshan W. Fault diagnosis method and simulation analysis for photovoltaic array. *2011 International Conference on Electrical and Control Engineering*, 2011, pp. 1569-1573. doi: <https://doi.org/10.1109/ICECENG.2011.6058271>.
15. Schirripa Spagnolo G., Del Vecchio P., Makary G., Papalillo D., Martocchia A. A review of IR thermography applied to PV systems. *2012 11th International Conference on Environment and Electrical Engineering*, 2012, pp. 879-884. doi: <https://doi.org/10.1109/EEEIC.2012.6221500>.
16. Chouder A., Silvestre S. Automatic supervision and fault detection of PV systems based on power losses analysis. *Energy Conversion and Management*, 2010, vol. 51, no. 10, pp. 1929-1937. doi: <https://doi.org/10.1016/j.enconman.2010.02.025>.
17. Syafaruddin, Karatepe E., Hiyama T. Controlling of artificial neural network for fault diagnosis of photovoltaic array. *2011 16th International Conference on Intelligent System Applications to Power Systems*, 2011, pp. 1-6. doi: <https://doi.org/10.1109/ISAP.2011.6082219>.
18. Cheng Z., Zhong D., Li B., Liu Y. Research on Fault Detection of PV Array Based on Data Fusion and Fuzzy Mathematics. *2011 Asia-Pacific Power and Energy Engineering Conference*, 2011, pp. 1-4. doi: <https://doi.org/10.1109/APPEEC.2011.5749018>.
19. Mahmoud S.A., Mohamed H.N. Novel modeling approach for photovoltaic arrays. *2012 IEEE 55th International Midwest Symposium on Circuits and Systems (MWSCAS)*, 2012, pp. 790-793. doi: <https://doi.org/10.1109/MWSCAS.2012.6292139>.
20. Alajmi B.N. *Design and Control of Photovoltaic Systems in Distributed Generation*. Thesis for the degree of Doctor of Philosophy, University of Strathclyde, Department of Electronic and Electrical Engineering. 2013. Available at: <https://stax.strath.ac.uk/downloads/gt54kn312> (accessed 16 May 2021).
21. Khan S.A., Mahmood T., Awan K.S. A nature based novel maximum power point tracking algorithm for partial shading conditions. *Electrical Engineering & Electromechanics*, 2021, no. 6, pp. 54-63. doi: <https://doi.org/10.20998/2074-272X.2021.6.08>.

Received 23.03.2022
Accepted 15.06.2022
Published 07.09.2022

Latreche Samia¹, Doctor of Technical Science, Associate Professor,
Khenfer Amar¹, PhD Student,
Khemliche Mabrouk¹, Doctor of Technical Science, Professor,
¹Technology Faculty, Electrical Engineering Department,
Automation Laboratory of Setif, University of Setif 1, Algeria.
e-mail: ksamia2002@yahoo.fr (Corresponding Author),
khenferamar@yahoo.fr, mabroukkhemliche@univ-setif.dz

How to cite this article:

Latreche S., Khenfer A., Khemliche M. Sensors placement for the faults detection and isolation based on bridge linked configuration of photovoltaic array. *Electrical Engineering & Electromechanics*, 2022, no. 5, pp. 41-46. doi: <https://doi.org/10.20998/2074-272X.2022.5.07>

M.O. Poliakov, V.V. Vasylevskyi

Method for assessing unevenness of cellulose insulation layers aging of power transformers winding

Introduction. Improving the methods of estimating the insulation aging of the oil-immersed power transformer windings is an urgent task for transformer condition monitoring systems. The **scientific novelty** of the work is to take into account the uneven distribution of temperature and humidity along the vertical axis of the winding in modeling the aging of insulation and to develop methods for determining the conditions under which the aging rate of insulation in the intermediate layer will exceed aging rate in the hottest layer. The **purpose** of the work is to evaluate the wear unevenness of cellulose insulation based on modeling the distribution of temperature and humidity along the vertical axis of the power transformer winding. **Methods.** The transformer winding is mentally divided into horizontal layers of equal height, the reduction of service life is calculated in parallel for all horizontal layers. Layer with the maximum degree of aging for the entire period of operation and storage of the transformer is recognized as determining the reduction in the service life of the insulation of the transformer as a whole. A model of the interaction of winding layers is developed, with determination of temperatures, humidity, relative rate of aging of each layer due to temperature and humidity as a function of traditional design parameters such as load, cooling temperature, heat capacity and thermal resistance of transformer. The index of exceeding the aging rate by the layered method in comparison with this rate for the hottest layer is offered. The method of genetic algorithms determines the conditions for obtaining the maximum value of this index. **Results.** A computer model has been developed to predict the aging of the cellulose insulation of transformer windings. According to the proposed method, a layer with significantly shorter insulation aging time (in the example, time reduced by 39.18 %) than for the upper layer was determined, which confirms the feasibility of layer-by-layer monitoring and modeling of insulation aging processes of power oil-immersed transformer windings. References 25, tables 2, figures 4.

Key words: power oil-immersed transformer, cellulose insulation aging, computer model of layer-by-layer aging of winding insulation.

Вступ. Вдосконалення методик оцінки старіння целюлозної ізоляції обмоток силового маслонаповненого трансформатора є актуальним завданням для систем моніторингу стану трансформаторів. **Наукова новизна** роботи полягає в урахуванні нерівномірності розподілів температури та вологості вздовж вертикальної осі обмотки при моделюванні процесів старіння ізоляції та у розробці методики визначення умов, за яких швидкість зносу ізоляції у проміжному шарі буде максимально перевищувати швидкість у найбільш нагрітому шарі обмотки. **Метою** роботи є оцінка нерівномірності зносу целюлозної ізоляції на основі моделювання розподілу температури та вологості вздовж вертикальної осі обмотки силових трансформаторів. **Методи.** Обмотка трансформатора подумки розділена на горизонтальні шари рівної висоти, підрахунок скорочення строку служби виконується паралельно за усіма горизонтальними шарами, а шар, що має максимальний ступінь старіння за весь період експлуатації та зберігання трансформатора визнається найбільш ресурс витратним шаром, який визначає скорочення строку служби ізоляції трансформатора в цілому. Розроблена модель взаємодії шарів обмотки, з визначенням температур, вологості, відносної швидкості старіння кожного шару внаслідок дії температури та вологи як функції традиційних розрахункових параметрів, таких як навантаження, температура охолодного середовища, теплоємність та тепловий опір трансформатора. Запропонований показник перевищення швидкості скорочення строку служби пошаровим методом у порівнянні з цією швидкістю для найбільш нагрітого шару. Методом генетичних алгоритмів визначені умови для отримання максимального значення цього показника. **Результати.** Розроблена комп'ютерна модель для прогнозування старіння целюлозної ізоляції обмоток. За запропонованою методикою визначено найбільш ресурс витратний шар зі значно меншим часом старіння ізоляції (у прикладі час зменшено на 39,18 %), ніж для верхнього шару, що підтверджує доцільність пошарового моніторингу та моделювання процесів старіння ізоляції обмоток силового маслонаповненого трансформатора. Бібл. 25, табл. 2, рис. 4.

Ключові слова: силовий маслонаповнений трансформатор, старіння целюлозної ізоляції, комп'ютерна модель пошарового старіння ізоляції обмоток.

Introduction. The issues of assessing the technical condition of power transformers, including the aging of the cellulose insulation of oil-immersed power transformer windings, are invariably in the focus of research by the world energy community [1, 2]. As is known [3], the residual service life of cellulose insulation is determined by the time during which the degree of polymerization of cellulose molecules decreases to 250 units. In turn, the aging rate depends on a number of operational factors, the main of which is considered to be temperature.

The result of comparing the assessment of insulation aging for a particular transformer with the assigned resource determines the moment the transformer is decommissioned and the probability of a transformer failure when it continues to operate [4].

The state of oil-immersed power transformer insulation is determined by the following methods: by

means of analyzing cellulose degree of polymerization [3]; by indirect methods, for example, by the presence of certain gases in transformer oil [5, 6]; by online monitoring of operating conditions [7, 8]; based on the statistics of transformer accidents [9]; by modeling the reactions of the transformer to the predicted changes in operating factors [10].

The advantage of the latter method for determining the state of power transformers insulation is the ability to take into account the predicted dynamics of external operating factors. Therefore, this method is discussed in more detail below.

Previous research. Modeling of cellulose insulation aging includes modeling the thermodynamic and moisture-dynamic processes in the transformer, as well as modeling the effect of these processes on the insulation aging rate.

Known thermodynamic models are built on the basis of various differential equations of the heat balance of the transformer, which use various transformer equivalent circuits [11, 12]. Solutions of these equations are found both by analytical methods [13] and by computer simulation [11, 14-16].

Thermal modeling techniques are based on dynamic analogies of electrical and thermal processes, Computational Fluid Dynamics (CFD) and Thermal Hydraulic Network Model (THNM). Models based on the first technique do not take into account the nonlinear dependences of transformer thermal parameters. Models based on the other mentioned techniques require large computing resources and expensive commercial software for implementation.

The basic model for assessing the rate of insulation aging is the Montsinger equation [17], which determines the instantaneous rate of relative thermal aging of the insulation. Integration of this rate in a certain time interval gives the value of thermal aging of the insulation in this interval. The corresponding expression is called the «aging integral». Over time, multipliers were added to the aging integral, taking into account the influence on the cellulose insulation aging rate of its humidity, as well as the acid number of transformer oil [9, 11]. In other studies [4], these factors are taken into account in the expression of the aging rate through the values of the activation energy E and the pre-exponential factor A , due to the influence of humidity, acids, and oxidation.

There are studies in which the influence of the humidity of cellulose insulation on the deterioration of its technical condition is experimentally confirmed [18, 19].

At the same time, the known models of insulation aging do not take into account the relationship between the temperature and moisture distribution in the winding insulation along its vertical axis. The intensity of transformer insulation aging is determined by the hot-spot temperature (HS) which is located in the upper part of the winding. Accordingly, it is assumed that the greatest service life reduction also occurs at the top of the transformer. On the other hand, the aging rate of cellulose insulation, in addition to temperature, is affected by the degree of cellulose humidity and the oxidation of transformer oil. It is known that the wettest spot, (WS) in an operating transformer is located in the lower part of the winding.

In [20], the concept of the most resource consumption spot (RCS) is introduced, it is shown that this spot may not coincide with the HS and WS spots, can change its position in the direction of the vertical axis of the winding depending on the dynamics of the load current of the transformer, humidity of cellulose insulation and other factors.

During the simulation of temperature and humidity distributions, the transformer winding with height H is mentally divided into N layers of the same height, as it shown in Fig. 1.

The number of layers is chosen in such a way that, within each layer, changes in temperature and humidity along the vertical axis of the winding can be neglected [20].

Winding layers are numbered from bottom to top. In this case, the n -th layer number ($1 \leq n \leq N$) characterizes the excess of the layer boundaries over the bottom of the

winding. The excess of the upper h_m and lower h_{bn} boundaries of the n -th layer is determined by the expressions:

$$h_m = \frac{Hn}{N}; \quad h_{bn} = \frac{H(n-1)}{N}.$$

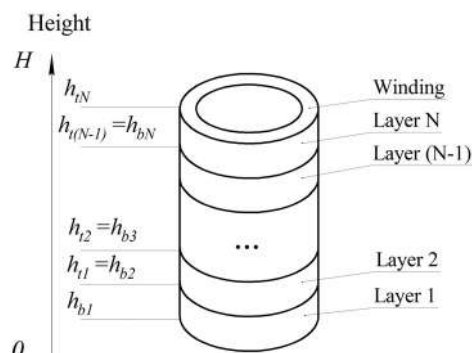


Fig. 1. Structure of the winding layers

Thus, in the case of a change in the value of N (for sufficiently large N), the excess of h will correspond to another layer. For example, with $H = 2$ m and $N = 10$, the point located at a height of 1.4 m lies on the boundary of the seventh, and with $N = 20$, the 14th layer.

Due to the oppositely directed temperature and humidity gradients in the layers, accelerated aging of the different winding layers at different points in time is possible.

Therefore, it is necessary to take into account the aging rate of the insulation for each layer and, by integration, determine the most aged layer since the manufacture of the transformer. It can be assumed that the aging of this layer determines the aging of the winding insulation as a whole.

It should be noted that in the layered model given in [16] there is no mechanism for the interaction of the processes of dynamic redistribution of temperatures and humidity of cellulose along the vertical axis of the winding. This, in turn, does not allow performing computer simulation of layer-by-layer aging of insulation under non-stationary load conditions of the transformer.

The purpose of this work is to evaluate the aging unevenness of cellulose insulation based on modeling the distribution of temperature and humidity along the vertical axis of the winding of power transformers.

The task of the work is to develop a computer model for calculating the reduction in the service life of winding insulation layers based on the current values of the transformer load, ambient temperature, winding humidity and thermodynamic parameters of the transformer, as well as to develop a methodology for determining conditions under which cellulose insulation aging in the intermediate layer is greater than in the layer with the hottest spot.

Layer-by-layer model of power oil-immersed transformers cellulose insulation aging. To solve the set tasks, a computer layer-by-layer thermo- and moisture-dynamic model of the transformer is proposed. The structure of the model is shown in Fig. 2. The model as a whole and its elements are external models (black box models), that is, models that establish the dependence of outputs on inputs without detailing the physical processes in the transformer and in its parts.

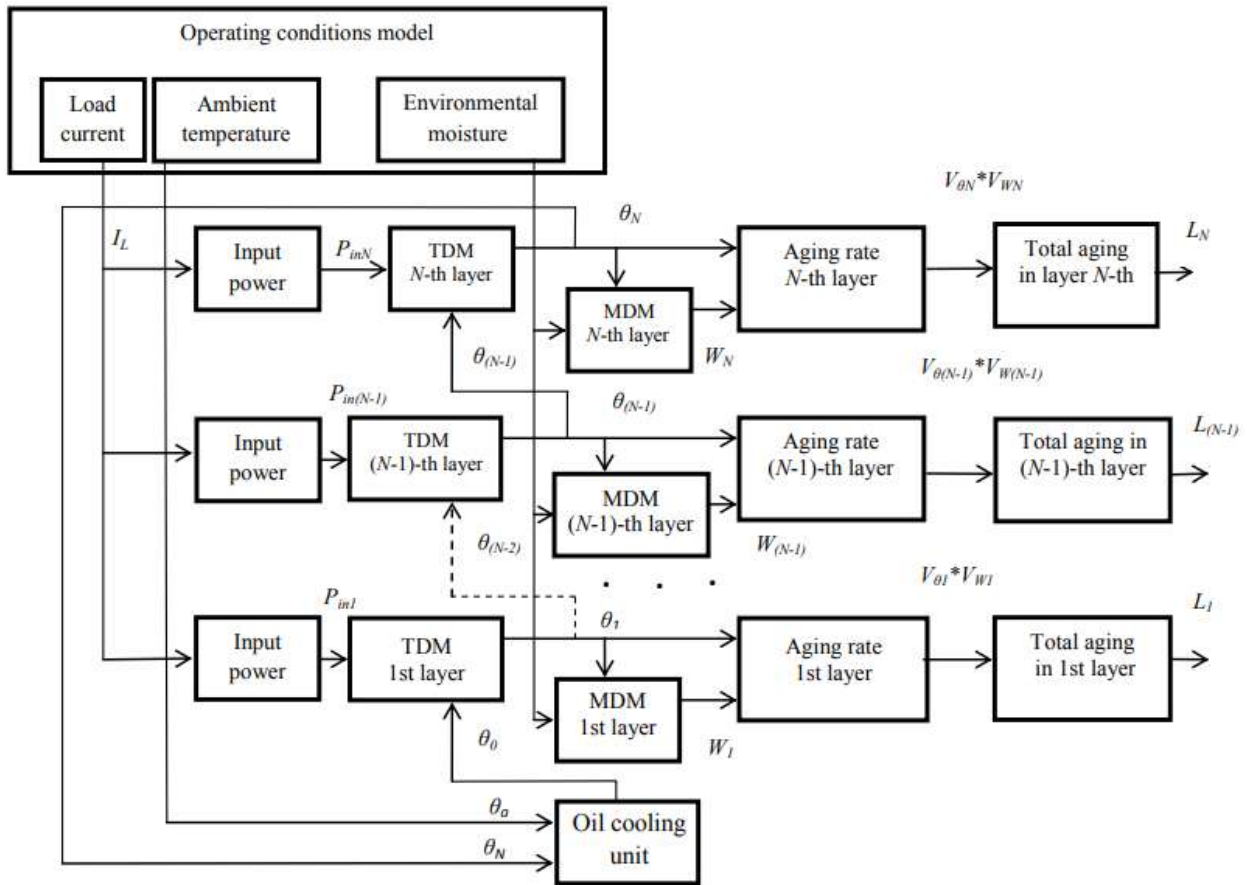


Fig. 2. Structural diagram of the layer-by-layer model of transformer winding insulation aging (TDM – thermodynamic model; MDM – moisture dynamic model)

The model consists of the unit for the formation of operating conditions, models of layers and units for determining the layer-by-layer insulation aging.

The operating conditions formation unit sets the values of the transformer load currents, the ambient temperature and the amount of moisture penetrating into the transformer tank. The layer model determines the input power, temperature and absolute humidity in the layer at the boundary of the «cellulose insulation-transformer oil» system. According to these data, the unit for determining the layer-by-layer aging of the insulation calculates the instantaneous rate of relative aging and the value of the aging of the cellulose insulation in the layer in accordance with the «aging integral» [4, 9-11].

Thus, the layer model consists of the input power model, thermodynamic and moisture dynamic models.

The input power of the n -th layer is determined from the expression [1]:

$$P_{n\text{ in}} = \frac{P_{in}}{N} = \frac{I^2 Z + P_{il}}{N}, \quad (1)$$

where P_{in} is the transformer power losses, W; I is the load current, A; Z is the winding resistance, Ω ; P_{il} is the no-load loss, W; N is the number of layers.

The thermodynamic model of the n -th layer is based on the heat balance equation in the winding cellulose insulation layer immersed in transformer oil. In the proposed model, the differential equation of the first degree is chosen as the heat balance equation:

$$\frac{d\theta_n}{dt} = \frac{P_{n\text{ in}}}{C_n} - \frac{1}{C_n R_n} (\theta_n - \theta_{(n-1)}), \quad (2)$$

where θ_n , $\theta_{(n-1)}$ is the temperature of the n -th, $(n-1)$ -th layer, $^{\circ}\text{C}$; $d\theta_n/dt$ is the time derivative of the temperature of the n -th layer; C_n is the heat capacity of the n -th layer, J/K; R_n is the thermal resistance of the n -th layer, K/W.

A feature of the thermodynamic model of each layer is that it describes the thermal balance between the thermal power that is released in the layer winding as a result of the flow of load current and no-load losses and the thermal power that is transmitted through the moving oil to the overlying layers of the winding. Taking into account the direction of oil movement in the transformer tank from bottom to top, the thermal energy received by oil in the lower layer is involved in heating all layers of the winding. At the same time, the thermal energy released in the intermediate layer does not participate in the heating of the underlying layers of the winding. We also note that the oil heated in the N -th (upper) layer enters the cooler inlet, in which the oil temperature drops to the value θ_0 and contacts the lower layer of the winding.

To determine the values of parameters – heat capacity C_n , and thermal resistance R_n of the n -th layer, methods of comparing these parameters with the results of thermal tests or transformer condition monitoring were used [21].

The method takes into account the conditions (load current, ambient temperature, cooling modes) and the results (temperature of the upper layer of transformer oil, thermal constant of the transformer) of thermal tests. These parameters determine the requirements for the coefficients of the computer model of the heat balance equation of the transformer as a material point:

$$\frac{d\theta_m}{dt} = \frac{P_{min}}{C_m} - \frac{1}{C_m R_m} (\theta_m - \theta_a), \quad (3)$$

where $d\theta_m/dt$ is the time derivative of the top oil temperature; θ_m is the top-oil temperature, °C; θ_a is the ambient temperature, °C; P_{min} is the input thermal power (power loss), W; C_m is the heat capacity of the transformer, J/K; R_m – thermal resistance of the transformer, K/W.

The values of the equation coefficients of this model are chosen experimentally to ensure that the simulation results coincide, with a given accuracy, with the results of thermal tests.

If during transformer operation the current value of the thermal parameters changes over time, then it is advisable to use condition monitoring data to determine the thermal parameters. For this purpose, we substitute the results of measuring the top-oil temperature and the ambient temperature for two points in time into the heat balance equations (3). Then we solve the resulting system of algebraic equations with respect to the coefficients of the original differential equation – the heat capacity and thermal resistance of the transformer [21].

At the next stage, the equation (2) coefficients are expressed in terms of the equation (3) coefficients. The following assumptions are taken into account:

1. Top-oil temperatures in these models must be equal. I.e. $\theta_m = \theta_N$.
2. The lower layer inlet receives oil from the cooler outlet, which has a temperature θ_o . The moisture content of the oil in the cooler does not change.
3. The thermal resistance R_n of the section «cellulose insulation-transformer oil» in the layer model is expressed through the thermal resistance R_m of the transformer model as a material point:

$$R_n = R_m(N+1-n)/g, \quad (4)$$

where $(N+1-n)$ reflects the increase in thermal resistance R_n relative to the resistance R_m ; g is an empirical coefficient that takes into account the decrease in the thermal resistance of the «winding layer-transformer oil» section of the layered model compared to the thermal resistance of the «top oil layer-environment» section of the «single point» model, which is used to adjust the layered model.

As follows from (4), when n increases, R_n decreases and, consequently, the dissipated power in the layer increases. This leads to a decrease in the power going to the heating of the layer substance and a decrease in the layer temperature increment.

4. The heat capacity of the layer and the thermal power that is released in the layer n is N times less than the corresponding values of the transformer model as a material point:

$$C_n = \frac{C_m}{N}; \quad (5)$$

$$P_{nin} = \frac{P_{min}}{N}. \quad (6)$$

After substituting expressions (4) – (6) in (2) we get:

$$\frac{d\theta_n}{dt} = \frac{P_m}{C_m} - \frac{Ng}{C_m R_m(N+1-n)} (\theta_n - \theta_{(n-1)}). \quad (7)$$

The temperature values θ_n of the n -th layer obtained as a result of application in the layer model are used to

determine the absolute humidity, the rate of relative aging of the insulation of this layer and determine the temperature of the $(n+1)$ -th layer.

The moisture-dynamic model of the layer is based on the well-known method for calculating the degree of cellulose insulation humidity from the measured value of the relative humidity of transformer oil [22]. The calculated humidity of cellulose insulation of the n -th layer at a certain point in time is determined from the expression:

$$W(n) = A_w \cdot e^{-B_w \cdot \theta_n} \cdot p^{k_w + a_w \cdot \theta_n},$$

where $W(n)$ is the calculated humidity of cellulose insulation of the n -th layer, %; A_w , B_w , k_w , a_w are the empirical coefficients [24]; θ_n is the temperature of the n -th layer of the transformer winding, ($n = 1, N$), °C; p is the partial pressure of water vapor, mmHg.

The value of the partial pressure of water vapor depends on the relative humidity of the transformer oil in the n -th layer at the corresponding temperature of this layer [24]:

$$p(n) = \phi' \cdot 10^{(8,0589 - 1729,9875 / (\theta_n + 273,856))},$$

where ϕ' is the relative humidity of oil at the temperature of the n -th winding layer θ_n , %.

Relative humidity at θ_n is determined from the expression [24]:

$$\phi' = \frac{W_M}{C(\theta_n)},$$

where $C_M(\theta_n)$ is the limiting humidity of oil at the temperature of the n -th layer, g/t; W_M is the absolute humidity of oil, taking into account the temperature of the n -th layer, g/t.

The value of the absolute humidity of transformer oil can be either determined by direct measurements or obtained empirically (for example, a value corresponding to a low degree of the oil humidity is taken). To take into account the dynamics of humidity in the system «cellulose insulation-transformer oil» due to changes in the thermal regime of the transformer, a model is used in the form of a state diagram [22]. This model is characterized by three states – moisture transfer from cellulose insulation to transformer oil, moisture transfer from transformer oil to cellulose insulation and an equilibrium state (is the initial one).

Thus, the moisture-dynamic model of the layer determines the absolute humidity in the layer based on the temperature value θ_n .

The oil at the outlet of the cooler has a moisture vapor pressure corresponding to the temperature of the upper layer. Therefore, moisture removed from the cellulose insulation in the top layer is returned to the cellulose insulation in the bottom layer. Similar processes occur in other layers, which together form the distribution of moisture along the vertical axis of the winding.

Simulation using the model on Fig. 2 was carried out for the conditions given in [22]. The initial data for setting up the model were the results of thermal tests of the transformer ATДЦН100000/220/150. During these tests, the transformer was placed in a climatic chamber, in which the temperature was maintained at $\theta_a = 40$ °C and kept under a load of $I_L = 244$ A in a certain cooling mode

for a time significantly longer than its thermal constant. In this case, the temperature θ_m of the upper oil layers was constantly measured. According to the measurement data, the temperature of the excess of the upper oil layers $\Delta\theta = 40^\circ\text{C}$ and the thermal time constant $\tau = 2.4$ hours were established. Based on these data and the passport value of the no-load loss parameter P_{il} , the coefficients C_m, R_m of equation (3) were determined using the method [21, 25]. To solve equation (3), a computer model was used in the Simulink environment with the values of the input variables corresponding to the conditions of the thermal tests performed. The deviations of the values of τ and $\Delta\theta$ obtained as a result of modeling from the results of thermal tests do not exceed 5 %.

At the next stage, using this computer model, the temperature of the upper oil layers was determined for the conditions of the experiment with a layered model (Fig. 2): the load current I_L changed according to the profile shown in Fig. 3, and the temperature θ_a is taken equal to 40°C . Further, the parameters of the layered model, in particular, the coefficient g , were selected in such a way ($g = 11.11$) that the temperature of the upper oil layers in the layered model was equal to the corresponding temperature of the original «one-point» model. After that, the temperatures obtained in the course of modeling using a layered model were used to determine the moisture distributions and aging rates.

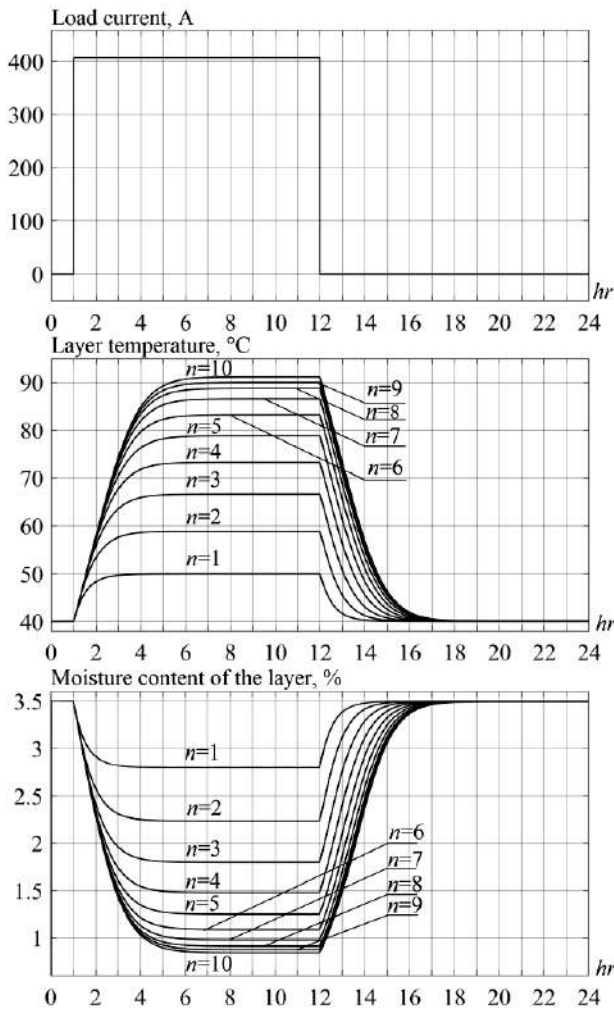


Fig. 3. Simulation results

The moisture content of cellulose insulation was calculated for the following initial data: $A_w = 6.1$; $B_w = 0.04$; $k_w = 0.33$; $a_w = 0.0033$ (empirical coefficients correspond to K-120 cable paper [24]). The mass of cellulose insulation of the transformer is assumed to be 6 tons, the mass of transformer oil is 47 tons. The graphs of changes in the parameters of these processes obtained as a result of modeling are shown in Fig. 3.

The steady-state values of temperatures, humidity, rates of relative aging of cellulose insulation and the aging itself in the layers of the model are given in Table 1.

Table 1

Results of modeling by layers

Layer	$\theta(n), ^\circ\text{C}$	$W(n), \%$	V_θ	V_W	$V_\theta \cdot V_W$
10	91,10	0,846	0,4403	2,2545	0,9927
9	89,90	0,877	0,4111	2,3912	0,9830
8	88,86	0,913	0,3485	2,5588	0,8917
7	86,55	0,980	0,2666	2,8323	0,7551
6	83,23	1,089	0,1830	3,2981	0,6036
5	78,80	1,250	0,1120	4,0648	0,4553
4	73,27	1,480	0,0609	5,2739	0,3212
3	66,61	1,800	0,0292	7,1129	0,2077
2	58,82	2,237	0,0123	9,8245	0,1208
1	49,97	2,800	0,0045	13,7142	0,0617

From the results obtained it follows:

- under these conditions, the most consumable resource and the most heated is the upper layer of the transformer winding;
- the increase in temperature and humidity from layer to layer is not a constant value. That is, the functions $\theta(n)$ and $W(n)$ are non-linear.

The following notation is used: $\theta_{\max} = \theta(N)$; $\theta_{\min} = \theta(1)$; $\Delta\theta = (\theta_{\max} - \theta_{\min})$; $W_{\max} = W(1)$; $W_{\min} = W(10)$; $\Delta W = W_{\max} - W_{\min}$.

Using the simulation results, the coefficients of temperature change relative to the maximum values and humidity relative to the minimum values in the winding are calculated:

$$k_\theta(n) = \frac{\theta_{\max} - \theta(n)}{\Delta\theta}; \quad k_W(n) = \frac{W(n) - W_{\min}}{\Delta W}.$$

The obtained dependencies $k_\theta(n)$ and $k_W(n)$ are approximated by polynomials of the third degree. These polynomial functions and the resulting quality of approximation are shown in Fig. 4. Approximation quality was assessed using the determination coefficient R^2 . The calculated values of R^2 are close to 1, which indicates a sufficient quality of the approximation.

Using the obtained dependences of the coefficients $k_\theta(n)$ and $k_W(n)$, the dependences of the temperature $\theta(n)$ and humidity $W(n)$ of the layer as a function of θ_{\max} , $\Delta\theta$, W_{\min} , ΔW and n are obtained:

$$\theta(n) = \theta_{\max} - \Delta\theta \cdot k_\theta(n); \quad (8)$$

$$W(n) = W_{\min} + \Delta W \cdot k_W(n). \quad (9)$$

When assessing the rate of relative aging of the insulation, the hot-spot temperature of each layer was used, which is determined by the expression:

$$\theta_h(n) = \theta(n) + \Delta\theta_h, \quad (10)$$

where $\Delta\theta_h$ is the temperature rise of the winding above the oil temperature in this (n -th) layer, which, in accordance with the recommendations of IEC [4], is assumed to be 22°C for all layers.

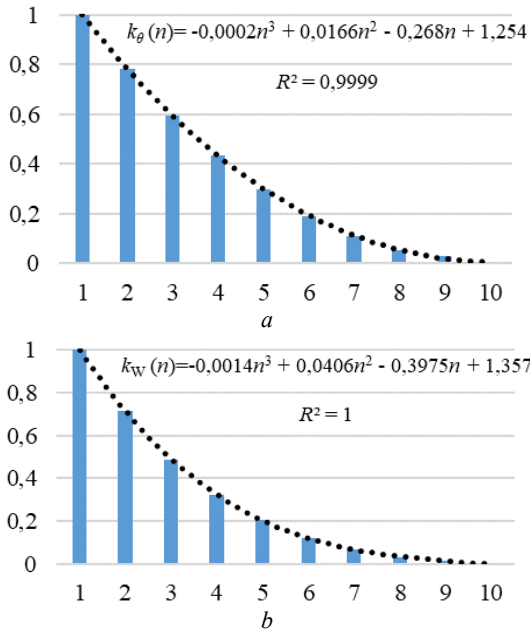


Fig. 4. Graphs of dependencies: a – $k_{\theta}(n)$; b – $k_W(n)$

The values of $W(n)$ and $\theta_h(n)$ from expressions (9) and (10) are substituted into the expressions for determining the rates of relative insulation aging. As a result of the action of temperature [6, 7]:

$$V_{\theta}(n) = 2^{\frac{(\theta_h(n)-98)}{6}} \quad (11)$$

and humidity

$$V_W(n) = \left(\frac{W(n)}{W_{BASE}} \right)^{1,493} \quad (12)$$

where W_{BASE} is the base humidity of cellulose insulation, %.

The designation for the product of the relative rates of thermal and moisture aging of insulation for layers n and N has been introduced:

$$V_n = V_{\theta}(n) \cdot V_W(n); \quad (13)$$

$$V_N = V_{\theta}(N) \cdot V_W(N). \quad (14)$$

Evaluation of the effectiveness of the proposed method is based on the assumption that there is some non-top (n -th) layer with a higher insulation aging rate than in the top layer (N -th). Without taking this fact into account, we underestimate the intensity of insulation aging. Thus, the conditions under which the resource is underestimated are determined from the expressions:

$$V_N < V_n \quad (15)$$

or

$$V_N - V_n < 0. \quad (16)$$

In this case, it is assumed that V_N and V_n are positive and different from zero and infinity. The following index is proposed:

$$F = \frac{V_N}{V_n}. \quad (17)$$

Then condition (15) can be rewritten in the form:

$$F < 1 \quad (18)$$

Moreover, the greatest underestimation of the aging intensity is achieved with a minimum index F . Substituting expressions (11-14) into expression (17), we obtain an expression for determining F :

$$F = \frac{V_N}{V_n} = \frac{V_{\theta}(N) \cdot V_W(N)}{V_{\theta}(n) \cdot V_W(n)} = \frac{V_{\theta}(N)}{V_{\theta}(n)} \cdot \frac{V_W(N)}{V_W(n)}, \quad (19)$$

where

$$\frac{V_{\theta}(N)}{V_{\theta}(n)} = \frac{2^{\frac{(\theta_N-98)}{6}}}{2^{\frac{(\theta_n-98)}{6}}} = 2^{\frac{(\theta_N-\theta_n)}{6}}; \quad (20)$$

$$\frac{V_W(N)}{V_W(n)} = \frac{\left(\frac{W(N)}{W_{BASE}} \right)^{1,493}}{\left(\frac{W(n)}{W_{BASE}} \right)^{1,493}} = \left(\frac{W(N)}{W(n)} \right)^{1,493}. \quad (21)$$

Substituting (20, 21) into (19), taking into account (8), (9) and approximation results in Fig. 4, we obtain:

$$\frac{V_{\theta}(N)}{V_{\theta}(n)} = 2^{\frac{(\Delta\theta(-0,0002n^3 + 0,0166n^2 - 0,268n + 1,254))}{6}}; \quad (22)$$

$$\frac{V_W(N)}{V_W(n)} = \left(\frac{1}{1 + \frac{\Delta W}{W_{min}}(-0,0014n^3 + 0,0406n^2 - 0,3975n + 1,357)} \right)^{1,493} \quad (23)$$

Analysis of expressions (15) and (16) shows that:

$$\frac{V_{\theta}(N)}{V_{\theta}(n)} \leq 1 \quad \text{and} \quad \frac{V_W(N)}{V_W(n)} \geq 1.$$

Therefore, the F index can be either less or greater than 1. When $F > 1$, the greatest insulation aging occurs in the upper layer of the winding.

To determine the conditions under which F_{min} is achieved, the method of genetic algorithms [23] was applied. In accordance with this method, expression (19), taking into account expressions (22) and (23), is a fitness function, the minimum of which is to be determined.

The search for F_{min} was carried out using the *ga* function from the MATLAB software package. The initial restrictions on the input variables, the obtained value F_{min} of the value of the input parameters and the number of the layer at which F_{min} is reached are given in Table 2. This is a method of finding a function extremum by directional iteration of the values of the function arguments. Its advantage is that it does not impose requirements on the complexity of the function.

Table 2

The results of determining the indicator F_{min}

Name, designation, unit measurements, variable type	Value range	Value for F_{min}	F_{min} value	Layer number
Number of layers, N , pieces, integer	$N=10$	10	0,6182	8
Oil temperature range, $\Delta\theta$, °C, real	$20 < \Delta\theta < 60$	20		
Absolute humidity of the upper layer, $W(N)$, %, real	$0,3 < W(N) < 1$	0,3		
Winding humidity change range, ΔW , %, real	$0 < \Delta W < 1,5$	1,5		

As can be seen from Table 2, the value of the index $F_{\min} = 0,6182$ obtained during the operation of the genetic algorithm takes place for the eighth layer. From here, according to expression (17):

$$V_n = V_N / F_{\min} = 1,6176 V_N. \quad (24)$$

Thus, the adjusted value of the insulation aging rate is 61.76 % higher than that calculated by the original method. If we assume that the wear rates V_n, V_N have a constant value, then the service life of the insulation will be reduced at these rates for different times. Wherein

$$V_n t_1 = V_N t_2. \quad (25)$$

where t_1, t_2 are expected service life of cellulose insulation of the n -th and upper (N -th) layers of the winding, respectively, years.

Since for $F_{\min} < 1$ we have $V_n > V_N$, then $t_1 < t_2$. Then, taking into account (24) and (25), we have a reduction in the service life:

$$\Delta t = (t_2 - t_1) = t_2(1 - F_{\min}). \quad (26)$$

Where does the relative reduction in service life, expressed as a percentage, be defined as:

$$\Delta t / t_2 [\%] = (\Delta t / t_2) \cdot 100\% = (1 - F_{\min}) \cdot 100\%. \quad (27)$$

For example, with $t_2 = 10$ years and $F_{\min} = 0,6182$ we get $\Delta t = 3,918$ years, $t_1 = 6.182$ years, $\Delta t / t_2 [\%] = 39,18$ %. That is, the calculation of the resource consumption time rate according to the proposed method gives a significantly lower (in the example by 39,18 %) residual insulation life.

Conclusions.

1. It has been established that the distribution in the layers of the winding of the average values of temperature and humidity of cellulose insulation in the direction of the vertical axis of the winding is multidirectional. Therefore, under certain conditions in which the insulation operates (for example, at high absolute humidity, a large temperature difference along the vertical axis of the winding, etc.), it is possible that the aging rate of the insulation under the action of temperature and moisture in the intermediate horizontal layer of the winding exceeds the aging rate in the layer with the most hot point, and as a result, greater wear of the intermediate layer.

2. The index F is proposed for assessing the excess rate of aging of cellulose insulation under the influence of temperature and moisture.

3. Using the method of genetic algorithms, the maximum excess of the rate of relative wear of insulation in the intermediate layer F_{\min} was estimated under given restrictions on the parameters of temperature and moisture distribution, as well as the number of layers into which the transformer winding is mentally divided.

4. The method for determining the dynamics of the distribution of temperature and humidity along the vertical axis of the winding has been improved with experimentally obtained results of measurements of the ambient temperature, load current and calculated values of the thermophysical parameters of cellulose insulation, which makes it possible to improve the accuracy of assessing its technical condition.

5. The expressions obtained in the work for determining the index F refer to one variant of estimates of the average rate of relative wear of insulation from among those presented in the known literature. Namely, ratings:

- for thermally unimproved cellulose insulation;
- with the determination of the thermal wear rate according to the Montsinger equation;
- taking into account the relationship of various factors (temperature, humidity, and others) in the form of a product of aging rates as a result of the action of one factor.

5. In the future, it is planned to obtain an analytical expression for determining the index F for other assessment options: aging of paper insulation with improved thermal characteristics; determining the average rate of aging as a function of the activation energy E and the pre-exponential factor A ; an additive form of the relationship of average aging rates, taking into account individual factors.

Conflict of interest. The authors declare no conflict of interest.

REFERENCES

1. James H. Harlow *Electric Power Transformer Engineering*. CRC Press, 2007. doi: <https://doi.org/10.1201/9781420008715>.
2. Krause C., Alfonso de Pablo, Devaux F., Ding H., Katshuna V., Lukic J., Melzer L., Miyazaki S., Munro M., Peixoto A., Scala M., Walker D. The Condition of Solid Transformer Insulation at End-of-Life. *Electra*, 2022, no. 321. Available at: <https://electra.cigre.org/321-april-2022/reference-paper/the-condition-of-solid-transformer-insulation-at-end-of-life.html> (Accessed 10 January 2022).
3. Lelekakis N., Martin D., Wijaya J. Ageing rate of paper insulation used in power transformers Part 1: Oil/paper system with low oxygen concentration. *IEEE Transactions on Dielectrics and Electrical Insulation*, 2012, vol. 19, no. 6, pp. 1999–2008. doi: <https://doi.org/10.1109/TDEI.2012.6396958>.
4. IEC 60076-7 Edition 2.0 2018-01. *Power transformers – Part 7: Loading guide for mineral-oil-immersed power transformers*. 2018, 89 p.
5. Fan J., Fu C., Yin H., Wang Y., Jiang Q. Power transformer condition assessment based on online monitor with SOFC chromatographic detector. *International Journal of Electrical Power & Energy Systems*, 2020, vol. 118, art. no. 105805. doi: <https://doi.org/10.1016/j.ijepes.2019.105805>.
6. Münster T., Werle P., Hämel K., Preusel J. Thermally Accelerated Aging of Insulation Paper for Transformers with Different Insulating Liquids. *Energies*, 2021, vol. 14, no. 11, art. no. 3036. doi: <https://doi.org/10.3390/en14113036>.
7. Saha T.K., Purkait P. *Transformer Ageing: Monitoring and Estimation Techniques*. John Wiley & Sons Singapore Pte. Ltd., 2017. doi: <https://doi.org/10.1002/9781119239970>.
8. Evdokimov S.A., Kondrashova Y.N., Karandaeva O.I., Gallyamova M.S. Stationary System for Monitoring Technical State of Power Transformer. *Procedia Engineering*, 2016, vol. 150, pp. 18-25. doi: <https://doi.org/10.1016/j.proeng.2016.07.270>.
9. Vasin V.P., Dolin A.P. Insulation resource of oil-immersed power transformers. *ELEKTRO. Electrical Engineering, Electric Power Industry, Electrotechnical Industry*, 2008, no. 3, pp. 12-17. (Rus).
10. Polyakov M.A., Vasilevskij V.V. Prediction of wearing out of power transformer winding insulation. *Technical Electrodynamics*, 2014, vol. 5, pp. 65-67.
11. Poliakov M.A., Vasilevskij V.V. Evaluation of power transformer insulation residual life based on its individual life cycle characteristics. *Electrical Engineering & Electromechanics*, 2014, vol. 3, pp. 38-41. (Rus). doi: <https://doi.org/10.20998/2074-272X.2014.3.07>.
12. Tang W.H., Wu Q.H. Thermoelectric Analogy Thermal Models of Power Transformers. In: *Condition Monitoring and Assessment of Power Transformers Using Computational Intelligence. Power Systems*. Springer, London, 2011. doi: https://doi.org/10.1007/978-0-85729-052-6_4.

13. Grabko V., Tkachenko S., Palaniuk O. Determination of temperature distribution on windings of oil transformer based on the laws of heat transfer. *ScienceRise*, 2021, no. 5, pp. 3-13. doi: <https://doi.org/10.21303/2313-8416.2021.002140>.
14. Juarez-Balderas E.A., Medina-Marin J., Olivares-Galvan J.C., Hernandez-Romero N., Seck-Tuoh-Mora J.C., Rodriguez-Aguilar A. Hot-Spot Temperature Forecasting of the Instrument Transformer Using an Artificial Neural Network. *IEEE Access*, 2020, vol. 8, pp. 164392–164406. doi: <https://doi.org/10.1109/ACCESS.2020.3021673>.
15. Radakovic Z.R., Sorgic M.S. Basics of Detailed Thermal-Hydraulic Model for Thermal Design of Oil Power Transformers. *IEEE Transactions on Power Delivery*, 2010, vol. 25, no. 2, pp. 790-802. doi: <https://doi.org/10.1109/TPWRD.2009.2033076>.
16. Ruan J., Deng Y., Huang D., Duan C., Gong R., Quan Y., Hu Y., Rong Q. HST calculation of a 10 kV oil-immersed transformer with 3D coupled-field method. *IET Electric Power Applications*, 2020, vol. 14, no. 5, pp. 921-928. doi: <https://doi.org/10.1049/iet-epa.2019.0469>.
17. Montsinger V.M. Loading Transformers By Temperature. *Transactions of the American Institute of Electrical Engineers*, 1930, vol. 49, no. 2, pp. 776-790. doi: <https://doi.org/10.1109/T-AIEE.1930.5055572>.
18. Martin D., Saha T., Gray T., Wyper K. Determining water in transformer paper insulation: effect of measuring oil water activity at two different locations. *IEEE Electrical Insulation Magazine*, 2015, vol. 31, no. 3, pp. 18-25. doi: <https://doi.org/10.1109/MEI.2015.7089118>.
19. Martin D., Saha T., Dee R., Buckley G., Chinnarajan S., Caldwell G., Zhou J. Bin, Russell G. Determining water in transformer paper insulation: analyzing aging transformers. *IEEE Electrical Insulation Magazine*, 2015, vol. 31, no. 5, pp. 23-32. doi: <https://doi.org/10.1109/MEI.2015.7214442>.
20. Poliakov M., Vasilevskij V., Andrienko P. Layered Model of the Consumption of the Insulation Resource of the Windings of a Power Oil-Immersed Transformer. *2020 IEEE Problems of Automated Electrodrive. Theory and Practice (PAEP)*, 2020, pp. 1-4. doi: <https://doi.org/10.1109/PAEP49887.2020.9240834>.
21. Poliakov M.O. Identification of thermal parameters of a power oil-immersed transformer according to monitoring parameters. *Bulletin of East Ukrainian National University*, 2007, no. 11, vol. 1 (117), pp. 167-173. (Rus).
22. Vasilevskij V.V. Dynamics model of moisture in paper insulation-transformer oil system in non-stationary thermal modes of the power transformer. *Electrical Engineering & Electromechanics*, 2016, no. 3, pp. 17-20. doi: <https://doi.org/10.20998/2074-272X.2016.3.02>.
23. Yang X.-S. *Nature-Inspired Optimization Algorithms*. Elsevier, 2014. 263 p. doi: <https://doi.org/10.1016/C2013-0-01368-0>.
24. Arakelyan V.G. Diagnostics of the insulation state of oil-filled electrical equipment based on the moisture content of the oil. *Electrical Engineering*, 2004, no. 3, pp. 34-39. (Rus).
25. Tikhomirov P.M. *Calculation of Transformers. Textbook for Higher Educational Institutions*. Energoatomizdat Publ., 1986. (Rus).

Received 07.02.2022
Accepted 30.06.2022
Published 07.09.2022

M.O. Poliakov¹, Doctor of Technical Science, Professor,
V.V. Vasylevskiy¹, PhD,
¹Zaporizhzhia Polytechnic National University,
64, Zhukovsky Str., Zaporizhzhia, Ukraine, 69063,
e-mail: polyakov@zntu.edu.ua;
lisses@ukr.net (Corresponding author)

How to cite this article:

Poliakov M.O., Vasylevskiy V.V. Method for assessing unevenness of cellulose insulation layers aging of power transformers winding. *Electrical Engineering & Electromechanics*, 2022, no. 5, pp. 47-54. doi: <https://doi.org/10.20998/2074-272X.2022.5.08>

M. Abid, S. Laribi, M. Larbi, T. Allaoui

Diagnosis and localization of fault for a neutral point clamped inverter in wind energy conversion system using artificial neural network technique

Introduction. To attain high efficiency and reliability in the field of clean energy conversion, power electronics play a significant role in a wide range of applications. More effort is being made to increase the dependability of power electronics systems. **Purpose.** In order to avoid any undesirable effects or disturbances that negatively affect the continuity of service in the field of energy production, this research provides a fault detection technique for insulated-gate bipolar transistor open-circuit faults in a three-level diode-clamped inverter of a wind energy conversion system predicated on a doubly-fed induction generator. **The novelty** of the suggested work ensures the regulation of power exchanged between the system and the grid without faults, advanced intelligence approaches based on a multilayer artificial neural network are used to discover and locate this type of defect; the database is based on the module and phase angle of three-phase stator currents of induction generators. The proposed methods are designed for the detection of one or two open-circuit faults in the power switches of the side converter of a doubly-fed induction generator in a wind energy conversion system. **Methods.** In the proposed detection method, only the three-phase stator current module and phase angle are used to identify the faulty switch. The primary goal of this fault diagnosis system is to effectively detect and locate failures in one or even more neutral point clamped inverter switches. **Practical value.** The performance of the controllers is evaluated under different operating conditions of the power system, and the reliability, feasibility, and effectiveness of the proposed fault detection have been verified under various open-switch fault conditions. The diagnostic approach is also robust to transient conditions posed by changes in load and speed. The proposed diagnostic technique's performance and effectiveness are both proven by simulation in the SimPower/Simulink® MATLAB environment. References 31, tables 2, figures 7.

Key words: artificial neural network, insulated-gate bipolar transistors, fault diagnosis technique, neutral point clamped inverter, wind energy conversion system.

Вступ. Для досягнення високої ефективності та надійності у галузі чистого перетворення енергії силова електроніка відіграє важливу роль у широкому спектрі застосування. Докладаються зусилля для підвищення надійності систем силової електроніки. **Мета.** Щоб уникнути будь-яких небажаних ефектів або перешкод, що негативно впливають на безперервність роботи в галузі виробництва енергії, у цьому дослідженні пропонується методика виявлення несправностей біполярних транзисторів із ізольованим затвором при обриві ланцюга в трирівневому інверторі з діодною фіксацією системи перетворення енергії вітру, що ґрунтується на асинхронному генераторі з подвійним живленням. **Новизна** запропонованої роботи забезпечує регулювання потужності, що обмінюється між системою та мережею, без збоїв, для виявлення та локалізації цього типу дефекту використовуються передові інтелектуальні підходи, засновані на багатошаровій штучній нейронній мережі; база даних заснована на модулі та фазовому куті трифазних статорних струмів асинхронних генераторів. Запропоновані методи призначені для виявлення одного або двох обривів у силових ключах бокового перетворювача асинхронного генератора подвійного живлення у системі перетворення енергії вітру. **Методи.** У запропонованому методі виявлення для ідентифікації несправного вимикача використовуються тільки трифазний модуль струму статора і фазовий кут. Основною метою цієї системи діагностики несправностей є ефективне виявлення та локалізація відмов в одному або навіть кількох інверторних перемикачах з фіксованою нейтральною точкою. **Практична цінність.** Робочі характеристики контролерів оцінюються за різних умов роботи енергосистеми, а надійність, здійсненість та ефективність запропонованого виявлення несправностей були перевірені за різних умов відмови розімкнутого вимикача. Діагностичний підхід також стійкий до перехідних станів, спричинених змінами навантаження та швидкості. Продуктивність та ефективність запропонованого діагностичного методу підтверджені моделюванням у середовищі SimPower/Simulink® MATLAB. Бібл. 31, табл. 2, рис. 7.

Ключові слова: штучна нейронна мережа, біполярні транзистори з ізольованим затвором, метод діагностики несправностей, інвертор з фіксацією нейтралі, система перетворення енергії вітру.

Introduction. The latest global reports on the state of wind energy in the world show that this energy has become an important investment sector in major industrialized countries. This is due to various factors such as the significant drop in production costs and the development of the field of power electronics that has solved many problems regarding the quality of the energy produced and the possibility of integrating this energy into the grid [1].

The wind turbines are equipped with a double fed induction generator (DFIG) to produce electricity at variable speeds. It is connected to a multi-level inverter of neutral point clamped (NPC) structure, to improve the performance of this system.

During operation, NPC inverter faces various constraints that can cause certain faults which is why production lines must be equipped with efficient fault detection and diagnostic systems, because any failure even the most trivial, can lead to multiple mandatory damages. The causes of IGBT failure in NPC inverters can be

classified into three categories: control faults, transient operating regimes, in particular those concerning terminal voltages, thermal overloads, and environmental conditions of use [2]. The environmental conditions leading to IGBT failure are mainly extreme ambient temperatures, humidity, natural ionizing radiation, and mechanical vibration [3, 4]. Less frequently, contamination and dust are also sources of IGBT malfunction.

A simple switch-open or circuit-open defect usually results in the whole or partial loss of operation of one of the IGBTs constituting the static converter it occurs due to a gate failure or a break in a connecting wire in the transistor, this break can be caused by thermal cycling or a short circuit fault [5]. An open circuit (OC) fault is one of the most prevalent faults of the IGBT in NPC inverter, it is necessary to examine and fault diagnosis in the arm of the inverter and detect it [6-8].

Recently, several methods for detecting faults in power transformers have been developed to correspond to

the diversity of problems encountered [9-17]. Park's vector-based methods [18-22] unfortunately require complex pattern recognition algorithms. Voltage-based methods require the use of additional sensors [23, 24]; The proposed diagnostic approach [25] is based on analyzing the inverter's output pole voltages and output currents. In [26] utilized a diagnostic procedure based on the phase current's instantaneous frequency after analyzing it with the Hilbert transform. In [27, 28] an artificial neural network (ANN) based multiple open-switch fault diagnostic approach was proposed. Using the DC components and total harmonic distortion (THD) of the stator currents, the 21 fault modes of multiple open-switch faults were localized. In this article, we focus on sophisticated intelligent techniques based on ANN to identify and detect these faults. We are interested in intermittent faults of the open circuit type of IGBT in the rotor side converter (RSC) to diagnose and locate them, to avoid degradation of the performance in the wind energy conversion system (WECS).

Topology of a three-level diode-clamped inverter and fault detection method. Topology of an inverter. Figure 1 depicts the NPC inverter topology [29, 30]. The DC-link supply was shared by each phase of the inverter, as indicated in Fig. 1. The common point of the series capacitors is connected to the center of each phase. The inverter is powering a three-phase load with an AC. According to the DC-bus voltage, the output has 3 levels: $(-V_{dc})$, 0, and $(+V_{dc})$.

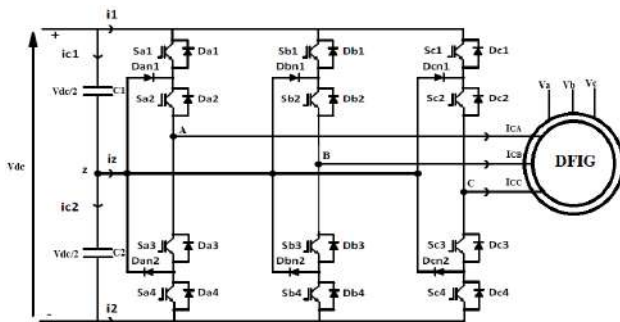


Fig. 1. NPC inverter circuit

The working principle is shown in Table 1. The converter should offer complementarities between both the couples of switches (S_{i1}, S_{i4}) and (S_{i2}, S_{i3}) in obtaining to get the appropriate 3-level voltages, where i denote the indication of phase ($i = A, B, C$), and V_{io} is the phase-to-fictive midway point value.

Table 1

The functioning principle for NPC inverter

Switching states	NPC inverter i -phase				Voltage
	S_{i1}	S_{i2}	S_{i3}	S_{i4}	
N	1	1	0	0	$+V_{dc}/2$
O	0	1	0	1	0
P	0	0	1	1	$-V_{dc}/2$

Table 1 depicts i -phase switching in Fig. 1 with switching stages and output voltage levels.

To simplify the intricacy of the structure of a 3-level inverter, each pair (transistor – diode) semiconductor is marked by a single bidirectional switch S_a and can be seen

that, the structure is symmetric. Figure 2 illustrated the structure of a single leg, with an open circuit fault in S_{a1} .

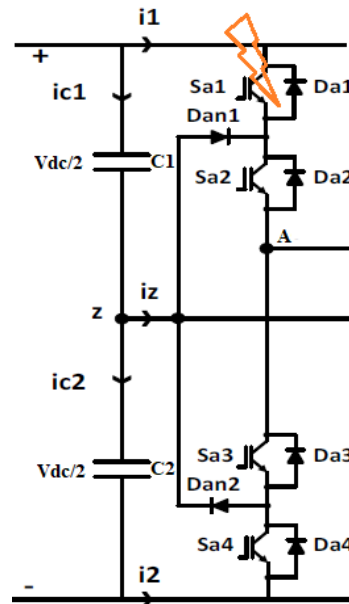


Fig. 2. A single leg of a 3-level NPC inverter

The OC fault is influences by raising the oscillations of the power signals and the deformity at the level of the stator-phase current with the increase of their amplitudes. In order to avoid these faults, which negatively affect the work of the power conversion system, we must put in place mechanisms to monitor and detect these faults in order to avoid any disaster that may arise. Among the detection techniques, we have presented in this work a technique based on the neural network, which has shown us a satisfactory performance.

Fault detection method. Diagnosis by neural networks (NN) is a computational model whose design is very schematically inspired by the functioning of real human neurons, so the principle is inspired by biological neurons, to identify faults in a system, the diagnosis carried out by NN must have an adequate number of examples of good functioning and defects to be able to learn them. During the training phase, the features are provided to the input network, and the output network receives the required diagnosis [31].

Firstly, we apply a Fourier analysis technique to the stator current properties presented in Fig. 3 in this model. After the neuron network processes, the data, the system monitors the phase angle and amplitude of the 3-phase stator currents (I_{sabc}), which will be the inputs to the NN; the semi-faulty driver is recognized and identified by the network. The selected features of each fault, which are specified in the tabular form of samples to be investigated, are used to extract features.

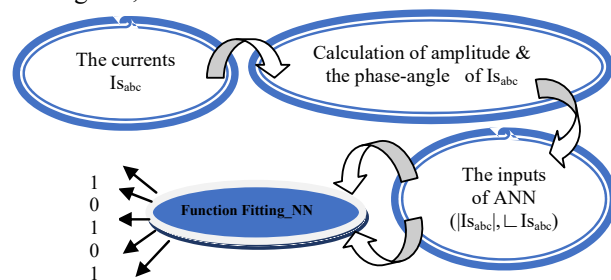


Fig. 3. The neuron network's structure

Simulation of system studies. In this work, for power conditioning in the WECS applications, various topologies of power converters have been suggested (Fig. 4). The multilevel converters, particularly the NPC topology, are widely utilized in the creation of high voltage and high power, wind power plants because of their benefits, which include the optimum waveform of the output voltage and a reduction in overall harmonic distortion.

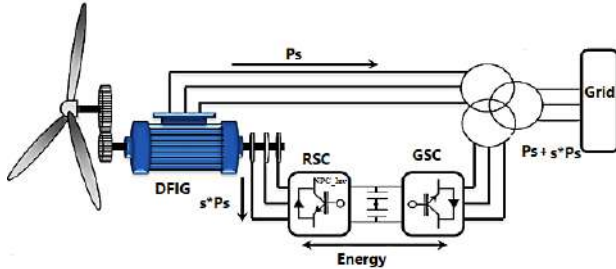


Fig. 4. Structure of the wind power conversion chain based on DFIG with NPC structure of RSC

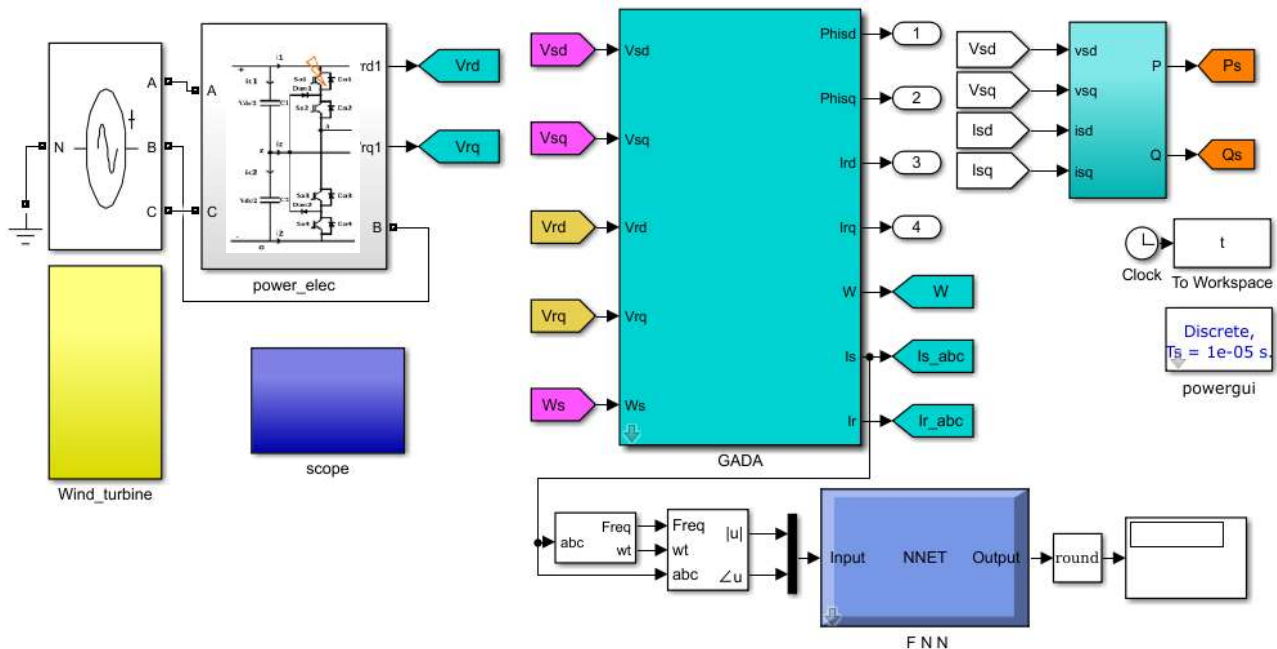


Fig. 5. Model Simulink of WECS and fault diagnosis using neural network

Tests of ANN. The NN achieved higher learning performance to discover the fault position in the circuit after numerous tests; Fig. 6,*a,b,c* shows the training performance, regression, and error histogram of the study. To achieve and assess the NN learning and training performance, we use the mean quadratic error (MQE).

The ANN in our case reached a value of $1.9656 \cdot 10^{-20}$. The goal error has been reached after just 470 of the 1000 training epochs of the training parameter, and the regression figure shows an acceptable regression (R equal to 1) among both network outputs and network targets.

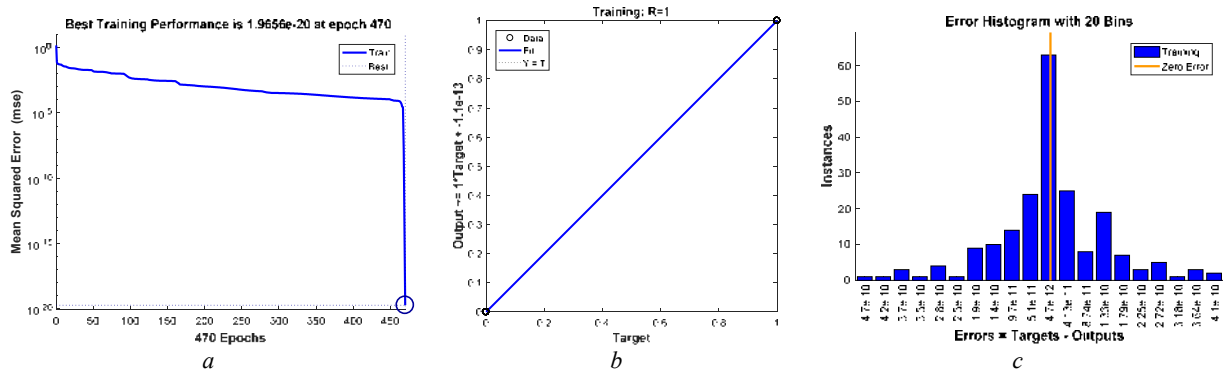


Fig. 6. *a* – Training performance plot for the classifier; *b* – NN-training regression and *c* – error histogram

Table 2

Neural network training data

Faulty switch	Training_data		Output code of neural network	Faulty switch	Training_data		Output code of neural network
	$ I_{abc} $	$\angle I_{abc}$			$ I_{abc} $	$\angle I_{abc}$	
Normal	22.26	-0.01744	000000000000	Sc1	45.52	-1.21	000100000000
Sa1	46	-0.3975	000000000001	Sc2	45.91	-1.106	001000000000
Sa2	47.46	1.233	000000000010	Sc3	51.17	23.51	010000000000
Sa3	47.05	2.59	000000000100	Sc4	47.93	0.3295	100000000000
Sa4	45.78	-0.2721	000000001000	Sa1 & Sa2	49.54	-1.683	000000000011
Sb1	45.69	0.3253	000000010000	Sa1 & Sb1	42.37	-0.2402	000000010001
Sb2	48.93	-0.9666	000000100000	Sa1 & Sc1	39.95	4.864	000100000001
Sb3	45.99	3.038	000001000000	Sa1 & Sb1 & Sc1	45.71	-0.02463	000100010001
Sb4	49.12	2.8	000010000000				

Checking the performance of the neural network.

We did tests for numerous sorts of operations, and the results are displayed in Fig. 7. Once the ANN was established and our learning had attained an acceptable level, we made tests for various types of operations.

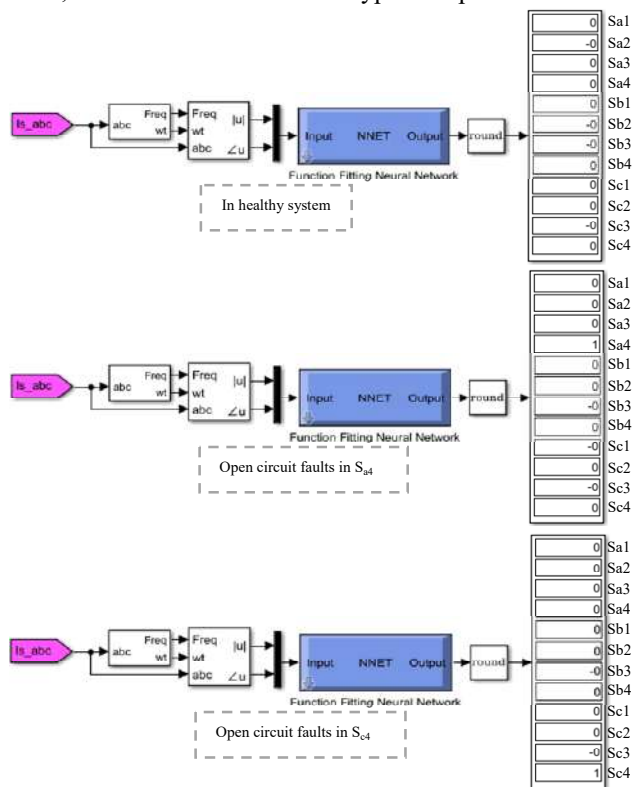


Fig. 7. ANN testing

Conclusion. This work proposes an open-switch fault detection approach for a rotor side converter with a neutral point clamped topology in a wind energy conversion system; where a neural network was used to obtain fault codes for open-circuit switches, the system was able of analyzing circuit faults when tested with two inputs, the first representing the current module and the second representing the phase shift. Simulation in a MATLAB environment was used to create open circuit failures in one or more insulated-gate bipolar transistors. The detection and diagnostic system monitor and records the module and argument values of these currents, which will be the neural network's inputs, after extracting the three-phase stator currents for healthy and fault-free functioning. After the neural network has trained and

processed this information, it recognizes and locates the malfunctioning insulated-gate bipolar transistors.

A 3-phase neutral point clamped inverter monitoring system is built using the stator current spectrum analysis technique paired with the artificial neural network. Where the suggested feature extraction is simple because it does not require any complexity, and we proved that the system's performance has vastly improved in terms of accurately detecting faults; where the mean squared error was approximately $1.9656 \cdot 10^{-20}$, and training regression was equal to 1 which indicates that the training performance of the network was good, which facilitated the rapid detection process. Therefore, the system is capable of identifying the various operating causes of neutral point clamped inverter (the healthy and the open-circuit faulty of insulated-gate bipolar transistors).

Conflict of interest. The authors declare that they have no conflicts of interest.

REFERENCES

- Liton H. *Control of a Multilevel Inverter for Wind Energy Conversion System with Energy Storage and Condition Monitoring Options*. Doctoral Thesis. Curtin University, April 2020. Available at: <http://hdl.handle.net/20.500.11937/81986> (accessed 16 May 2021).
- Blaabjerg F., Pecht M.M. Special Issue on Robust Design and Reliability of Power Electronics, *IEEE Transactions on Power Electronics*, May 2015. *IEEE Transactions on Power Electronics*, 2015, vol. 30, no. 5, pp. 2373-2374. doi: <https://doi.org/10.1109/TPEL.2014.2376271>.
- Choi U.-M., Blaabjerg F., Lee K.-B. Study and Handling Methods of Power IGBT Module Failures in Power Electronic Converter Systems. *IEEE Transactions on Power Electronics*, 2015, vol. 30, no. 5, pp. 2517-2533. doi: <https://doi.org/10.1109/TPEL.2014.2373390>.
- Kadum A.A. PWM control techniques for three phase three level inverter drives. *TELKOMNIKA (Telecommunication Computing Electronics and Control)*, 2020, vol. 18, no. 1, p. 519. doi: <https://doi.org/10.12928/telkomnika.v18i1.12440>.
- Hang C., Ying L., Shu N. Transistor open-circuit fault diagnosis in two-level three-phase inverter based on similarity measurement. *Microelectronics Reliability*, 2018, vol. 91, pp. 291-297. doi: <https://doi.org/10.1016/j.microrel.2018.10.009>.
- Ben Mahdhi H., Ben Azza H., Jemli M. Inverter open-circuit fault diagnosis method in PMSG based wind energy conversion system. *Electrical Engineering*, 2022, vol. 104, no. 3, pp. 1317-1330. doi: <https://doi.org/10.1007/s00202-021-01354-x>.
- Trabelsi M., Boussak M., Benbouzid M. Multiple criteria for high performance real-time diagnostic of single and multiple open-switch faults in ac-motor drives: Application to IGBT-based voltage source inverter. *Electric Power Systems Research*, 2017, vol. 144, pp. 136-149. doi: <https://doi.org/10.1016/j.epr.2016.11.021>.

8. Ben Mahdhi H., Ben Azza H., Jemli M. Experimental investigation of an open-switch fault diagnosis approach in the IGBT-based power converter connected to permanent magnet synchronous generator-DC system. *International Transactions on Electrical Energy Systems*, 2020, vol. 30, no. 8. doi: <https://doi.org/10.1002/2050-7038.12436>.
9. Cherif B.D.E., Bendiabdellah A., Bendjebbar M., Souad L. A Comparative Study on Some Fault Diagnosis Techniques in Three-Phase Inverter Fed Induction Motors. In (Ed.), *Fault Detection and Diagnosis. IntechOpen*. 2018. doi: <https://doi.org/10.5772/intechopen.79960>.
10. Asghar F., Talha M., Kim S.H. Neural Network Based Fault Detection and diagnosis system for a three-phase inverter in Variable Speed Drive with Induction Motor. *Journal of Control Science and Engineering*, 2016, pp. 1-12. doi: <https://doi.org/10.1155/2016/1286318>.
11. Abid M., Laribi S., Larbi M., Belabbas B., Sobh A.A. Fault detection and diagnosis system for a three-phase inverter using artificial neural network. *International Hazar Scientific Researches Conference – II*, 2021, vol. 1, pp. 725-734. Available at: <https://www.izdas.org/books> (accessed 16 May 2021).
12. Abid M., Laribi S.S., Al-asgar Z.S., Larbi M. Artificial Neural Network Approach Assessment of Short-Circuit Fault Detection in a Three Phase Inverter. *2021 International Congress of Advanced Technology and Engineering (ICOTEN)*, 2021, pp. 1-5. doi: <https://doi.org/10.1109/ICOTEN52080.2021.9493498>.
13. Ahmadi S., Poure P., Saadate S., Arab Khaburi D. Open-Switch and Open-Clamping Diode Fault Diagnosis for Single-Phase Five-Level Neutral-Point-Clamped Inverters. *IEEE Journal of Emerging and Selected Topics in Power Electronics*, 2021, vol. 9, no. 4, pp. 4676-4686. doi: <https://doi.org/10.1109/JESTPE.2020.3017923>.
14. Li C., Yang T., Kulsangcharoen P., Calzo G. Lo, Bozhko S., Gerada C., Wheeler P. A Modified Neutral Point Balancing Space Vector Modulation for Three-Level Neutral Point Clamped Converters in High-Speed Drives. *IEEE Transactions on Industrial Electronics*, 2019, vol. 66, no. 2, pp. 910-921. doi: <https://doi.org/10.1109/TIE.2018.2835372>.
15. Choi U.-M., Lee J.-S., Blaabjerg F., Lee K.-B. Open-Circuit Fault Diagnosis and Fault-Tolerant Control for a Grid-Connected NPC Inverter. *IEEE Transactions on Power Electronics*, 2015, pp. 1-1. doi: <https://doi.org/10.1109/TPEL.2015.2510224>.
16. Abari I., Lahouari A., Hamouda M., Slama J.B.H., Al-Haddad K. Fault Detection Methods for Three-Level NPC Inverter Based on DC-Bus Electromagnetic Signatures. *IEEE Transactions on Industrial Electronics*, 2018, vol. 65, no. 7, pp. 5224-5236. doi: <https://doi.org/10.1109/TIE.2017.2777378>.
17. Kou L., Liu C., Cai G., Zhou J., Yuan Q., Pang S. Fault diagnosis for open-circuit faults in NPC inverter based on knowledge-driven and data-driven approaches. *IET Power Electronics*, 2020, vol. 13, no. 6, pp. 1236-1245. doi: <https://doi.org/10.1049/iet-pel.2019.0835>.
18. Rothenhagen K., Fuchs F.W. Performance of diagnosis methods for IGBT open circuit faults in three phase voltage source inverters for AC variable speed drives. *2005 European Conference on Power Electronics and Applications*, 2005, art. no. 1665616. doi: <https://doi.org/10.1109/EPE.2005.219426>.
19. Sital-Dahone M., Saha A., Sozer Y., Mpanda A. Multiple device open circuit fault diagnosis for neutral-point-clamped inverters. *2017 IEEE Applied Power Electronics Conference and Exposition (APEC)*, 2017, pp. 2605-2609. doi: <https://doi.org/10.1109/APEC.2017.7931065>.
20. Selvakumar P., Muthukumaran G. Multiple Device Open Circuit Fault Diagnosis for Modified Neutral-Point-Clamped Inverters. *2022 4th International Conference on Smart Systems and Inventive Technology (ICSSIT)*, 2022, pp. 1275-1281. doi: <https://doi.org/10.1109/ICSSIT53264.2022.9716291>.
21. Rothenhagen K., Fuchs F.W. Performance of diagnosis methods for IGBT open circuit faults in voltage source active rectifiers. *2004 IEEE 35th Annual Power Electronics Specialists Conference (IEEE Cat. No.04CH37551)*, 2004, pp. 4348-4354. doi: <https://doi.org/10.1109/PESC.2004.1354769>.
22. Mendes A.M.S., Marques Cardoso A.J. Voltage source inverter fault diagnosis in variable speed AC drives, by the average current Park's vector approach. *IEEE International Electric Machines and Drives Conference. IEMDC'99. Proceedings (Cat. No.99EX272)*, 1999, pp. 704-706. doi: <https://doi.org/10.1109/IEMDC.1999.769220>.
23. Kim H.S., Jang M.J., Jang M.J., Lai N.B., Song J.H., Kim K.H. Open-switch fault detection and faulty switch identification of PWM inverter in PMSM drives using DOB based voltage information. *International Journal of Applied Engineering Research*, 2016, vol. 11, no. 2, pp. 1494-1502.
24. An Q.-T., Sun L.-Z., Zhao K., Sun L. Switching Function Model-Based Fast-Diagnostic Method of Open-Switch Faults in Inverters Without Sensors. *IEEE Transactions on Power Electronics*, 2011, vol. 26, no. 1, pp. 119-126. doi: <https://doi.org/10.1109/TPEL.2010.2052472>.
25. Abadi M.B., Mendes A.M.S., Cruz S.M.A. Method to diagnose open-circuit faults in active power switches and clamp-diodes of three-level neutral-point clamped inverters. *IET Electric Power Applications*, 2016, vol. 10, no. 7, pp. 623-632. doi: <https://doi.org/10.1049/iet-epa.2015.0644>.
26. Xu S., Wang J., Ma M. Open-circuit fault diagnosis method for three-level neutral point clamped inverter based on instantaneous frequency of phase current. *Energy Conversion and Economics*, 2020, vol. 1, no. 3, pp. 264-271. doi: <https://doi.org/10.1049/enc2.12021>.
27. Kim W., Kim S. ANN design of multiple open-switch fault diagnosis for three-phase PWM converters. *IET Power Electronics*, 2020, vol. 13, no. 19, pp. 4490-4497. doi: <https://doi.org/10.1049/iet-pel.2020.0795>.
28. Han P., He X., Ren H., Wang Y., Peng X., Shu Z., Gao S., Wang Y., Chen Z. Fault Diagnosis and System Reconfiguration Strategy of Single-phase Three Level Neutral-Point-Clamped Cascaded Inverter. *IEEE Transactions on Industry Applications*, 2019, vol. 55, no. 4, pp. 3863-3876. doi: <https://doi.org/10.1109/TIA.2019.2901359>.
29. Zhang X., Wu X., Geng C., Ping X., Chen S., Zhang H. An Improved Simplified PWM for Three-Level Neutral Point Clamped Inverter Based on Two-Level Common-Mode Voltage Reduction PWM. *IEEE Transactions on Power Electronics*, 2020, vol. 35, no. 10, pp. 11143-11154. doi: <https://doi.org/10.1109/TPEL.2020.2978724>.
30. Wu X., Tan G., Ye Z., Yao G., Liu Z., Liu G. Virtual-Space-Vector PWM for a Three-Level Neutral-Point-Clamped Inverter With Unbalanced DC-Links. *IEEE Transactions on Power Electronics*, 2018, vol. 33, no. 3, pp. 2630-2642. doi: <https://doi.org/10.1109/TPEL.2017.2692272>.
31. Frank P.M. Application of Fuzzy Logic to Process Supervision and Fault Diagnosis. *IFAC Proceedings Volumes*, 1994, vol. 27, no. 5, pp. 507-514. doi: [https://doi.org/10.1016/S1474-6670\(17\)48077-3](https://doi.org/10.1016/S1474-6670(17)48077-3).

Received 15.04.2022
Accepted 21.06.2022
Published 07.09.2022

Mimouna Abid¹, PhD Student,
Souad Laribi¹, Senior Lecturer,
M'hamed Larbi¹, Full Professor,
Tayeb Allaoui¹, Full Professor,

¹ Department of Electrical Engineering,

L2GEGI Laboratory, University of Tiaret, Algeria.

e-mail: mimouna.abid@univ-tiaret.dz (Corresponding Author),

souad.laribi@univ-tiaret.dz, larbi_mh@yahoo.fr,

tayeb.allaoui@univ-tiaret.dz

How to cite this article:

Abid M., Laribi S., Larbi M., Allaoui T. Diagnosis and localization of fault for a neutral point clamped inverter in wind energy conversion system using artificial neural network technique. *Electrical Engineering & Electromechanics*, 2022, no. 5, pp. 55-59. doi: <https://doi.org/10.20998/2074-272X.2022.5.09>

S. Muthubalaji, G. Devadasu, S. Srinivasan, N. Soundiraraj

Development and validation of enhanced fuzzy logic controller and boost converter topologies for a single phase grid system

Introduction. Solar photovoltaic system is one of the most essential and demanding renewable energy source in the current days, due to the benefits of high efficiency, reduced cost, no pollution, and environment friendly characteristics. Here, the maximum power point tracking controller has been implemented for obtaining an extreme power from the photovoltaic array. For this purpose, there are different controller and converter strategies have been deployed in the conventional works. It includes perturb and observation, incremental conductance, fuzzy logic systems, and hill climbing, and these techniques intend to extract the high amount of power from the solar systems under different climatic conditions. Still, it limits with the issues like increased design complexity, high cost consumption, high harmonics, and increased time consumption. **The goal** of this work is to deploy an improved controlling and converter topologies to regulate the output voltage and power fed to the single phase grid systems. **The novelty** of the work aims to develop an enhanced fuzzy logic controller based maximum power point tracking mechanism with the boost DC-DC converter topology for a single phase grid tied photovoltaic systems. **Practical value.** Also, the higher order harmonics suppression and unbalanced current elimination are handled by the use of LCL filtering technique, which efficiently reduces the harmonics in the output of inverter voltage and current. Moreover, it helps to obtain the reduced total harmonics distortion value with improved accuracy and efficiency. **Results.** There are different performance indicators have been evaluated for validating the proposed enhanced fuzzy logic controller–maximum power point tracking controlling technique. Moreover, the obtained results are compared with some of the conventional controlling algorithms for proving the betterment of the proposed work. References 30, tables 5, figures 7.

Key words: photovoltaic systems, boost DC-DC converter, enhanced fuzzy logic controller, maximum power point tracking, LCL filtering, pulse generation, single-phase grid system.

Вступ. Сонячна фотоелектрична система є одним з найбільш важливих та затребуваних відновлюваних джерел енергії в наші дні завдяки перевагам високої ефективності, низької вартості, відсутності забруднення та екологічно безпечним характеристикам. При цьому було реалізовано контролер стеження за точкою максимальної потужності для отримання екстремальної потужності від фотогальванічної батареї. З цією метою у традиційних роботах використовуються різні стратегії контролерів та перетворювачів. Це включає збурення та спостереження, інкрементну провідність, системи нечіткої логіки та сходження на пагорб, і ці методи призначені для отримання великої кількості енергії із сонячних систем у різних кліматичних умовах. Тим не менш, це обмежується такими проблемами, як підвищена складність конструкції, високі витрати, високі гармоніки та збільшення витрат часу. **Метою** цієї роботи є розвиток вдосконаленого управління та топології перетворювача для регулювання вихідної напруги та потужності, що подається до однофазних мережевих систем. **Новизна** роботи спрямована на розробку вдосконаленого механізму відстеження точки максимальної потужності на основі контролера з нечіткою логікою з топологією перетворювача постійного струму, що підвищує, для однофазних фотоелектричних систем, прив'язаних до мережі. **Практична цінність.** Крім того, придушення гармонік вищих порядків та усунення незбалансованого струму здійснюється за допомогою методу LCL-фільтрації, який ефективно зменшує гармоніку на виході інвертора напруги та струму. Крім того, це допомагає отримати зменшене значення повного гармонійного спотворення з покращеною точністю та ефективністю. **Результати.** Існують різні показники ефективності, які були оцінені для перевірки запропонованого покращеного контролера нечіткої логіки – методу керування відстеженням точки максимальної потужності. Крім того, отримані результати порівнюються з деякими звичайними алгоритмами контролю для доведення кращості запропонованої роботи. Бібл. 30, табл. 5, рис. 7.

Ключові слова: фотогальванічні системи, перетворювач постійного струму, що підвищує, удосконалений контролер з нечіткою логікою, відстеження точки максимальної потужності, LCL-фільтрація, генерація імпульсів, однофазні мережеві системи.

Introduction. Solar photovoltaic (PV) systems have gained a significant attention [1, 2] in the recent days due to their benefits of easy accessibility and availability. Also, it has been widely applied in various application sectors like residential, transportation, and construction. Typically, the PV systems [3] can produce the required amount of energy from solar for the grid connected systems with the help of appropriate methodologies and equipment. The important features of the solar PV systems are cost efficiency, pollution free, maintenance free, and high availability rate [4]. The major challenges that are associated with the grid integrated PV systems [5] can be categorized under the components of PV panel, power converters, and grid system. In which, the processes of optimization, voltage/current maintenance, and panel monitoring are need to be highly concentrated on the PV panel. Then, the efficiency, high reliability, temperature measurement, communication, monitoring and safety measures are need to be satisfied by the power converter topologies. Moreover, the power quality improvement, voltage level maintenance, and fault ride through capability are the dependable factors of the

converter and controller topologies, and these factors supports to obtain an improved system performance [6]. In the solar PV systems, the PV array can be categorized with respect to the solar irradiation and temperature measures. So, it required an operating point for extracting the maximum power from the PV array that is represented as an MPPT controller [7].

Then, it helps the PV arrays to obtain the maximum efficiency under varying climatic conditions. Generally, there are different types of maximum power point tracking (MPPT) controlling techniques have been utilized in the traditional works, which includes incremental conductance (IC) [8], fuzzy controller [9], perturb and observe (P&O) [10], and temperature gradient [11]. Also, various power converter design topologies have been utilized in the existing works [12] like buck converter, bi-directional converter, SEPIC converter, and Luo converter. But, these techniques limits with the issues like increased circuit design complexity, high cost consumption, reduced speed, and requires an accurate model. Moreover, harmonics elimination and current

© S. Muthubalaji, G. Devadasu, S. Srinivasan, N. Soundiraraj

balancing are also plays an important role in a single phase grid integrated PV systems [13, 14]. The filtering techniques can be used to suppress the level of harmonics for improving both efficiency and system stability [15, 16]. Thus, the proposed work focused on the development of an advanced controlling mechanism for a single phase tied PV systems. The major objectives behind the proposed work are as follows:

- to obtain the maximum power extraction from the PV panels, the functionalities of an enhanced fuzzy logic controller (EFLC) is incorporated with the MPPT controlling technique;
- to improve the operating efficiency of the entire grid system, the boost converter topology is utilized;
- to reduce the unbalanced current, and harmonics distortion, a higher order LCL filtering technique is employed.

Related works. This sector reviews some of the existing controlling techniques and converter topologies related to the solar PV power generation and extraction. Also, the working operations of the converter and controller topologies have been discussed with its own merits and demerits.

Podder, et al. [17] conducted an extensive review about the MPPT methods used for generating the power from solar PV systems. The different methods analyzed in this work were P&O, IC, and hill climbing (HC). Also, various types of DC-DC converter topologies such as buck, boost, bidirectional, CUK, flyback, SEPIC and Zeta were compared based on the measures of computation performance, input current, and output voltage. From this study, it was analyzed that the P&O was the most suitable MPPT technique for solar PV systems due to the benefits of simplicity and reduced cost consumption. Kumar, et al. [18] deployed a neural network based controlling technique for improving the performance of grid based solar PV systems. The key factor of this work was to obtain the maximum power extraction with increased utilization factor and efficiency by using the HC-MPPT mechanism. Still, this work failed to reduce the harmonics distortion for obtaining the better performance rate. Basha and Rani [2] analyzed the performance 5 different MPPT techniques such as HC-FLC (fuzzy logic controller), ANFIS (adaptive neuro-fuzzy inference system), PSO (particle swarm optimization), ACS (adaptive cuckoo search), and P&O for selecting the suitable technique to get an extreme power extraction from PV systems. Here, it was stated that the operating point estimation plays an essential role during MPP extraction, which could be more helpful to reduce both the operating and installation costs.

Venkatraman and John [19] intended to increase the performance of MPPT with the use of buck converter topology for PV charging system. Here, the P&O algorithm has been utilized to reduce the settling time, increase the bandwidth, and improve the tracking performance. From the paper, it was perceived that the P&O scheme offered the better results with minimum possible updation. Keyrouz [20] aimed to gain the maximum power obtainment from the solar PV systems under varying temperature and irradiation values. For this purpose, a machine learning technique, named as, Bayesian function has been utilized to obtain global MPP in a specified time. Moreover, the PID (proportional

integral derivative) controller was used to reduce the overshoot and rise time with high tracking efficiency. Priyadharshi, et al. [21] employed a hybrid Gravitational Search Algorithm (GSA) – PSO technique for improving the tracking performance of MPP. In this design, the CUK-SEPIC converter was adopted to reduce the ripple content and to obtain the optimum PV value. During optimization, the processes of fitness evaluation, global best solution estimation, and position updation have been performed. The major benefit of this work was, it has the ability to work under low sun isolation level with reduced cost consumption.

Basha and Rani [22] suggested high step-up boost converters for increasing the tracking efficiency of MPPT controlling technique. In this work, there were different MPPT techniques have been surveyed that includes variable step size P&O, fractional open circuit voltage (FOCV) and modified IC (MIC). Also, the working descriptions of these mechanisms have been described with its pros and cons. Hassan, et al. [23] recommended an FLC controller and push-pull converter for optimizing the output power of PV systems with increased gain value. The work focused on tracking the power from PV panels without any oscillations and noise with the help of FLC MPPT mechanism. From this work, the importance and benefits of using FLC mechanism in solar PV systems have been studied. Li, et al. [24] implemented the beta parameter based FLC mechanism for improving the performance of MPP in solar PV systems. Here, the number of fuzzy rules has been reduced for simplifying the process of membership function generation. Rezk, et al. [25] employed an adaptive FLC (AFLC) based controller topology for obtaining an improved efficiency of PV applications. This methodology was mainly deployed to attain an accurate and optimum tracking performance with reduced power fluctuations. The key advantages of this controller were faster convergence, high accuracy, and simplicity. Karafil, et al. [26] designed a high frequency resonant converter design with the pulse density modulation – MPPT mechanism for a single phase grid based PV systems. In this controlling algorithm, certain controlling pulses have been eliminated with respect to the command sequences without any deviation in the frequency value.

Sun, et al. [27] utilized an artificial neural network (ANN) based controlling strategy for an efficient power tracking from the PV array. The main scope of this work was to ensure the factors of reliability, safety, improved performance and controllability of a grid connected PV systems. Here, some of the major requirements that could be used for controlling the solar PV system have been discussed, which includes:

1. Exact tracking of MPP under varying irradiance and temperature measures.
2. Accurate locating of MPP.
3. Maintain the same MPP value under different climatic conditions.

Bhattacharya, et al. [28] applied an advanced controlling mechanism based on ANN algorithm for a grid connected PV systems. In this work, the conventional PI (proportional integral) controlling mechanism has been replaced with the functionality of ANN algorithm. Then,

it offered an improved system performance with improved dynamic response and reduced settling time. Rajput, et al. [29] suggested a second order filtering technique for increasing the power extraction of single phase grid associated PV systems. Here, a robust controlling mechanism with the boost converter topology has been implemented and validated under various power quality enhancement features. Gomes, et al. [30] implemented an LCL filtering technique for eliminating the harmonic distortions in the grid connected voltage source converters. Here, a detailed analysis about harmonics elimination, and clear illustration about the damping techniques were discussed.

From this study, the impact of different MPPT controlling mechanisms, converter designs, and filtering approaches were analyzed with its working definitions. Then, it will be more helpful for selecting the suitable approaches that are used for improving the overall performance of solar PV systems.

EFLC-MPPT based controlling strategy. In this segment, a clear description about the proposed EFLC based MPPT mechanism is presented for a single phase grid systems. The purpose of this paper is to extract the maximum amount of power from the solar PV systems under varying climatic conditions by implementing an advanced converter and controlling techniques. Here, the boost DC-DC converter has been utilized to increase the efficacy of overall system performance. In addition to that, the reactive power support and harmonics elimination are also concentrated to provide the reliable output for the single phase grid systems. For this purpose, the LCL filtering technique is employed to decrease the harmonics and unbalanced current in the grid systems. The block and schematic representations of the proposed EFLC-MPPT based controller design are presented in Fig. 1, 2 respectively, which comprises the following stages:

- power extraction using EFLC-MPPT;
- boost DC-DC converter design;
- LCL filtering.

The purpose of this work is to obtain the maximum amount of energy from the solar panels by implementing an advanced controlling and converter topologies. Normally, the performance of entire power generation system is highly depends on the controlling signals generated by the controller. Here, the switching pulses generated by the proposed EFLC-MPPT controlling mechanism are fed to boost converter for operating the switching components. When compared to the other controlling models reviewed in the literature, the proposed EFLC-MPPT integrated with boost topology could efficiently produces the regulated output voltage fed to single phase grid systems. Also, it suppresses the harmonic contents by regulating the output of PV panels with reduced loss of power.

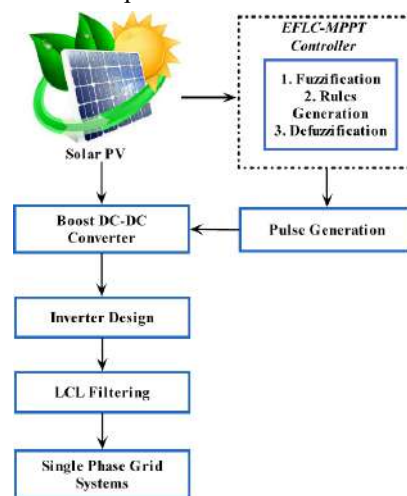


Fig. 1. Block representation of EFLC-MPPT based controller design

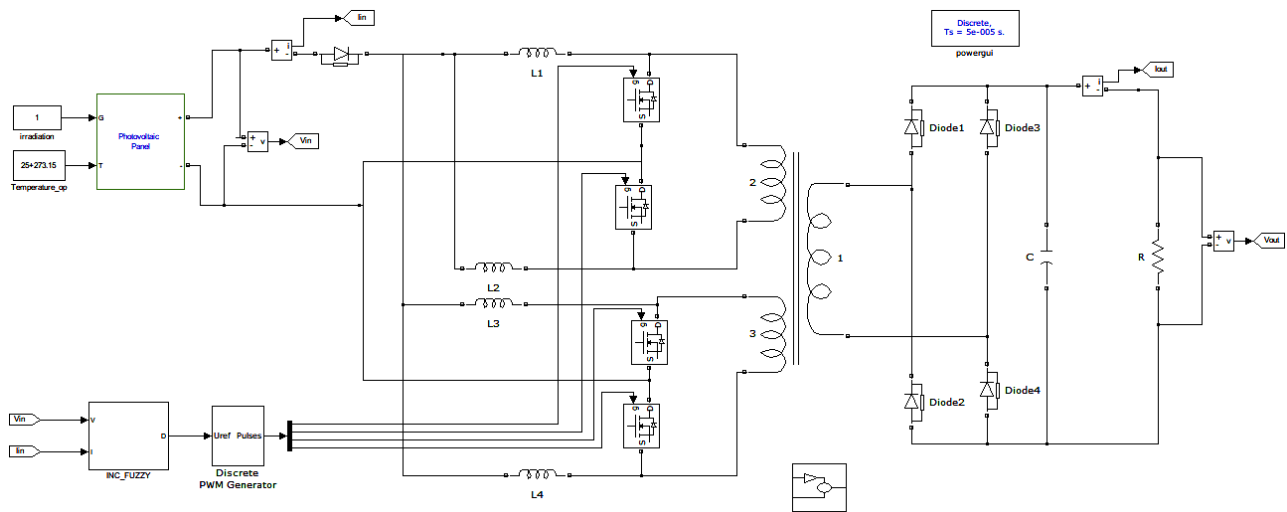


Fig. 2. Schematic representation of the EFLC-MPPT controller design

EFLC-MPPT based power extraction. At first, the maximum power tracking from the PV panel is performed by using the controlling technique. The essential part of the PV system is PV array, which is used to generate the required power from the solar. The MPPT controller has been used to increase the amount of power generation from PV array. Conventionally, there are different types of MPPT techniques are available for power extraction, in

which the FLC is one of the extensively used controlling mechanism due to the non-linear structure of the converter. Also, it could act as a controller that helps to obtain the requirements and specifications of the plants. In this work, an EFLC based MPPT mechanism is deployed for extracting the maximum power from the solar PV systems with increased static and dynamic performance. The typical illustration of the EFLC system

is depicted in Fig. 3, which comprises the following stages: fuzzification, inference rule generation, and defuzzification. During fuzzification, the set of inputs like temperature and irradiation are incorporated with the stored membership function, which can be assigned to each fuzzy input. Then, the rule evaluation process is performed with the help of linguistic rules, which is used to determine the control action with respect to the set of input values. From the rule evaluation, the fuzzy output can be obtained for each subsequent action. At last, the expected output variable is computed based on the isolation of the output fuzzy sets during defuzzification.

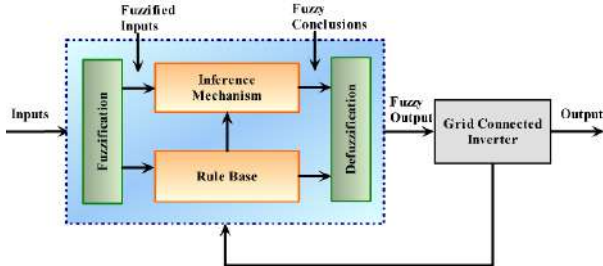


Fig. 3. Working strategy of fuzzy controller

Let consider the inputs as error (E_r) and change of error (CE_r), which are represented as follows:

$$E_r(x) = \frac{P_{PV}(x) - P_{PV}(x-1)}{V_{PV}(x) - V_{PV}(x-1)}; \quad (1)$$

$$CE_r(x) = E_r(x) - E_r(x-1); \quad (2)$$

where $P_{PV}(x)$ is the PV power; $V_{PV}(x)$ is the PV voltage; $P_{PV}(x-1)$ and $V_{PV}(x-1)$ are the previous power and voltage respectively.

Then, the rule generation process can be carried out based on the Mamdani model. Here, the 5 set of rules such Very Low (VL), Low (L), Very High (VH), High (H), and Medium (M) have been generated with respect to the error and change of error values as shown in Table 1.

Table 1

Fuzzy rules generation

$E_r \backslash CE_r$	VL	L	M	H	VH
VL	VH	VH	H	VL	VL
L	H	H	H	VL	L
M	H	H	N	L	L
H	H	H	L	L	VL
VH	H	H	L	L	VL

After inference rules generation, the defuzzification process can be applied to get the output that is denoted as the duty cycle D_c , which is represented as follows:

$$D_c = \frac{\sum_{i=1}^n \mu(D_{ci}) - D_{ci}}{\sum_{i=1}^n \mu(D_{ci})}; \quad (3)$$

Moreover, the key benefits of using ELFC-MPPT controller are as follows:

- it has the ability to handle an inaccurate input;
- it does not require any exact mathematical model;
- it has a non-linearity structure;
- it helps to obtain the maximum power output under different climatic conditions;
- it offers reduced complexity in design;
- it increased robustness.

The P-V and I-V characteristics of the proposed EFLC-MPPT controlling mechanism are depicted in Fig. 4, a, b. These characteristics can be used to validate the overall efficacy of the MPPT controlling technique. Based on the I-V and P-V characteristics analysis, it is evident that the EFLC-MPPT provides the better current and power values with respect to different voltage levels.

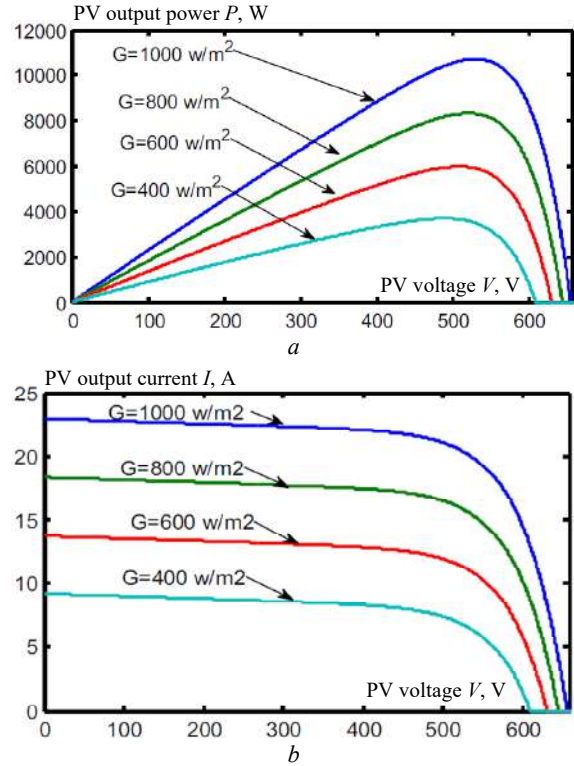


Fig. 4. P-V (a) and I-V (b) characteristics

Boost DC-DC converter design. Here, the boost DC-DC converter is placed between the PV panel and grid system for changing the output voltage with respect to the maximum power point. The corresponding circuit model of boost converter is represented in Fig. 5, which contains the components of input source voltage V_{in} , inductor L , diode D , switch Q , capacitor C , and output load. Based on the requirement of output, the switch can be either opened or closed, in which the output voltage is always greater than the value of input voltage source. The main factor of using this converter design is to increase the voltage level without use of transformer. Also, it offers an increased efficiency with the inclusion of single switching component.

The transfer function of the boost converter can be illustrated as follows:

$$V_o = D_c \cdot V_{PV}; \quad (4)$$

where V_o is the output voltage; D_c is the duty cycle of the control; V_{PV} is the output voltage of PV array.

Based on the Kirchhoff's voltage and current law, the relationship between the input and output of boost converter is illustrated as follows:

$$L \cdot \frac{dI_o}{dt} = V_{PV} - V_L; \quad (5)$$

$$C \cdot \frac{dV_{PV}}{dt} = I_o - V_L/R; \quad (6)$$

where R is the resistance; L is an inductor; I_o is the output DC-DC current.

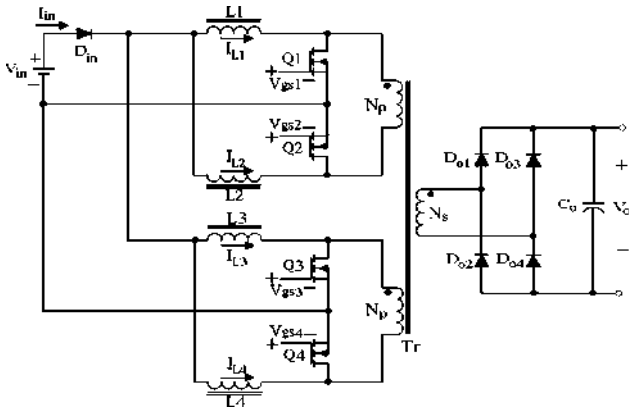


Fig. 5. Schematic representation of the circuit design

LCL filtering. The output of boost converter is given to the filtering unit for removing the harmonics and unbalanced current. Here, an LCL filtering technique is mainly deployed to protect the grid system from switching harmonics, and to obtain improved dynamic performance. Moreover, it offers better decoupling between the grid impedance and filtering with good ripple attenuation. The LCL filter can be composed based on the series connected $L_1 + R_1$, $L_2 + R_2$, and $C + R_c$ components, which helps to eliminate the injected harmonics on the grid. The mathematical model of LCL filtering technique can be illustrated as follows:

$$\begin{cases} L_1 \cdot \frac{di_1}{dt} + R_1 \cdot i_1 = x_i - x_c - R_c \cdot i_c; \\ L_2 \cdot \frac{di_g}{dt} + R_2 \cdot i_2 = x_c - x_g - R_c \cdot i_c; \\ C \cdot \frac{dx_c}{dt} = i_c; \\ i_1 = i_g + i_c. \end{cases} \quad (7)$$

Then, the resonant frequency is estimated as follows:

$$R_{fr} = \frac{1}{2\pi} \cdot \sqrt{\frac{L_1 + L_2}{L_1 \cdot L_2 \cdot C}}, \quad (8)$$

where R_{fr} is the resonant frequency of filter; L_1 , L_2 are the inductors; R_1 , R_2 are the resistors; C is the capacitor.

The key merits of using LCL filtering technique in this design are efficient total harmonics distortion (THD) elimination, high attenuation ability, and better system stability.

Results and discussion. The performance evaluation of the proposed EFCL-MPPT controlling mechanism is done in this sector with respect to different performance indicators. This controlling system has been designed by using the MATLAB/Simulink software, where the PV array under irradiance of 1000 W/m^2 and temperature of $25 \text{ }^\circ\text{C}$.

Simulation results. Figure 6 shows the output power (a), irradiance (b) and temperature (c) analysis with respect to varying time. In this simulation, the system is tested under different irradiance levels of 800 W/m^2 , 400 W/m^2 , and 1000 W/m^2 . This results shows that the proposed EFCL-MPPT technique efficiently tracks the maximum power of 200 W, 150 W, and 250 W respectively with the time of 5 ms.

Figure 7 shows the inverter output voltage (a) and current (b) after eliminating the harmonics by using the LCL filtering technique. To validate the output of inverter voltage and current, the THD is estimated for the proposed controlling mechanism.

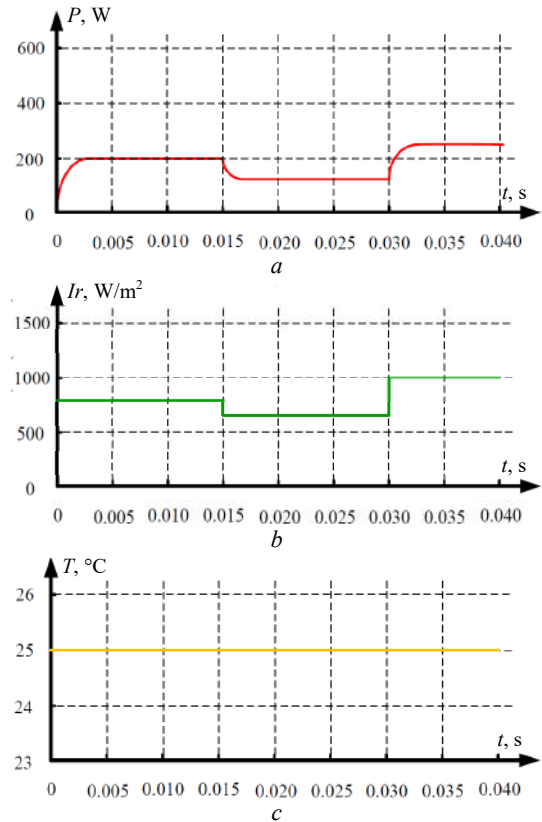


Fig. 6. Output power (a); irradiance (b); temperature (c)

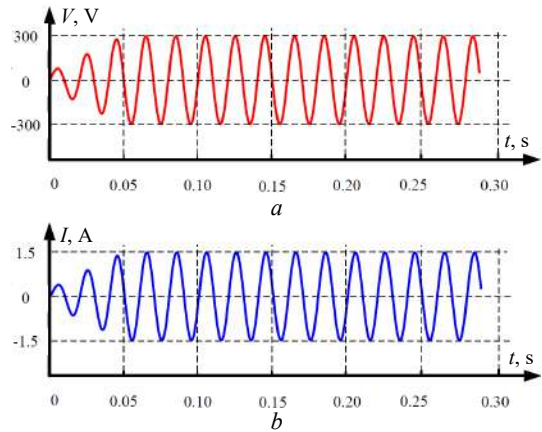


Fig. 7. Inverter output voltage (a) and current (b)

Comparative analysis. Generally, the efficiency of the filtering technique can be determined based on the analysis of THD. Table 2 depicts the THD analysis of existing and proposed techniques with respect to varying irradiance (W/m^2). In this work, an LCL filtering circuit is implemented in this design for suppressing the high order harmonics and unbalanced current in an efficient manner. Based on the result outcomes, it is evident that the proposed mechanism EFCL-MPPT with LCL filtering could efficiently reduce the THD value, when compared to the existing filtering technique.

Table 2

THD analysis			
Irradiation I_r , W/m^2	400	800	1000
Existing THD, %	1.72	1.95	2.14
Proposed THD, %	1.68	1.93	1.95

Table 3 compares the existing FLC, P&O and proposed EFCL-MPPT controlling techniques with

respect to the measures of input voltage V_{in} , input current I_{in} , input power P_{in} , output voltage V_o , output current I_o and output power P_o . Based on the comparative analysis, it is proved that the EFLC-MPPT could offer an improved results compared than the conventional techniques.

Table 3
Comparative analysis between existing and proposed controlling techniques

Topologies	V_{in} , V	I_{in} , A	P_{in} , W	V_o , V	I_o , A	P_o , W
Conventional FLC	12.08	1.03	12.44	24.6	0.485	11.93
Conventional P&O	8.5	2.5	21.25	31.30	0.622	19.3
EFLC-MPPT	12.08	2.932	59.94	35.42	2.785	166.9

Moreover, the proposed EFLC-MPPT technique could efficiently extract the maximum power from the solar PV systems by the use of boost converter and LCL filtering components. Also, it helps to obtain an improved performance rate of the single phase grid systems.

Table 4 shows the comparative analysis between the existing and proposed MPPT controlling techniques under varying irradiance measures such as 400 W/m², 800 W/m² and 1000 W/m². The measures that have been compared in this analysis are PV voltage V_{PV} , duty cycle D_c , output voltage V_o and output power P_o . When compared to the existing controlling techniques, the proposed EFLC-MPPT technique provides improved results for the varying irradiance measures.

Table 4

Comparative analysis between the existing and proposed MPPT mechanisms

MPPT method*	under 800 w/m ² (0 to 0.6 s)				under 400 w/m ² (0.6 to 1.2 s)					under 1000 w/m ² (1.2 to 1.8 s)				
	V_{PV} , V	D_c	V_o , V	P_o , W	V_{PV} , V	D_c	V_o , V	P_o , W	V_{PV} , V	V_{PV} , V	D_c	V_o , V	P_o , W	V_{PV} , V
VSS-P&O	34.0	0.604	86.0	148.44	17.0	0.711	59.0	77.0	17.0	38	0.59	94	196.31	38
MIC	34.3	0.601	86.1	150.7	17.5	0.7	59.6	77.8	17.5	39.2	0.58	95.31	197.48	39.2
FOCV	33.8	0.62	89	155	17.0	0.715	59.8	78.0	17.0	39.28	0.59	96	197.5	39.28
FSS-RBFA	33.0	0.627	87.0	155.76	17.4	0.719	62	79.53	17.4	40.1	0.586	96.8	198.78	40.1
VSS-RBFA	34.2	0.609	87.5	156.5	18.5	0.72	66.4	79.6	18.5	39.8	0.6	100.5	200.2	39.8
AFLC	34.8	0.614	90.32	158.2	24.0	0.64	68.0	80.0	24.0	45.3	0.56	105	201.8	45.3
PSO	34.71	0.622	92.0	158.5	24.8	0.66	73.7	82.0	24.8	47.07	0.64	132	204.40	47.07
CS	37.27	0.59	93.17	161.73	25.76	0.65	73.89	82.2	25.76	47.54	0.65	138	205.18	47.54
Proposed EFLC-MPPT	39.28	0.55	94.23	162.35	26.2	0.59	74.2	83.5	26.2	48.20	0.62	139	206.25	48.20

*VSS-P&O – variable step size- perturb and observe; MIC – modified incremental conductance; FOCV – fractional open circuit voltage; FSS-RBFA – fixed step size-radial basis function algorithm; VSS-RBFA – variable step size-radial basis function algorithm; AFLC – adaptive fuzzy logic controller; PSO – particle swarm optimization; CS – cuckoo search; EFLC-MPPT – enhanced fuzzy logic controller-maximum power point tracking.

Table 5 depicts the tracking time of the existing P&O and IC, and proposed MPPT controlling mechanisms. Typically, the tracking time is one of the important measures to validate the tracking efficiency of the controlling technique. Moreover, it is defined as how much amount of time that the controller could take for tracking the maximum power point from the PV panel. From the results, it is evident that the proposed EFLC-MPPT provides the reduced tracking time of 5 ms, when compared to the other controlling techniques.

Table 5
Tracking time of existing and proposed MPPT techniques

MPPT mechanisms	Tracking time, s
P&O	0.3
IC	0.25
Proposed EFLC-MPPT	0.005

Conclusions. A new enhanced fuzzy logic controller integrated with boost converter topology design is implemented in this paper for obtaining an extreme power extraction from the solar panels. Here, the boost DC-DC converter is mainly used to increase the voltage level without use of transformer. Also, the proposed controlling topology intends to extract the power under varying climatic conditions with increased accuracy. In addition to that, an LCL filtering circuit is employed in the proposed design for suppressing the harmonics and unbalanced current in the inverter output. The major benefits of the proposed design are, it has the ability to handle an inaccurate input and does not require any exact mathematical model for controlling. During performance evaluation, the controlling technique could be tested under different irradiance values of 400 W/m², 800 W/m², and 1000 W/m². Moreover, some of the traditional controlling techniques are compared with the proposed controlling mechanism based on the measures of harmonic distortions, tracing time, PV output power, voltage, and current. Based on

the comparative analysis, it is studied that the proposed controlling technique offers an improved performance results compared than the conventional techniques.

In future, this work can be extended by implementing an optimization based controlling mechanism for a single-phase grid system.

Conflict of interest. The authors declare that they have no conflicts of interest.

REFERENCES

1. Khanam N., Khan B.H., Imtiaz T. Maximum Power Extraction of Solar PV System using Meta-Heuristic MPPT techniques: A Comparative Study. *2019 International Conference on Electrical, Electronics and Computer Engineering (UPCON)*, 2019, pp. 1-6. doi: <https://doi.org/10.1109/UPCON47278.2019.8980060>.
2. Hussaian Basha C.H., Rani C. Performance Analysis of MPPT Techniques for Dynamic Irradiation Condition of Solar PV. *International Journal of Fuzzy Systems*, 2020, vol. 22, no. 8, pp. 2577-2598. doi: <https://doi.org/10.1007/s40815-020-00974-y>.
3. Dhanalakshmi B., Rajasekar N. A novel Competence Square based PV array reconfiguration technique for solar PV maximum power extraction. *Energy Conversion and Management*, 2018, vol. 174, pp. 897-912. doi: <https://doi.org/10.1016/j.enconman.2018.08.077>.
4. Babu T.S., Ram J.P., Dragicevic T., Miyatake M., Blaabjerg F., Rajasekar N. Particle Swarm Optimization Based Solar PV Array Reconfiguration of the Maximum Power Extraction Under Partial Shading Conditions. *IEEE Transactions on Sustainable Energy*, 2018, vol. 9, no. 1, pp. 74-85. doi: <https://doi.org/10.1109/TSSTE.2017.2714905>.
5. Kumar R., Sahu B., Shiva C.K., Rajender B. A control topology for frequency regulation capability in a grid integrated PV system. *Archives of Electrical Engineering*, 2020, vol. 69, no. 2, pp. 389-401. doi: <https://doi.org/10.24425/aece.2020.133033>.
6. Priyadarshi N., Padmanaban S., Holm-Nielsen J.B., Blaabjerg F., Bhaskar M.S. An Experimental Estimation of Hybrid ANFIS-PSO-Based MPPT for PV Grid Integration Under Fluctuating Sun

- Irradiance. *IEEE Systems Journal*, 2020, vol. 14, no. 1, pp. 1218-1229. doi: <https://doi.org/10.1109/JSYST.2019.2949083>.
7. Elmelegi A., Aly M., Ahmed E.M., Alharbi A.G. A simplified phase-shift PWM-based feedforward distributed MPPT method for grid-connected cascaded PV inverters. *Solar Energy*, 2019, vol. 187, pp. 1-12. doi: <https://doi.org/10.1016/j.solener.2019.05.021>.
 8. Necaibia S., Kelaiaia M.S., Labar H., Necaibia A., Castronuovo E.D. Enhanced auto-scaling incremental conductance MPPT method, implemented on low-cost microcontroller and SEPIC converter. *Solar Energy*, 2019, vol. 180, pp. 152-168. doi: <https://doi.org/10.1016/j.solener.2019.01.028>.
 9. Samal S., Barik P.K., Sahu S.K. Extraction of maximum power from a solar PV system using fuzzy controller based MPPT technique. *2018 Technologies for Smart-City Energy Security and Power (ICSESP)*, 2018, pp. 1-6. doi: <https://doi.org/10.1109/ICSESP.2018.8376721>.
 10. Satif A., Hlou L., Benbrahim M., Erguig H., Elgouri R. Simulation and analysis of a PV system with P and O MPPT algorithm using a PI controller for Buck converter. *ARNP Journal of Engineering and Applied Sciences*, 2018, vol. 13, no. 9, pp. 3014-3022. Available at: http://www.arnpjournals.org/jeas/research_papers/rp_2018/jeas_0518_7027.pdf (accessed 20 May 2021).
 11. Belkaid A., Colak I., Kayisli K., Bayindir R., Bulbul H.I. Maximum Power Extraction from a Photovoltaic Panel and a Thermoelectric Generator Constituting a Hybrid Electrical Generation System. *2018 International Conference on Smart Grid (ICSmartGrid)*, 2018, pp. 276-282. doi: <https://doi.org/10.1109/ISGWCP.2018.8634534>.
 12. Vanajaa V.R., Kathirvel C. DC-DC converter topology with maximum power point tracking strategies for renewable energy systems – A survey. *2017 Innovations in Power and Advanced Computing Technologies (i-PACT)*, 2017, pp. 1-5. doi: <https://doi.org/10.1109/IPACT.2017.8244941>.
 13. Singh Y., Hussain I., Singh B., Mishra S. Single-Phase Single-Stage Grid Tied Solar PV System with Active Power Filtering Using Power Balance Theory. *Journal of The Institution of Engineers (India): Series B*, 2018, vol. 99, no. 3, pp. 301-311. doi: <https://doi.org/10.1007/s40031-018-0326-8>.
 14. Singh D., Singh H. Technical Survey and review on MPPT techniques to attain Maximum Power of Photovoltaic system. *2019 5th International Conference on Signal Processing, Computing and Control (ISPCC)*, 2019, pp. 265-268. doi: <https://doi.org/10.1109/ISPCC48220.2019.8988382>.
 15. Ehtesham M., Jamil M. Enhancement of Power Quality Using Active Power Filter for PV Systems with Model Based MPPT. *2017 14th IEEE India Council International Conference (INDICON)*, 2017, pp. 1-6. doi: <https://doi.org/10.1109/INDICON.2017.8487544>.
 16. Babu Y.R., Srivasa R.R., Linga Reddy P. Shunt Active Power Filter connected to MPPT based photovoltaic Array for PQ enhancement. *International Journal of Pure and Applied Mathematics*, 2017, vol. 114, no. 9, pp. 389-398. Available at: <https://acadpubl.eu/jsi/2017-114-7-ICPCIT-2017/articles/9/35.pdf> (accessed 20 May 2021).
 17. Podder A.K., Roy N.K., Pota H.R. MPPT methods for solar PV systems: a critical review based on tracking nature. *IET Renewable Power Generation*, 2019, vol. 13, no. 10, pp. 1615-1632. doi: <https://doi.org/10.1049/iet-rpg.2018.5946>.
 18. Kumar N., Singh B., Panigrahi B.K. PNKLMF-Based Neural Network Control and Learning-Based HC MPPT Technique for Multiobjective Grid Integrated Solar PV Based Distributed Generating System. *IEEE Transactions on Industrial Informatics*, 2019, vol. 15, no. 6, pp. 3732-3742. doi: <https://doi.org/10.1109/TII.2019.2901516>.
 19. Venkatramanan D., John V. Dynamic Modeling and Analysis of Buck Converter Based Solar PV Charge Controller for Improved MPPT Performance. *IEEE Transactions on Industry Applications*, 2019, vol. 55, no. 6, pp. 6234-6246. doi: <https://doi.org/10.1109/TIA.2019.2937856>.
 20. Keyrouz F. Enhanced Bayesian Based MPPT Controller for PV Systems. *IEEE Power and Energy Technology Systems Journal*, 2018, vol. 5, no. 1, pp. 11-17. doi: <https://doi.org/10.1109/JPETS.2018.2811708>.
 21. Priyadarshi N., Bhaskar M.S., Padmanaban S., Blaabjerg F., Azam F. New CUK-SEPIC converter based photovoltaic power system with hybrid GSA-PSO algorithm employing MPPT for water pumping applications. *IET Power Electronics*, 2020, vol. 13, no. 13, pp. 2824-2830. doi: <https://doi.org/10.1049/iet-pel.2019.1154>.
 22. Basha C.H., Rani C. Different Conventional and Soft Computing MPPT Techniques for Solar PV Systems with High Step-Up Boost Converters: A Comprehensive Analysis. *Energies*, 2020, vol. 13, no. 2, p. 371. doi: <https://doi.org/10.3390/en13020371>.
 23. Hassan T., Abbassi R., Jerbi H., Mehmood K., Tahir M.F., Cheema K.M., Elavarasan R.M., Ali F., Khan I.A. A Novel Algorithm for MPPT of an Isolated PV System Using Push Pull Converter with Fuzzy Logic Controller. *Energies*, 2020, vol. 13, no. 15, p. 4007. doi: <https://doi.org/10.3390/en13154007>.
 24. Li X., Wen H., Hu Y., Jiang L. A novel beta parameter based fuzzy-logic controller for photovoltaic MPPT application. *Renewable Energy*, 2019, vol. 130, pp. 416-427. doi: <https://doi.org/10.1016/j.renene.2018.06.071>.
 25. Rezk H., Aly M., Al-Dhaifallah M., Shoyama M. Design and Hardware Implementation of New Adaptive Fuzzy Logic-Based MPPT Control Method for Photovoltaic Applications. *IEEE Access*, 2019, vol. 7, pp. 106427-106438. doi: <https://doi.org/10.1109/ACCESS.2019.2932694>.
 26. Karafil A., Ozbay H., Oncu S. Design and Analysis of Single-Phase Grid-Tied Inverter With PDM MPPT-Controlled Converter. *IEEE Transactions on Power Electronics*, 2020, vol. 35, no. 5, pp. 4756-4766. doi: <https://doi.org/10.1109/TPEL.2019.2944617>.
 27. Sun Y., Li S., Lin B., Fu X., Ramezani M., Jaithwa I. Artificial Neural Network for Control and Grid Integration of Residential Solar Photovoltaic Systems. *IEEE Transactions on Sustainable Energy*, 2017, vol. 8, no. 4, pp. 1484-1495. doi: <https://doi.org/10.1109/TSTE.2017.2691669>.
 28. Bhattacharyya S., Singh B., Chandra A., Al-Haddad K. Artificial Neural Network Based Advanced Current Control for Grid-Tied Photovoltaic System. *2019 National Power Electronics Conference (NPEC)*, 2019, pp. 1-6. doi: <https://doi.org/10.1109/NPEC47332.2019.9034761>.
 29. Rajput A., Beniwal N., Singh B., Mishra S. Second-order sequence filter based control algorithm for single-phase grid interfaced solar PV system. *IET Generation, Transmission & Distribution*, 2019, vol. 13, no. 12, pp. 2382-2390. doi: <https://doi.org/10.1049/iet-gtd.2018.6560>.
 30. Gomes C.C., Cupertino A.F., Pereira H.A. Damping techniques for grid-connected voltage source converters based on LCL filter: An overview. *Renewable and Sustainable Energy Reviews*, 2018, vol. 81, pp. 116-135. doi: <https://doi.org/10.1016/j.rser.2017.07.050>.

Received 28.03.2022

Accepted 29.06.2022

Published 07.09.2022

Muthubalaji Sankaramoorthy¹, Professor,
 Devadasu Ghanta¹, Professor,
 Srinivasan Sundararajan¹, Associate Professor,
 Soundiraraj Nallasamy², Assistant Professor,
¹ Department of Electrical & Electronics Engineering,
 CMR College of Engineering & Technology,
 Hyderabad, Telangana, 501401, India,
 e-mail: muthusa15@gmail.com (Corresponding Author),
 gdevadas10@gmail.com; s.srinivasan2906@gmail.com
² Department of Electronics and Communication Engineering,
 PSNA College of Engineering and Technology,
 Dindigul, Tamil Nadu, 624622, India
 e-mail: soundar@psnacet.edu.in

How to cite this article:

Muthubalaji S., Devadasu G., Srinivasan S., Soundiraraj N. Development and validation of enhanced fuzzy logic controller and boost converter topologies for a single phase grid system. *Electrical Engineering & Electromechanics*, 2022, no. 5, pp. 60-66. doi: <https://doi.org/10.20998/2074-272X.2022.5.10>

Solar flat plate collector enhanced by two reflectors: optimum tilts of reflectors

Introduction. In some solar concentrating system applications, in which the incoming sunlight is augmented by using commercial flat plate reflectors placed on different sides of the planar collector, it is very important to choose the optimum tilts of boosters (attached edge-to-edge on the top and bottom sides of the solar collector) for each month, to enhance their received solar irradiation over the year in the southern Algeria. The **novelty** of the proposed work consists of the development of a novel mathematical model in which the reference of the reflector's tilt angles is the collector plane, and optimal tilts are optimized on the average day of each month. **Purpose.** This paper proposes a novel analytical model of two identical planer reflectors, placed on the top and bottom of a latitude tilted flat plate solar collector, for optimizing their optimal inclination angles during the daytime throughout the year in Ouargla city, southeast of Algeria. **Methods.** Optimal tilt angles of reflectors were obtained by searching for the optimum captured solar irradiation on the collector's surface from each reflector in the representative day of each month of the year. After that, the obtained tilts were used for calculating incoming solar irradiation on the received area and comparing them to the solar collector without reflectors. **Results.** The findings of this paper showed that the reflector's inclination angles were variable from one month to another in which the upper reflector's tilts reached its maximum in June and minimum in December, contrarily for the lower reflector. Again, an increase of 28.05 % in the daily received solar irradiation on the collector surface with reflectors compared to the conventional one. References 17, table 1, figures 4.

Key words: booster reflectors, flat plate collector, optimum tilts, solar irradiation.

Вступ. У деяких сонячних концентруючих системах, в яких сонячне світло, що падає, посилюється за рахунок використання комерційних плоских відбивачів, розміщених по різні сторони плоского колектора, дуже важливо вибрати оптимальні нахили підсилювачів (прикріплених кромкою до кромки зверху), і нижні сторони сонячного колектора для кожного місяця, щоб збільшити одержуване ними сонячне випромінювання протягом року в південному Алжирі. **Новизна** запропонованої роботи полягає у розробці нової математичної моделі, в якій еталоном кутів нахилу рефлектора є площина колектора, а оптимальні нахили оптимізуються у середній день кожного місяця. **Мета.** У цій статті пропонується нова аналітична модель двох ідентичних плоских відбивачів, розміщених зверху та знизу плоского сонячного колектора з нахилом по широті, для оптимізації їх оптимальних кутів нахилу вдень протягом року у місті Уаргла, на південний схід від Алжиру. **Методи.** Оптимальні кути нахилу рефлекторів були отримані шляхом пошуку оптимального сонячного випромінювання на поверхню колектора від кожного рефлектора в репрезентативні дні кожного місяця року. Після цього отримані нахили використовувалися для розрахунку сонячної радіації на отриману площу і порівняння їх з сонячним колектором без відбивачів. **Результати** цієї статті показали, що кути нахилу рефлектора змінювалися від місяця до місяця, коли нахил верхнього рефлектора досягав максимуму в червні і мінімуму в грудні, на відміну від нижнього рефлектора. Знову ж таки, збільшення на 28,05 % щоденно одержуваного сонячного випромінювання на поверхню колектора з відбивачами порівняно зі звичайним. Бібл. 17, табл. 1, рис. 4.

Ключові слова: підсилювачі відбивачі, плоский колектор, оптимальні нахили, сонячне випромінювання.

Introduction. In recent years, the use of solar energy has become persistent all over the world, which has attached significant efforts. So, for the no-tracking flat plate solar collector, augmenting solar-gain using booster reflectors is a key area of interest in the context of reducing the cost factor of the system. Moreover, it is an economical solution for enhancing the output of solar collectors, which is strongly influenced by the amount of received solar irradiation [1-4]. For that, many reports about the effect of adding multi-reflectors on different sides of a flat plate solar collector on the received solar irradiation have been presented. Garg et al. [5] studied the maximization of the solar energy received by the collector attached to two mirrors at their top and bottom sides. Bhowmik et al. [6] examined two mirrors on the right and left sides of the solar collector and their effects on the power output of the whole system. They obtained that the average energy yield was about 10-19.84 % in the summer period and 10-13.23 % in the winter. Huang et al. [7] experimented with the effect of top-bottom side mirrors on photovoltaic panel power output. They found that the PV power generation was increased by about 23 % compared to the panel without mirrors. Bahaidarah et al. [8] investigated the performance of the V-trough PV system. They obtained that the power output was enhanced by 34.6 % on March 13th and by 37 % on September 16th. Baig et al. [9] analyzed and experimented

with the seasonally tracked V-Trough PV/T system in India. They observed an average augmentation of 35 % in the electrical power output from the V-Trough PV/T system as compared to the conventional one. Kostić et al. [10] examined the influence of the position of reflectors made of aluminum sheet on the thermal efficiency of a solar thermal collector. They have found that the reflectors made of aluminum sheet have a positive effect on the thermal efficiency of the PV/T system. An energy gain of about 35-44 % has been attained in this study [10]. Rahman et al. [11] examined the performance enhancement of a PV solar system by mirror reflection. They achieved an average increase of around 25 % in short-circuit current, as high as the sun tracking, can be obtained. Bione et al. [12] compared the performance of PV water pumping systems driven by fixed, tracking, and V-Trough generators. They realized a cost reduction of 19 % for the tracking system and a reduction of 48 % for the concentrating system compared to the static configuration. Tabet et al. [13] optimized tilts of reflectors placed in left-right sides of PV/T collector. They obtained an increase of about 23 % in received solar irradiation on the collector's surface by using reflectors compared to the conventional one.

Those boosters must be tilted at their optimal inclination angle to capture more incoming sunlight

during the whole year, which is the **aim of this paper**, where an optimization tilt of two flat plate reflectors, placed on the top-bottom sides of a fixed solar collector in the southeast of Algeria [14], will be exposed.

2. Method.

2.1. Description of the system. In order to enhance incoming sunlight, the south-oriented solar collector with a tilt angle equal to the latitude of the Ouargla region ($\beta = 31^\circ 57' N$ fixed over the year) in the southeast of Algeria, is attached to two identical reflectors (on the top side tilted at α_1 from collector plane and on the bottom side inclined at α_2 from collector plane as illustrated in Fig. 1), which have the same dimensions as the solar collector, for constructing a V-Trough concentrator.

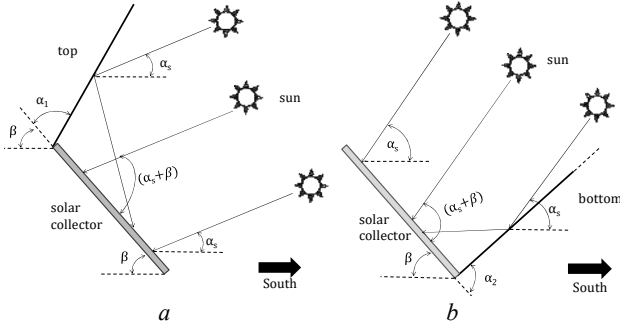


Fig. 1. Schematic diagram of the solar collector with: (a) top and (b) bottom reflectors

2.2. Mathematical model. The total received solar irradiation by the collector surface $I_{tot,col}$ is estimated using Capderou's model [15], and is equal to the sum of solar irradiation on its surface without reflectors $I_{net,col}$ ($I_{net,col}$ is equal to the sum of the direct solar irradiation $I_{dir,col}$, solar irradiation diffused from the sky $I_{sky,col}$, and the reflected solar irradiation from the ground $I_{gr,col}$) and the sum of the reflected solar irradiation from the top reflector $I_{refl,1}$ and the bottom one $I_{refl,2}$, which are calculated by using the following expressions:

$$I_{tot,col} = I_{net,col} + I_{refl,col}, \quad (1)$$

$$I_{net,col} = I_{dir,col} + I_{sky,col} + I_{gr,col}, \quad (2)$$

$$I_{dir,col} = I_{dir,h} \cdot \cos(\theta), \quad (3)$$

where $I_{dir,h}$ is the direct solar irradiation on a horizontal plane and θ is the angle of incidence of the beam irradiation.

The α_s and δ_s are the sun's altitude and declination angles, which can be calculated using the expressions [16]:

$$\alpha_s = \arcsin[\cos(\delta_s) \cdot \cos(\omega_s) \cdot \cos(\phi) + \sin(\delta_s) \cdot \sin(\phi)], \quad (4)$$

$$\delta_s = 23.45 \cdot \sin[(360 \cdot (N_j - 121)) / 365], \quad (5)$$

where ω_s is the hour angle of the sun; ϕ is the longitude of the localization; N_j is day of the year.

The sun's azimuth angle γ_s can be found using [16]:

$$\gamma_s = \arcsin[(\cos(\delta_s) \cdot \cos(\omega_s)) / \cos(\alpha_s)], \quad (6)$$

where $I_{refl,col}$ is the sum of the reflected solar irradiation from 2 reflectors and given by:

$$I_{refl,col} = I_{refl,1} + I_{refl,2}, \quad (7)$$

$$I_{refl,1} = \rho \cdot I_{dir,h} \cdot \sin(2 \cdot \alpha_1 + \alpha_s + \beta - 180^\circ) \cdot \sin(180^\circ - (\alpha_s + \alpha_1 + \beta)), \quad (8)$$

$$I_{refl,2} = \rho \cdot I_{dir,h} \cdot \sin(2 \cdot \alpha_2 - \alpha_s - \beta) \cdot \sin(\alpha_s - \alpha_2 + \beta), \quad (9)$$

where ρ is the reflector's reflectance.

The solar irradiation diffused from the sky $I_{sky,col}$ and the reflected solar irradiation from the ground $I_{gr,col}$ are given by:

$$I_{sky,col} = I_{dir,h} \cdot (1 + \cos(\beta)) / 2, \quad (10)$$

$$I_{gr,col} = \rho_{gr} \cdot I_{dir,h} \cdot (1 - \cos(\beta)) / 2, \quad (11)$$

where $I_{dir,h}$ is the diffuse solar irradiation on a horizontal plane; $I_{tot,h}$ is the global solar irradiation on a horizontal plane; ρ_{gr} is the reflectance of the ground.

2.3. Simulation procedure. The previous equations have been implemented in a MATLAB program. $I_{refl,i}$ ($i = 1$ and 2) have been measured for different values of α_i ($i = 1$ and 2) varied from 0° to 90° in each perfect day of the month (Table 1). The optimal tilt angles of reflectors $\alpha_{opt,i}$ ($i = 1$ and 2), corresponds to the optimum of $I_{refl,i}$ ($i = 1$ and 2) over the perfect day of each month. This procedure has been repeated for all average days of months [17].

3. Results and discussion. The optimal inclination angles of reflectors $\alpha_{opt,i}$ ($i = 1$ and 2) are achieved by searching the maximum of the reflected solar irradiation from each booster alone $I_{refl,i}$ ($i = 1$ and 2) described in (8) and (9), for the average day of each month (Table 1).

Table 1

Average days of months [17]	
Date	Perfect Day Number
17 January	17
16 February	47
16 March	75
15 April	105
15 May	135
11 June	162
16 July	198
16 August	228
15 September	258
15 October	288
14 November	318
10 December	344

Figure 2 shows the variation of the reflected solar irradiation from each reflector on the solar collector surface in the average day of December (December 10th), as a function of local time and angles α_i ($i = 1$ and 2).

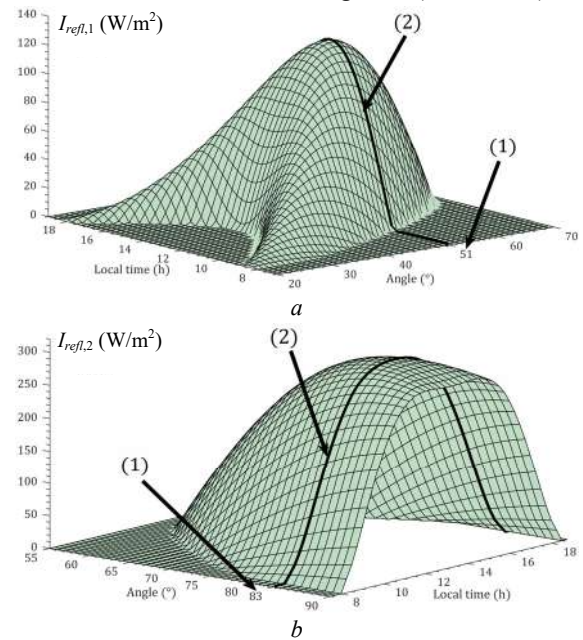


Fig. 2. Variation of reflected solar irradiation from (a) top and (b) bottom reflectors on December 10th. 1 – optimal tilts; 2 – optimal reflected solar irradiation

For the top side reflector (Fig. 2,a), to obtain the maximum reflected solar irradiation from this booster in December, it must be tilted at 51° from the collector plan, which is the optimum tilt of the top reflector in this month.

Similarly, for the bottom reflector (Fig. 2,b), the optimal inclination angle in December for this reflector is 83° calculated from the receiver plan.

Doing the same steps for the other months, the obtained results are presented in Fig. 3.

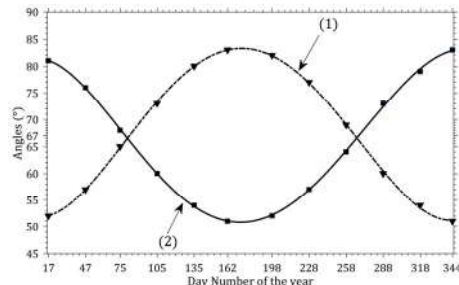


Fig. 3. Annual variation of optimal tilts of:
(1) top and (2) bottom reflectors

Figure 3 shows the annual variation of optimal tilt angles of reflectors, as a function of the day number of the year. $\alpha_{opt,1}$ achieved a maximum in June (83°) and a minimum in December (51°). Furthermore, $\alpha_{opt,2}$ touched its uppermost in December (83°) and lowermost in June (51°).

Figure 4 illustrates the annual variation of the reflected solar irradiation from the top and bottom reflectors as a function of local time and days number of the year. $I_{refl,1}$ take a minimum in the summer period and a maximum in spring and autumn. On the other hand, $I_{refl,2}$ extended their superior in the summer months when the sun will be at its highest, and inferior in winter when it will be at its lowest.

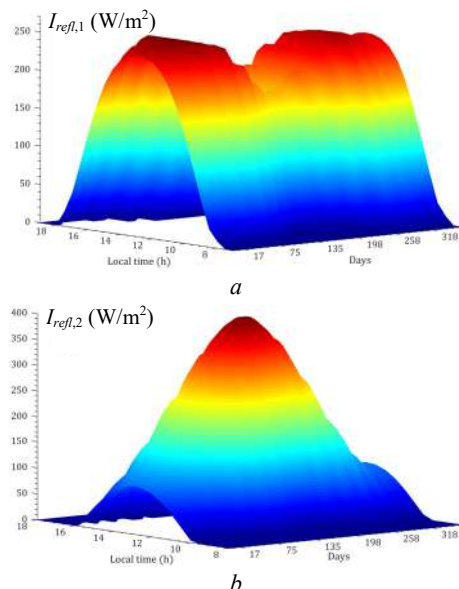


Fig. 4. Annual variation of the reflected solar irradiation from the (a) top and (b) bottom reflectors

4. Conclusions.

In this paper, optimal tilt angles of two flat plate reflectors, attached edge to edge on the top and bottom sides of a solar collector, are optimized. The impact of adding reflectors on the amount of incoming solar

irradiation is examined. The principal results obtained in this paper are:

- the quantity of solar irradiation reflected from the top side reflector can be increased by tilting this booster forward during the summer and backward during the winter, in contrast to the bottom reflectors.

- Due to the difference in the sun's altitude angle, the optimal tilts of the top and bottom reflectors were observed to fluctuate significantly from month to month.

- The model described in this work can be utilized anywhere for all solar applications with the exception of photovoltaic applications that do not require cooling, particularly during the hot months of April to August in hot climates.

Conflict of interest. The authors declare that they have no conflicts of interest.

REFERENCES

1. Saeed H., Mehmood T., Khan F.A., Shah M.S., Ullah M.F., Ali H. An improved search ability of particle swarm optimization algorithm for tracking maximum power point under shading conditions. *Electrical Engineering & Electromechanics*, 2022, no. 2, pp. 23-28. doi: <https://doi.org/10.20998/2074-272X.2022.2.04>.
2. Praveen Kumar T., Ganapathy S., Manikandan M. Improvement of voltage stability for grid connected solar photovoltaic systems using static synchronous compensator with recurrent neural network. *Electrical Engineering & Electromechanics*, 2022, no. 2, pp. 69-77. doi: <https://doi.org/10.20998/2074-272X.2022.2.10>.
3. Akbar F., Mehmood T., Sadiq K., Ullah M.F. Optimization of accurate estimation of single diode solar photovoltaic parameters and extraction of maximum power point under different conditions. *Electrical Engineering & Electromechanics*, 2021, no. 6, pp. 46-53. doi: <https://doi.org/10.20998/2074-272X.2021.6.07>.
4. Sahraoui H., Mellah H., Drid S., Chrifi-Alaoui L. Adaptive maximum power point tracking using neural networks for a photovoltaic systems according grid. *Electrical Engineering & Electromechanics*, 2021, no. 5, pp. 57-66. doi: <https://doi.org/10.20998/2074-272X.2021.5.08>.
5. Garg H.P., Hrishikesan D.S. Enhancement of solar energy on flat-plate collector by plane booster mirrors. *Solar Energy*, 1988, vol. 40, no. 4, pp. 295-307. doi: [https://doi.org/10.1016/0038-092X\(88\)90002-3](https://doi.org/10.1016/0038-092X(88)90002-3).
6. Bhowmik H., Amin R. Efficiency improvement of flat plate solar collector using reflector. *Energy Reports*, 2017, vol. 3, pp. 119-123. doi: <https://doi.org/10.1016/j.egyr.2017.08.002>.
7. Huang B.J., Sun F.S. Feasibility study of one axis three positions tracking solar PV with low concentration ratio reflector. *Energy Conversion and Management*, 2007, vol. 48, no. 4, pp. 1273-1280. doi: <https://doi.org/10.1016/j.enconman.2006.09.020>.
8. Bahaidarah H., Tanweer B., Gandhidasan P., Rehman S. A Combined Optical, Thermal and Electrical Performance Study of a V-Trough PV System – Experimental and Analytical Investigations. *Energies*, 2015, vol. 8, no. 4, pp. 2803-2827. doi: <https://doi.org/10.3390/en8042803>.
9. Baig H., Jani R., Markam B.K., Maiti S., Mallick T.K. Modelling and experimental analysis of a seasonally tracked V-trough PV/T system in India. *Solar Energy*, 2018, vol. 170, pp. 618-632. doi: <https://doi.org/10.1016/j.solener.2018.06.018>.
10. Kostić L.T., Pavlović Z.T. Optimal position of flat plate reflectors of solar thermal collector. *Energy and Buildings*, 2012, vol. 45, pp. 161-168. doi: <https://doi.org/10.1016/j.enbuild.2011.10.059>.
11. Rahman R., Khan M.F. Performance enhancement of PV Solar System by mirror reflection. *International Conference on Electrical & Computer Engineering (ICECE 2010)*, 2010, pp. 163-166. doi: <https://doi.org/10.1109/ICECE.2010.5700652>.
12. Bione J., Vilela O.C., Fraidenraich N. Comparison of the performance of PV water pumping systems driven by fixed,

tracking and V-trough generators. *Solar Energy*, 2004, vol. 76, no. 6, pp. 703-711. doi: <https://doi.org/10.1016/j.solener.2004.01.003>.

13. Tabet I., Touafek K., Khelifa A., Baissi M.T., Bellel N. Optimization tilts angle of flat plate reflectors placed in left-right side of Hybrid Photovoltaic thermal collector. *2016 International Renewable and Sustainable Energy Conference (IRSEC)*, 2016, pp. 343-347. doi: <https://doi.org/10.1109/IRSEC.2016.7983946>.

14. Rachedi M.Y., Bechki D., Marif Y., Bouguettaia H. Solar Flat Plate Collector Enhanced by Two Reflectors: Optimum Tilts of Reflectors. *2022 1st International Conference on Modern Electrical Engineering and Technology (CIETM)*, 2022.

15. Capderou M. *Atlas Solaire de l'Algérie* [Solar Atlas of Algeria], Tome 1, vols. 1 and 2, Algeria, University Publication Office, 1987. 399 p. (Fra).

16. Duffie J.A., Beckman W.A., Blair N. *Solar Engineering of Thermal Processes, Photovoltaics and Wind*. 5th ed., New York, Willey Publ., 2020. 906 p.

17. Klein S.A. Calculation of monthly average insolation on tilted surfaces. *Solar Energy*, 1977, vol. 19, no. 4, pp. 325-329. doi: [https://doi.org/10.1016/0038-092X\(77\)90001-9](https://doi.org/10.1016/0038-092X(77)90001-9).

Received 08.04.2022
Accepted 13.06.2022
Published 07.09.2022

Mohamed Yacine Rachedi^{1,3}, PhD, Assistant Professor,
Djamel Bechki^{2,3}, Doctor of Physics, Professor,
Yacine Marif^{2,3}, Doctor of Physics, HDR, MCA,
Hamza Bouguettaia^{2,3}, Doctor of Physics, Professor,
¹ Department of Electrical Engineering,
Faculty of Applied Sciences,
University of Ouargla, Algeria.
² Department of Physics,
Faculty of Mathematics & Matter Sciences,
University of Ouargla, Algeria.
³ LENREZA Laboratory,
University of Ouargla, Algeria.
e-mail: rachedi.yacine@univ-ouargla.dz (Corresponding Author),
d_bechki@yahoo.fr, yacine.marif@yahoo.fr;
h_bouguettaia@yahoo.co.uk

How to cite this article:

Rachedi M.Y., Bechki D., Marif Y., Bouguettaia H. Solar flat plate collector enhanced by two reflectors: optimum tilts of reflectors. *Electrical Engineering & Electromechanics*, 2022, no. 5, pp. 67-70. doi: <https://doi.org/10.20998/2074-272X.2022.5.11>

V.Yu. Rozov, S.Yu. Reutskyi, D.Ye. Pelevin, K.D. Kundius

Approximate method for calculating the magnetic field of 330-750 kV high-voltage power line in maintenance area under voltage

Problem. In order to organize effective protection of working personnel from the action of strong electromagnetic influence when performing work on live high-voltage power lines (HVPL), the existing methods of calculating the magnetic field (MF) need to be developed in the direction of their simplification during operational use. **Goal.** The purpose of the work is to develop an approximate method and a simplified methodology for calculating the magnetic field flux density near the surface of the 330-750 kV HVPL wires for the prompt determination of the safe distance of the working personnel to the surface of the HVPL wires at the current value of their operating current. **Methodology.** A new approximate method of calculating the flux density of the MF in the area of work on live HVPL based on the Biot-Savart law and determining the maximum values of the flux density of the MF on the axes of symmetry N of the suspension of N wires, which are decisive for the protection of working personnel, is proposed. **Results.** Exceeding the maximum acceptable level of the MF for individual power lines at their nominal currents, adopted in the European Union, and the need to implement measures to reduce MF were revealed. **Originality.** It is shown that the distribution of the 330-750 kV HVPL near N of its split wires with an error of no more than 2.5 % can be determined by the current of only one of the phases of the HVPL. This distribution of MF, which is uneven, is determined by the order of axial symmetry N with the maximum values of the flux density of the MF lying on the axes of symmetry N of the suspension of the phase wires. **Practical value.** The development of an approximate method and a simplified methodology for calculating the flux density of the MF near the surface of the wires of 330-750 kV HVPL, which allows you to quickly, without the use of a computer, calculate the safe distance to the wires of a specific HVPL at the current value of its operating current, as well as determine the necessary measures for the protection of personnel from the MF, which can be implemented either by physically limiting the minimum distance from the worker's body to the surface of the wires to a dangerous one, or by necessary reduction of the HVPL operating current during repair work. **Verification.** An experimental verification of the proposed method and methodology was carried out on a laboratory installation with a mock-up of a phase of a 330 kV HVPL from AC 400 type wires at 1500 A current, which confirmed the correctness of the proposed calculation relationships. References 30, figures 9.

Key words: high-voltage power line, live-line maintenance, magnetic field near wires, calculation method.

Проблема. Для організації ефективного захисту робочого персоналу від дії сильного електромагнітного впливу при виконанні робіт на високовольтних лініях електропередачі (ЛЕП) під напругою, потребують розвитку існуючі методи розрахунку магнітного поля (МП) в напрямі їх спрощення при оперативному використанні. **Мета.** Метою роботи є розробка наближеного методу та спрощеної методики розрахунку індукції магнітного поля поблизу поверхні проводів ЛЕП 330-750 кВ для оперативного визначення безпечної дистанції робочого персоналу до поверхні проводів ЛЕП при поточному значенні їх робочого струму. **Методологія.** Запропоновано новий наближений метод розрахунку індукції МП в зоні виконання робіт на ЛЕП під напругою, що ґрунтується на законі Біо-Савара, та визначенні максимальних значень індукції МП ЛЕП на осях симетрії N підвісу N проводів, що є визначальними для захисту робочого персоналу. **Результати.** Виявлено перевищення прийнятого в Європі гранично допустимого рівня МП для окремих ЛЕП при їх номінальних струмах, та необхідність реалізації заходів із зменшення МП. **Оригінальність.** Показано, що розподіл МП ЛЕП 330-750 кВ поблизу N її розщеплених проводів з похибкою не більш 2,5 % може визначатися за МП тільки однієї із фаз ЛЕП. Цей розподіл МП, що є нерівномірним, визначається порядком осевої симетрії N з максимальними значеннями індукції магнітного поля, що лежать на осях симетрії N підвісу проводів фаз. **Практична цінність.** Виконана розробка наближеного методу і спрощеної методики розрахунку індукції магнітного поля поблизу поверхні проводів високовольтної ЛЕП 330-750 кВ, що дозволяють оперативно, без використання комп'ютера, розраховувати безпечну відстань до проводів конкретної ЛЕП при поточному значенні її робочого струму, а також визначити необхідні заходи із захисту персоналу від МП, які можуть бути реалізовані або шляхом фізичного обмеження мінімальної відстані від тіла робітника до поверхні проводів до небезпечної, або необхідного зменшення робочого струму ЛЕП на час ремонтних робіт. **Верифікація.** Здійснено експериментальну перевірку запропонованих метода та методики на лабораторній установці з макетом фази ЛЕП 330 кВ із проводів типу АС 400 при струмі 1500 А, яка підтвердила коректність запропонованих розрахункових співвідношень. Бібл. 30, рис. 9.

Ключові слова: високовольтна лінія електропередачі, роботи без зняття напруги, магнітне поле поблизу проводів, метод розрахунку.

Introduction. One of the effective ways of increasing the profitability of main power networks is to carry out the repair work on overhead power lines (PLs) of ultra-high voltage under working voltage [1-6]. This allows to preserve the power supply of consumers during the repair period. However, when organizing such works, which are carried out in Ukraine by the staff of the National Energy Company NPC Ukrenergo near power lines (Fig. 1), there is a problem of protecting personnel from the action of a strong electromagnetic field of power frequency, which is characterized by the current values of the strength E of the electric field (EF) and the flux

density B of the magnetic field (MF) and can reach a dangerous level [7, 8].

At present, the problem of personnel protection from the EF is practically solved with the help of special shielding protective suits (Fig. 1) made of electrically conductive material [9-13]. But these suits do not shield the MF [14, 15]. The known methods for passive and active shielding of the PL's MF used to reduce it in residential and public buildings [16-20] also cannot be applied near PLs' wires, as they require a significant amount of free space for placing shielding elements,

© V.Yu. Rozov, S.Yu. Reutskyi, D.Ye. Pelevin, K.D. Kundius



Fig. 1. Execution of repair works by NPC «Ukrenergo» on the 330 kV power line under voltage

which is not near PL's wires. Therefore, the protection of personnel from the PL's MF near its wires, which is potential [21, 22] and decreases when moving away from the PL, can be carried out in the traditional way – distance protection [19] by introducing a safe distance between the wires and the worker's body. Such distance should ensure that the flux density of the MF on the worker's body falls to the maximum permissible level (6 mT), which is regulated by the requirements of the European Union [7, 8]. To determine this safe distance, it is necessary to quickly, in the field, after receiving data on the current load of the PL, perform calculations of the flux density of the MF in the working area of the PL (Fig. 1). The working zone is formed at a distance of 2 mm from the surface of the PL's wires. Here, 2 mm is the thickness of the protective suit, which limits the minimum distance between the wire and the worker's body when he/she touches the wire, and L is the safe distance at which the flux density of the PL's MF is guaranteed to fall to the maximum permissible level.

However, the known methods of calculating MF, near PL's wires [23-27], are based on numerical calculations that are quite difficult for the practical use and require the use of the computer special code. This makes it difficult to perform an operational determination in the field of the flux density of the MF near the PL's wire, which is necessary for the organization of safe work of personnel from point of view of the MF when performing repair work on the PL under load under voltage. Analytical methods based on Biot-Savart law [21, 22, 28] are more acceptable for operational calculation of the MF of the PL. But these methods are justified only for calculating the MF at a significant distance from the PL, which exceeds the interphase distance between its wires [21, 22, 29]. In addition, the specified methods do not take into account such a feature of the design of the phase wires of the 330-750 kV PL's wires as their splitting, which is essential for the calculation of the MF [2, 3, 30] and also require the use of a computer. Thus, the known methods of calculating MF near 330-750 kV PL's wires need to be developed.

The goal of the work is to develop an approximate method and a simplified technique for calculating the flux density of the magnetic field near the surface of 330-750 kV PL's wires for operational determination of the safe

distance of working personnel to the surface of PL's wires at the current value of their operating current.

Design of 330-750 kV power lines. The analysis of the geometric dimensions of the suspension of wires of real 330-750 kV PLs [2, 30] shows that their phases are performed by split into $N \in (2-5)$ wires, the axes of which lie at the vertices of regular symmetrical polygons (Fig. 2) with the radius of the circumscribed circle R .

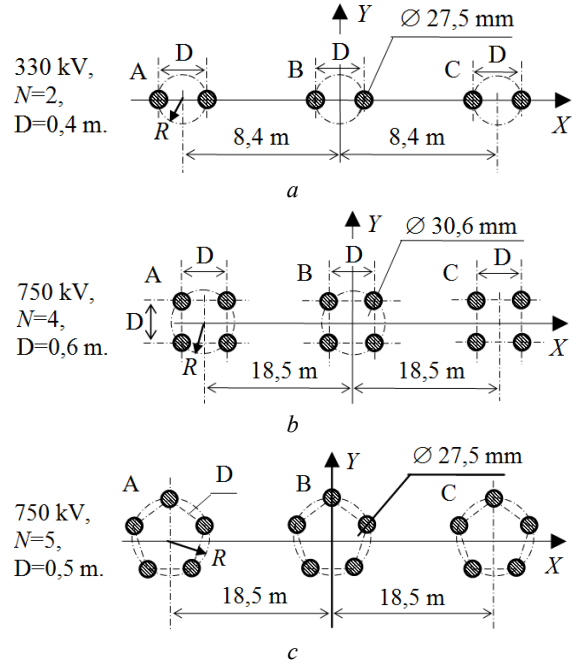


Fig. 2. Design of the suspension of the wires of the 330-750 kV PLs working in Ukraine

As follows from Fig. 2, diameters d of the PL's wires of 27-31 mm is an order of magnitude smaller than the distance D of 0.4-0.6 m between split phase wires and the interphase distance of 8.4-18.5 m. This makes it possible to ignore the non-uniformity of the current density in the wires caused by the proximity effect when calculating the MF, and to successfully use the analytical method [22] for the approximate calculation of the MF's flux density of the PL at observation points P (Fig. 3), which are located near the surface of the wires ($l_r \in (0.002-500 \text{ mm})$).

Method of calculation of the MF. We substantiate the possibility of performing the calculation of the flux density of the MF when placing the observation point P (Fig. 3) near the surface of the PL's wires, based on the use of the method proposed by the authors in [22, 29], which is based on the Biot-Savart law and has undergone thorough experimental verification.

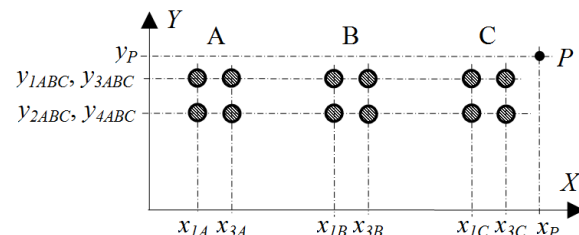


Fig. 3. Coordinates of the location of the wires of the PL's phases and observation point P on the example of a 750 kV PL

We perform the analysis on a plane oriented normal to the direction of the PL's axis direction for the suspension of wires in accordance with Fig. 4 with typical assumptions [21, 22] about potentiality and plane-parallelism of the PL's MF. These assumptions must be supplemented with the provisions that the currents in the split wires of the individual phases of the PL are identical, have a uniform density, and the wires are made of a homogeneous material and have the correct right shape with diameter d .

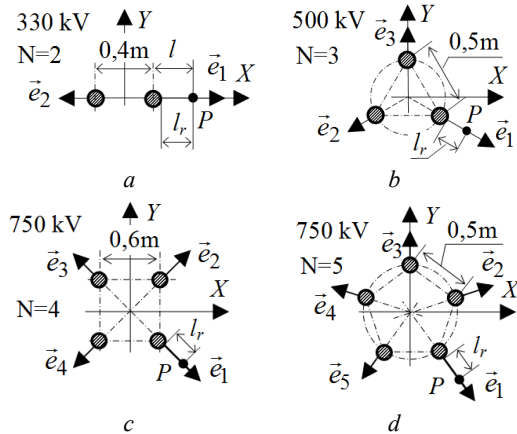


Fig. 4. Geometry of the suspension of the phase wires of the 330-750 kV PLs

Then, according to [22, 29], the effective values of the components of the MF's flux density vector of each phase $\xi \in A, B, C$ at the observation point P (Fig. 3) when the phases of the power line are split into N wires can be calculated as:

$$B_{x,\xi,n}(P) = \frac{\mu_0 I}{2\pi N} \sum_{n=1}^N \frac{y_P - y_{\xi,n}}{(x_P - x_{\xi,n})^2 + (y_P - y_{\xi,n})^2}, \quad (1)$$

$$B_{y,\xi,n}(P) = -\frac{\mu_0 I}{2\pi N} \sum_{n=1}^N \frac{x_P - x_{\xi,n}}{(x_P - x_{\xi,n})^2 + (y_P - y_{\xi,n})^2}, \quad (2)$$

$$B_d(P) = \sqrt{(B_x(P))^2 + (B_y(P))^2}, \quad (3)$$

where I is the phase current of the PL; x_P, y_P are the coordinates of the observation point P ; $x_{\xi,n}, y_{\xi,n}$ are the coordinates of the intersection of the axes of the wires of n phases $\xi \in A, B, C$ of the plane, perpendicular to the axis of the PL, $B_d(P)$ is the module of the MF's flux density vector at the point P .

The results of the calculation of the magnetic flux density distribution of phase A of the PL according to (1)-(3) at different N (Fig. 2) and nominal current are presented in Fig. 5. The distribution of the MF for other phases of the PL is identical.

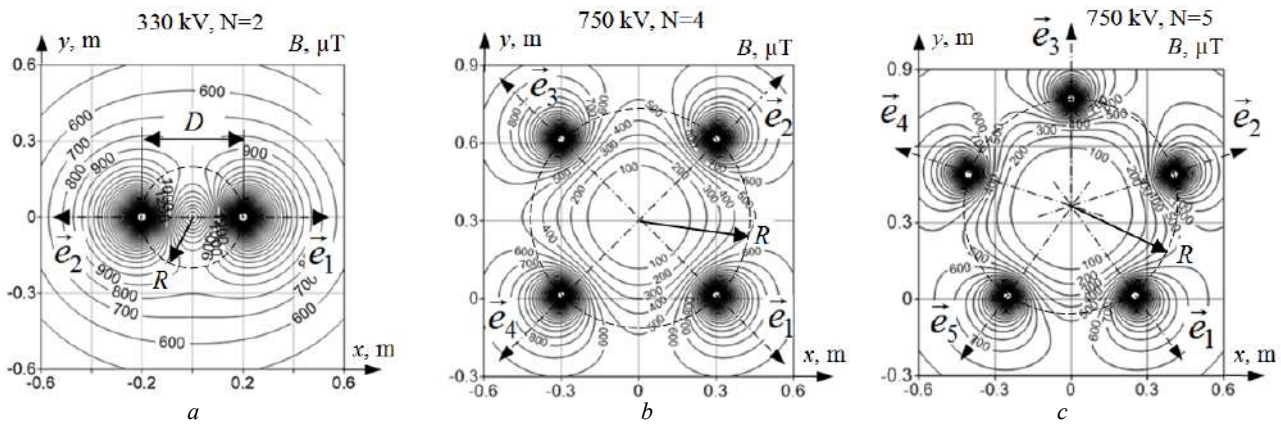


Fig. 5. Distribution of the MF's flux density near phase wires of different PLs in a plane normal to its axis

The analysis of the nature of the distribution of the MF's flux density (Fig. 5) shows that it is irregular and has zones with maximum values that coincide with the directions \vec{e} (Fig. 4, 5), which are determined by the order of axial symmetry of N wires of the PL's phase. Therefore, it is proposed to calculate the MF on the axes of symmetry under the conditions $P \in \vec{e}$, which correspond to the worst cases for the working personnel with the maximum values of the MF's flux density and at the same time make it possible to significantly simplify the calculation.

Figure 6 presents the results of the calculation according to (1)-(3) of the flux density of the MF phases of different PLs at nominal currents and remote observation points from the surface of the wires by distance l_r . As follows from Fig. 6, at nominal currents, the flux density of the MF at the minimum distance from P to the wires (2 mm) ranges from 11.4 mT for 330 kV PL to 6.4 mT for 750 kV PL and exceeds the maximum permissible level of 6 mT in 1.9-1.07 times.

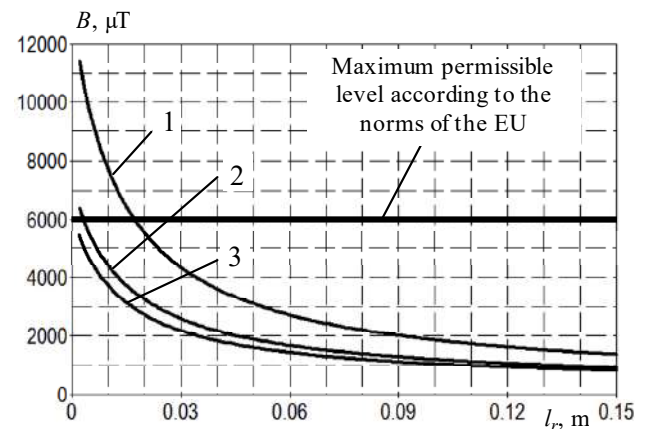


Fig. 6. Dependence of maximum values of the MF's flux density of different PLs on the distance l_r to the surface of their wires (1 – PL 330, $N=2, I_n=1.7$ kA; 2 – PL 750, $N=4, I_n=2$ kA; 3 – PL 750, $N=5, I_n=2$ kA)

For the worst case (for 330 kV PL, Fig. 2,a), the flux density of the MF drops to the maximum permissible level only at $l_r = 17$ mm, which indicates the need to limit the working distance by 15 mm, or to reduce the load of the PL and its operating current accordingly to 0.52 from the nominal. Here, the working zone L of the PL in the calculation can be limited to a distance of $l_r = 20$ mm, at which the mutual influence of the MF from the currents of different phases of the PL can be neglected. Then the calculation of the maximum values of the flux density of the MF near the PL's wires can be performed for one phase and according to (1)-(3) will be described by the following relationships:

$$P \in \vec{e}, \sqrt{(x_p - x_n)^2 + (y_p - y_n)^2} > R, \quad (4)$$

$$B_{\max x,n}(P) = \frac{\mu_0 I}{2\pi N} \sum_{n=1}^N \frac{y_p - y_n}{(x_p - x_n)^2 + (y_p - y_n)^2}, \quad (5)$$

$$B_{\max y,n}(P) = -\frac{\mu_0 I}{2\pi N} \sum_{n=1}^N \frac{x_p - x_n}{(x_p - x_n)^2 + (y_p - y_n)^2}, \quad (6)$$

$$B_{\max d}(P) = \sqrt{(B_{\max x}(P))^2 + (B_{\max y}(P))^2}, \quad (7)$$

where \vec{e} is the vector the direction of which coincides with one of the N axes of symmetry of split PL's wires.

Here, the relative error of the calculation when using (4)-(7), which do not take into account the mutual influence of the MF from the currents of different phases of the PL compared to the calculation based on (1)-(3), does not exceed 2.5 % (Fig. 7) and is quite acceptable for approximate calculation.

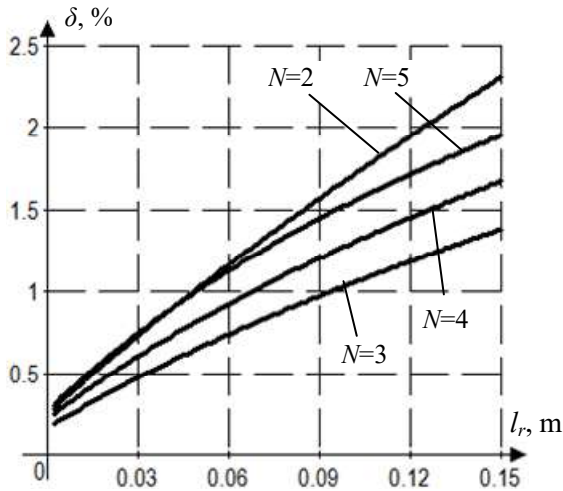


Fig. 7. Calculated by (4)-(7) and (1)-(3) the relative error of calculation of the MF of different PLs near wires of one phase without taking into account the influence of the MF from currents of other phases ($N \in 2-5$)

To further simplify the calculation, we transform the ratios (4)-(7), moving from the coordinates of the location of the wires x_p, y_p, x_n, y_n to the geometric parameters of the suspension of the wires R, D and the distance l (Fig. 2-4) and obtain the following simplified calculation relations for different N :

$$B_{N=2}(l) = I \cdot \frac{\mu_0}{2\pi} \frac{(l+R)}{l(l+2R)}, \quad (8)$$

$$B_{N=3}(l) = I \cdot \frac{\mu_0}{6\pi} \left[\frac{1}{l} + \frac{2(l+1.5R)}{l^2 + 3Rl + 3R^2} \right], \quad (9)$$

$$B_{N=4}(l) = I \cdot \frac{\mu_0}{2\pi} \frac{(l+R)^3}{(l+R)^4 - R^4}, \quad (10)$$

$$B_{N=5}(l) = I \cdot \frac{\mu_0}{10\pi} \left[\frac{1}{l} + \frac{2(l+R - R\cos(2\pi/5))}{(l+R - R\cos(2\pi/5))^2 + (R\sin(2\pi/5))^2} + \frac{2(l+R - R\cos(4\pi/5))}{(l+R - R\cos(4\pi/5))^2 + (R\sin(4\pi/5))^2} \right], \quad (11)$$

where $R = \frac{D}{2\sin(\pi/N)}$; l is the distance from the axis of

the wire to the point of observation P .

The obtained calculation relationships (4)-(11) are the scientific basis for a simplified calculation method and allow to quickly, with the help of a calculator, calculate the maximum values of the magnetic flux density of the PL for the current values of the load current as a function of the distance l to the PL's wires, taking into account the geometry of their suspension.

Thus, on the basis of the above analysis, an approximate calculation method (4)-(7) and a simplified calculation technique (8)-(11) built on its basis can be proposed for the operational determination of the flux density of the MF in the area of performance of works on live PL, which is based on the Biot-Savart law and determining the maximum values of flux density for any of the phases lying on the axes of symmetry of the suspension of the split wires and determining the safe distance to the wires of a specific PL at the current value of its operating current.

The use of the proposed method and technique allows to quickly determine specific measures to protect personnel from the MF when performing work under voltage, which can be implemented either by limiting the minimum distance from the worker's body to the wires (installation of capes or mats of the required thickness on the PL's wires in the working area), or a corresponding reduction in the operating current of the PL for the period of repair works.

Experimental verification of the proposed method and calculation technique. The experimental verification of the proposed calculation relationships (8)-(12) was carried out on an experimental installation with a laboratory model of a phase of the 330 kV PL (Fig. 8), which was created at the magnetomeasuring stand of the magnetodynamic complex of the Department of Magnetism of Technical Objects of the Institute of A.M. Pidhornyi Institute of Mechanical Engineering Problems of the National Academy of Sciences of Ukraine.

The model is made on the basis of 2 PL's wires of AC 400 type with $d = 28$ mm and length of 5 m and their arrangement according to Fig. 2,a. The experimental installation allows to carry out research with current in each wire from 100 to 750 A (200-1500 A per phase). A three-phase induction regulator of the IR62 type

($P_n = 30$ kVA, $U_n = 22-382$ V), loaded on two step-down single-phase transformers of the OSU-80/0.5 type ($P_n = 100$ kVA, $U_n = 12.2$ V, $I_n = 8140$ A), which are connected to the corresponding wires of the laboratory installation, was used as a regulated power source. The MF's flux density was measured by a Gaussmeter 410 type magnetometer with a special sensor positioning system (Fig. 8), and the current in the model wires was measured using TNFP3000/5 A type current transformers and E526 type ammeters.



Fig. 8. Experimental installation with a laboratory model of a 330 kV PL's phase and a magnetometer sensor positioning device

The results of the experimental studies are presented in Fig. 9 and confirm the coincidence of the results of the calculation and the experiment at nominal current in the wires of 500-750 A with a spread of no more than 10 %, which is quite acceptable for a physical experiment.

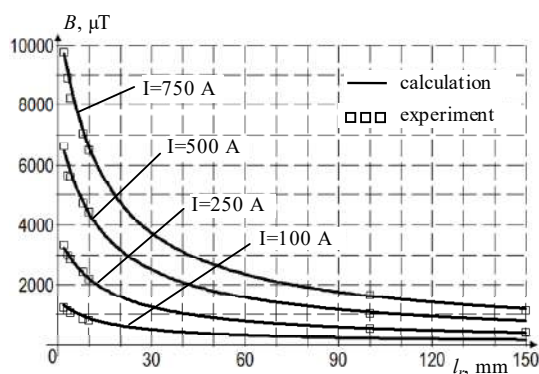


Fig. 9. Results of measuring the flux density of the MF on the laboratory model of the phase of the PL 330 (Fig. 8) at $l_r = 0.002-0.150$ m and currents in wires of 100-750 A and their comparison with the calculation

This spread is mainly related to the imperfection of the AC 400 type wire (it is made of twisted cores, see Fig. 8) and requires further analysis. When the current decreases, the error increases which is associated with an increase in the influence of interference from the power supply cables of the model (Fig. 8).

Conclusions.

1. An analysis of the geometric dimensions of the suspension of wires of typical 330-750 kV PLs was performed, based on which it was shown that for the approximate calculation of the magnetic flux density near their wires, an analytical method based on the Biot-Savart law can be used with the determination of the magnetic field only for one of its phases, without taking into account the influence of the magnetic field of the currents of other phases, which allows to simplify the calculation with a limited error not exceeding 2.5 %.

2. The calculation of the magnetic flux density near the wires of operating overhead power lines 330-750 kV was carried out at their nominal currents, which showed an excess of the maximum permissible magnetic flux density level adopted in the European Union (6 mT) for 330 kV power lines with $N=2$ (at distance from the surface of the wires of 17 mm) and 750 kV with $N=4$ (at distance of 3 mm) and the need to take measures to reduce the magnetic field acting on personnel when performing live work.

3. An approximate method of calculating the magnetic flux density near the surface of N the split wires of the phases of the 330-750 kV power lines, the axes of which lie at the vertices of symmetric polygons with the order of symmetry N , is proposed, which is based on determining only the maximum values of the magnetic flux density lying on the axes of symmetry of N suspension of wires and are decisive for the organization of protection of working personnel from the action of the magnetic field. The method allows to significantly simplify the calculation, performing it only for the axes of symmetry, and not for the entire space.

4. On the basis of the proposed approximate method, a simplified technique of calculating the magnetic field has been developed, which can be implemented without the use of a computer, which allows in the field to quickly calculate the safe distance to the wires of the specific power line at the current value of its operating current and to determine the measures necessary to protect personnel from the MF when performing live work, which can be implemented either by physically limiting the distance from the worker's body to the surface of the wires to a dangerous distance, or by necessary reducing the operating current of the power line during repair work.

5. Experimental verification of the proposed approximate method and the simplified technique of calculating the magnetic field based on it was carried out on a laboratory installation with a phase model of a 330 kV power line made of wires of the AC 400 type at nominal current of 1500 A (750 A per wire). The experiment confirmed the coincidence of the results of the calculation and the experiment with an acceptable error for engineering calculations of no more than 10 %, and the correctness of the proposed calculation method, as well as the feasibility of developing on their basis

normative documents of the Ministry of Energy of Ukraine on the protection of working personnel from the negative impact of the magnetic field when performing work on power transmission lines under voltage.

Acknowledgment. The authors express their gratitude to the Engineers of the Department of Magnetism of Technical Objects of the Institute of Mechanical Engineering Problems of the National Academy of Sciences of Ukraine A.V. Yerisov and O.V. Sokol for the creative approach and courage shown during the creation under fire, under martial law, an experimental installation and successful testing of a laboratory model of the PL 330 kV.

Conflict of interest. The authors declare no conflict of interest.

REFERENCES

1. Lovrencic A., Racz L., Gocsei G., Nemeth B. Improving the Reliability of the Transmission and Distribution Network. *2019 7th International Youth Conference on Energy (IYCE)*, 2019, pp. 1-6. doi: <https://doi.org/10.1109/IYCE45807.2019.8991565>.
2. *Pravila ulashtuvannya electroustanovok* [Electrical installation regulations]. Kharkiv, Fort Publ., 2017. 760 p. (Ukr).
3. *SOU-N EE 20.666:2007 Instrukciya z vikonannya robit pid naprugoyu na PL 110-750 kV* [SOU-N EE 20.666:2007 Instructions for performing live work on 110-750 kV power lines]. Kyiv, OEP GRIFRE Publ., 2007. (Ukr).
4. Sobchuk V.S., Sobchuk N.V. *Tehnologiyi robit pid naprugoyu* [Technologies of works under voltage]. Vinnytsia, VNTU Publ., 2006. 101 p. (Ukr).
5. Kazanskij S.V. *Ekspluatatsiya elektrichnih system. Obslugoivuвання elektrichnih merezh pid robochoyu naprugoyu* [Operation of electrical systems. Maintenance of electrical networks under working voltage]. Kyiv, NTUU «KPI» Publ., 2016. 237 p. (Ukr).
6. *IEEE Guide for Maintenance Methods on Energized Power Lines*. IEEE Std 516-2021, 2022, pp. 1-159. doi: <https://doi.org/10.1109/IEEESTD.2022.9678146>.
7. Directive 2013/35/EU of the European Parliament and of the Council of 26 June 2013 on the minimum health and safety requirements regarding the exposure of workers to the risks arising from physical agents (electromagnetic fields). *Official Journal of the European Union*, 2013, L 179, pp. 1-21. Available at: <https://eur-lex.europa.eu/LexUriServ/LexUriServ.do?uri=OJ:L:2013:179:0001:0021:EN:PDF> (Accessed 12 May 2022).
8. Stam R. Comparison of international policies on electromagnetic fields (power frequency and radiofrequency fields). *National Institute for Public Health and the Environment Ministry of Health, Welfare and Sport*, 2018, 18 p. doi: <https://doi.org/10.21945/rivm-document-electromagnetic-fields>.
9. Su Y., Wang X., Li Y., Pan Z., Liu Z. Analysis of the conductivity property of live working shielding clothing. *Journal of Industrial Textiles*, 2018, vol. 48, no. 3, pp. 643-659. doi: <https://doi.org/10.1177/1528083717732071>.
10. Gocsei G., Nemeth B., Tarcsa D. Extra low frequency electric and magnetic fields during live-line maintenance. *2013 IEEE Electrical Insulation Conference (EIC)*, 2013, pp. 100-104. doi: <https://doi.org/10.1109/EIC.2013.6554212>.
11. Gocsei G., Nemeth B., Tamus Z.A., Kiss I., Meixner J. Shielding efficiency of conductive clothing during live-line maintenance. *2014 11th International Conference on Live Maintenance (ICOLIM)*, 2014, pp. 1-5. doi: <https://doi.org/10.1109/ICOLIM.2014.6934339>.
12. Gocsei G., Nemeth B., Tamus Z.A., Kiss I. Face protection investigation against electric field on live line workers. *2012 IEEE International Symposium on Electrical Insulation*, 2012, pp. 535-539. doi: <https://doi.org/10.1109/ELINSL.2012.6251527>.
13. Malgesini R., Valagussa C., Villa A., Carraro R., De Dona G., Milanello C.D., Parizia A.A. Conductive clothing for live line working. *2014 11th International Conference on Live Maintenance (ICOLIM)*, 2014, pp. 1-4. doi: <https://doi.org/10.1109/ICOLIM.2014.6934340>.
14. Gocsei G., Nemeth B., Kiss I., Berta I. Shielding efficiency of conductive clothing in magnetic field. *Journal of Electrostatics*, 2013, vol. 71, no. 3, pp. 392-395. doi: <https://doi.org/10.1016/j.elstat.2013.01.001>.
15. Gocsei G., Nemeth B., Kiss I., Berta I. Health effects of magnetic fields during live-line maintenance. *2014 11th International Conference on Live Maintenance (ICOLIM)*, 2014, pp. 1-6. doi: <https://doi.org/10.1109/ICOLIM.2014.6934329>.
16. Kuznetsov B.I., Nikitina T.B., Bovdii I.V., Voloshko O.V., Kolomiets V.V., Kobylanskiy B.B. Comparison of the effectiveness of triple-loop and double-loop systems of active shielding of a magnetic field in a multi-storey old buildings. *Electrical Engineering & Electromechanics*, 2022, no. 3, pp. 21-27. doi: <https://doi.org/10.20998/2074-272X.2022.3.04>.
17. Kuznetsov B.I., Nikitina T.B., Bovdii I.V., Voloshko O.V., Kolomiets V.V., Kobylanskiy B.B. Method of adjustment of three circuit system of active shielding of magnetic field in multi-storey buildings from overhead power lines with wires triangular arrangement. *Electrical Engineering & Electromechanics*, 2022, no. 1, pp. 21-28. doi: <https://doi.org/10.20998/2074-272X.2022.1.03>.
18. Rozov V.Y., Pelevin D.Y., Pielievina K.D. External magnetic field of urban transformer substations and methods of its normalization. *Electrical Engineering & Electromechanics*, 2017, no. 5, pp. 60-66. doi: <https://doi.org/10.20998/2074-272X.2017.5.10> (Rus).
19. Rozov V.Yu., Reutskiy S.Yu., Pelevin D.Ye., Pyliugina O.Yu. The magnetic field of power transmission lines and the methods of its mitigation to a safe level. *Technical Electrodynamics*, 2013, no. 2, pp. 3-9. (Rus).
20. Conti R., Giorgi A., Rendina R., Sartore L., Sena E.A. Technical solutions to reduce 50 Hz magnetic fields from power lines. *2003 IEEE Bologna Power Tech Conference Proceedings*, 2003, vol. 2, pp. 1016-1021. doi: <https://doi.org/10.1109/PTC.2003.1304685>.
21. Rozov V.Yu., Reutskiy S.Yu., Pelevin D.Ye., Yakovenko V.N. The research of magnetic field of high-voltage ac transmissions lines. *Technical Electrodynamics*, 2012, no. 1, pp. 3-9. (Rus).
22. Rozov V.Yu., Reutskiy S.Yu., Pyliugina O.Yu. Method of calculating the magnetic field of three-phase power lines. *Technical Electrodynamics*, 2014, no. 5, pp. 11-13. (Rus).
23. Kim Y.S. Analysis of Magnetic Field for Power Transmission Line With Multiple AC Singular Currents by Coupling of Fourier Series Expansion and FEM. *IEEE Transactions on Magnetics*, 2013, vol. 49, no. 5, pp. 2013-2016. doi: <https://doi.org/10.1109/TMAG.2013.2242451>.
24. Pao-la-or P., Isaramongkolrak A., Kulworawanichpong T. Finite Element Analysis of Magnetic Field Distribution for 500-kV Power Transmission Systems. *Engineering Letters*, 2010, vol. 18, no. 1, pp. 1-9.
25. Li Q., Rowland S.M., Shuttleworth R. Calculating the Surface Potential Gradient of Overhead Line Conductors. *IEEE Transactions on Power Delivery*, 2015, vol. 30, no. 1, pp. 43-52. doi: <https://doi.org/10.1109/TPWRD.2014.2325597>.
26. Krajewski W. Numerical evaluation of the magnetic field exposure near the transition tower of an overhead-underground HV line. *Progress In Electromagnetics Research M*, 2010, vol. 14, pp. 247-261. doi: <https://doi.org/10.2528/PIERM10101102>.
27. Moro F., Turri R. Accurate calculation of the right-of-waywidth for power line magnetic field impact assessment.

Progress In Electromagnetics Research B, 2012, vol. 37, pp. 343-364. doi: <https://doi.org/10.2528/PIERB11112206>.

28. Moro F., Turri R. Fast Analytical Computation of Power-Line Magnetic Fields by Complex Vector Method. *IEEE Transactions on Power Delivery*, 2008, vol. 23, no. 2, pp. 1042-1048. doi: <https://doi.org/10.1109/TPWRD.2007.915212>.

29. SOU-N EE 20.179:2008 *Rozrahunok elektrichnogo i magnitnogo poliv linij elektroperedavannya. Metodika (zi zminami) (u redakciyi nakazu Minenergo vugillya vid 01 lipnya 2016 r. №423)*. [SOU-N EE 20.179:2008 Calculation of electric and magnetic fields of power lines. Methodology (with changes) (in the edition of the order of the Minenergugillya dated July 1, 2016, no. 423)]. Kyiv, Minenergugillya Ukraine Publ., 2016. 37 p. (Ukr).

30. Kirik V.V. *Elektrichni merezhi ta sistemi* [Electrical networks and systems]. Kyiv, NTUU «KPI» Publ., Politehnika Publ., 2021. 324 p. (Ukr).

How to cite this article:

Rozov V.Yu., Reutskiy S.Yu., Pelevin D.Ye., Kundius K.D. Approximate method for calculating the magnetic field of 330-750 kV high-voltage power line in maintenance area under voltage. *Electrical Engineering & Electromechanics*, 2022, no. 5, pp. 71-77. doi: <https://doi.org/10.20998/2074-272X.2022.5.12>

Received 08.04.2022

Accepted 23.06.2022

Published 07.09.2022

V.Yu. Rozov¹, Doctor of Technical Science, Professor,
Corresponding member of NAS of Ukraine,
S.Yu. Reutskiy¹, PhD, Senior Research Scientist,
D.Ye. Pelevin¹, PhD, Senior Researcher,
K.D. Kundius¹, Leader Engineer, Post Graduate Student,
¹ A.M. Pidhornyi Institute of Mechanical Engineering Problems
of the National Academy of Sciences of Ukraine,
2/10, Pozharskogo Str., Kharkiv, 61046, Ukraine,
e-mail: vyurozov@gmail.com; sergiyreutskiy@gmail.com;
pelevindmitro@ukr.net (Corresponding Author);
kundiuckateryna@ukr.net

Матеріали приймаються за адресою:

Кафедра "Електричні апарати", НТУ "ХПІ", вул. Кирпичева, 2, м. Харків, 61002, Україна

Електронні варіанти матеріалів по e-mail: a.m.grechko@gmail.com

Довідки за телефонами: +38 067 359 46 96 Гречко Олександр Михайлович

Передплатний індекс: 01216